

# **Nanocarbon Aerogels as Electrically-Heatable Support Frameworks for Functional Nanoparticles**

**Dong Xia**

Supervised by Dr Robert Menzel

Co-Supervisor: Prof Fiona Meldrum

Submitted in accordance with the requirements for the degree of  
Doctor of Philosophy

The University of Leeds  
School of Chemistry  
Faculty of Mathematics and Physical Sciences

August, 2020

I confirm that the work submitted is my own and that appropriate credit has been given where reference has been made to the work of others.

This copy has been supplied on the understanding that it is copyright material and that no quotation from the thesis may be published without proper acknowledgement.

## Acknowledgements

Sincere appreciation goes to my honorific supervisor, Dr Robert Menzel, for his patient teaching, training, and helping during my whole PhD career. He gave me a free atmosphere to meditate and discuss, which are a lifetime wealth for me. Without the suggestions from my supervisor, I cannot improve my writing and managing skills, as well as presenting abilities. He actively encouraged me attending scientific conferences, seminars, and stimulated me talking with scholars from different fields for broadening my research backgrounds, I've gained a wealth of new knowledges despite I'm a shy guy. Importantly, his rigorous and seriously-minded attitudes towards scientific research have encouraged me to become a deeply-thinking scholar. Languages and words limit my gratitude to my supervisor, but all the grateful feelings have been branded in my mind.

Deeply respect to my co-supervisor, Prof Fiona Meldrum, who is a wonderful and celebrated female scientist, for her helps in providing scientific apparatuses and advice for report improvements. She's research achievements published on *Nature* and *Science* journals spurring me working hard and thinking out of the box.

I also want to thank my internal assessor, Prof Dejian Zhou, who is a scholar full of rigorousness and preciseness, for his high-level feedbacks on my reports that have improved my PhD research quality and level significantly.

I very thank Dr Thomas Chamberlain, who encouraged me to take part in various seminars and taught me how to maintain the lab orderly and clean. Also, for his sincerely reminds me of lab safety. I also appreciated him for frequently bring us tasty snacks and for buying the coffee machine.

Deep thanks also go to Dr Alexander Kulak, for his tireless helps with scientific apparatuses training and materials characterizations. I also want to thank Dr Heng Li, Dr Daniel Baker, Dr Umair Zafar, Dr Diana Iruretagoyena, Dr Mohammed Ismail, and Dr Yifei Xu, for their helps in characterizing my samples.

I really thank my friends, Jamie Mannering, Rebecca Stone, Alex Massy, Maha Alsebai, Heng Li, Peng Huang, Xiangyi Chen, Zexi Xu, Ziyu Gao, for their assistances in my PhD career and life. I sincerely appreciate my girlfriend, Huayang Yu, for her loving encouragements and supports, offering me an unforgettable life in the UK.

I appreciate my family members for their unselfish loves and unconditional concerns during my PhD study. At last, I sincerely appreciate the China Scholarship Council and the University of Leeds sponsored my PhD research at University of Leeds.

## Abstract

Nanocarbon aerogels, such as reduced carbon nanotube (rCNT) aerogels and reduced graphene oxide (rGO) aerogels, are promising porous 3D macroscopic materials that have been investigated in a number of fields due to a unique combination of remarkable materials properties, including high specific surface areas, tuneable microstructures, very high porosities and ultralow density. This PhD research will explore the use of nanocarbon aerogels as support materials for functional inorganic nanoparticles in the context of commercially and environmentally-important sorption applications. In contrast to other porous support materials (MOFs, zeolites, mesoporous silicas) used in this context, nanocarbon aerogels exhibit excellent electrical conductivity. This conductivity provides unique capability for direct electrical heating (so called Joule-heating) of the nanocarbon support framework and supported nanoparticles. The Joule-heating of nanocarbon aerogel supports has not been studied in detail yet and will be the focus of this PhD work.

As starting point, the thesis investigates fundamental structure-property relationships for the Joule-heating of different, un-decorated aerogels, produced via ice-templating and emulsion-templating synthetic approaches. Results show that important Joule-heating parameters, such as heating efficiency and heating kinetics, can be controlled through structural nanocarbon aerogel parameters, such as nanocarbon type, aerogel porosity, and nanocarbon graphitization. Joule-heating shows a pronounced linear, anti-proportional correlation with the aerogels' thermal conductivity, showing that aerogels with lowest thermal conductivity show the best Joule-heating performances (and therefore are best suited for Joule-heating applications in sorption, catalysis or sensing). Equivalent interrelationships between nanocarbon aerogel structure, thermal conductivity and heating performance were found for solar thermal heating of nanocarbon aerogels, an alternative heating mode, based on aerogel irradiation with light. The importance of controlling heating performance via structural aerogel control is demonstrated for solar water evaporation, where tuning of aerogel structure can be exploited to increase performance by at least 30 %.

The thesis further analyses how the excellent Joule-heating properties of nanocarbon aerogels can be exploited for sorption related applications. To this end, MMO/rGO hybrid aerogels (MMO = mixed metal oxides) are produced through a new synthetic approach, based on the decoration of GO with inorganic, layered-double-hydroxide (LDH) precursor-particles, followed by hydrogel assembly, freeze-drying and thermal conversion into MMO/rGO aerogels. As second set of

complementary hybrid aerogels, BN/rCNT aerogels (BN = boron nitride) were produced through decoration of CNTs with organic precursor compounds in solution, followed by hydrogel assembly and thermal precursor conversion. The hybrid inorganic/nanocarbon aerogels were systemically characterized via a range of materials characterisation methods, including XRD, TGA, Raman, BET, XPS, SEM-EDX and TEM, showing that both rGO and rCNT aerogels can be decorated at very high particle loading fractions with great uniformity. Both rGO aerogels and rCNT aerogels act as highly effective support framework, providing a range of important functional benefits, including increased surface areas, inhibited nanoparticle aggregation and open, accessible porosity. This excellent support function translates into substantially improved sorption performance (in terms of sorption capacity, uptake kinetics, sorbent regeneration stability) for commercially-relevant and environmentally-important sorption applications, including adsorptive desulfurisation of liquid hydrocarbons and pre-combustion CO<sub>2</sub> capture. Optimised BN/rCNT aerogel shows remarkable sorption capacities for organosulfur compounds (such as dibenzothiophene, DBT) of up to 43 mg·S·g<sup>-1</sup> BN. Optimised MMO/rGO aerogels perform particularly well for elevated-temperature, high-pressure CO<sub>2</sub> capture, exhibiting remarkable high-pressure CO<sub>2</sub> sorption capacities of up to 2.36 mmol CO<sub>2</sub>·g<sup>-1</sup> ads at T = 300 °C and p<sub>CO2</sub> = 8 bar (outperforming other known high-pressure solid-state sorbent materials).

For both inorganic/nanocarbon aerogel systems, Joule-heating provides highly valuable, additional functionality. The decorated aerogels can be heated up to 700 °C at relatively low power inputs. The kinetics of the Joule-heating process are extremely fast at up to 74 °C·s<sup>-1</sup> (4400 °C·min<sup>-1</sup>) for the BN/rCNT aerogels. Local heating of the aerogel framework can be exploited for very rapid thermal regeneration of the sorbent nanoparticles, allowing for sorbent recycling at much lower energy costs than possible via conventional, external heating approaches.

Lastly, Joule-heating at very high electrical power inputs is exploited for nanocarbon aerogel heating to extremely high temperatures. Specifically, hydrothermally produced GO aerogels were annealed at ultrahigh temperature (>2500 °C) via very short Joule-heating treatments at high power input (P = 120 W). The Joule-heating annealed GO aerogels show substantially increased electrical conductivity and graphitic crystallinity after high-temperature Joule-heating of 30 seconds or shorter. The ultrahigh temperature Joule-heating can be readily adapted for a range of new applications, including (i) ultrafast thermal desorption of dye-saturated rGO aerogels (>2500 °C, 30 sec per cycle), (ii) size-controlled synthesis of metallic Pt nanoparticles (~1.5 nm) via flash Joule-heating of precursor-decorated rGO aerogels, (iii) and flash-

heating synthesis of MoO<sub>2</sub> nano-catalysts (~10 nm) with excellent performance in catalytic organosulfur oxidation.

## List of Publications

1. **Dong Xia\***, Peng Huang, Heng Li and Noelia Rubio, Fast and Efficient Electrical-Thermal Responses of Functional Nanoparticles Decorated Nanocarbon Aerogels, *Chemical Communications*, 2020.

DOI: 10.1039/d0cc03784b

2. **Dong Xia**, Heng Li, Jamie Mannering, Peng Huang, Xiarong Zheng, Alexander Kulak, Daniel Baker, Diana Iruetagoiena and Robert Menzel, Electrically-Heatable Graphene Aerogels as Nanoparticle Supports in Adsorptive Desulfurisation and High-Pressure CO<sub>2</sub> Capture. *Advanced Functional Materials*, 2020, 2002788.

DOI: 10.1002/adfm.202002788

3. **Dong Xia**, Heng Li, Peng Huang, Jamie Mannering, Umair Zafar, Daniel Baker and Robert Menzel, Boron-Nitride/Carbon-Nanotube Hybrid Aerogels as Multifunctional Desulfurisation Agents. *Journal of Materials Chemistry A*, 2019 (41), 24027-24037.

DOI: 10.1039/c9ta06599g

4. Ziyu Gao, Pablo Carames-Mendez, **Dong Xia**, Christopher Pask, Patrick McGowan, Paul Bingham, Alex Scrimshire, Giuseppe Tronci and Paul Thornton, The Facile and Additive-Free Synthesis of a Cell-friendly Iron(III)-Glutathione Complex. *Dalton Transactions*, 2020 (30), 10574-10579.

DOI: 10.1039/d0dt02331k

45 Peng Huang, **Dong Xia**, Algy Kazlauciusas, Paul D. Thornton, Long Lin, and Robert Menzel, Dye-mediated Interactions in Chitosan-based Polyelectrolyte/Organo-clay Hybrids for Enhanced Adsorption of Industrial Dyes. *ACS Applied Materials & Interfaces*, 2019 (12), 11961-11969.

DOI: 10.1021/acsami.9b01648

## Table of Contents

Acknowledgements .....	III
Abstract.....	IV
List of Publications .....	VII
Table of Contents.....	VIII
List of Figures .....	XI
List of Tables .....	XXII
List of Abbreviations .....	XXIV
Chapter - 1 Introduction and Literature Review.....	1
1.1 Introduction .....	1
1.2 Literature Review.....	4
1.2.1 Nanocarbons.....	4
1.2.2 Nanocarbon aerogels.....	10
1.2.2.1 Conventional aerogels .....	10
1.2.2.2 Nanocarbon aerogel synthesis .....	10
1.2.3 Adsorption applications .....	17
1.2.3.1 Liquid-phase adsorption .....	17
1.2.3.2 Gas-phase adsorption .....	20
1.2.3.3 Typical inorganic adsorbents .....	23
1.2.4 Hybrid adsorbents.....	26
1.2.4.1 Inorganic/nanocarbon powder adsorbents.....	26
1.2.4.2 Inorganic/nanocarbon aerogel adsorbents .....	28
1.2.5 Joule-heating of nanocarbon materials.....	31
Chapter - 2 Experimental .....	40
2.1 Materials .....	40
2.2 Synthesis of Nanocarbon Aerogels .....	41
2.3 Materials Characterization .....	43
2.4 Joule-Heating Measurements.....	45
Chapter - 3 Tuning the Heating Properties of Pure Nanocarbon Aerogels through Structural Control .....	49
3.1 Introduction .....	49
3.2 Results and Discussion .....	51

3.3 Conclusions .....	65
3.4 Experimental .....	66
3.4.1 Materials synthesis .....	66
3.4.2 Materials characterisation .....	66
3.4.3 Joule-heating measurements .....	68
Chapter - 4 Electrically-Heatable Graphene Aerogels as Nanoparticle Supports in Adsorptive Desulfurisation and High-Pressure CO <sub>2</sub> Capture .....	70
4.1 Introduction .....	70
4.2 Results and Discussion .....	73
4.2.1 Hybrid aerogel synthesis.....	73
4.2.2 Hybrid aerogel characterisation .....	74
4.2.3 Liquid-phase organosulfur sorption .....	85
4.2.3 Thermal sorbent regeneration via electrical framework heating .....	90
4.2.4 High-pressure, elevated-temperature CO <sub>2</sub> adsorption .....	94
4.3 Conclusions .....	98
4.4 Experimental .....	100
4.4.1 Materials synthesis .....	100
4.4.2 Materials characterisation .....	101
4.4.3 Adsorption measurements .....	102
4.4.4 Joule-heating measurements .....	104
Chapter-5 Boron-Nitride/Carbon-Nanotube Hybrid Aerogels as Multifunctional Desulfurisation Agents.....	105
5.1 Brief introduction.....	105
5.2 Results and Discussion .....	107
5.2.1 BN/rCNT aerogel synthesis and characterisation .....	107
5.2.2 Adsorptive desulfurisation.....	115
5.2.3 Joule-heating of BN/rCNT aerogel for sorbent regeneration.....	121
5.2.4 BN/rCNT aerogels fabrication at lower temperatures .....	123
5.3 Conclusions .....	124
5.4 Experimental .....	125
5.4.1 BN/rCNT aerogel synthesis .....	125
5.4.2 Materials characterisation .....	126
5.4.3 Adsorption measurements .....	126

5.4.4 Joule-heating of aerogel adsorbents .....	127
Chapter - 6 High-Temperature Joule-Heating of Graphene Oxide Aerogels.....	128
6.1 Brief introduction.....	128
6.2 Results and Discussion .....	130
6.2.1 High-temperature Joule-heating of reduced GO aerogels .....	130
6.2.2 High-temperature Joule heating of un-reduced GO[HT] aerogels.....	135
6.2.3 Joule-heating annealing of GO[HT] aerogels at prolonged heating duration .....	140
6.2.4 Flash sorbent regeneration.....	145
6.2.5 Joule-heating-based synthesis of metallic nanoparticles.....	147
6.2.6 Joule-heating-based synthesis of metal-oxide nano-catalysts....	152
6.3 Conclusions .....	156
6.4 Experimental .....	157
6.4.1 Materials synthesis .....	157
6.4.2 Materials characterisation .....	158
6.4.3 Ultrahigh temperature Joule-heating.....	158
6.4.4 Dye adsorption/desorption measurements .....	159
6.4.5 Pt NPs/rGO aerogel and MoO <sub>2</sub> NPs/GO[30sec] aerogel syntheses .....	159
6.4.6 Oxidative catalytic desulfurisation measurements .....	160
Chapter - 7 Conclusions and Outlook .....	161
7.1 Conclusions .....	161
7.2 Outlook .....	164
7.3 Concluding Remarks .....	165
References .....	165
Appendix 1 .....	179
Appendix 2 .....	184
Appendix 3 .....	193
Appendix 4 .....	196

## List of Figures

Figure 1 Research overview. ....	3
Figure 1.1 (a) Scanning electron micrograph of single layer graphene crystal. (b) Transmission electron micrograph of single layer graphene lattice in atomic resolution. (c) Scanning tunnelling micrograph of suspended graphene.....	4
Figure 1.2 Schematic illustration of the main graphene production techniques. ....	5
Figure 1.3 Graphene is the mother material for other carbon materials, including wrapped into 0D fullerenes, rolled into 1D carbon nanotubes or stacked into 3D graphite. ....	6
Figure 1.4 (a) Schematic description the chemical structures of graphene, graphene oxide, and rGO. (b) Approach of graphite to rGO.....	7
Figure 1.5 Overview of structure of Single-, double-, and multi-walled CNTs.....	8
Figure 1.6 (a) Chirality of individual SWCNTs with related colours (cited from reference 112), (b) synthesis of SWNTs with controlled chirality in ethanol CVD via a two-stage nucleation-growth process.....	9
Figure 1.7 Preparation of oxidised MWCNT and reduction of oxidised MWCNT after processing. ....	9
Figure 1.8 Sol-gel preparation of conventional inorganic aerogels, such as silica aerogels. ....	10
Figure 1.9 Schematic description of the macroscopic assemblies and architectures of nanocarbons: principles, strategies, and advantages.....	11
Figure 1.10 (a) Digital images of different stages of forming graphene hydrogel at 70 °C. (b) Freezing and freeze-drying procedures to make graphene oxide aerogel. ....	12
Figure 1.11 (a) Hydrothermal approach to producing CNT/rGO hybrid aerogel without addition of reducing agents. (b-c) SEM images of CNT/rGO hybrid aerogels.....	13
Figure 1.12 Self-assembly mechanism of GO sheets: (a) self-assembly between two parallel GO sheets, (b) self-assembly between two non-parallel GO sheets .....	13
Figure 1.13 (a-b) Digital photos of rGO aerogels. (c-g) Schematic descriptions of synthesizing rGO aerogels . ....	14
Figure 1.14 (a) Illustrations of both the directional-freezing and freeze-drying; (b) top-view and (c) side-view SEM images of anisotropic porous structure of graphene aerogel ( $8.7 \text{ mg}\cdot\text{cm}^{-3}$ ). ....	15
Figure 1.15 Schematics of synthesizing graphene oxide aerogels by using emulsion-templated method. (a) Detailed procedures to synthesize emulsion-templated GO aerogels. (b-c) SEM images of emulsion-templated GO aerogels produced using different GO concentrations. ....	16
Figure 1.16 (a) Schematics of air-bubble-templated method to synthesize rGO hydrogel. (b) SEM image of air-bubble-templated rGO hydrogel. (c) A digital photo of rGO hydrogel 'building' constructed by the wet-press assembly method. (d) A digital photo of a huge rGO aerogel 'wall' prepared by rGO hydrogel 'bricks' after air-drying.....	17
Figure 1.17 The molecular formula of BT, DBT and DMDBT.....	18

Figure 1.18 (a) Adsorption capacities of different compounds over the $\text{Ti}_{0.9}\text{Ce}_{0.1}\text{O}_2$ adsorbent. (b) Adsorption configurations of organosulfur compounds over a Ce-doped $\text{TiO}_2$ surface via DFT calculation.....	19
Figure 1.19 (a) BT sorption performance over the pristine and CuCe-modified MIL-101s adsorbents (the initial BT concentration was 1000 ppm). (b) BT sorption performance over the pristine, Cu-modified MIL-101, Ce-modified MIL-101 and the Cu-Ce/MIL-101 adsorbents. (c-d) Schematics of adsorption mechanisms of BT/Cu(I) sites and BT/Ce(IV) sites in the Cu-Ce/MIL-101 adsorbent. ....	20
Figure 1.20 (a) Schematics of synthesizing holey graphene frameworks. (b) TEM image of holey graphene frameworks. (c) $\text{CO}_2$ sorption kinetics of holey graphene frameworks at different temperatures. ....	21
Figure 1.21 (a) SEM image of the CNT/Silica composite adsorbent. (b) $\text{CO}_2$ adsorption kinetics of the CNT/silica/polyethylenimine composite adsorbent (impregnated with 5 wt% polyethylenimine solution measured using using a gas mixture of 15 % $\text{CO}_2$ and 85 % $\text{N}_2$ , CNT : silica = 30 wt% : 70 wt%). (c) Graphical abstract of $\text{CO}_2$ adsorption over the CNT/silica/polyethylenimine composite adsorbent in a microtube. ....	21
Figure 1.22 (a) $\text{CO}_2$ adsorption isotherms of GO, $\text{TiO}_2$ and $\text{TiO}_2/\text{GO}$ hybrid adsorbents at 0 °C. (b) Graphical abstract of $\text{CO}_2$ adsorption onto the $\text{TiO}_2/\text{GO}$ adsorbent. ....	22
Figure 1.23 Schematics of $\text{CO}_2$ adsorption in a water gas shift reaction. ....	23
Figure 1.24 Schematic representation of the LDH structure. ....	24
Figure 1.25 Structures of (a) BN and (b) graphene. ....	25
Figure 1.26 Schematic representation of the LDH and GO hybrid composites. ....	26
Figure 1.27 DBT uptake from dodecane by CoAl-MMO, CuAl-MMO and MgAl-MMO in their pure (MMO) and hybrid (MMO/GO; containing 5 wt% GO) form.....	27
Figure 1.28 (a) Graphical abstract of MgAl-LDH/GO, MgAl-LDH/MWCNT and MgAl-LDH/GO&MWCNT(1:1), and (b) $\text{CO}_2$ adsorption capacities of different adsorbents (all decorated nanocarbons were 50wt%).....	28
Figure 1.29 Overview of approaches to supporting inorganic nanoparticles within nanocarbon aerogels. ....	29
Figure 1.30 Schematic of co-assembly synthesis of GO/LDH hydrogels and aerogels. ....	29
Figure 1.31 Schematic of impregnation synthesis of iron oxide nanoparticle decorated rGO aerogels. ....	30
Figure 1.32 Schematic of in situ precipitation synthesis of CoAl-LDH/GO hybrid aerogel. ...	31
Figure 1.33 (a) SEM image of CNT/PVA film surface (Insert: A digital image of a large spray-coated CNT/PVA membrane). (b) SEM image of CNT/PVA cross-section on PTFE support (Inserts: contact angles of PTFE surface and CNT/PVA-deposited PTFE membrane). (c) Direct Joule heating of the interconnected CNTs using electrical power. (d) Schematics depict self-heating membranes for thermal desalination via CNT Joule heating.....	32
Figure 1.34 (a) Emulsion-templated rGO aerogel, (b) (c) SEM images of rGO aerogel, (d) Thermal images of surface temperature of rGO aerogel at different voltages. ....	33
Figure 1.35 Schematic presentation of Joule-heated graphene wrapped foam for a viscous crude-oil spill cleaning. ....	34

- Figure 1.36 (a) Flexible manufacturing of GO-CNT hybrid nanocarbon papers. (b) 3D printing fo GO-CNT hybrid nanocarbon as a light bulb. (c) Rod-like GO-CNT hybrid nanocarbon paper for a ligh bulb. (d) Flexible GO-CNT nanocarbon paper for lighting. (e) M-like foldable nanocarbon paper for lighting ..... 35
- Figure 1.37 (a) Experimental set-up for measuring the incandescent radiation emission from rGO film. (b) Digital images of rGO films reach to different Joule heating temeporatures. (c) The measure emission spectrum fiited by the Planck function. (d) Electrical conductivity vesus Joule heating temoerature after 3300 K treatment. (e) rGO films working at 6.30 V for 50 h after 3300 K treatment ..... 36
- Figure 1.38 (a) Sechems to describe CNF welding via Joule heating approach. (b) Raman results of CNF before and after Joule heating. SEM images of pristine CNF (c), and the welded CNF (d)..... 37
- Figure 1.39 (a) Schematics for description of metal precusour on carbon substrate and in situ high temperature Joule heating shock. (grey: carbon atoms, cyan: metal precursor, red; metallic atoms). (b) Joule heating temperature and a heated CNF film. (c) On/off Joule heating temepreure for 10 cycles to make single atoms. TEM images of one-time Joule heating shock (d) and ten-time Joule heating shock (e) ..... 38
- Figure 1.40 (a) SEM image of CNF fims with  $\text{PtCl}_2$  and  $\text{NiCl}_2$  salts, digital image of CNF film with metal salts, and CNF film after 55 ms Joule heating. (b) Schematics of 55 ms Joule heating and temeprature changes versus Joule heating time. (c) High resolution microspcoy imaging of a binary PtNi alloy. (D) Elemental maps of octonay HEA nanoparticles. .... 39
- Figure 2.1 Schematic illustrating the synthesis of CNT aerogels via polymer-assisted ice-templating (rIT-CNT aerogel) and polymer-assisted emulsion-templating (rET-CNT aerogel). The same approach was used to produce the equivalent rIT-GO aerogel samples.....42
- Figure 2.2 (a) Digital photos of bespoke cylindrical moulds in which the initial aqueous nanocarbon mixtures set into LDH/GO hydrogels. The copper base of the moulds allows for unidirectional heat transfer (cooling) through the bottom of the hydrogel monolith, enabling unidirectional hydrogel freezing. (b) Digital image of moulds emerged via their copper base in a liquid nitrogen bath for unidirectional hydrogel freezing..... 42
- Figure 2.3 Schematics of thermally reduced hydrothermal GO (rHT-GO) aerogel synthesis for Joule heating. .... 43
- Figure 2.4 Schematic of a nanocarbon aerogel under Joule heating using a custom-made setup. .... 46
- Figure 2.5 Digital photograph of Joule-heating sample holder. .... 47
- Figure 2.6 Joule heating setup used to characterize the Joule heating characteristic of the MgAl-MMO/rGO aerogels and to thermally regenerate the hybrid aerogel adsorbent via Joule heating: (a) digital photograph of container with gas inlet/outlets and gas-tight electrical connectors, enabling experiments under inert gas atmospheres, (b) a circuit diagram of Joule-heating set-up; (c) digital photograph of Joule heating setup (outside of gas-tight container for clarity). .... 47
- Figure 2.7 (a-b) Joule-heating preconditioning of emulsion-templated CNT aerogel and ice-templated CNT aerogel at 200 °C for 20 minutes. (c-d) Step-wise Joule-heating of emulsion-templated CNT aerogel and ice-templated CNT aerogel (Each step maintained for 10 minutes). .... 48
- Figure 3.1 Microstructure of (a) rET-CNT aerogel and (b) rIT-CNT aerogel as imaged by SEM (sampled from the core region of the monolithic aerogel samples).....52

Figure 3.2 Size distribution of predominant pore type in rIT-CNT aerogels and rET-CNT aerogels, as determined by SEM imaging. ....	52
Figure 3.3 (a) Nitrogen velocity-pressure relationships for extracting gas permeability values in the rIT-CNT aerogel and rET-CNT aerogel. (b) Through-plane gas permeability testing in N <sub>2</sub> atmosphere of the rIT-CNT aerogel and rET-CNT aerogel. ....	53
Figure 3.4 Materials characterization of rET-CNT and rIT-CNT aerogels: (a) TGA in air atmosphere; (b) N <sub>2</sub> adsorption-desorption isotherms; (c) XRD patterns. (d) Raman spectra. ....	54
Figure 3.5 Electrical properties of rET-CNT and rIT-CNT aerogels: (a) I-V curves; (b) Electrical conductivity and relative resistivity as function of Joule-heating temperature. ....	55
Figure 3.6 Joule-heating characterisation of rET-CNT and rIT-CNT aerogels via current-step experiments: steady-state Joule-heating core temperature as function of electrical power. ....	56
Figure 3.7 Joule-heating and cooling kinetic of rIT-CNT and rET-CNT aerogels: a) Joule-heating kinetics: increase in core temperature over time after an electrical heating current (electrical power input 2W) has been switched on; (c) Natural cooling kinetics: decrease of core temperature over time after electrical heating current (electrical power input 2W) has been switched off. ....	57
Figure 3.8 Radial temperature gradient of rET-CNT aerogel and rIT-CNT aerogel, Joule-heated at inputs of electrical power 2W. ....	58
Figure 3.9 The relationship between Joule-heating efficiency and electrical conductivity (a) and density (b) of different nanocarbon aerogels. ....	59
Figure 3.10 The relationship between Joule-heating efficiency and thermal conductivity of different nanocarbon aerogels. Inserted thermal images were taken at electrical power 2 W. ....	60
Figure 3.11 (a) Solar absorption measurements and (b) contact angles of rIT-CNT aerogel and rET-CNT aerogel, respectively. ....	61
Figure 3.12 Temperature gradient distributions of the rIT-CNT aerogel and rET-CNT aerogel at shining time 300s (from aerogel top to the middle). ....	61
Figure 3.13 Schematics of rCNT aerogel membranes on top of water for solar steam generation. ....	62
Figure 3.14 Solar steam generation performance of rET-CNT and rIT-CNT aerogels: Water mass change normalised to water surface area under one sun irradiation over time for pure water, water topped with rIT-CNT aerogel, and water topped with rET-CNT aerogel (Insert shows digital photos of aerogel membranes on top of water). ....	63
Figure 3.15 Solar steam water evaporation rates of different nanocarbon-based solar evaporators from literature under one sun illumination. ....	63
Figure 4.1 Synthetic procedure for the fabrication of electrically-conducting, high-weight loading sorbent-nanoparticle/rGO hybrid aerogel. MMO = mixed-metal-oxide; MNP = metal nanoparticle. ....	74
Figure 4.2 Zeta potential of the initial MgAl-LDH and GO suspensions at different pH values. ....	75
Figure 4.3 TGA of MgAl-MMO powder and MgAl-MMO/rGO aerogel in air. ....	75

Figure 4.4 (a) Digital image of an MgAl-LDH/GO aerogel monolith (78 wt% LDH loading) before thermal treatment. (b) - (c) SEM images of the internal microstructure and LDH-decorated GO surfaces for the same MgAl-LDH/GO aerogel (78 wt%). (d) - (g) SEM images showing MgAl-LDH nanoparticle decoration for MgAl-LDH/GO aerogels produced at different LDH loadings.....	76
Figure 4.5 (a) Digital image of a MgAl-MMO/rGO aerogel monolith. (b) and (c) SEM images of MgAl-MMO/rGO aerogel. (d) – (f) TEM images of the MgAl-MMO/rGO aerogel at different magnifications.....	77
Figure 4.6 (a) EDX line scan spectrum of MgAl-MMO/rGO aerogel. (b) EDX mapping of MgAl-MMO/rGO aerogel. The experimental atomic Mg:Al ratio is close to the nominal ratio of 2:1. ....	78
Figure 4.7 (a) XRD patterns of MgAl-LDH powder and MgAl-LDH/GO aerogel. (b) XRD pattern of the MgAl-MMO powder and MgAl-MMO/rGO aerogel. ....	79
Figure 4.8 High-resolution Mg1s (a) and Al2p (b) XPS spectra of MgAl-MMO powder and MgAl-MMO/rGO aerogel. ....	80
Figure 4.9 Raman spectra of initial MgAl-LDH/GO aerogel (product of Step 2) and final MgAl-MMO/rGO aerogel (Product of Step 3).....	81
Figure 4.10 (a) BET N <sub>2</sub> adsorption-desorption isotherms of the MgAl-MMO powder and the MgAl-MMO/rGO aerogel. (b) corresponding BJH pore-size distributions.....	82
Figure 4.11 XRD of CuAl-MNP powder and NiAl-MNP powder, and the corresponded rGO hybrid aerogels.....	83
Figure 4.12 SEM images of the aerogel flakes sampled from the cores of (a) MgAl-MMO/rGO aerogel, (c) CuAl-MNP/rGO aerogel, and (e) NiAl-MNP/rGO aerogel, and EDX mapping of the corresponding (b) Mg, (d) Cu, and (f) Ni distributions. ....	84
Figure 4.13 (a) I-V characteristics of the CuAl-MNP/rGO aerogel and the NiAl-MNP/rGO aerogel. (b) Digital images of the initial NiAl-LDH/GO aerogel and the final NiAl-MNP/rGO aerogel next to a magnet. ....	85
Figure 4.14 Uptake isotherms for sorption of DBT from n-octane (initial concentrations tested at 100 ppm, 200 ppm, 300 ppm and 500 ppm, respectively). The dash line is fitted via Freundlich model and the solid line is fitted via Langmuir model.....	86
Figure 4.15 Liquid-phase organosulfur sorption characteristics of MgAl-MMO/rGO aerogels, compared to MgAl-MMO powders: Equilibrium uptake capacities for sorption of DBT and DMDBT from n-octane (initial concentration 500 ppm). ....	87
Figure 4.16 Uptake kinetics for sorption of DBT from n-octane (initial concentration 500 ppm). ....	88
Figure 4.17 (a) Molecular structures of biphenyl and dibenzothiophene. (b) Organosulfur selectivity: DBT uptake capacities from n-octane (initial concentration 500 ppm) in the presence of biphenyl (initial concentration 500 ppm). ....	89
Figure 4.18 Digital images of an MgAl-MMO/rGO aerogel (78 wt% nanoparticle loading) in a Joule heating set-up. (b) Relationship between electrical input power and aerogel Joule-heating temperature (measured at the aerogel surface); the right-hand y-axis shows the relative electrical through-volume resistivity of the aerogels at different Joule-heating temperatures. ....	90

Figure 4.19 Joule-heating related characteristics of MgAl-MMO/rGO aerogels: (a) Electrical conductivity ( $\sigma$ ) and thermal conductivity ( $\kappa$ ) of the MgAl-MMO aerogel at different Joule heating temperatures and, (b) Rapid thermal cycling of MgAl-MMO/rGO aerogel between 300 °C and 400 °C via Joule heating. (c) Joule-heating temperature stability of MgAl-MMO/rGO aerogel over extended time periods at temperatures relevant to MMO applications in pre-combustion CO <sub>2</sub> capture.....	91
Figure 4.20 (a) Schematic description of liquid-phase DBT adsorption onto a hybrid aerogel monolith; (b) Schematic representation of Joule-heating regeneration of a hybrid aerogel sorbent after DBT adsorption. ....	92
Figure 4.21 Joule heating regeneration of exhausted MgAl-MMO/rGO hybrid aerogel sorbents. Thermal regeneration stability of MgAl-MMO powder (regenerated in a Muffle furnace, black curve), and MgAl-MMO/rGO aerogel (regenerated via Joule-heating, purple curve); insert: thermal image of the Joule-heated MgAl-MMO/rGO aerogel.....	92
Figure 4.22 XPS analysis of the MgAl-MMO/rGO aerogel sorbent in its pristine state (as-synthesised sorbent), post-sorption state (i.e. sorbent after maximum adsorptive DBT uptake from n-octane), and post-regeneration state (i.e. after Joule-heating regeneration of the post-sorption sorbent): a) C1s, b) Mg1s and c) Al2p high-resolution XPS spectra.....	93
Figure 4.23 a) Joule-heating kinetics of MgAl-MMO/rGO aerogel and, b) Natural cooling kinetics of MgAl-MMO/rGO aerogel.....	94
Figure 4.24 (a) Schematics of high-pressure pre-combustion CO <sub>2</sub> adsorption on MgAl-MMO/rGO aerogels. (b) CO <sub>2</sub> adsorption isotherms onto MgAl-MMO powder and MgAl-MMO/rGO aerogel at 300 °C across CO <sub>2</sub> pressure range of 0.2-10 bar, capacities shown with standard errors. ....	95
Figure 4.25 (a) Relative CO <sub>2</sub> capacity retention of the MgAl-MMO/rGO aerogel over five thermal regeneration cycles at 400 °C at 0.2, 1, and 8 bar CO <sub>2</sub> pressure. (b) High-pressure CO <sub>2</sub> sorption capacities (8 bar, 300 °C) of the MgAl-MMO powder and MgAl-MMO/rGO aerogel sorbents prepared in this work, compared against different solid-state sorbent systems, reported in the literature (see above Table 4.6).....	98
Figure 4.26 Digital photo of an MgAl-MMO/rGO aerogel monolith for DBT adsorption. ...	102
Figure 4.27 Conventional thermal regeneration of MgAl-MMO/rGO aerogel via external heating: DBT adsorption performance of MgAl-MMO/rGO aerogel over three cycles of DBT adsorption and thermal regeneration in a muffle furnace at 250 °C (same DBT sorption conditions and temperature as in sorbent Joule-heating regeneration experiments, described in the main text, see above Figure 4.21).....	104
Figure 5.1 Synthesis of BN/rCNT aerogels via high-temperature conversion of B- and N-containing precursors supported within a CNT aerogel network.....	107
Figure 5.2 (a) Digital images of BN/rCNT aerogels (40 wt% BN); (b) Digital images of BN/rCNT aerogel adsorbents with 2.5 wt% and 10 wt% BN loading. ....	108
Figure 5.3 (a) TGA of the BN powder adsorbent and the BN/rCNT aerogel adsorbent. (b) Raman spectra of BN/CNT aerogel adsorbent before and after thermal reduction.....	108
Figure 5.4 (a) Powder XRD patterns of BN powder and BN/rCNT aerogel. (b) IR spectra of BN and BN/rCNT aerogel. ....	109
Figure 5.5 XPS full spectra of BN powder (a) and BN/CNT aerogel (b) adsorbents.....	110
Figure 5.6 (a-b) XPS analysis (B1s high-resolution scan; N1s high-resolution scan) of BN powder and BN/rCNT aerogel.....	110

Figure 5.7 (a) SEM image of BN powder adsorbent. (a1 - a4) EDX mapping of C, B and N distribution across an individual in-hybridised BN structure. (b) SEM image of BN/rCNT aerogel adsorbent. (b1 - b3) High magnification SEM of BN/rCNT aerogel internal structure. ....	111
Figure 5.8 TEM images of un-hybridised BN mesostructures: (a) low-resolution TEM image of a thin BN structure; (b) higher-resolution TEM of a thin corrugated edge of one of the nanostructures. Red circles indicate pores with diameters < 5nm. ....	112
Figure 5.9 TEM images of BN/rCNT aerogel fragment. (a) Low-resolution TEM image. The red arrows indicate the BN mesostrcutures, the blue arrows indicate the rCNT network. (b) Higher resolution TEM image of the rCNT network.....	112
Figure 5.10 (a) N <sub>2</sub> adsorption isotherms and (e) BJH pore distributions of BN powder and BN/rCNT aerogel. ....	113
Figure 5.11 (a) I-V curve of BN/rCNT aerogel. (b) Radial thermal gradient of an uninsulated BN/rCNT aerogel (Joule-heated at 2W), used for the calculation of the thermal conductivity, $\kappa$ , of the hybrid aerogel.....	114
Figure 5.12 Compressibility measurements of BN/rCNT aerogel and pure rCNT aerogel..	115
Figure 5.13 (a) DBT adsorption kinetics of BN powder and BN/rCNT aerogel (DBT, 500 ppm S, n-octane). (b) DBT adsorption isotherms of BN powder and BN/rCNT aerogel (100 ppm S, 200 ppm S, 300 ppm S and 500 ppm S DBT in n-octane).....	116
Figure 5.14 (a) Chemical structures and abbreviation of inorganic sulfur compound and organic aromatic sulfur compounds. (b) Adsorption desulfurisation performance of various sulfur-containing onto BN/rCNT aerogels (sorption from n-octane; initial concentration for all compounds 500 ppm S). ....	118
Figure 5.15 (a) Selectivity: Adsorption capacities of BN powder and BN/rCNT aerogel as measured in BP/DBT mixtures (2873 ppm BP, 500ppm S DBT in n-octane). (b) DMDBT adsorption performance of BN powder and BN/rCNT aerogel in the presence of DBT (250 ppm S DMDBT and 250 ppm S DBT in n-octane). ....	119
Figure 5.16 (a) IR spectra of BN and BN/rCNT aerogel adsorbents after DBT adsorption. Post-sorption XPS analysis: (b) S2p XPS peaks of DBT powder, BN powder after DBT adsorption and BN/rCNT aerogel after DBT adsorption; (c) B1s XPS peak of BN powder before and after DBT sorption.....	120
Figure 5.17 (a) Electrical power versus Joule-heating temperature. (b) Heating and cooling curves of the Joule-heated BN/rCNT aerogel. ....	121
Figure 5.18 (a) Joule-heating regeneration of an exhausted BN/rCNT aerogel adsorbent via thermal DBT desorption under Joule-heating. (b) Temperature stability over 1 h of Joule-heating regeneration. ....	122
Figure 5.19 Regeneration stability of BN/rCNT aerogel adsorbent: Organosulfur uptake (relative to initial organosulfur capacity) over five Joule-heating regeneration cycles.....	123
Figure 5.20 (a) Joule heating performance and (b) Raman spectra of BN/rCNT thermally treated at 800 °C and 1000 °C.....	124
Figure 6.1 High-temperature Joule-heating studies of GO-based aerogels in this chapter	129
Figure 6.2 (a) Schematic of an aerogel under flash Joule-heating and a digital picture of rGO[HT] aerogel under Joule-heating covered by glass wool. (b) Voltage and current for an rGO[HT] aerogel experienced 60 seconds long Joule-heating. Inserted digital picture shows the black-body radiation. ....	131

Figure 6.3 Electrical conductivity and electrical power input versus Joule-heating temperature of rGO aerogel and rrGO aerogel. ....	132
Figure 6.4 (a) Raman spectra and (b) XPS full spectra of the rGO[HT] aerogel and rrGO[HT] aerogel. ....	133
Figure 6.5 Surface temperature Joule-heating kinetics of the rrGO[HT] aerogel at 46.85 W electrical power input and corresponding cooling curves. ....	134
Figure 6.6 Controlled high-temperature Joule-heating from 1000 °C to 1200 °C at 50 °C increments controlled through electrical power input. ....	134
Figure 6.7 (a) Rapid thermal cycling between room temperature and 1200 °C of the rrGO aerogel. (b) Long-term (1 hour) Joule-heating stability of the rrGO aerogel at 1000 °C. ....	135
Figure 6.8 (a) Digital photo of a GO[HT] aerogel under flash Joule-heating at $I = 10.12$ A. (B) The electrical current and voltage curves of a GO[HT] aerogel under 30 seconds Joule-heating with strong black-body irradiation. The resulting aerogel is referred to as GO[30sec] aerogel for the rest of this section. ....	136
Figure 6.9 Electrical conductivity/density of GO[HT], GO[HT] after preconditioning and GO[30sec] aerogels as function of Joule-heating core temperature. ....	137
Figure 6.10 (a-b) Contact angles of GO[HT] aerogel and GO[30sec] aerogel. (c-d) Nitrogen adsorption-desorption curves and pore size distributions of GO[HT] aerogel and GO[30sec] aerogel. ....	138
Figure 6.11 (a) Joule-heating core temperature versus electrical power input and resistance of GO[HT] aerogel (black), GO[HT] aerogel after preconditioning (blue) and GO[30sec] aerogel (red). (b) Joule-heating cycling of GO[30sec] aerogel at core temperature 1000 °C. (c) Precise Joule-heating temperature control of GO[30sec] aerogel. ....	139
Figure 6.12 TGA, heat-flow profiles and DTGA traces of GO[HT] aerogel (a), GO[30sec] aerogel (b) and GO[300sec] aerogel (c). ....	141
Figure 6.13 TGA-FTIR of (a) GO[HT] aerogel, (b) GO[30sec] aerogel and (c) GO[melted] aerogel in air. The time axis relates to the TGA temperature (0 min equivalent to a TGA temperature of 20 °C, 80 min equivalent to a TGA temperature of 800 °C). The wavenumber and absorbance axis relate to the IR spectroscopic analysis of the gases evolved at different TGA temperatures. ....	142
Figure 6.14 Raman maps of the intensity ratio of the 2D peak to the G peak ( $I_{2D}/I_G$ ) for the GO[HT] aerogel, GO[30sec] aerogel and GO[300sec] aerogel, accordingly. ....	143
Figure 6.15 High resolution TEM images of GO[HT] aerogel (a) and GO[30sec] aerogel (b). High resolution TEM images of GO[300sec] aerogel with observed graphene sheet welding, such as increased graphene sizes and crossover areas (c-d). ....	144
Figure 6.16 (a) Adsorption kinetics of methylene blue and rhodamine onto rGO aerogels. (b) Schematics of flash Joule-heating regeneration of dye-saturated rGO aerogels. ....	145
Figure 6.17 (a) 30 second flash Joule-heating regeneration of post-sorption rGO aerogels at electrical power input of $P = 120$ W, and corresponding voltage and current evolution over time. The digital photo shows rGO[HT] aerogel under ultrahigh Joule-heating conditions, emitting black body radiation. (b) Dye uptake of rGO[HT] aerogels after flash Joule-heating regeneration over three re-use cycles. ....	146

Figure 6.18 (a-c) Joule-heating time versus voltage of Cu NP/rGO aerogels. Digital photos to display strong black-body radiations of rGO aerogels. (d-f) SEM images of various initial concentrations of Cu(acac) <sub>2</sub> in chloroform to make Cu NP/rGO aerogels using different time Joule heating. ....	148
Figure 6.19 (a) Schematics of producing Pt nanoparticles via flash Joule-heating using rGO[HT] aerogel as nanoscale furnace. (b) Schematics for describing long time flash Joule-heating leads to large Pt nanoparticles. ....	149
Figure 6.20 (a) SEM image of Pt-NP/rGO aerogel using 10 second Joule-heating duration and (b) Pt-NP/rGO aerogel using 1-second Joule heating. The inserts show corresponding digital photos of the Joule-heated precursor-decorated rGO[HT] aerogels and Pt nanoparticle diameter distributions, obtained from SEM image analysis.....	149
Figure 6.21 TEM images/particle size distributions of 10 seconds (a) and 1 second (e) flash Joule-heating of Pt/rGO aerogel. High resolution TEM images/lattice distance images for 10 seconds (b-c) and 1 second (f-g) flash Joule heating Pt/rGO aerogel. EDX mapping of 10 seconds (d) and 1 second (h) flash Joule heating Pt/rGO aerogel.....	150
Figure 6.22 Raman spectra (a)/XPS full spectra (b) of 10 seconds and 1 second flash Joule-heating of Pt/rGO aerogel. (c) Pt 4f peak analysis of 1 second flash Joule-heating of Pt NP/rGO aerogel.....	151
Figure 6.23 (a-c) SEM images of Pt NPs/rGO aerogel with 10 seconds long flash Joule heating using 0.001M Pt(acac) <sub>2</sub> precursors in chloroform solution. ....	152
Figure 6.24 (a) SEM image of GO[30sec] aerogel. (b-d) Different resolution SEM images of MoO <sub>2</sub> /GO[30sec] aerogel using 1 second flash Joule heating. (e) SEM image of MoO <sub>2</sub> /GO[30sec] aerogel and the corresponding EDX mappings. ....	153
Figure 6.25 XRD patterns of GO[30sec] aerogel and MoO <sub>2</sub> /GO[30sec] aerogel. ....	153
Figure 6.26 Schematics to illustrate MoO <sub>2</sub> catalysts oxidative desulfurisation of DBT. ....	154
Figure 6.27 Catalytic oxidative desulfurisation performance of MoO <sub>2</sub> /GO[30sec] aerogel.	155
Figure 6.28 (a) Schematic overview of hydrothermal approach to produce GO[HT] aerogels and (b) schematic overview of Joule-heating setup to produce Joule-heating annealed samples, such as the GO[30sec] aerogel discussed in the text.....	157
Figure 7.1 Table of Contents of Chapter 3.....	161
Figure 7.2 Table of Contents of Chapter 4. ....	162
Figure 7.3 Table of Contents of Chapter 5. ....	163
Figure 7.4 Table of Contents of Chapter 6. ....	164
Figure A1.1 (a) Thermal images of Joule-heating rET-CNT and rIT-CNT aerogels cooling at core temperature 150 °C, and (b) switching on the power heating aerogels to core temperature 150 °C.....	179
Figure A1.2 (a) The relationship between electrical power input and the Joule-heating temperature of rIT-GO aerogels. (b) Raman spectra analysis of different temperature treated rIT-GO aerogels. (c) The Joule-heating efficiency of different rIT-GO aerogels at electrical power 2W.....	180

Figure A1.3 (a) Joule-heating temperature distributions of rIT-CNT aerogel and rET-CNT aerogel from centre to edge at power 2W. (b) Thermal images of rIT-CNT membrane on or not on water at lighting time 300s, and the corresponding axis temperature distributions. (c) Thermal images of pure water, rIT-CNT membrane, and rIT-CNT membrane on the top of water at different time interval under one sun. ....	182
Figure A1.4 Joule-heating performance of hydrothermal rGO aerogels (rHT-GO aerogels) with different densities. ....	183
Figure A2.1 Digital images of MgAl-LDH/GO hybrid aerogels with different MgAl-LDH loadings. (a) Side view and (b) top view.....	184
Figure A2.2 Magnified view of the rGO (002) peak in the XRD pattern of the MgAl-MMO/rGO aerogel (see also main text, Figure 4.7b).....	185
Figure A2.3 SEM image of the MgAl-MMO/rGO aerogel (78 wt% MMO loading), and particle size distribution (as measured from the longest particle dimension via the Image J software). ....	185
Figure A2.4 SEM images of the unsupported MgAl-MMO powders. (Insert small picture is the nanoparticle size distribution obtained via Image J analysis).....	185
Figure A2.5 (a) N <sub>2</sub> adsorption-desorption isotherms and, (b) BJH pore-size distributions of CuAl-MMP powder and CuAl-MNP/rGO aerogel. (c) N <sub>2</sub> adsorption isotherms and, (d) BJH pore-size distributions of NiAl-MNP powder and NiAl-MNP/rGO aerogel. ....	186
Figure A2.6 (a) TGA profile of the CuAl-MNP powder and the CuAl-MNP/rGO aerogel. (b) TGA profile of the NiAl-MNP powder and the NiAl-MNP/rGO aerogel. All TGA profiles collected in oxidative air atmosphere. The increase in weight upon temperature ramping is due to metal oxidation and further confirms the metallic nature of the LDH-derived CuAl and NiAl nanoparticles.....	186
Figure A2.7 XPS analysis of Mg1s and Al2p of MgAl-MMO powder and MgAl-MMO/rGO aerogel adsorbents before and after DBT adsorption. (a) Mg1s and (b) Al2p spectra of MgAl-MMO powder before DBT sorption (black trace) and after DBT sorption (red trace). (c) Mg1s and (d) Al2p spectra of the MgAl-MMO/rGO aerogel before DBT sorption (yellow trace) and after DBT sorption (blue trace). ....	188
Figure A2.8 Evolution of aerogel surface temperature upon Joule heating at constant power input (Heating curves) and upon natural cooling once input of the electrical power is stopped (Cooling curves). Data were collected for three cycles of Joule-heating and subsequent natural heating of MgAl-MMO/rGO aerogel, with each data set fitted with an exponential function. ....	188
Figure A2.9 Raman analysis of pristine MgAl-MMO/rGO aerogel and the exhausted aerogel after Joule heating regeneration. ....	190
Figure A3.1 SEM image and EDX mappings of BN/rCNT aerogel.....	193
Figure A3.2 (a) DBT uptake capacities for rCNT aerogel, BN powder and BN/rCNT aerogel (DBT in n-octane, initial DBT concentration 500 ppm S). (b) DBT adsorption onto BN powder at different temperatures (DBT in n-octane, initial DBT concentration 500 ppm S). ....	193
Figure A3.3 XPS spectra of BN powder before and after DBT adsorption. (a) C1s, (b) O1s and (c) N1s spectra of BN powder before and after DBT adsorption. ....	194
Figure A3.4 (a) Heating curves and (b) cooling curves of post-adsorption BN/rCNT aerogel over 5 Joule-heating cycles .....	194

Figure A3.5 Voltage and temperature control of BN/rCNT aerogel under Joule-heating. (a) Preconditioning of BN/rCNT aerogel at around 200 °C for 20 minutes to remove impurities (e.g. water and gases). (b) Stepwise Joule-heating.....	195
Figure A3.6 Joule-heating temperature versus electrical conductivity of the produced BN/rCNT aerogel adsorbent.....	195
Figure A3.7 Joule-heating of BN/rCNT aerogel in air atmosphere. ....	195
Figure A4.1 Direct stepwise Joule heating of GO[HT] aerogels above 400 °C is not working, owing to high fractions of impurities and highly defective GO sheets. Digital images show that the GO[HT] aerogel will be burning due to sudden pulse of voltage surging.....	196
Figure A4.2 Long time Joule heating working temperature at 800 °C and 900 °C of GO[30sec] aerogels.....	197
Figure A4.3 XPS C1s peak analyses of rGO[HT] aerogel (a) and rrGO[HT] aerogel (b), respectively. XPS O1s peak analyses of rGO[HT] aerogel (c) and rrGO[HT] aerogel (d), respectively. ....	197
Figure A4.4 (a) 1D VRH model fitting and (b) 2D VRH model fitting of GO[HT] aerogel. (c) 3D VRH model of GO[HT] aerogel, GO[HT] aerogel after preconditioning and GO[30sec] aerogel. (d) Arrhenius model fitting of GO[HT] aerogel and GO[30sec] aerogel (bandgap for GO[HT] aerogel is 0.09 eV and for GO[30sec] aerogel is 0.01 eV).....	199
Figure A4.5 SEM images of GO[HT] aerogel (a-b), GO[30sec] aerogel (c-d) and GO[300sec] aerogel (e-f) at different magnification. (g) XRD patterns and (h) Raman spectra of GO[HT] aerogel, GO[30sec] aerogel and GO[300sec] aerogel.....	201
Figure A4.6 (a-c) Raman mappings of the intensity ratio of the D peak to the G peak ( $I_D/I_G$ ) for the GO[HT] aerogel, GO[30sec] aerogel and GO[300sec] aerogel. TEM images of GO[HT] aerogel (d) and GO[30sec] aerogel (e) and GO[300sec] aerogel (f). ....	202
Figure A4.7 (a) XPS full spectra of GO[HT] aerogel, GO[30sec] aerogel and GO[300sec] aerogel. XPS C1s spectra of GO[HT] aerogel (b), GO[30sec] aerogel (c) and GO[300sec] aerogel (d). XPS O1s spectra of GO[HT] aerogel (e), GO[30sec] aerogel (f) and GO[300sec] aerogel (g). ....	203
Figure A4.8 Energy consumption comparison of dye-saturated adsorbent via traditional thermal methods from reported studies and flash Joule-heating in this work. Clearly, the sudden generated >2500 °C will decompose the dyes immediately, therefore the Joule heating time can also be shortened to save more energies, for example only 1 second Joule heating in future. ....	203
Figure A4.9 XPS C1s peak of Pt NP/rGO aerogel_1sec (a) and Pt NP/rGO aerogel_10sec (b). XPS O1s peak of Pt NP/rGO aerogel_1sec (c) and Pt NP/rGO aerogel_10sec (d). XPS Pt 4f peak of Pt NP/rGO aerogel_10sec (e). XRD patterns of pure rGO, Pt NP/rGO aerogel_1sec and Pt NP/rGO aerogel_10sec (f). Raman spectra of pure rGO, Pt NP/rGO aerogel_1sec and Pt NP/rGO aerogel_10sec (g). ....	204

## List of Tables

Table 2.1 Lists of materials used in this PhD project. ....	40
Table 3.1 Aerogel materials characteristics, reflecting pronounced differences in aerogel microstructure of rET-CNT and rIT-CNT aerogels.....	51
Table 3.2 Physico-chemical materials characteristics of rET-CNT aerogel and rIT-CNT aerogel. ....	54
Table 3.3 Joule-heating characteristics of rET-CNT aerogel and rIT-CNT aerogel (all parameters as measured under steady-state conditions at a power input of 2W). ....	56
Table 3.4 Physical materials parameters of different ice-templated nanocarbon aerogels.	59
Table 3.5 Solar steam generation performance comparison under one sun illumination between nanocarbon-based materials reported from literature and this study. ....	64
Table 4.1 Materials characteristics of MgAl-MMO powder (pure, unsupported MgAl-MMO nanoparticles) and MgAl-MMO/rGO hybrid aerogel (MgAl-MMO nanoparticles supported within rGO aerogels at a weight loading of 78 wt%).....	80
Table 4.2 Materials characteristics of CuAl-MNP/rGO aerogels (78 wt% CuAl-MNP loading) and NiAl-MNP/rGO aerogel (88 wt% NiAl-MNP loading).....	83
Table 4.3 Structural characterisation and organosulfur sorption capacities of LDH-derived metal nanoparticles (MNP) in their pure and aerogel-supported form. ....	83
Table 4.4 Relative enhancements in liquid-sorption characteristics of MgAl-MMO/rGO aerogels (sorbent nanoparticles supported within rGO aerogels, loading fraction 78 wt%) compared to MgAl-MMO powder (unsupported sorbent nanoparticles), as measured via DBT uptake from n-octane solution (500 ppm DBT, 20 °C).....	87
Table 4.5 CO <sub>2</sub> uptake of MgAl-MMO powder and MgAl-MMO/rGO aerogel at different pressures (300 °C working temperature).....	96
Table 4.6 High-pressure CO <sub>2</sub> sorption capacities ( $p_{CO_2}$ = 8-10 bar) at high temperatures (T=300 °C) of different solid-state sorbent systems, reported in the literature, compared against MgAl-MMO powders and MgAl-MMO/rGO aerogel sorbent prepared in this work. ....	97
Table 5.1 Organosulfur Uptake and materials characterisation of BN powder and BN/rCNT aerogel.....	113
Table 5.2 Isotherm fitting parameters for DBT sorption onto BN powder and BN/rCNT aerogel .....	117
Table 5.3 Organosulfur uptake of various ADS adsorbents. ....	117
Table 5.4 Density, electrical conductivity and DBT sorption capacity of BN/rCNT aerogel under 800 °C and 1000 °C treatments. ....	124
Table 6.1 Parameters of GO[HT] aerogel and GO[30sec] aerogel, including electrical conductivity ( $\sigma$ ), specific surface area (SSA), Volume of meso-porosity ( $V_{Meso-porosity}$ ), micro-pore volume ( $V_{micro}$ ) and average pore size ( $D_p$ ).....	138
Table 6.2 DBT oxidative catalytic performance of using different catalysts and experimental conditions.....	155

Table A1.1 The physical parameters of density-different rHT-GO aerogels.....	183
Table A2.1 Average crystallite size ( $D_p$ ) and lattice spacing ( $d_{\text{spacing}}$ ) of MgAl-LDH powder and MgAl-LDH/GO aerogel from Figure 4.7a.....	184
Table A2.2 Isotherms fitting parameters for DBT sorption onto MgAl-MMO powder and MgAl-MMO/rGO aerogel .....	187
Table A2.3 Lifetime parameters for the Joule heating and natural cooling of MgAl-MMO/rGO aerogel, as obtained by exponential fitting of the temperature evolution data in Figure A2.11. ....	189
Table A2.4 Estimated energy consumptions of furnace-based and Joule-heating-based thermal regenerations. ....	189
Table A2.5 Composition analysis of XPS C1s from the pristine MgAl-MMO/rGO aerogel and after Joule heating regeneration .....	190
Table A2.6 Low-pressure CO <sub>2</sub> sorption capacities (0.05-0.2 bar) at elevated temperature (300 °C) of carbon-supported MgAl-MMO sorbents, reported in the literature, compared against MgAl-MMO/rGO aerogel sorbent prepared in this work. ....	191
Table A2.7 CO <sub>2</sub> sorption capacities at 1 bar pressure ( $p_{\text{CO}_2} = 1$ bar) and high temperature ( $T = 300$ °C) of different solid-state sorbent systems, reported in the literature, compared against MgAl-MMO powders and MgAl-MMO/rGO aerogel sorbent prepared in this work. ....	191
Table A3.1 Parameters of the Joule heated post-adsorption BN/rCNT aerogel, including temperature (T), electrical current (I), voltage (U), resistance (R), input electrical power (P), energy consumption (Q).....	194

## List of Abbreviations

1,4-Dichlorobenzene - <b>C<sub>6</sub>H<sub>4</sub>Cl<sub>2</sub></b>	5% Hydrogen/Nitrogen - <b>5% H<sub>2</sub>/N<sub>2</sub></b>
Acetonitrile - <b>CH<sub>3</sub>CN</b>	Activated carbon - <b>AC</b>
Activated carbon beads - <b>ACB</b>	Barrett-Joyner-Halenda - <b>BJH</b>
Benzothiophene - <b>BT</b>	Biphenyl - <b>BP</b>
Bis(acetylacetonato)dioxomolybdenum(VI) - <b>MoO<sub>2</sub>(acac)<sub>2</sub></b>	Boron nitride/reduced carbon nanotube - <b>BN/rCNT</b>
Boron nitride - <b>BN</b>	Brunauer-Emmett-Teller - <b>BET</b>
Boron nitride/reduced carbon nanotube - <b>BN/rCNT</b>	Commercial metal-organic frameworks - <b>Cu-BTC</b>
Carbon dioxide - <b>CO<sub>2</sub></b>	Carbon disulfide - <b>CS<sub>2</sub></b>
Carbon nanofibers - <b>CNF</b>	Carbon nanotube - <b>CNT</b>
Catalytic hydrodesulfurisation - <b>HDS</b>	Chemical vapour deposition - <b>CVD</b>
Chloroform - <b>CHCl<sub>3</sub></b>	CO <sub>2</sub> capture and storage - <b>CCS</b>
Core temperature - <b>T<sub>core</sub></b>	Dibenzothiophene - <b>DBT</b>
Dibenzothiophene sulfone - <b>DBTO<sub>2</sub></b>	Dichloromethane - <b>CH<sub>2</sub>Cl</b>
Dimethyldibenzothiophene - <b>DMDBT</b>	Double-walled CNT - <b>DWCNT</b>
Inorganic/Nanocarbon aerogels - <b>INCAs</b>	Emulsion-templated - <b>ET</b>
Energy dispersive X-ray spectroscopy - <b>EDX</b>	Ni nanoparticles decorated activated carbon beads - <b>Ni-ACB</b>
Flash Joule heating - <b>FJH</b>	Full width at half maximum - <b>FWHM</b>
Gas chromatography - <b>GC</b>	Graphene oxide - <b>GO</b>
GO[HT] aerogel after 30 sec Joule-heating - <b>GO[30sec] aerogel</b>	GO[HT] aerogel after 300 sec Joule-heating - <b>GO[300sec] aerogel</b>
High-entropy-alloy - <b>HEA</b>	Hydrochloride acid - <b>HCl</b>
Hydrothermal - <b>HT</b>	Hydrothermal GO - <b>GO[HT]</b>
Ice-templated - <b>IT</b>	Infrared spectroscopy - <b>IR</b>
Layered-double-hydroxides - <b>LDH</b>	Metal-organic frameworks - <b>MOFs</b>

Methyldibenzothiophene - <b>MDBT</b>	Methylene blue - <b>MB</b>
Mixed-metal-nanoparticle - <b>MNP</b>	Mixed-metal-oxide - <b>MMO</b>
Multi-walled CNT - <b>MWCNT</b>	Nanoparticle - <b>NP</b>
Nitrogen - <b>N<sub>2</sub></b>	Oxidised CNT - <b>oCNT</b>
Periclase - <b>MgO</b>	Platinum(II) acetylacetonate - <b>Pt(acac)<sub>2</sub></b>
Polyvinyl alcohol - <b>PVA</b>	Reduced graphene oxide - <b>rGO</b>
Powder X-ray diffraction - <b>XRD</b>	Reduced carbon nanotube - <b>rCNT</b>
Reduced emulsion-templated carbon nanotube - <b>rET-CNT</b>	Reduced hydrothermal graphene oxide - <b>rHT-GO</b>
Reduced ice-templated carbon nanotube in nitrogen - <b>rIT-CNT<sub>N<sub>2</sub></sub></b>	Reduced ice-templated carbon nanotube - <b>rIT-CNT</b>
Reduced ice-templated graphene oxide - <b>rIT-GO</b>	Reduced ice-templated graphene oxide in nitrogen - <b>rIT-GO<sub>N<sub>2</sub></sub></b>
Joule-heating-reduced rGO[HT] - <b>rrGO[HT]</b>	Surface temperature - <b>T<sub>surface</sub></b>
Scanning electron microscopy - <b>SEM</b>	Single-walled CNT - <b>SWCNT</b>
Sodium Carbonate- <b>Na<sub>2</sub>CO<sub>3</sub></b>	Sodium hydroxide - <b>NaOH</b>
Solar thermal conversion materials - <b>STCM</b>	Sorption enhanced reaction - <b>SER</b>
Steam methane reforming - <b>SMR</b>	Spinel - <b>MgAl<sub>2</sub>O<sub>4</sub></b>
Thermogravimetric analysis - <b>TGA</b>	Tert-Butyl hydroperoxide - <b>TBHP</b>
Thiophene - <b>TP</b>	Thermal conductivity - <b>κ</b>
Water evaporation rates - <b>WER</b>	Transmission electron microscopy - <b>TEM</b>
Water gas shift - <b>WGS</b>	X-ray photoelectron spectroscopy - <b>XPS</b>

# Chapter - 1

## Introduction and Literature Review

### 1.1 Introduction

Nanocarbon materials (e.g. graphene, graphene oxide and carbon nanotubes)<sup>1-3</sup> have attracted enormous attention due to their superior mechanical properties,<sup>4-6</sup> huge theoretical surface areas,<sup>7-9</sup> exceptional electrical and thermal conductivities<sup>10-12</sup> as well as superb chemical stability.<sup>13-15</sup> In order to maximise the usability of their exceptional properties, three-dimensional structures can be assembled from one-dimensional carbon nanotubes<sup>16-18</sup> or two-dimensional graphene building blocks.<sup>19-22</sup> Nanocarbon aerogels, formed by removing the liquid phase from a carbon nanostructure wet-gel, are of particular interest due to their ultralight weight,<sup>23-26</sup> their large accessible porosities and surface areas,<sup>27-30</sup> and the conductive nature of the nanocarbon framework.<sup>31-34</sup> Not surprisingly, nanocarbon-based three-dimensional aerogels (carbon nanotube aerogels and graphene aerogels) have started to attract attention in various research communities, and are investigated in a variety of applications, including contaminant adsorption,<sup>35-37</sup> photocatalytic materials,<sup>38-40</sup> antimicrobial applications,<sup>41-43</sup> electrodes for sensing,<sup>44, 45</sup> energy storage and conversion,<sup>46-49</sup> and catalysis.<sup>50-53</sup>

In this PhD project the utilisation of nanocarbon aerogels as truly multifunctional support frameworks for functional inorganic nanoparticles will be investigated. This project focusses specifically on the utilisation of inorganic nanoparticles in pollutant adsorption, where a variety of nanoparticle types have been extensively studied due to their excellent sorption capacity and/or catalytic activities.<sup>54-56</sup> However, inorganic particle systems in their pure powder form often suffer from significant shortcomings like low specific surface area, poor mass transfer, or challenging particle regeneration/recycling.<sup>57, 58</sup> One strategy to overcome these limitations is to support functional inorganic nanoparticles onto nanocarbon aerogels.<sup>59</sup> Spreading the adsorbent nanoparticles across a well-structured, mechanically and chemically stable, high-surface-area framework is hoped to increase accessibility of active particle sites while anchoring adsorbents firmly to a solid support can suppress nanoparticle aggregation and deactivation during operation or regeneration.<sup>60, 61</sup> Monolithic inorganic/nanocarbon aerogel also provides a practical materials form that facilitates commercially important particle recovery and regeneration as well as in the integration of nanoparticles into continuous flow processes.<sup>62-65</sup>

An important secondary feature of nanocarbon aerogels in the context of nanoparticle supports is their high electrical and thermal conductivity. Such high conductivities are not available in other more conventional porous materials, such as zeolites,<sup>66</sup> metal-organic frameworks (MOFs)<sup>67</sup> or conventional silica aerogels,<sup>68</sup> which are typically electrically insulating. In addition to their support function, nanocarbon aerogels therefore offer an important new capability for accurate and energy efficient local temperature control via electrical heating (Joule heating).<sup>31, 69</sup> Aerogel-mediated nanoparticle heating is highly attractive in the context of the investigated sorption and catalysis applications, in theory opening up opportunities to control activity via simple and fast temperature control, while also allowing for energy efficient thermal regeneration processes to re-activate spent functional particle systems.

This PhD project will therefore investigate the synthesis, characterisation, sorption, and catalysis applications of inorganic/nanocarbon aerogels (INCAs), with a specific focus on the understanding and exploitation of nanocarbon aerogel Joule-heating.

To this end, Chapter 2 and Chapter 3 will focus on the synthesis and study of pure nanocarbon aerogels, with the aim to improve understanding of how the Joule-heating characteristics of nanocarbon aerogels are linked to their microstructure. Pure nanocarbon aerogels are produced through a variety of wet-chemical assembly methods (hydrothermal, ice-templating, emulsion templating) and their Joule heating characteristics, such as heating efficiency and heating kinetics, will be determined. These Joule heating measurements are accompanied by a variety of materials characterisation activities (electron microscopy, surface area, porosity, electrical and thermal conductivities) to establish fundamental structure-property relationships between aerogel microstructure and Joule-heating performance. As a side investigation, the established principles will be translated to a different heating methodology, namely solar thermal heating, and tested in the context of solar steam generation, an important, emerging technology for water desalination.

In Chapters 4 and 5, electrical Joule-heating will be explored for nanoparticle-decorated nanocarbon aerogels in the context of important sorption applications. In Chapter 4, graphene-based aerogels will be decorated with layered double hydroxide nanoparticles, while, in Chapter 5, carbon nanotube aerogels will be decorated with boron nitride. The structurally and chemically different INCA will then be tested for commercially and environmentally important gas-phase and liquid-phase adsorption applications, specifically desulfurisation (i.e. the adsorption of organosulfur compounds from liquid hydrocarbons) and CO<sub>2</sub> adsorption. It will then be demonstrated how Joule-heating to moderately high temperatures (100-400 °C) can

be exploited to aid recycling of these high-value sorbent materials via fast and energy-efficient thermal regeneration processes.

In Chapter 6, the concept of nanocarbon aerogel is explored under more extreme conditions. High electrical power input will be exploited to induce nanocarbon aerogel heating to very high temperatures beyond 1000 °C. High temperature Joule heating will be studied in the context of a variety of potential applications, including flash sorbent regeneration, nanocarbon graphitisation, nanoparticle synthesis, and catalysis desulfurisation.

In conclusion, this PhD project will investigate the fabrication of a broad variety of novel INCAs in order to understand the correlation between the aerogels' 3D-microstructure/composition and their functional properties, as tested for two important adsorption applications (adsorptive desulfurisation and CO<sub>2</sub> sorption). The multifunctional nature of the nanocarbon aerogel support framework will be explored via fundamental and applied Joule-heating studies at both intermediate and high temperature ranges (Figure 1).

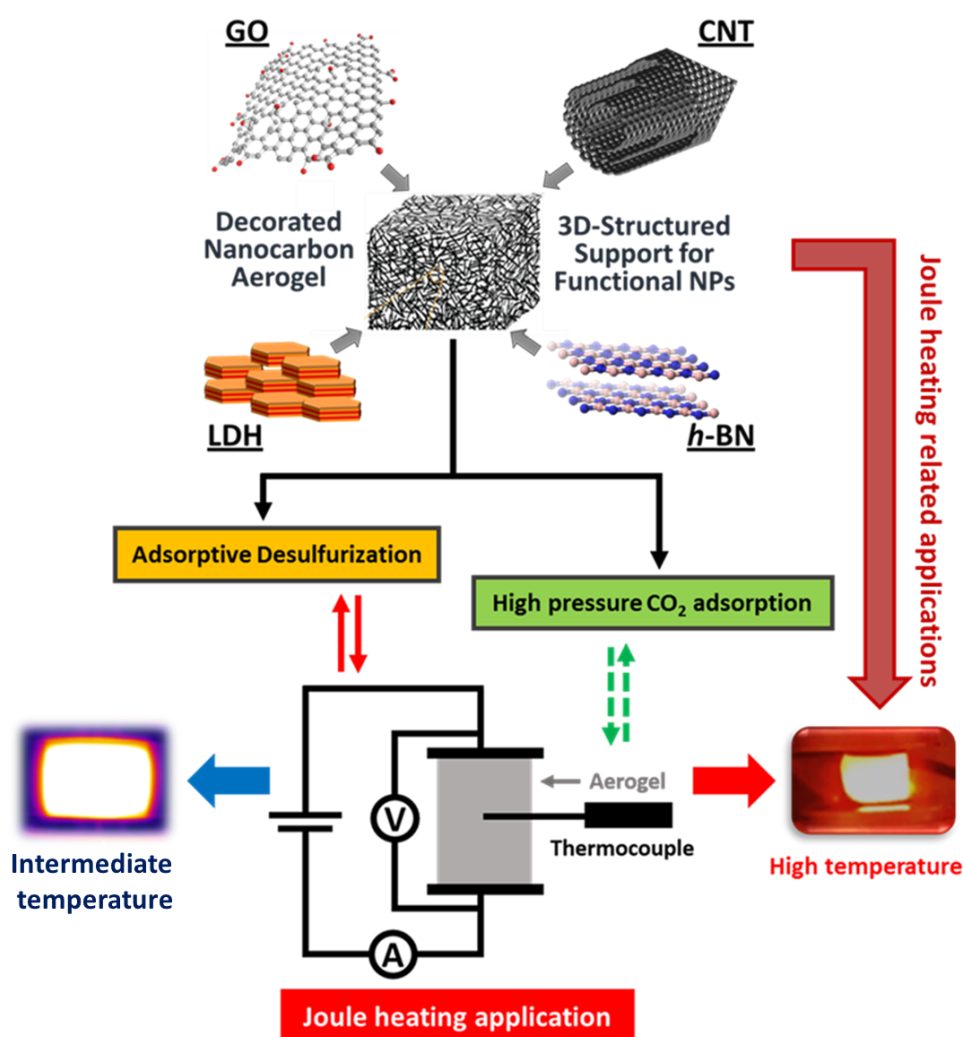


Figure 1 Research overview.

## 1.2 Literature Review

### 1.2.1 Nanocarbons

#### Graphene

Graphene is a carbon allotrope, consisting of a single layer sheet of  $sp^2$  hybridised carbon atoms that has only one-atom thickness.<sup>70</sup> Figure 1.1 shows the structure of a single layer graphene in different spatial resolutions.<sup>71-73</sup> Graphene has triggered immense interests in the scientific community due to its strong mechanical properties,<sup>74</sup> large theoretical surface area,<sup>75</sup> exceptional electrical (2000 S/m) and thermal conductivity<sup>76-78</sup> and high chemical stability.<sup>78</sup> For example, graphene exhibits excellent charge-carrier mobility of  $250000 \text{ cm}^2 \cdot \text{V}^{-1} \cdot \text{s}^{-1}$  at room temperature,<sup>79, 80</sup> a thermal conductivity of up to  $5000 \text{ W} \cdot \text{m}^{-1} \cdot \text{K}^{-1}$ ,<sup>76</sup> and a theoretical specific surface area of  $2630 \text{ m}^2 \cdot \text{g}^{-1}$ .<sup>81</sup> Graphene obtained its nickname of “miracle material” due to these advantageous properties.<sup>82</sup> Since its discovery in 2004,<sup>83</sup> it has been reported in an enormous number of applications such as catalysis,<sup>84</sup> renewable energy storage and conversion systems,<sup>85</sup> biotechnologies,<sup>86</sup> environmental pollutant removal and composite materials.<sup>87-89</sup>

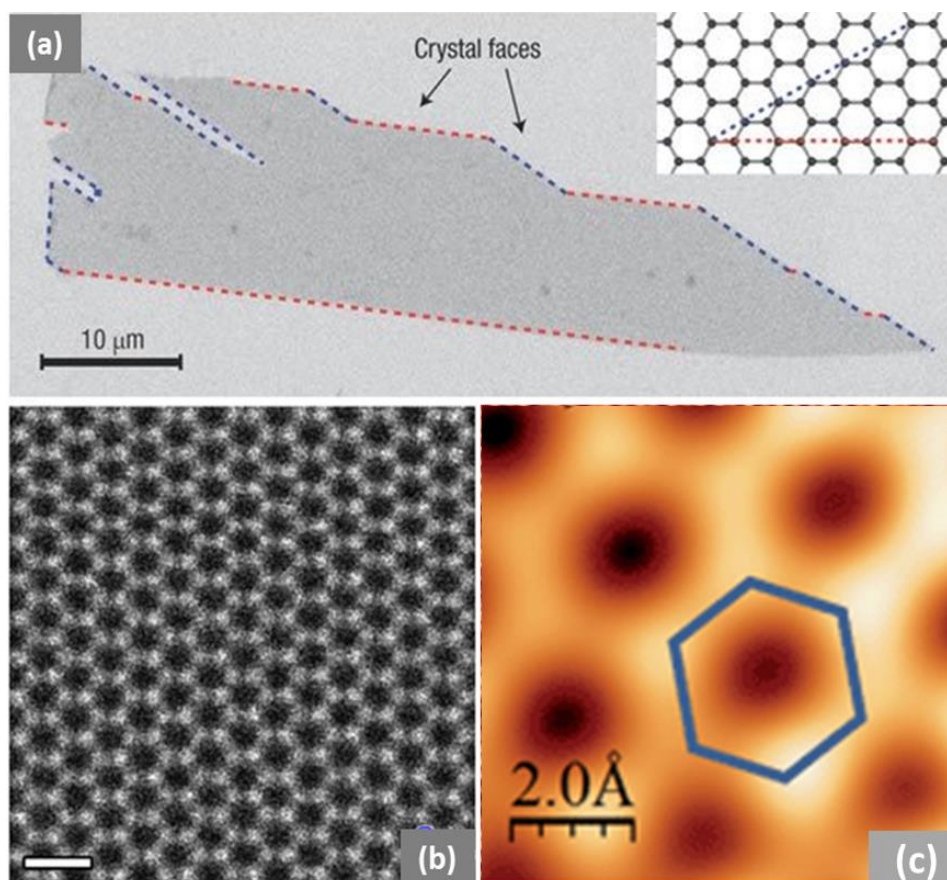


**Figure 1.1** (a) Scanning electron micrograph of single layer graphene crystal. (b) Transmission electron micrograph of single layer graphene lattice in atomic resolution. (c) Scanning tunnelling micrograph of suspended graphene (cited from Ref. 71-73).

Graphene can be produced by both bottom-up and top-down approaches.<sup>90</sup> For top-down methods, single sheet of graphene exfoliates from graphite which means that the van-der-Waals forces which hold the stacked sheets together must be overcome.<sup>91</sup> The bottom-up method produces graphene from molecular carbon-containing sources.<sup>92</sup> The delamination of graphene sheets by the top-down method tends to re-agglomeration through van-der-Waals forces and often introduces defects into the graphene structure (which will reduce its high performance metrics) due to the large energy input needed. On the other hand, bottom-up methods tend to produce more crystalline graphene, but often in a form that is strongly attached to a surface and highly hydrophobic, making further processing challenging.

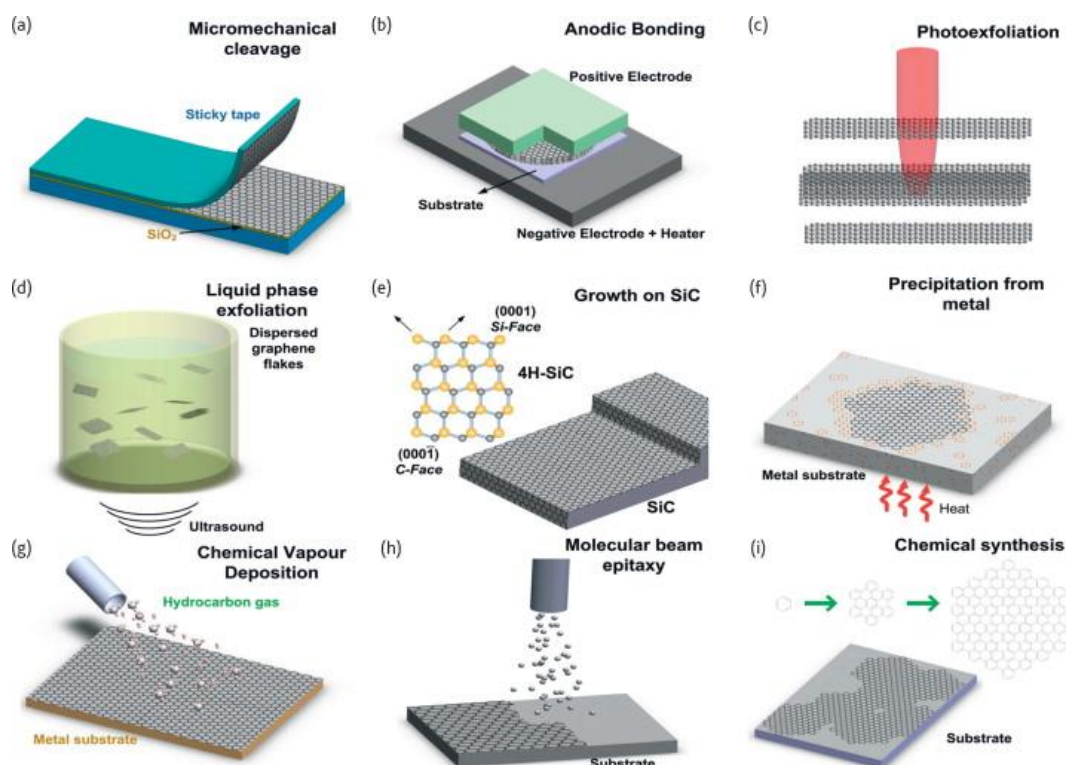


**Figure 1.2** Schematic illustration of the main graphene production techniques (cited from Ref. 93).

Figure 1.2 lists the main graphene production techniques.<sup>93</sup> The top-down method (Figure 1.2a-1.2d) includes micromechanical cleavage, anodic bonding, photoexfoliation and liquid phase exfoliation. Among these methods, liquid phase exfoliation to produce graphene is one of the most common methods which involves three steps: (1) dispersion of graphite in a liquid solvent; (2) sonication to generate individual layers of graphene (3) washing and purification of graphene. Bottom-up approaches (Figure 1.2e-1.2i) include growth on SiC, precipitation from metal, chemical vapour deposition, molecular beam epitaxy, and chemical synthesis. Chemical vapour deposition (CVD) is the most common bottom-up method to

synthesize large area graphene. The main method is CVD of hydrocarbons or alcohols onto the surface of transition metal catalysts to catalyse and template the growth of graphene.<sup>94</sup>

Conceptually, graphene is the basic building block from which other graphitic materials are derived. For example, it can be wrapped up into 0D fullerenes, rolled into 1D carbon nanotubes or stacked into 3D graphite, as shown in Figure 1.3.<sup>71</sup> Due to the highly hydrophobic characteristic of graphene nanosheet, it is difficult to be dispersed in water solutions, which makes its processing and integration into applications very challenging. Therefore, the chemical modification of graphene with functional groups to render the resulting graphene derivatives more compatible with other media are important for broadening graphene applications.

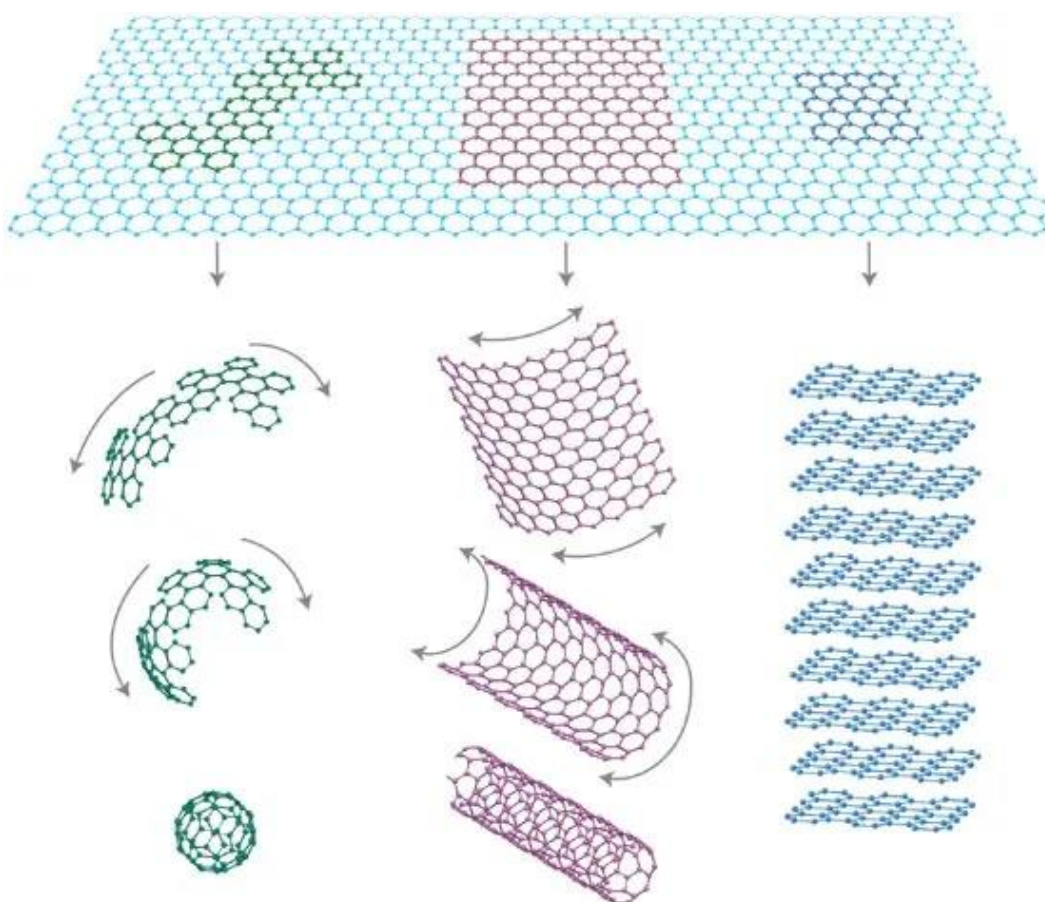


**Figure 1.3** Graphene is the mother material for other carbon materials, including wrapped into 0D fullerenes, rolled into 1D carbon nanotubes or stacked into 3D graphite (cited from Ref. 71).

### Graphene oxide (GO)

Graphene oxide (GO) is the oxidised form of graphene, with a high density of oxygen functional groups, including epoxide, hydroxyl, carbonyl and carboxylic groups.<sup>95</sup> Figure 1.4a shows the structure of different chemical graphene

derivatives.<sup>96</sup> Using GO instead of graphene is a common approach to fabricating more complex graphene nanomaterials, due to the relatively low costs of GO and its pronounced hydrophilicity (facilitating straightforward processing in water).<sup>36</sup> Chemical oxidation of graphite is the most common way to produce GO. The most extensively used oxidation method is the Hummers' method, which uses strong chemical oxidants (i.e.  $\text{HNO}_3$ ,  $\text{KMnO}_4$  and  $\text{H}_2\text{SO}_4$ ) to oxidise natural graphite powder and subsequently using ultrasonication to exfoliate (Figure 1.4b).<sup>36</sup> Although oxidation is a very efficient approach to obtain exfoliated sheets, the physical and chemical properties of GO are altered hugely, compared to pristine graphene due to the oxidative damage to the aromatic system of the graphene sheets. The high density of oxygen functional groups make GO more hydrophilic, enabling GO to stay well-dispersed in aqueous suspensions. However, in contrast to pristine graphene, GO is an electrical insulator,<sup>97</sup> shows weaker mechanical properties<sup>98</sup> and is chemically reactive.<sup>99</sup> In order to restore the properties of pristine graphene to some degree, different approaches including thermal, chemical, and photochemical methods are used for the reduction of GO.<sup>100, 101</sup> These approaches remove large amounts of oxygen to improve the graphitic quality, but the total reduction of GO is still difficult. Figure 1.4 exhibits the reduced GO (rGO) which still has significant number of defects in comparison with graphene, such as nanoholes.<sup>96</sup>

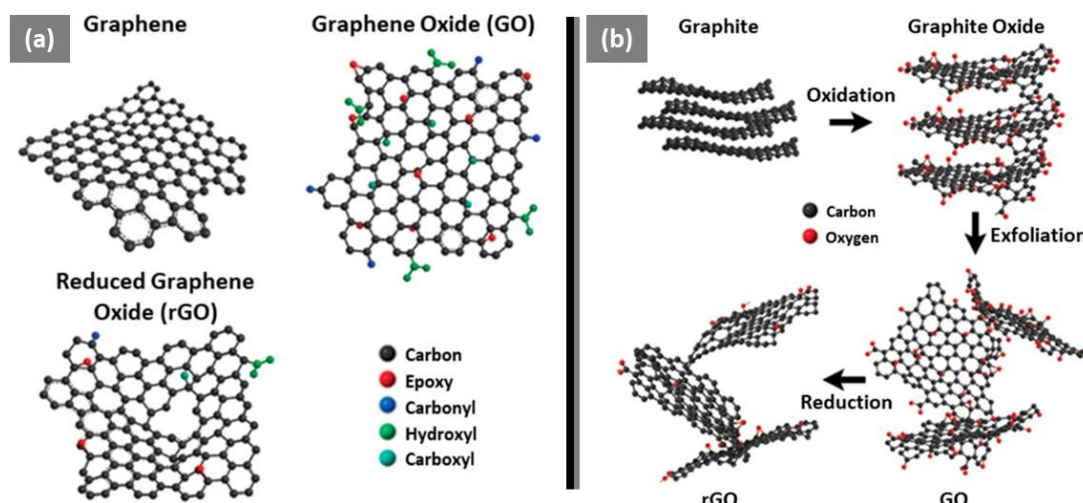


**Figure 1.4** (a) Schematic description the chemical structures of graphene, graphene oxide, and rGO. (b) Approach of graphite to rGO (adapted from Ref. 96).

## Carbon nanotubes (CNT)

Carbon nanotubes (CNT) are another allotrope of carbon, and exhibit a cylindrical hollow nanostructure with a sheet of graphitic carbon atoms rolled at specific angles. According to the number of the rolled sheets, CNTs are categorized as single-walled CNT (SWCNT), double-walled CNT (DWCNT) and multi-walled CNT (MWCNT) (Figure 1.5).<sup>102-104</sup> This project focussed exclusively on MWCNT which are

more cost effective and have wider commercial availability, compared to other CNT types.

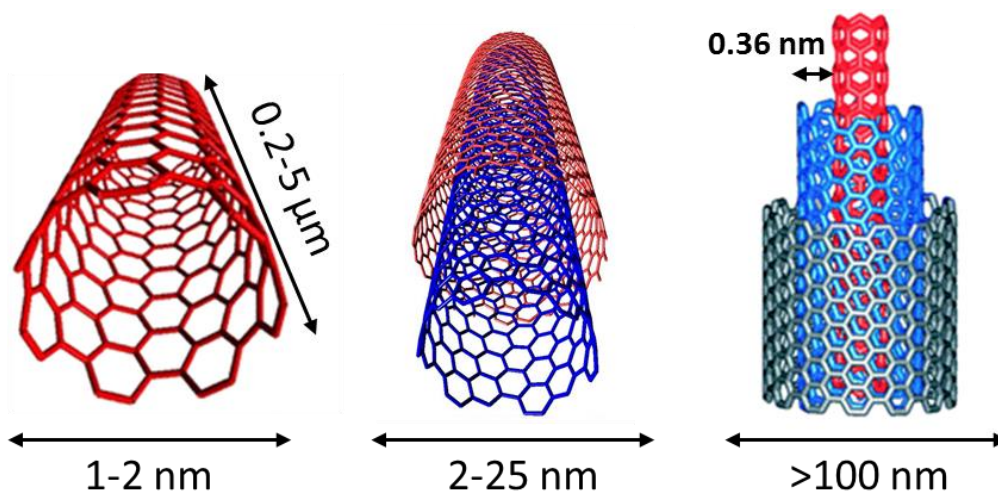


**Figure 1.5** Overview of structure of Single-, double-, and multi-walled CNTs (adapted from Ref. 103 and 104).

CNTs possess outstanding conductive and mechanical properties while also having very large aspect ratios ( $>1000$ ).<sup>105</sup> Due to these unique physical-chemical characteristics, CNTs have been employed in various fields, including thin-film conductors, hydrogen evolution reaction, structured polymer composites, etc.<sup>106-110</sup> Several methodologies have been employed to fabricate carbon nanotubes. For example, the electric arc technique and laser ablation can produce highly crystalline SWNTs. However, chemical vapour deposition (CVD) is the dominant approach of high-volume CNT production.<sup>102</sup> However, the electrical conductivity of SWCNT (e.g. metal or semiconductor) is determined by the chirality of  $(m, n)$  (where  $m$  and  $n$  are positive integers) resulting in different types of SWCNT, such as zigzag  $(n, 0)$ , armchair  $(n, n)$  and chiral  $(n, m)$  where  $n \neq m$  and  $m \neq 0$ . Nanotube chirality determines important properties of SWCNT, such as colour (Figure 1.6a).<sup>111, 112</sup> How to control the chirality of SWCNT is a challenging conundrum for the materials research community. Recently, much improved control of SWCNT's chirality was demonstrated through the use of nanocrystal catalysts ( $\text{MoO}_3$ ) with well-defined crystal facets of four-fold or six-fold crystal symmetry, enabling SWCNT growth with specific chirality (a chiral angle of  $19.1^\circ$ ) via ethanol CVD, as shown in Figure 1.6b.<sup>113</sup>

For MWCNT, the main nanotube type used in this work, chirality is less crucial as each MWCNT consists of a number of different, inter-nested SWCNT types. As a result, unmodified MWCNT of high graphitic crystallinity generally behave similar to metallic conductors.

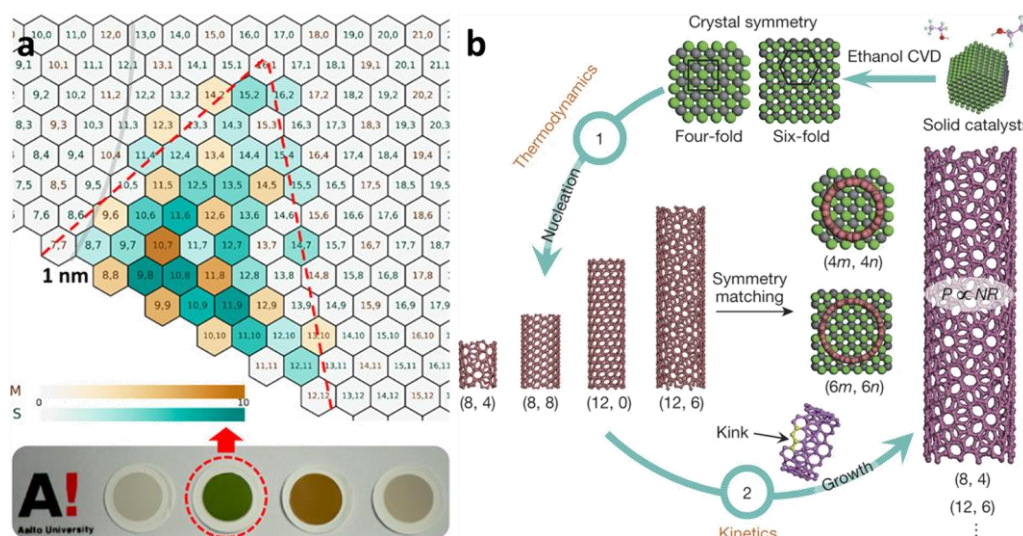


**Figure 1.6** (a) Chirality of individual SWCNTs with related colours (cited from reference 112), (b) synthesis of SWCNTs with controlled chirality in ethanol CVD via a two-stage nucleation-growth process (cited from Ref. 113).

This work focusses on the assembly of nanocarbon networks in aqueous solution (see also below) as key step during aerogel fabrication. However, pristine CNT are difficult to process in water due to their pronounced hydrophobicity. As with graphene, pristine CNT materials can be readily functionalised with hydrophilic oxygen-containing functional groups, such as carboxylic acid groups, to improve their compatibility with water. The introduction of carboxylic acid groups on MWCNTs can be easily achieved through acid-oxidation, e.g. through the treatment of MWCNTs in  $\text{H}_2\text{SO}_4/\text{HNO}_3$  mixture at  $80^\circ\text{C}$  for several hours, followed washing to pH neutral (Figure 1.7).<sup>114</sup> As with graphite oxidation, CNT oxidation can significantly degrade the structural properties of CNTs. However, degradation is less severe in case of MWCNT (compared to SWCNT) as only the outer walls are attacked while the inner nanotube walls are better protected. (This reduced susceptibility to structural damage upon oxidation is another reason why the main focus of this work is on MWCNT rather than SWCNT.) Once oxidised CNT (oCNT) have been processed or assembled, thermal or chemical reduction processes can be employed to remove the carboxylic acid groups and (partially) restore the original graphitic properties, including chemical stability, electro-thermal conductivity, and mechanical strength.<sup>96</sup>



**Figure 1.7** Preparation of oxidised MWCNT and reduction of oxidised MWCNT after processing (adapted from Ref. 114).

## 1.2.2 Nanocarbon aerogels

### 1.2.2.1 Conventional aerogels

An aerogel is a porous ultralight material derived from a wet-gel, in which the liquid component of the wet-gel has been replaced with a gas.<sup>115</sup> Aerogels made from inorganic materials have been applied and explored in many areas such as catalysis, adsorption, chemical sensors, acoustic transducers, energy storage devices, spacecrafts, skyscrapers, automobiles, electronic devices and clothing.<sup>115-118</sup> Aerogels exhibit a series of outstanding physical and chemical properties such as very large porosity, super lightweight, low density and high specific surface area.<sup>115</sup> The most widely used aerogels are silica, carbon and alumina aerogels. However, among these three types of aerogels, silica aerogel is the most widely explored and possesses interesting properties, such as excellent acoustic dampening, extremely low thermal conductivity, and translucent optical properties. These features make silica aerogels one of the most promising thermal insulating materials for building applications.<sup>119</sup> Many conventional aerogels, including silica aerogels, are produced via sol-gel methodologies which contain three fundamental steps<sup>115</sup>: (a) the reaction of molecular precursor to form a continuous network of colloidal particles (sol-gel step), (b) the growth of the continuous network in solution to form a wet-gel (aging step), and (c) removal of the liquid component of the wet-gel (drying step) to form an interconnected porous colloidal network filled with gas (Figure 1.8).

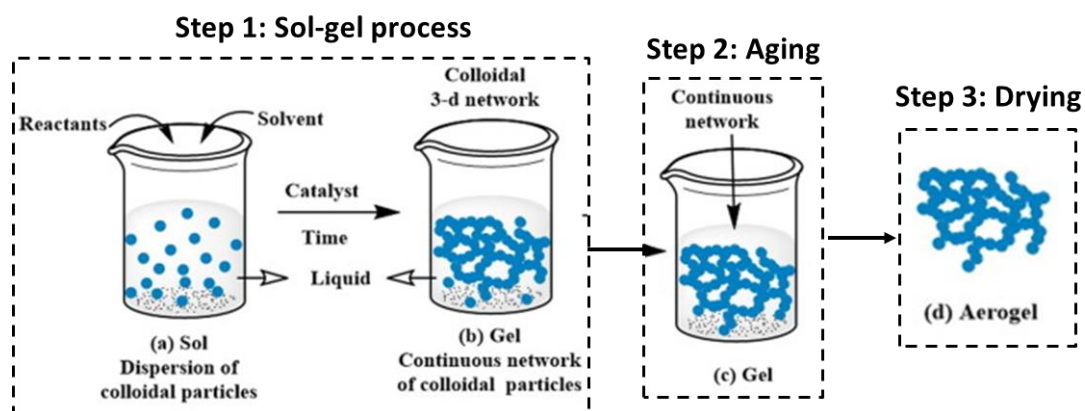


**Figure 1.8** Sol-gel preparation of conventional inorganic aerogels, such as silica aerogels (adapted from Ref. 115).

### 1.2.2.2 Nanocarbon aerogel synthesis

Nanocarbon aerogels are the products of the self-assembly of discrete carbon nanostructures, such as graphene, graphene oxide or carbon nanotubes, into continuous three-dimensional networks.<sup>120</sup> A very broad variety of synthetic strategies have been investigated to assemble carbon nanostructure (Figure 1.9),<sup>121</sup>

with the unifying aim to create macroscopic material forms that enable the utilisation of the unique properties of individual carbon nanostructures on the macro-scale.

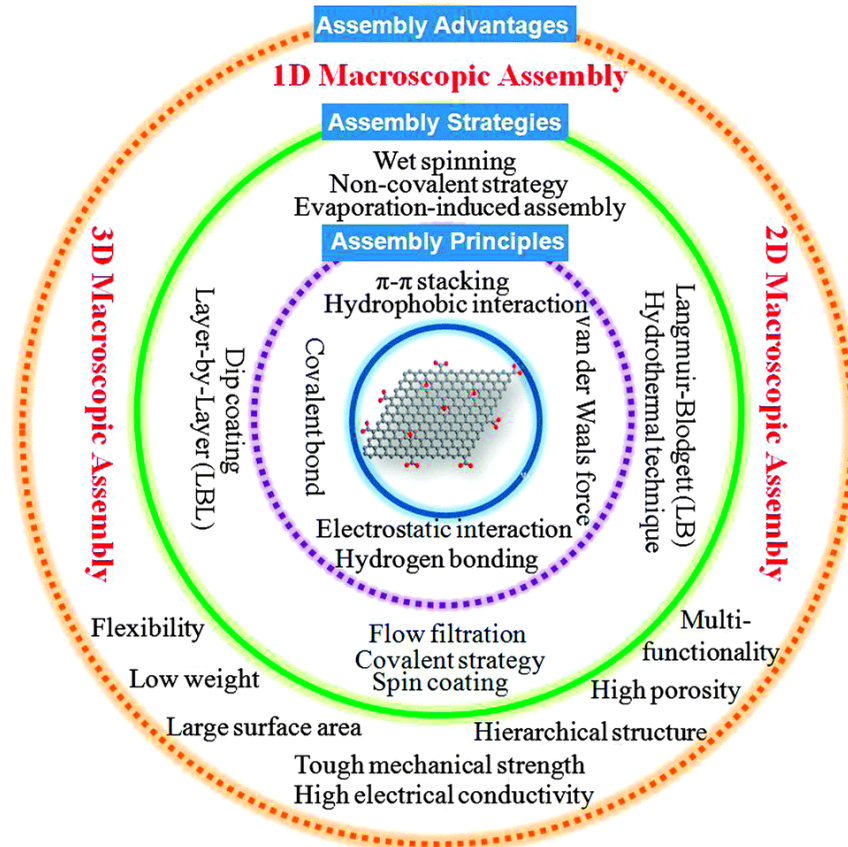


**Figure 1.9** Schematic description of the macroscopic assemblies and architectures of nanocarbons: principles, strategies, and advantages (cited from Ref. 121).

Aerogels are a three-dimensional macroscopic material form, characterised by a high degree of porosity, low-density and unique internal microstructures. Typical synthetic methodologies for the wet-chemical assembly of nanocarbon aerogels, include hydrothermal synthesis,<sup>122, 123</sup> evaporation-induced nanocarbon assembly<sup>124</sup> and templated nanocarbon assembly.<sup>125-128</sup> In this PhD project, two typical approaches to synthesis nanocarbon aerogels utilise: (a) random assembly via hydrothermal synthesis, and (b) templating strategies (e.g. templating around ice crystals or emulsion droplets).

### Aerogel synthesis via random nanocarbon self-assembly

For wet-chemical nanocarbon assembly methods, individualisation of the nanocarbons (i.e. exfoliation of graphene derivatives or de-bundling of CNTs) and the creation of stable nanocarbon dispersions are important, non-trivial pre-requisites. Individualisation and dispersion of carbon nanostructures is most commonly

achieved by chemical (covalent or non-covalent) nanocarbon functionalisation or addition of surfactants to improve compatibility with the dispersion medium and to induce electrostatic or steric nanocarbon stabilisation in solution. In order to form a continuous gel network, the stability of the nanocarbon dispersion is then disrupted through a physical or chemical stimulus (e.g. change in temperature, pH, ionic strength, nanocarbon concentration, nanocarbon surface chemistry). The subsequent crosslinking of the nanocarbon network can be achieved through either covalent chemistry (e.g. via addition of crosslinking agents) or through promoting non-covalent interactions such as van-der-Waals interactions (e.g. via increasing nanocarbon graphiticity).<sup>121</sup> Figure 1.10 displays a typical example for the fabrication of nanocarbon aerogels via random nanocarbon assembly. In Figure 1.10a, an aqueous GO dispersion was destabilised through addition of a reducing agent (ascorbic acid) leading to the removal of stabilising oxygen functional groups at 70 °C.<sup>129</sup> As a result, the nanocarbon dispersion collapses into a hydrogel-like network crosslinked via increased  $\pi$ - $\pi$  interactions after GO reduction by ascorbic acid (Figure 1.10a). The water is then removed from the network through mild freeze-drying to form the final GO aerogel (Figure 1.10b). This method can be adapted to produce hybrid nanocarbon aerogels via hydrothermal approaches (i.e. via reaction at elevated temperatures and high vapour pressures).

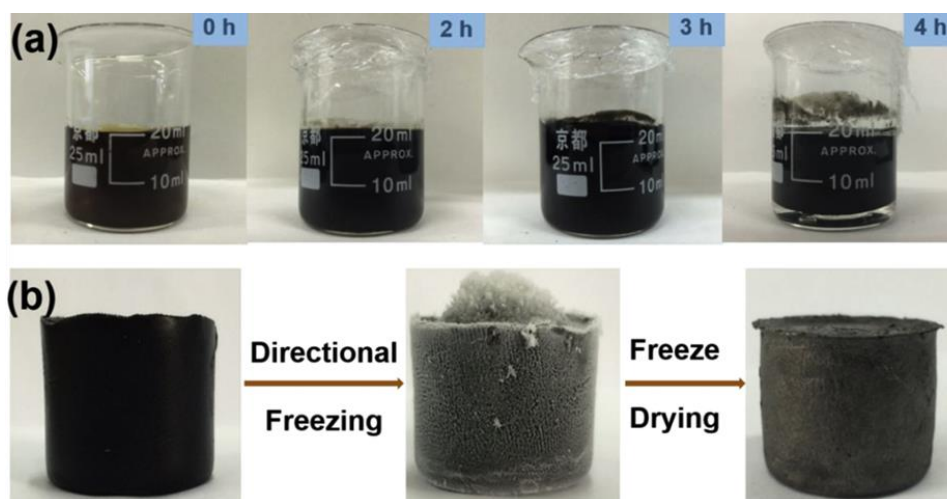


**Figure 1.10** (a) Digital images of different stages of forming graphene hydrogel at 70 °C. (b) Freezing and freeze-drying procedures to make graphene oxide aerogel (cited from Ref. 129).

Figure 1.11a shows an example,<sup>130</sup> where a mixture of dispersed GO and CNTs was treated in an autoclave at 180 °C to form a hydrogel (without additions of reducing agents), followed by lyophilisation to produce a CNT/rGO hybrid aerogel with various cellular microstructure (Figure 1.11b-c) and high thermal conductivity ( $88.5 \text{ W}\cdot\text{m}^{-1}\cdot\text{K}^{-1}$ ). The formed CNT/rGO aerogel with strong stability is due to the hydrothermal

process partially removing oxygen-containing functional groups of GO and CNTs, which leads to strong  $\pi$ - $\pi$  interaction between the rGO sheets and the CNTs.

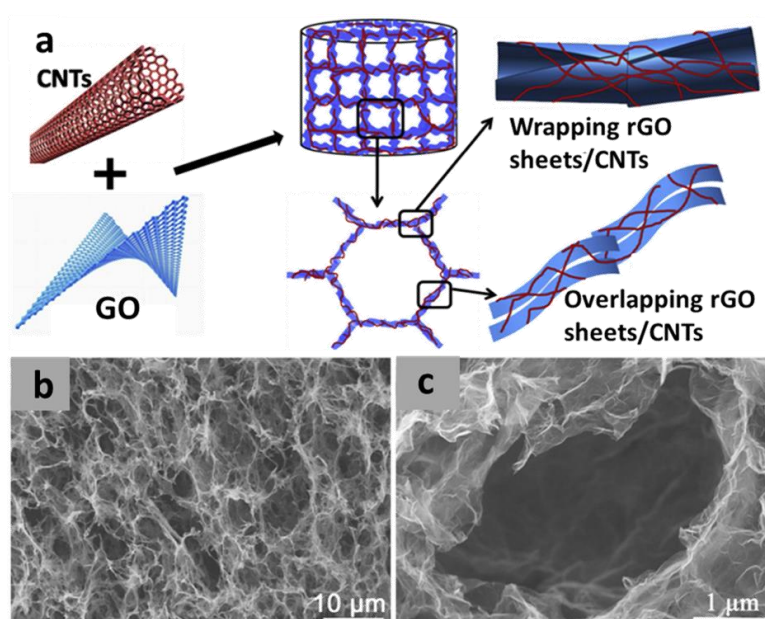


**Figure 1.11** (a) Hydrothermal approach to producing CNT/rGO hybrid aerogel without addition of reducing agents. (b-c) SEM images of CNT/rGO hybrid aerogels (adapted from Ref. 130).

It has been postulated that for GO, which carries up to 20 at% hydrophilic oxygen groups, crosslinking into continuous networks can also be promoted by hydrogen bonding. Figure 1.12 shows potential GO self-assembly configurations, based on non-covalent hydrogen bonding between GO sheets, as simulated by combining the results of Fourier-transform infrared spectroscopy, transmission electron microscope and X-ray diffraction.<sup>131</sup>

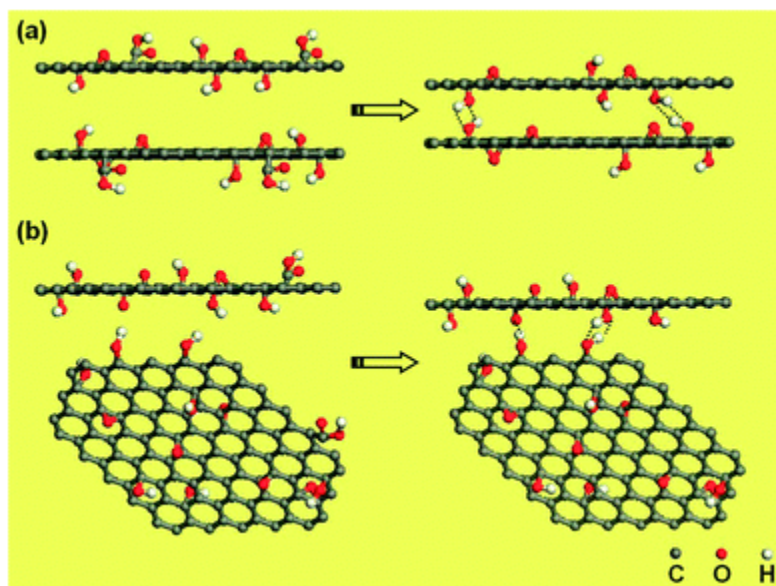


**Figure 1.12** Self-assembly mechanism of GO sheets: (a) self-assembly between two parallel GO sheets, (b) self-assembly between two non-parallel GO sheets (cited from Ref. 131).

Utilizing polymers as intermediates to covalently crosslink nanocarbons into 3D aerogels has been frequently exploited, including using polyvinyl alcohol (PVA), poly(m-phenylenediamine), poly(acrylic acid), polyethylenimine, polyimide, and etc.<sup>132-136</sup> For example, a modified polymer-induced covalent crosslinking assembly of GO sheets into rGO aerogels using PVA/glutaraldehyde is presented in Figure 1.13, where the glutaraldehyde molecules work as highly active crosslinkers to both the GO sheet and PVA. Therefore, glutaraldehyde molecules will react with the hydroxyl groups from the adjacent GO sheet and PVA, forming covalent intermolecular binding (Figure 1.13c-g).<sup>132</sup>

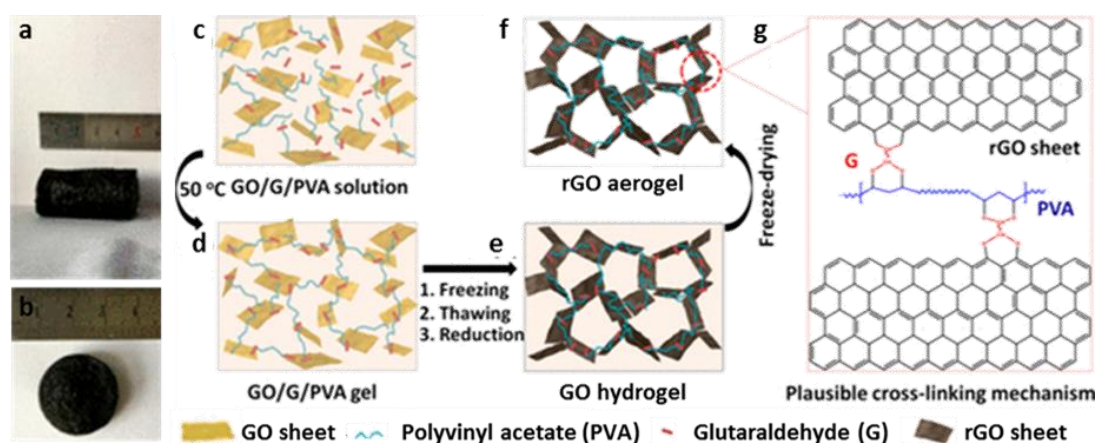


**Figure 1.13** (a-b) Digital photos of rGO aerogels. (c-g) Schematic descriptions of synthesizing rGO aerogels (cited from Ref. 132).

### Aerogel synthesis via templated nanocarbon assembly

Nanocarbon aerogels can also be synthesised by assembly of nanocarbons around a template structure, providing a route to control the internal aerogel microstructure. For this PhD research, aerogel templating by ice-crystals and emulsion droplets will be exploited. A typical example of ice-templating was investigated by Liu *et al.* who synthesised highly compressible, low density ( $8.7 \text{ mg}\cdot\text{cm}^{-3}$ ) reduced GO aerogels with anisotropic porosity through directional freeze-drying (Figure 1.14).<sup>129</sup> Aqueous mixtures of exfoliated GO and ascorbic acid (1:1, w/w) were heated at  $70^\circ\text{C}$  to acquire GO hydrogels. Crosslinking of the aerogels is induced through reduction of the GO by ascorbic acid, leading to a (partial) restoration of the graphitic properties and resulting in strong, cross-linking through van-der-Waals interactions between the sheets. During freezing of the GO hydrogel, solid ice particles form and pile up in-between GO sheets. Freezing is induced at the bottom of the hydrogel (by placing a hydrogel monolith on top of a liquid-nitrogen-cooled surface) so that ice crystals gradually grow in one direction from the bottom to the top of the aerogel. Consequently, after freeze-drying, the rGO aerogel exhibits

anisotropic porous structure presented in Figure 1.14b and 1.14c, with channel-like macropores with typical macro-pore sizes of several micrometre. This anisotropic pore structure, induced by directional freezing, plays a vital role in enhancing the mechanical property of the rGO aerogel.<sup>129</sup>

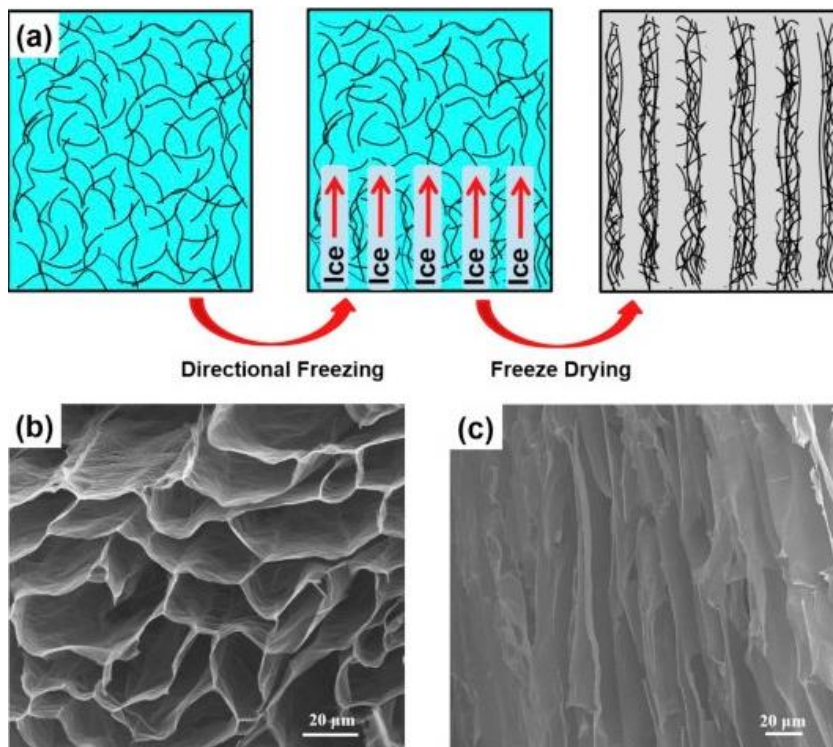


**Figure 1.14** (a) Illustrations of both the directional-freezing and freeze-drying; (b) top-view and (c) side-view SEM images of anisotropic porous structure of graphene aerogel ( $8.7 \text{ mg}\cdot\text{cm}^{-3}$ , cited from Ref. 129).

Emulsion-templated aerogel fabrication methods utilise GO sheets as surface-active amphiphiles in oil-water mixtures, with exfoliated GO stabilizing the interface between the oil phase and the water phase in emulsions (GO-stabilised Pickering emulsion).<sup>127</sup> Due to their high concentration of hydroxyl and carboxylic acid groups, the GO sheets' interfacial activity is highly depended on pH. At low pH, deprotonation of the functional groups is suppressed, which reduces the hydrophilicity of GO and leads to the preferential assembly of GO sheets at the oil/water interface of emulsion droplets. The emulsion droplets therefore act as effective spherical templates for the GO assembly. In a typical emulsion-templating aerogel synthesis (Figure 1.15), aqueous GO suspensions are emulsified with toluene (which acts as the oil phase) at low pH. The resulting GO-stabilised emulsions are cast into moulds and subsequently frozen in liquid nitrogen. After removing the solvents during freeze-drying, GO aerogel monoliths are obtained with spherical internal microstructure shaped by the micrometre-sized emulsion droplets.<sup>127</sup>

Thermal reduction treatments can be employed to further enhance GO crosslinking and therefore mechanical aerogel stability.

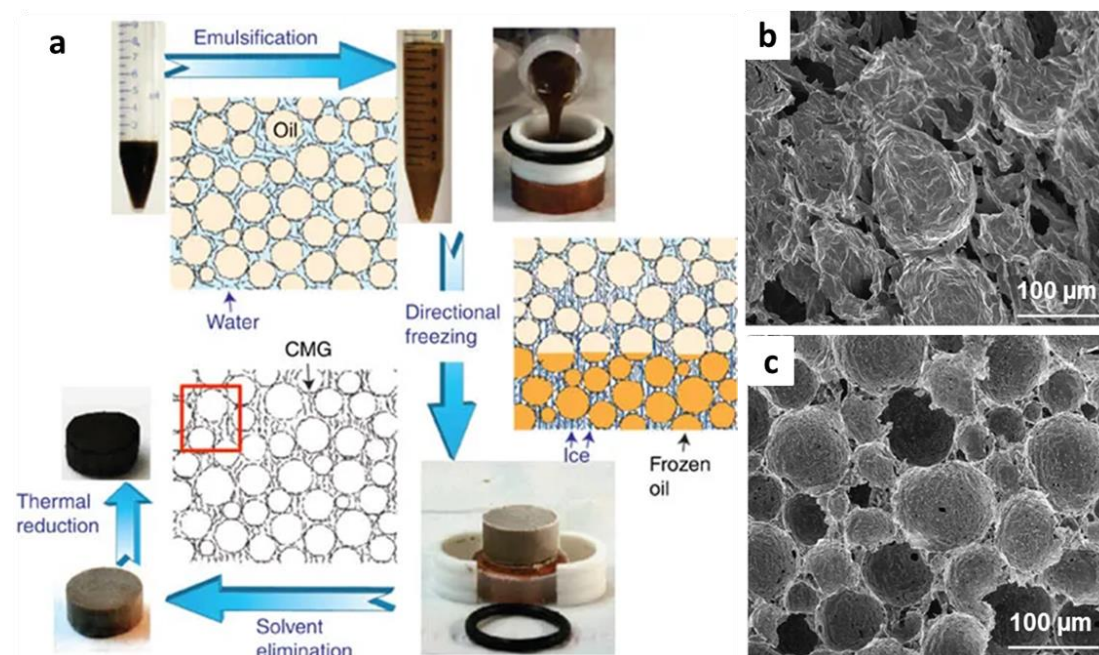


**Figure 1.15** Schematics of synthesizing graphene oxide aerogels by using emulsion-templated method. (a) Detailed procedures to synthesize emulsion-templated GO aerogels. (b-c) SEM images of emulsion-templated GO aerogels produced using different GO concentrations (cited from Ref. 127).

Recently, applying air-bubble-templated synthesis method has been reported to make aerogels within large bubble microstructures, which can be constructed to a huge rGO aerogel 'building' and 'wall' via the wet-press assembly approach followed by air drying, as profiled in Figure 1.16.<sup>137</sup> Generally, the GO aqueous solution ( $> 12 \text{ mg}\cdot\text{mL}^{-1}$ ) with reductant (ascorbic acid) and surfactant (alkyl glycoside) is intensely stirred with abundant air microbubbles to form foamed GO solution (Figure 1.16a), followed by hydrothermal and freezing steps to form rGO hydrogels. As the air bubbles are existed in the foamed GO solution, therefore the GO nanosheets will assembly around the air bubbles during hydrothermal reduction, to construct plenty of air-bubble-like microstructures (Figure 1.16b). The as-formed rGO hydrogels can be assembled into a huge 'building' or 'wall' by using the 3D wet-press following by air drying to become a superlight rGO aerogel 'building' or 'wall' (Figure 1.16c-d), owing to the formed microbubbles efficiently inhibiting microstructure collapses under press and air drying.

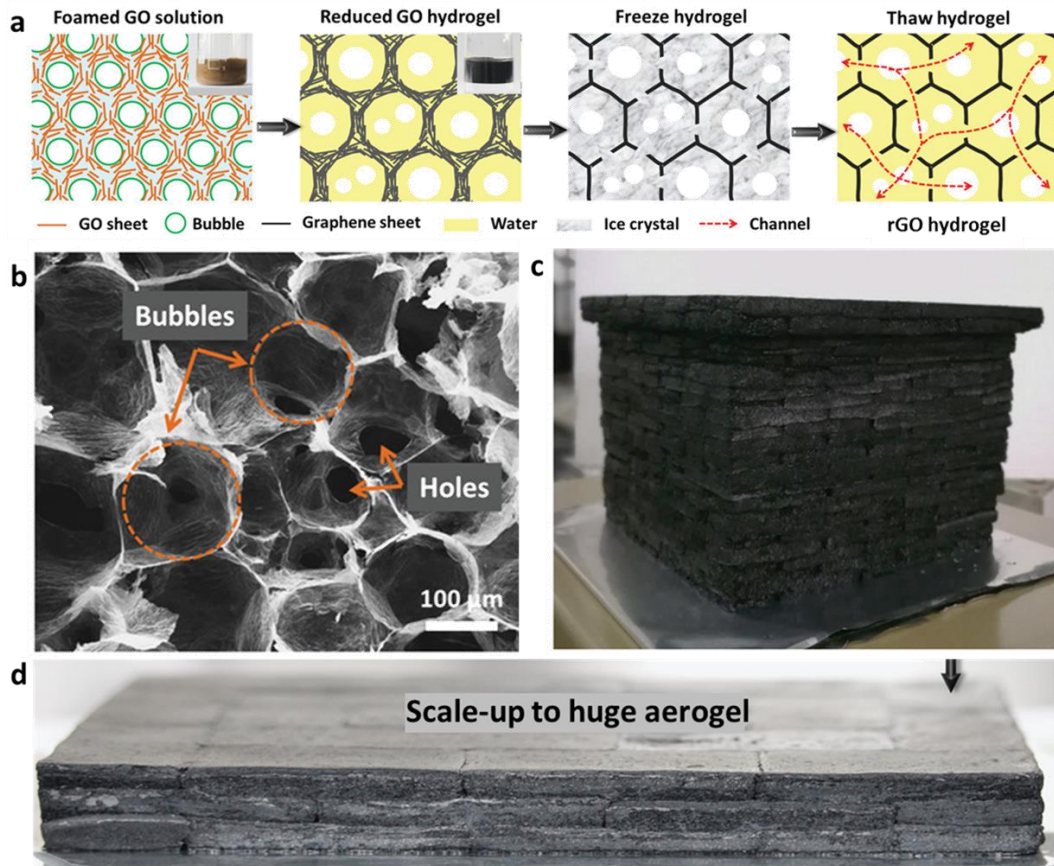


**Figure 1.16** (a) Schematics of air-bubble-templated method to synthesize rGO hydrogel. (b) SEM image of air-bubble-templated rGO hydrogel. (c) A digital photo of rGO hydrogel 'building' constructed by the wet-press assembly method. (d) A digital photo of a huge rGO aerogel 'wall' prepared by rGO hydrogel 'bricks' after air-drying (cited from Ref. 137).

### 1.2.3 Adsorption applications

#### 1.2.3.1 Liquid-phase adsorption

Liquid-phase adsorption has great societal and commercial importance, e.g. in the context of water treatment or for the purification of fossil fuels.<sup>138, 139</sup> Water treatment is one of the predominant problems in environmental fields because water is the most vital life substance for all life on earth. Providing clean water is a major challenge of all nations for the 21<sup>st</sup> century.<sup>140</sup> Diverse technologies have been employed for water purification, encompassing solar evaporation, photocatalysis, chemical precipitation, filtration, electrochemical precipitation, membrane separation, distillation, adsorption, etc.<sup>141-147</sup> Among them, the solar-thermal-induced water purification methods using nanocarbon-interconnected porous structures have been popularly exploited recently.<sup>148</sup> However, adsorption-based technologies are particularly promising and of importance for wastewater treatments, owing to their high adsorption abilities of contaminants, low-energy

costs, convenient implementation, fast sorption equilibrium kinetics and inexpensive production.<sup>149, 150</sup>

Pristine GO- and CNT-based adsorbents are extensively utilized to remove heavy metals, dyes, antibiotics, organic pollutants, etc., however, not showing very high capacities.<sup>151-153</sup> In terms of functional inorganic nanoparticles (such as metal oxide nanoparticles), they typically show higher adsorption performances.<sup>154-156</sup> Metal-oxide based inorganic adsorbents have been shown high efficiency to remove heavy metal ions, such as lead, copper, cadmium, nickel and mercury ions, from wastewater.<sup>157</sup> Some metal-oxide based inorganic adsorbents like magnetite and TiO<sub>2</sub> have much better arsenic adsorption capacity than activated carbon.<sup>158</sup> In terms of organic pollutant removal (for example anionic and cationic dyes, oils, pesticides and organosulfur compounds) from aqueous or organic liquid phases, inorganic adsorbents have also exhibited excellent uptake ability.<sup>159, 160</sup>

This project will investigate liquid-phase adsorption for the removal of organosulfur compounds from light fuels as an example of an important liquid-phase adsorption application. Desulfurisation is a pressing environmental problem in dealing with transportation fuel. Organosulfur compounds reduce the lifetime of metal catalysts of fuel cells, and the combustion of sulfur-containing fuels leads to the release of SO<sub>x</sub> exhaust gas which is the primary factor contributing to the formation of acid rain.<sup>161</sup> Generally, catalytic hydrodesulfurisation (HDS) is the main approach but has low efficiency in removing specific (aromatic and sterically hindered) sulfur-contained compounds, such as benzothiophene (BT), dibenzothiophene (DBT), dimethyldibenzothiophene (DMDBT) (Figure 1.17),<sup>162-164</sup> requiring high temperature, pressure, and large amounts of hydrogen.<sup>165</sup> Adsorptive desulfurisation has been deemed as a very promising alternative way because of its straightforward application and low-energy consumption.<sup>166-168</sup>

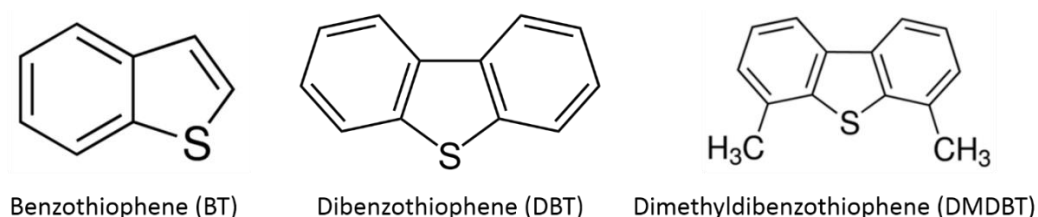


**Figure 1.17** The molecular formula of BT, DBT and DMDBT.

Various metal oxides, layered double hydroxides (LDHs), and boron nitride (BN) have shown promising ability for adsorbing sulfur-containing compounds.<sup>169-171</sup> As for metal oxides, they are the most largely implemented sorbents for adsorbing a variety of sulfur-containing compounds for fuel purification. For instance, the adsorption capacities of DMDBT, BT, methylthiophene (MT), DBT and

dibenzothiophene sulfone (DBTO<sub>2</sub>) over the Ti<sub>0.9</sub>Ce<sub>0.1</sub>O<sub>2</sub> adsorbents are presented in Figure 1.18a,<sup>172</sup> and the Ti<sub>0.9</sub>Ce<sub>0.1</sub>O<sub>2</sub> adsorbents preferred selectivity (adsorption configurations) for corresponding sulfur-containing compounds are calculated via DTF calculation (Figure 1.18b-f), which theoretically explains the adsorption affinity following with BT > DBT > DBTO<sub>2</sub> > MDBT > DMDBT, as a result of the steric hindrance.

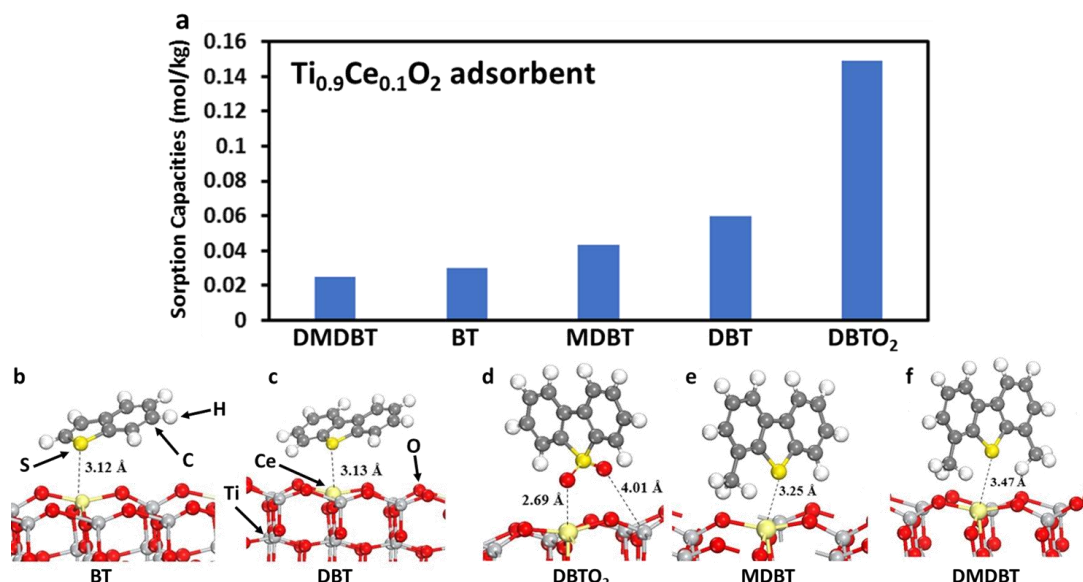


**Figure 1.18** (a) Adsorption capacities of different compounds over the Ti<sub>0.9</sub>Ce<sub>0.1</sub>O<sub>2</sub> adsorbent. (b) Adsorption configurations of organosulfur compounds over a Ce-doped TiO<sub>2</sub> surface via DFT calculation (adapted from Ref. 172).

The adsorptive desulfurisation capacities of MOFs can be dramatically enhanced via combination with metal oxide nanoparticles, such as chromium-benzenedicarboxylate (MIL-101) modified by copper and cerium oxides (i.e. Cu-Ce/MIL-101 adsorbent).<sup>173</sup> Specifically, the maximum BT adsorption capacity of Cu-Ce oxide nanoparticles impregnated MIL-101 adsorbent was tuneable ranging from 57 % to 188 % compared to the pure MIL-101 adsorbent, based on the dosage of Cu-Ce oxide nanoparticles (see below Figure 1.19a-b). The BT molecules adsorbed onto the Cu(I) sites and Ce(IV) sites are accredited to  $\pi$ -complexation and S-Ce binding mechanisms, respectively (Figure 1.19c-d).

Pure nanocarbon adsorbents also have been specifically investigated in adsorptive desulfurisation, mainly focusing on analysing adsorption mechanisms between nanocarbons and organosulfur compounds, but generally exhibit low sorption performance. While BN-based and LDH-derived materials are particularly interesting, which are accredited to their pronounced adsorptive desulfurisation capacities and adsorptive behaviours of organosulfur compounds (especially for sterically-hindered sulfur-containing compounds).

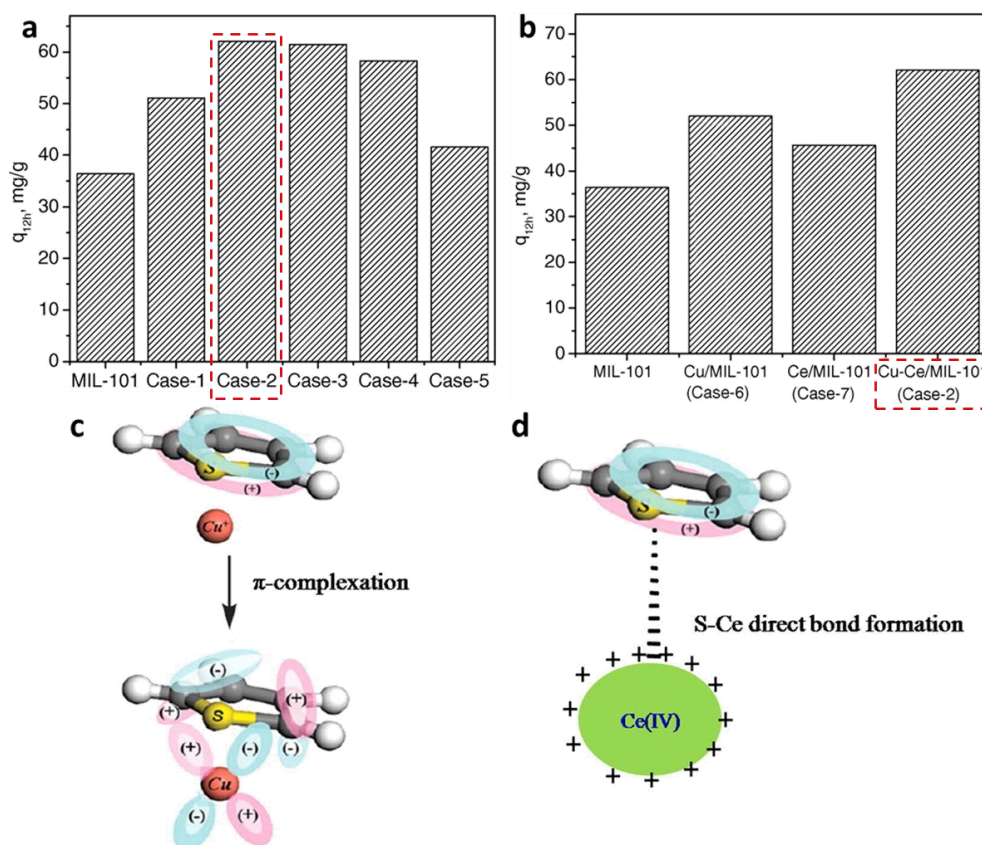


**Figure 1.19** (a) BT sorption performance over the pristine and CuCe-modified MIL-101s adsorbents (the initial BT concentration was 1000 ppm). (b) BT sorption performance over the pristine, Cu-modified MIL-101, Ce-modified MIL-101 and the Cu-Ce/MIL-101 adsorbents. (c-d) Schematics of adsorption mechanisms of BT/Cu(I) sites and BT/Ce(IV) sites in the Cu-Ce/MIL-101 adsorbent (cited from Ref. 173).

### 1.2.3.2 Gas-phase adsorption

The excessive discharge of carbon dioxide (CO<sub>2</sub>) is a major factor contributing to global warming and climate change. CO<sub>2</sub> capture and storage (CCS) is a crucially important technology to halt these negative effects.<sup>174, 175</sup>

In this context, post-combustion CCS, i.e. the removal of CO<sub>2</sub> from flue gases after combustion of fossil fuels, is a highly desirable technology. Post-combustion CCS is typically carried out at low to medium CO<sub>2</sub> partial pressures ( $p_{\text{CO}_2}$  = 0.1-1 bar), and low to medium operating temperatures ( $T$  = 20-300 °C), reflecting the conditions in typical flue gases. Functionalised porous nanocarbon materials also have been frequently adopted to probe post-combustion CO<sub>2</sub> capture, for example holey graphene frameworks.<sup>176</sup> As shown in Figure 1.20a, GO sheets are sonicated and strongly oxidised by HNO<sub>3</sub> to generate holey GO sheets, followed by reduction to obtain the holey graphene frameworks (see SEM image in Figure 1.20b), which shows good post-combustion CO<sub>2</sub> adsorption capacities (Figure 1.20c), owing to their high specific surface areas and well-generated meso-porosities.

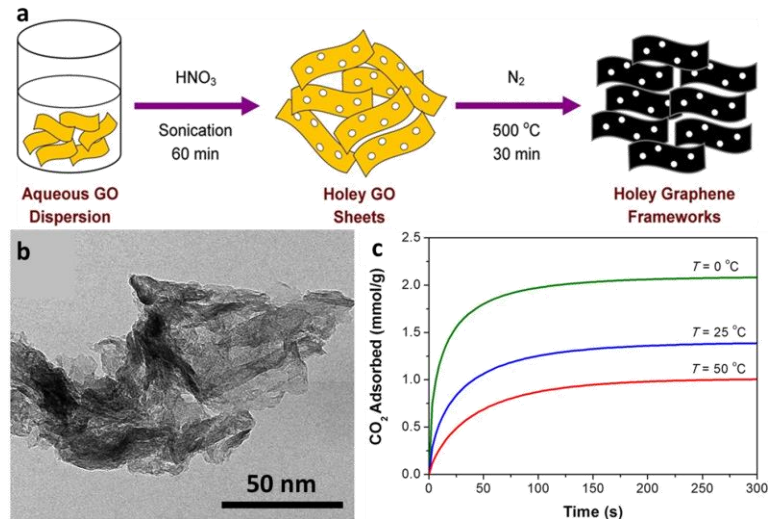


**Figure 1.20** (a) Schematics of synthesizing holey graphene frameworks. (b) TEM image of holey graphene frameworks. (c) CO<sub>2</sub> sorption kinetics of holey graphene frameworks at different temperatures (adapted from Ref. 176).

Silica particles impregnated with 5 wt% polyethylenimine solution are excellent post-combustion CO<sub>2</sub> adsorbents at very low partial pressures, owing to the strong CO<sub>2</sub> affinities of polymeric amines.<sup>177</sup> However, using CNT networks not only will separate the aggregated silica particles (Figure 1.21a), but also will considerably improve CO<sub>2</sub> adsorption capacities (owing to improved specific surface areas). Figure 1.21b indicates that the CNT/silica/polyethylenimine sorbents exhibit ultrafast CO<sub>2</sub> adsorption kinetics and require relatively low thermal regeneration temperature for reuse. The CO<sub>2</sub> molecules adsorbed onto the polyethylenimine-warpped CNT/silica composites is displayed in Figure 1.21c, where clearly elucidate how the mixed CO<sub>2</sub>/N<sub>2</sub> molecules are separated.

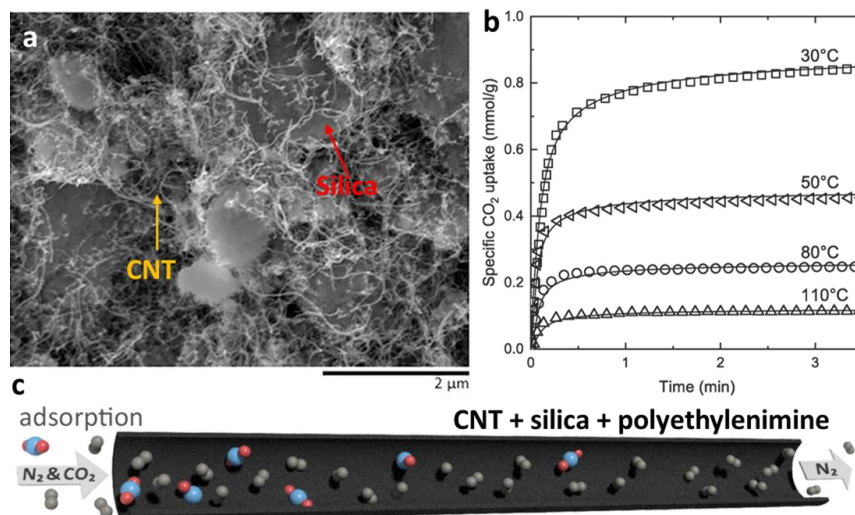


**Figure 1.21** (a) SEM image of the CNT/Silica composite adsorbent. (b) CO<sub>2</sub> adsorption kinetics of the CNT/silica/polyethylenimine composite adsorbent (impregnated with 5 wt% polyethylenimine solution measured using a gas mixture of 15 % CO<sub>2</sub> and 85 % N<sub>2</sub>, CNT : silica = 30 wt% : 70 wt%). (c) Graphical abstract of CO<sub>2</sub> adsorption over the CNT/silica/polyethylenimine composite adsorbent in a microtube (adapted from Ref. 177).

Additionally, tailoring the mass ratios of nanocarbons and inorganic nanoparticle hybrid adsorbents for optimizing post-combustion CO<sub>2</sub> capture also have been studied extensively. For instance, both the pure TiO<sub>2</sub> adsorbent and GO adsorbent exhibit lower CO<sub>2</sub> adsorption capacities compared to their hybrid TiO<sub>2</sub>/GO counterpart adsorbents (Figure 1.22a), owing to the GO nanosheets as support frameworks enabling to uniformly distribute TiO<sub>2</sub> particles leading to significantly increased specific surface areas and exposure of more active sites (Figure 1.22b).<sup>178</sup> However, the post-combustion CCS performance using solid-state sorbents are not competitive with conventional liquid media, such as liquid organic amines.<sup>179</sup>

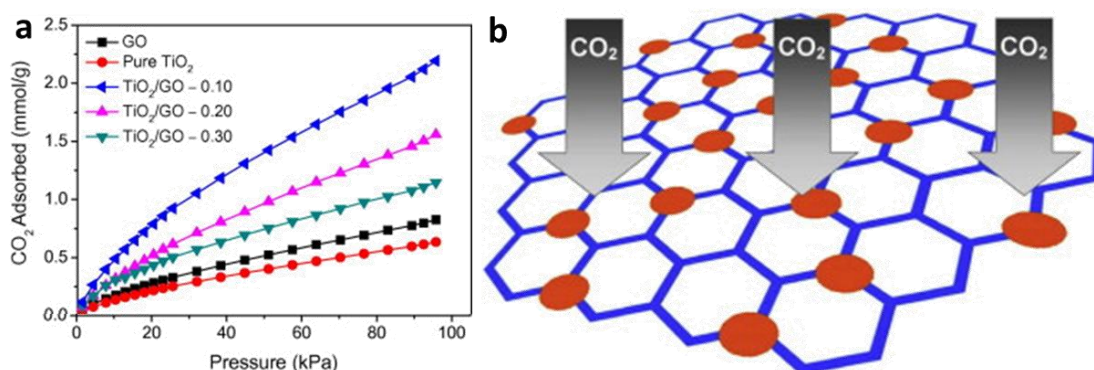


**Figure 1.22** (a) CO<sub>2</sub> adsorption isotherms of GO, TiO<sub>2</sub> and TiO<sub>2</sub>/GO hybrid adsorbents at 0 °C. (b) Graphical abstract of CO<sub>2</sub> adsorption onto the TiO<sub>2</sub>/GO adsorbent (cited from Ref. 178).

Solid-state sorbents, such as nanocarbons and inorganic particles, do however show great promise for pre-combustion CCS, a different CCS strategy, based on the removal of CO<sub>2</sub> during ‘gasification’ and ‘reforming’ processes (i.e. removal of CO<sub>2</sub> from fossil fuels before combustion). Pre-combustion CCS is also an important technology to produce hydrogen.<sup>180, 181</sup>

The overwhelming majority of hydrogen is currently produced through the steam methane reforming (SMR) reaction (i.e.  $\text{CH}_4 + \text{H}_2\text{O} \rightleftharpoons \text{CO} + 3\text{H}_2$ ).<sup>182</sup> Additional hydrogen can be generated by subsequent water gas shift (WGS) reaction which consumes CO and H<sub>2</sub>O to produce H<sub>2</sub> and CO<sub>2</sub> (i.e.  $\text{CO} + \text{H}_2\text{O} \rightleftharpoons \text{CO}_2 + \text{H}_2$ ).<sup>183</sup> Solid-state CO<sub>2</sub> sorbents can play an important role in the WGS reaction by removing CO<sub>2</sub> from the reaction system, shifting the reaction equilibrium to the product side and thereby maximising the hydrogen production (sorption-enhanced WGS reaction, Figure 1.23).<sup>184-186</sup> In this context, solid-state sorbents that show good CO<sub>2</sub> sorption performance at typical WGS reaction operating conditions, i.e. at elevated temperatures ( $T = 200\text{-}500\text{ °C}$ ) and high CO<sub>2</sub> pressures ( $p_{\text{CO}_2} = 1\text{-}10\text{ bar}$ ) are particularly attractive.

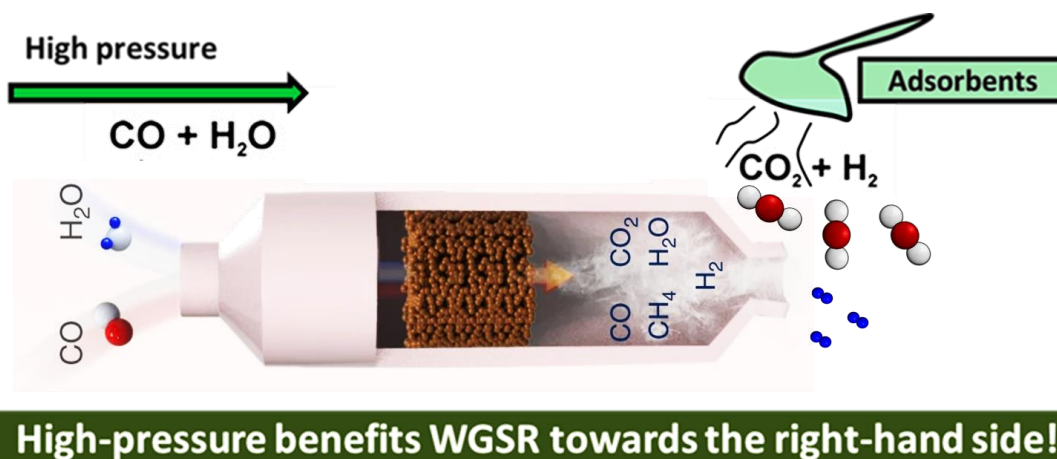


**Figure 1.23** Schematics of CO<sub>2</sub> adsorption in a water gas shift reaction (adapted from Ref. 186).

### 1.2.3.3 Typical inorganic adsorbents

A variety of inorganic adsorbents, like metal oxides, clays, and nanocarbon-based adsorbents, have all been investigated for their adsorptive properties in liquid-phase and gas-phase adsorption. This PhD project will focus on two inorganic adsorbents, specifically layered double hydroxides (LDHs) and boron nitride (BN), that are known to have high affinities for organosulfur compounds and CO<sub>2</sub>. The adsorbents are typically used in form of nanoparticles (nanoplatelets and nanosheets, respectively) which should allow to support these adsorbent nanoparticles within a nanocarbon aerogel framework.

#### Layered double hydroxides (LDHs)

LDHs are 2D lamellar structures (Figure 1.24) with a general formula of  $[M^{2+}_{1-x}M^{3+}_x(OH)_2](A^{n-})_{x/n} \cdot mH_2O$ , where  $M^{2+}$  are divalent cations (e.g. Mg<sup>2+</sup>, Co<sup>2+</sup>, Zn<sup>2+</sup>, Ni<sup>2+</sup>) and  $M^{3+}$  are trivalent cations (e.g. Al<sup>3+</sup>, Fe<sup>3+</sup>).  $A^{n-}$  represents interlayer anions like CO<sub>3</sub><sup>2-</sup>, SO<sub>4</sub><sup>2-</sup> and NO<sub>3</sub><sup>-</sup>, while  $x$  is the molar ratio of  $M^{3+}/(M^{2+}+M^{3+})$ . Different approaches have been reported for the preparation of pure LDH nanoparticles, however, co-precipitation of mixed metal salt solution under controlled pH conditions is the most utilized method because it is simple and convenient to conduct. LDH can be further processed via thermal calcination or annealing treatments to form LDH-derived mixed metal oxide (MMO) or metal nanoparticles (MNP).<sup>187-189</sup>

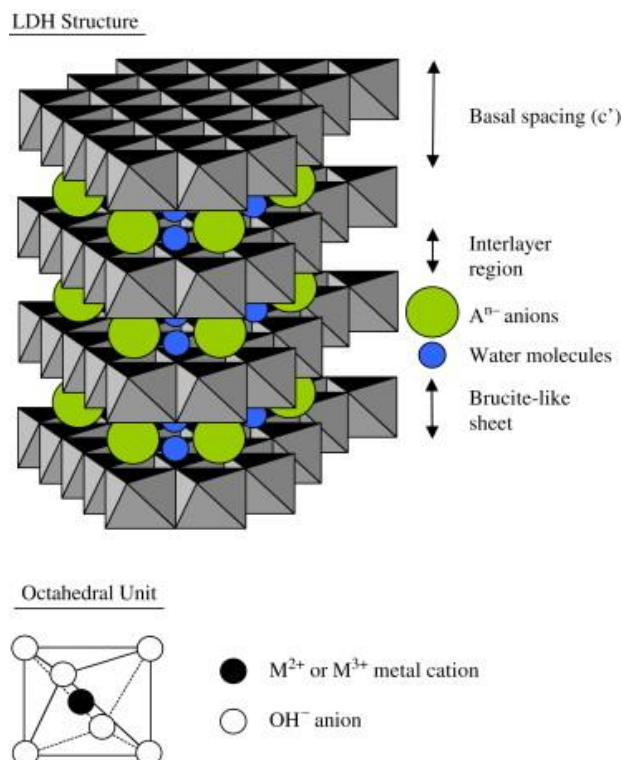


**Figure 1.24** Schematic representation of the LDH structure (cited from Ref. 188).

LDHs exhibit a large composition diversity as the cations of LDHs can be relatively easily replaced, allowing to tune the chemical properties of LDHs and adapt them to specific applications. Moreover, anions or molecules of polar solvents can enter into the interlayer space of LDHs modifying the LDH properties further. These properties broaden the application of LDH materials beyond adsorption applications, e.g. for applications in energy storage, heterogeneous catalysis or drug delivery.<sup>188</sup> LDH-derived MMO have been shown to have good adsorptive desulfurisation properties. While their capacities are only moderately high, they show other properties, important for practical applications, such as high selectivity towards the desired organosulfur impurities, excellent regeneration stability, and good performance in the presence of water.<sup>57</sup> For example, Menzel *et al.* prepared pure MgAl-LDH *via* a simple co-precipitation approach under basic conditions (pH 10), followed by calcination under 400 °C to form MgAl-MMO, which showed high DBT adsorption capacity ( $0.987 \text{ mg}\cdot\text{S}\cdot\text{g}^{-1}$ ) and very high selectivity towards organosulfur compounds in the presence of structurally similar, sulfur-free compounds such as biphenyl.<sup>57</sup> Notably, LDH-derived materials, such as MgAl-MMO, are also excellent  $\text{CO}_2$  adsorbents under pre-combustion CCS conditions due to their high thermal stabilities and increased  $\text{CO}_2$  capacity at elevated temperatures. Gao *et al.* fabricated MgAl-MMO through co-precipitation, followed by calcination under 400 °C, which exhibited high surface area ( $239 \text{ m}^2\cdot\text{g}^{-1}$ ) and excellent  $\text{CO}_2$  adsorption capacity ( $0.71 \text{ mmol}\cdot\text{g}^{-1}$ , at 200 °C in a constant flow of  $20 \text{ mL}\cdot\text{min}^{-1} \text{ CO}_2$ ).<sup>190</sup>

## Boron nitride (BN)

Hexagonal boron nitride (BN, Figure 1.25) has a similar structure to graphene, with a honeycomb lattice of covalently connected boron and nitrogen atoms forming one-atom thick layers (also similarly to graphene, the BN layers are bound together by van-der-Waals forces in the bulk material).<sup>191</sup> BN monolayers therefore share many analogous properties with graphene, including high surface areas, superb oxidation resistance, high mechanical strength, and thermal conductivity. However, BN also has some distinctly different properties compared to graphene, e.g. BN is electrically insulating.<sup>192</sup> Hexagonal boron nitride is typically produced by reacting a simple boron precursor (such as boron trioxide or boric acid) with a simple nitrogen precursor (such as ammonia or urea) in a nitrogen atmosphere at around 900 °C followed by an annealing treatment at around 1500 °C. To date, using BN to synthesize functionalized BN materials has attracted much attention due to their outstanding performance in the fields of environmental remediation, hydrogen storage, electrocatalysts and composites.<sup>193</sup> Graphene and BN sheets have been combined in thin composite films for applications in microelectronics due to the good conductive property of graphene and electrical insulation property of BN.<sup>194</sup> However, hybrid boron nitride/graphene hybrid aerogels for adsorptive applications have not been reported so far.

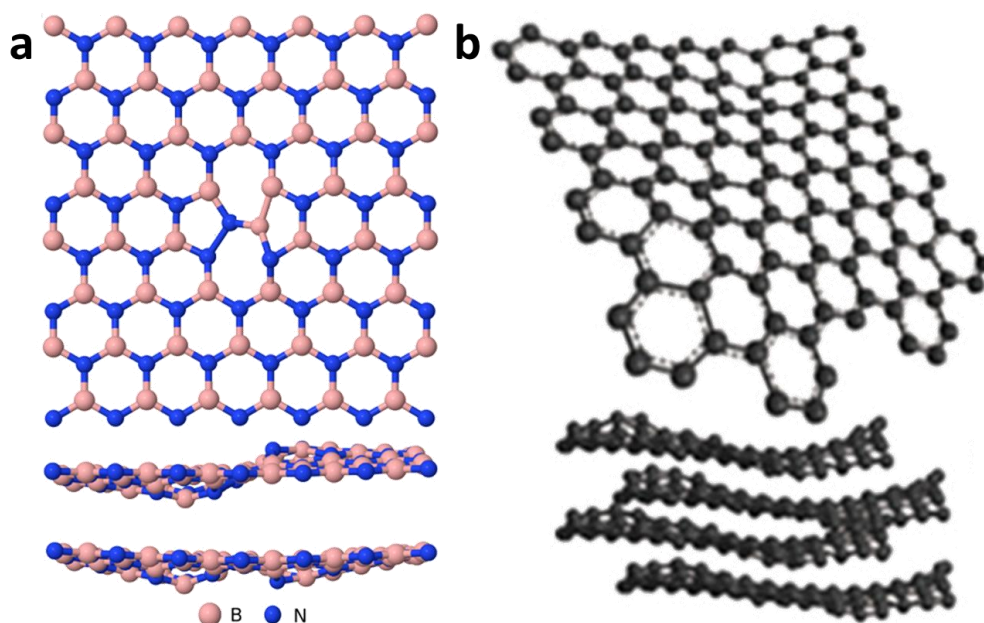


**Figure 1.25** Structures of (a) BN (cited from Ref. 191) and (b) graphene (cited from Ref. 96).

In terms of desulfurisation applications, BN showed excellent dibenzothiophene adsorption in fuels. Xiong *et al.* synthesised BN samples from urea precursors with DBT uptake capacities of up to was 28.17 mg·S·g<sup>-1</sup>. This work also proved that Lewis

acid-base interactions made great contribution to DBT adsorption onto BN.<sup>195</sup> The organosulfur adsorption capacity of BN was shown to further increase when using melamine as precursor in the synthesis, producing BN materials which exhibited an outstanding DBT adsorption capacity of  $57.5 \text{ mg}\cdot\text{S}\cdot\text{g}^{-1}$ , which was higher than other advanced DBT adsorbents, such as microporous polymers ( $24.3 \text{ mg}\cdot\text{S}\cdot\text{g}^{-1}$ ) and nanoporous activated carbon ( $19.5 \text{ mg}\cdot\text{S}\cdot\text{g}^{-1}$ ). This work reported the largest adsorption capacity for the adsorptive desulfurisation so far. However, after four desulfurisation cycles, the adsorption performance reduced by more than 50 % limiting its practical application.<sup>196</sup>

In a brief summary, BN as a ‘white graphene’ material show outstandingly desulfurisation performances in liquid-phase fuels. Therefore, this PhD project will investigate the decoration of BN particles onto nanocarbon aerogels for adsorptive desulfurisation applications, which have not been reported yet.

## 1.2.4 Hybrid adsorbents

### 1.2.4.1 Inorganic/nanocarbon powder adsorbents

Combining nanocarbons and functional nanoparticles together can magnify their unique properties, as the carbon nanostructures can act as supporting framework for the particles (Figure 1.26), improving accessibility to the adsorption sites and inhibiting particle aggregation (i.e. deactivation) during operation or regeneration.<sup>58</sup>

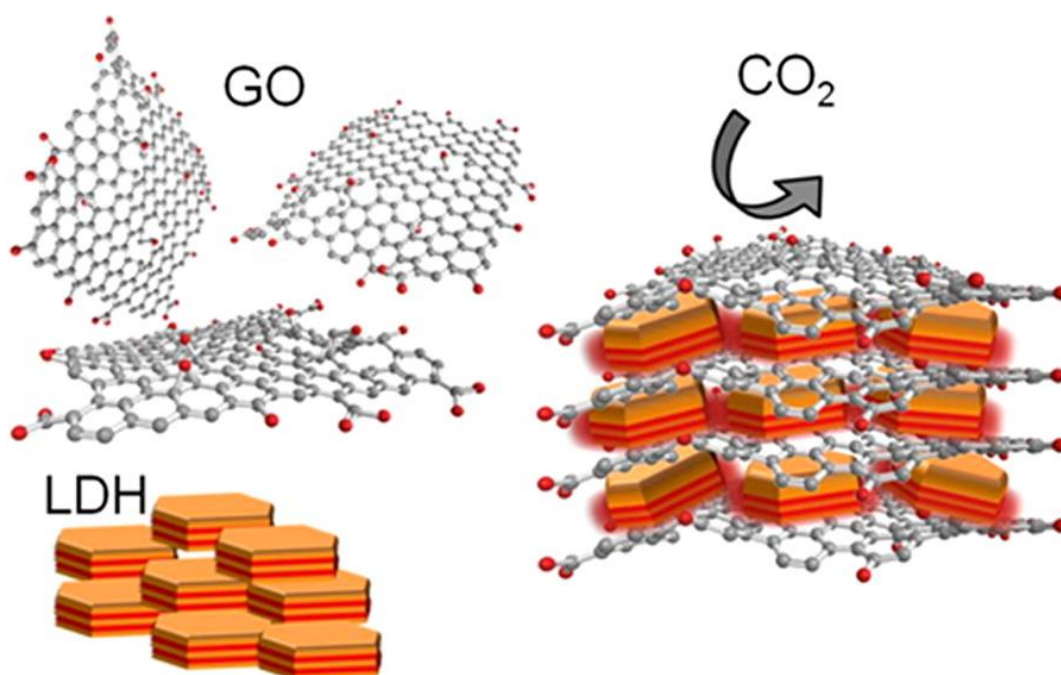


**Figure 1.26** Schematic representation of the LDH and GO hybrid composites (cite from Ref. 58).

For LDHs, there are a number of reports that describe the formation of LDH/nanocarbon hybrid powders. Generally, there are two main methods to obtain LDH/nanocarbon hybrids, one method is **co-assembly** and another is **in situ** synthesis.<sup>197</sup> Co-assembly is a popular method to produce LDH/GO hybrids based on the strong electrostatic force between the positive electrical charge of **pre-formed** LDH nanoparticles and the negative electrical charge of deprotonated GO. The **in situ** synthesis adopts GO as growth substrates to grow LDH in situ onto the substrates.

Presently, LDH/GO hybrid powders have attracted great attention in energy storage, catalysis, supercapacitors, and environmental protection. However, their application in ADS are rarely investigated. MgAl-, CuAl- and CoAl-LDH/GO adsorbents were synthesised through in situ precipitation of LDHs on GO surface followed by calcination to form MMO/GO hybrid powders. Compared with pristine MgAl-, CuAl- and CoAl-MMO adsorbents, the adsorptive performance of DBT on GO supported MMO adsorbents was significantly enhanced in terms of capacity, selectivity and regenerability, with MgAl-MMO/GO showing the largest DBT adsorption capacities (Figure 1.27). The specific surface areas of MgAl-LDH was  $135 \text{ m}^2\cdot\text{g}^{-1}$ , however, MgAl-MMO/GO reached to  $195 \text{ m}^2\cdot\text{g}^{-1}$ , the results indicated that GO can act as spacer between the MgAl-MMO nanoparticles which will provide more active adsorption sites, therefore, adsorption of organosulfur on the hybrid adsorbents were enhanced. After 5 adsorption-desorption cycles, the hybrid materials adsorption performance still remained stable.<sup>57</sup>

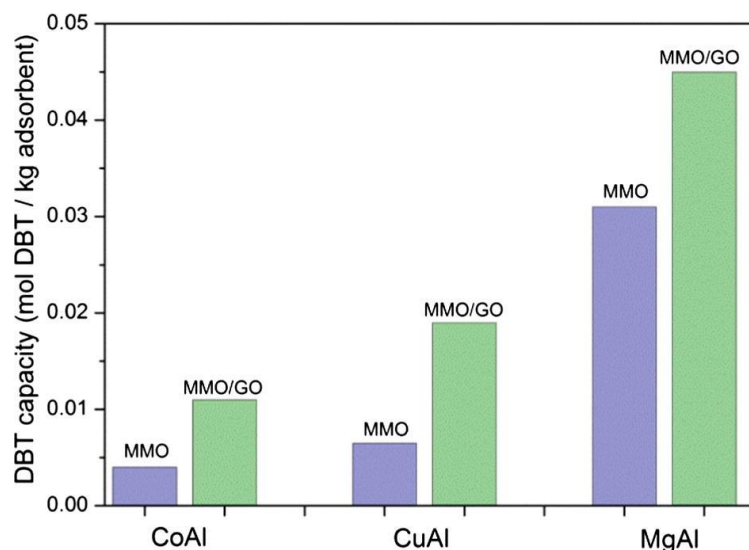


**Figure 1.27** DBT uptake from dodecane by CoAl-MMO, CuAl-MMO and MgAl-MMO in their pure (MMO) and hybrid (MMO/GO; containing 5 wt% GO) form (cited from Ref. 57).

In terms of  $\text{CO}_2$  adsorption, the effect of mixed nanocarbon supports was studied for MgAl-LDH sorbents. MgAl-MMO supported at 50 wt% on a 1:1 mixture of GO and MWCNT (MgAl-LDH/GO&MWCNT(1:1)) showed improved surface area and

enhanced CO<sub>2</sub> adsorption capacity (at T = 300 °C and p<sub>CO<sub>2</sub></sub> = 0.2 bar), compared to LDH adsorbents supported on either pure GO or pure MWCNT supports alone (MgAl-LDH/GO and MgAl-LDH/MWCNT). A graphic representation of postulated microstructure of the MgAl-LDH/GO, MgAl-LDH/MWCNT and MgAl-LDH/GO&MWCNT(1:1) hybrid sorbents is shown in Figure 1.28a. For the mixed-support sorbent MgAl-LDH/GO&MWCNT(1:1), N<sub>2</sub> adsorption and X-ray diffraction measurements showed that the presence of MWCNT hinders restacking of the GO sheets, resulting in an overall looser support framework structure with higher specific surface area, giving rise to the observed high CO<sub>2</sub> adsorption capacities for LDH supported on the mixed nanocarbon substrate (Figure 1.28b).<sup>198</sup>

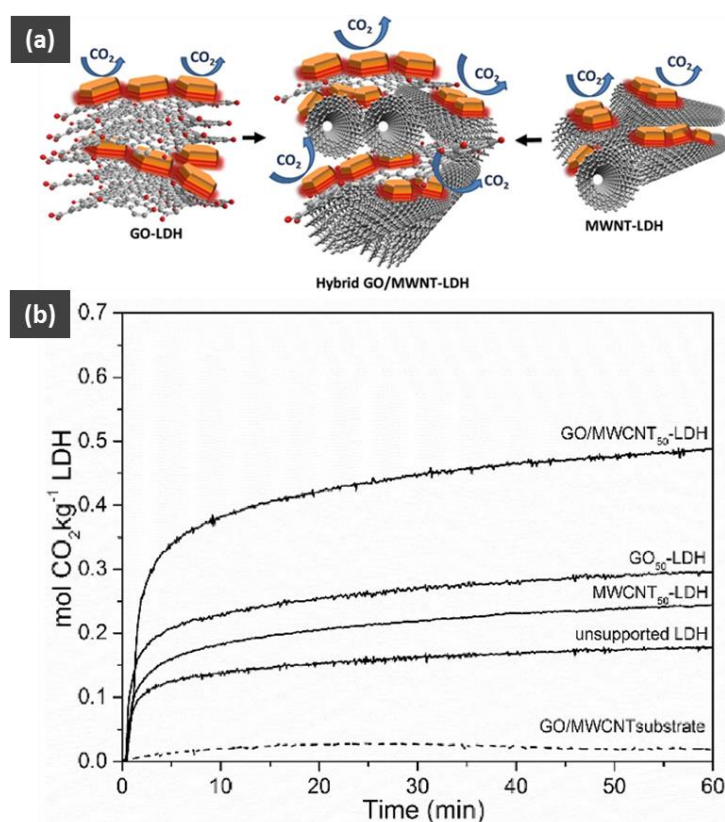


**Figure 1.28** (a) Graphical abstract of MgAl-LDH/GO, MgAl-LDH/MWCNT and MgAl-LDH/GO&MWCNT(1:1), and (b) CO<sub>2</sub> adsorption capacities of different adsorbents (all decorated nanocarbons were 50wt%) (adapted from Ref. 198).

#### 1.2.4.2 Inorganic/nanocarbon aerogel adsorbents

Many examples of inorganic adsorbents supported onto the surface of nanocarbon powders have been reported (see previous section). However, reports about inorganic nanoparticles supported within 3D nanocarbon networks for adsorption applications are relatively scarce. Inorganic adsorbent nanoparticles loaded onto the surface of nanocarbon aerogels not only benefit from the stable structure of aerogel framework, but also exhibit more accessible active sites, thereby

facilitating the adsorptive removal of pollutants from the liquid or gas phase. In addition, the use of particles supported within an aerogel monolith (rather than the use of powders) also provides other practical advantages, such as easier recovery and regeneration of spent sorbents.<sup>59, 61, 121</sup> Herein, the three approaches of inorganic nanoparticles decoration onto nanocarbon aerogels will be reviewed below, including co-assembly, aerogel impregnation and in situ precipitation (Figure 1.29).

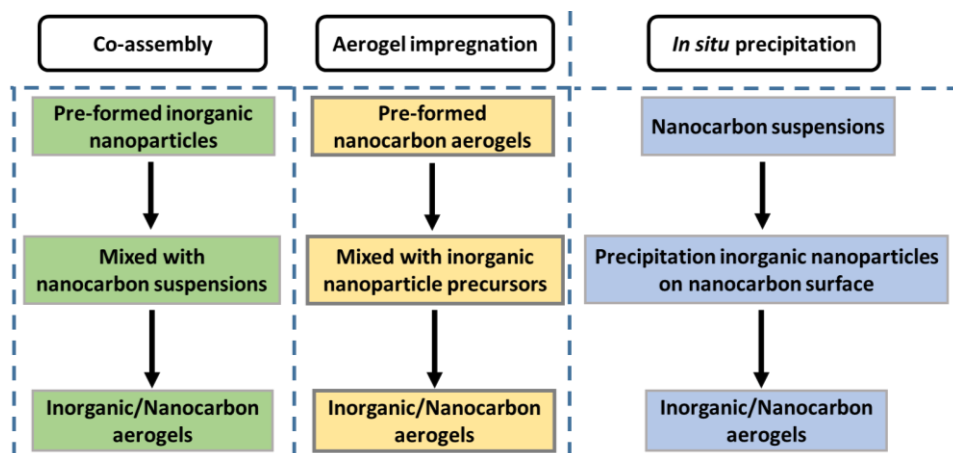


**Figure 1.29** Overview of approaches to supporting inorganic nanoparticles within nanocarbon aerogels.

The co-assembly method was reported as a facile way to synthesize LDH/GO aerogel. In the co-assembly process, exfoliated GO and pre-formed nanoparticles are assembled in aerogels, as shown in Figure 1.30. Specifically, MgAl-LDH powders were prepared first via a standard co-precipitation synthesis and then added to an aqueous GO suspension, followed by sonication to produce a homogeneous suspension. The resulting mixed solution was allowed to stand to form MgAl-LDH/GO hydrogel. Finally, the water in the hydrogels was removed to form MgAl-LDH/GO aerogels *via* freeze-drying.<sup>61</sup>

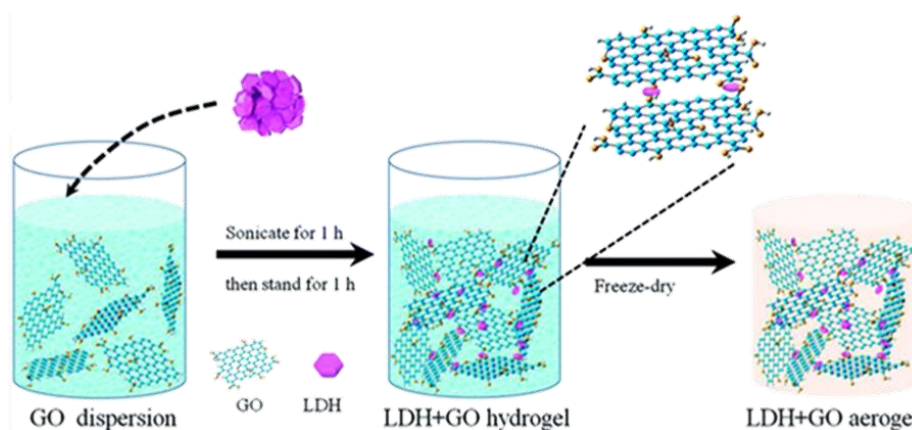


**Figure 1.30** Schematic of co-assembly synthesis of GO/LDH hydrogels and aerogels (cited from Ref. 61).

Magnetic GO aerogels can be synthesised using an aerogel impregnation approach, based on preparing the GO hydrogel first followed by infiltration with particle precursors, as shown in Figure 1.31.<sup>199</sup> In detail, ascorbic acid and GO flakes at a mass ratio of 3 : 1 were sonicated to form well dispersed suspensions. These GO suspensions were hydrothermally treated to form GO hydrogels. Then, the GO hydrogel was immersed in an iron resin precursor solution where the iron precursor compound could diffuse into the gel structure and deposit onto the GO surfaces. In a final step, the iron-precursor/GO-hydrogel hybrids were dried under vacuum at 40 °C and then thermally reduced at 750 °C in nitrogen atmosphere to produce GO aerogels decorated with iron oxide nanoparticles, producing an inorganic/GO hybrid aerogel with strong magnetism and high adsorption capacity for the dye rhodamine B ( $2.59 \times 10^{-5} \text{ mol}\cdot\text{g}^{-1}$ ).<sup>199</sup>

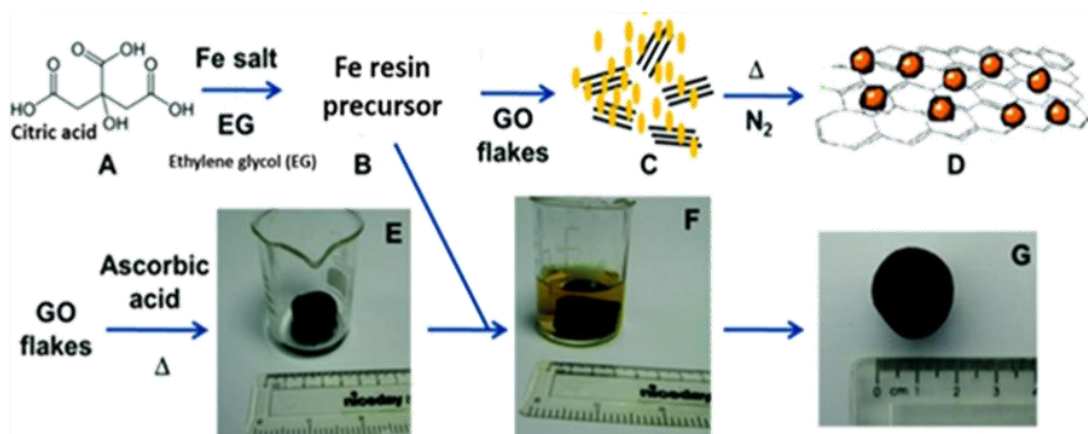


**Figure 1.31** Schematic of impregnation synthesis of iron oxide nanoparticle decorated rGO aerogels (cited from Ref. 199).

In the in situ precipitation process, the LDH nanoparticles are formed *via* the co-precipitation of divalent and trivalent metal cations in the presence of exfoliated GO. The precipitated LDH will grow in situ on the GO surfaces as the functional groups of the GO have the ability to bind and adsorb the cations. Figure 1.32 shows a schematic illustration of the in situ precipitation method for the fabrication of CoAl-LDH/GO hybrid aerogels.<sup>200</sup> Initially, the GO aqueous dispersion was prepared by sonicating GO flakes. Then, an aqueous solution, containing  $\text{Al}(\text{NO}_3)_3\cdot 9\text{H}_2\text{O}$ ,  $\text{Co}(\text{NO}_3)_2\cdot 6\text{H}_2\text{O}$  and urea, was slowly dropped into the GO aqueous suspensions under vigorous agitation. After that, the mixtures were hydrothermally treated to obtain the hybrid hydrogel, which was freeze-dried to obtain a hybrid CoAl-LDH/GO aerogel with excellent electrochemical capacitance, rendering this a promising material for supercapacitor applications. The in situ synthesis has been studied to support other LDHs on nanocarbon aerogels as well, including NiMn-LDH/GO<sup>201</sup> as electrode materials,  $\alpha\text{-FeOOH/GO}$  as pollutant adsorbents<sup>59</sup> and MgAl-LDH/GO for water purifications.<sup>61</sup>

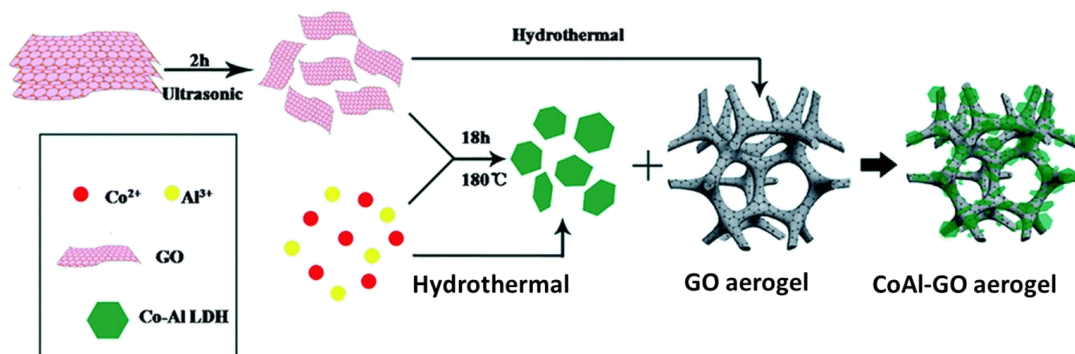


**Figure 1.32** Schematic of in situ precipitation synthesis of CoAl-LDH/GO hybrid aerogel (cited from Ref. 200).

In summary, a variety of approaches have been reported to incorporate inorganic nanoparticles into nanocarbon aerogels for a variety of applications. However, it is noteworthy that there are no literature reports on utilising nanocarbon aerogels as supporting substrates for organosulfur or  $\text{CO}_2$  adsorption applications, nor any reports of utilising the hybrid aerogels capability for Joule heating in the context of these applications. These areas of investigation will therefore form an important basis for investigations in this PhD project.

### 1.2.5 Joule-heating of nanocarbon materials

One of the main benefits provided by the nanocarbon network (both in hybrid powders and in hybrid aerogels) is the support function, i.e. the spreading and anchoring of the adsorbent nanoparticles across the nanocarbon surface for improved accessibility and stability. However, nanocarbon aerogels also provide a number of additional functional benefits beyond their support function. For example, recovery of the adsorbents for regeneration (or disposal), an important issue for their commercial use, is much easier for aerogel monoliths than for fine nanoparticles powders.

As outlined in the introduction, the 3D interconnected nanocarbon network in aerogels provides also a unique opportunity to locally heat the nanocarbon network, and therefore any supported functional nanoparticles, through the application of an electrical current (Joule-heating).<sup>31</sup> Joule heating, also known as resistive heating or Ohmic heating, is an electrothermal technique, which generates heat when an electric current passes through an electrically conductive material. Joule-heating is not available in loose inorganic/nanocarbon powders (nanocarbon network not continuously interconnected through the full powder volume) or other porous supports, such as MOFs,<sup>202</sup> zeolites,<sup>203</sup> or silica aerogels (electrically insulating materials).<sup>204</sup> Joule-heating therefore provides a valuable additional functionality in inorganic/nanocarbon aerogels in the context of sorption application, e.g. for energy

efficient thermal sorbent regeneration or accurate temperature control in elevated-temperature sorption processes.<sup>205</sup> Joule-heating of aerogel-supported sorbent particles has not yet been investigated and will be a major area of research for this PhD project. The following section will briefly discuss some recent findings on the Joule-heating properties of nanocarbon aerogels and other nanocarbon assemblies.

### Medium temperature Joule heating

Joule-heating at moderate electrical voltages and currents to medium temperatures ( $T = 25\text{-}500\text{ }^{\circ}\text{C}$ ) has been applied in a number of fields. For example, the graphene-nanoribbon/epoxy composites were successfully used for the de-icing of helicopter rotor blade segments at  $-20\text{ }^{\circ}\text{C}$ .<sup>206</sup> Additionally, nanofibrillated celluloses were homogeneously combined with electric-conducting graphene to form composite membranes in a weight ratio of 1 : 1, which was specifically exploited in terms of their Joule-heating performance, that can be stably Joule-heated to  $60\text{ }^{\circ}\text{C}$  in 3 min with a power density of  $2000\text{ W}\cdot\text{m}^{-2}$ .<sup>207</sup>

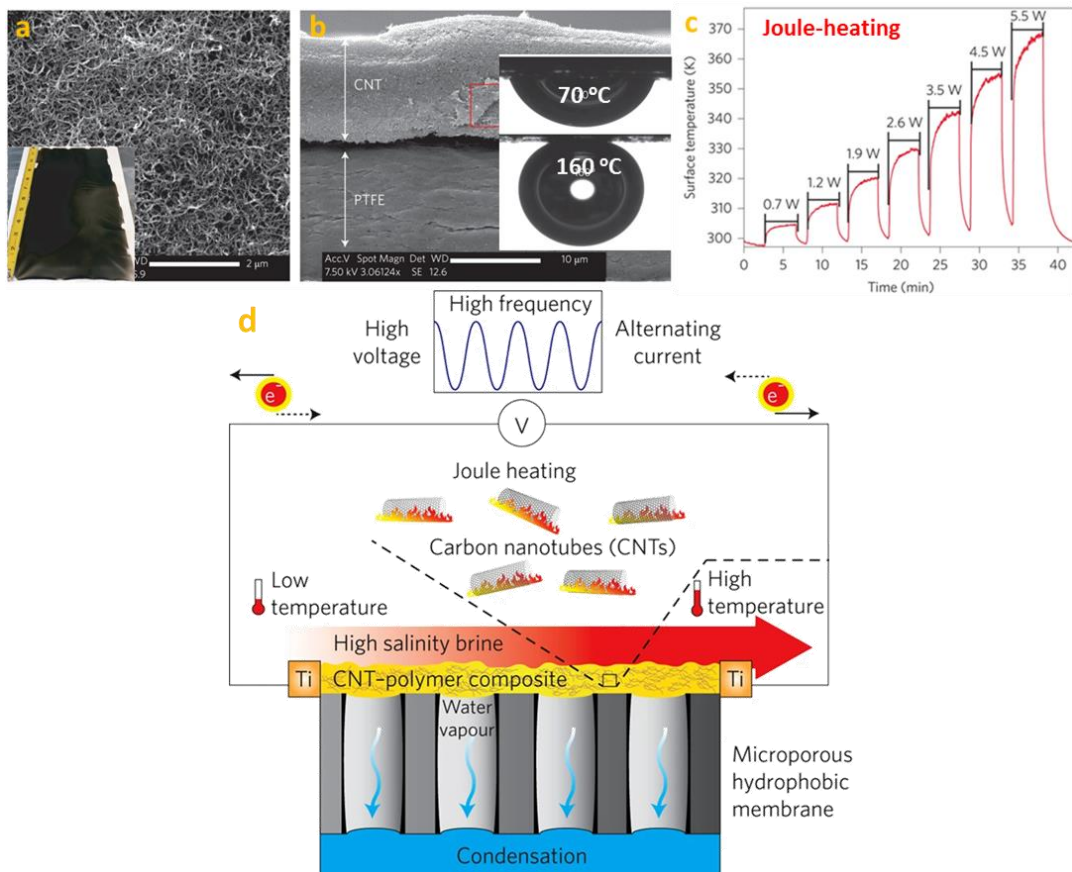


**Figure 1.33** (a) SEM image of CNT/PVA film surface (Insert: A digital image of a large spray-coated CNT/PVA membrane). (b) SEM image of CNT/PVA cross-section on PTFE support (Inserts: contact angles of PTFE surface and CNT/PVA-deposited PTFE membrane). (c) Direct Joule heating of the interconnected CNTs using electrical power. (d) Schematics depict self-heating membranes for thermal desalination via CNT Joule heating (adapted from Ref.33 and Ref. 208).

As for thermal desalination membranes, a highly conductive, hydrophilic and porous CNT/PVA thin film deposited on the top of a hydrophobic porous membrane (polytetrafluoroethylene, PTFE) adopting layer-by-layer spray coating approach, was elaborately fabricated for seawater desalination of high-salinity brines, as shown in Figure 1.33.<sup>33, 208</sup> The as-synthesised CNT/PVA membrane: profiles pronounced porous microstructures (Figure 1.33a); compacts tightly on the surface of PTFE membrane support (Figure 1.33b); shows clearly distinct contact angles (Figure 1.33b) and adjusts Joule-heating-induced surface temperatures stably and simply (Figure 1.33c, 370 K at 5.5 W). Owing to the Joule-heating of CNT at the membrane surface (Figure 1.33d), the high salinity brine will be warming up immediately resulting in water evaporation (water vapour) that will subsequently transport through the pores of the hydrophobic PTFE substrates followed by condensation, to achieve the purposes of water purifications.<sup>208</sup>

In the context of nanocarbon aerogels, Menzel *et al.* investigated the fundamental Joule heating characteristics of macrocellular rGO aerogels (Figure 1.34).<sup>31</sup> The aerogel monolith could be contracted through electrodes to pass a current through the entire aerogel and induce uniform and controlled Joule heating, as evidenced by thermal imaging (Figure 1.34d). The rGO aerogel could reach temperature around 200 °C at low input voltages (approximately 2V) and showed very fast heating and cooling rates (up to 10 K·s<sup>-1</sup>).<sup>31</sup> These findings demonstrate that graphene aerogels have outstanding Joule heating properties that allow energy-efficient, fast and uniform heating, which could be explored for heating of supported adsorbent nanoparticles.

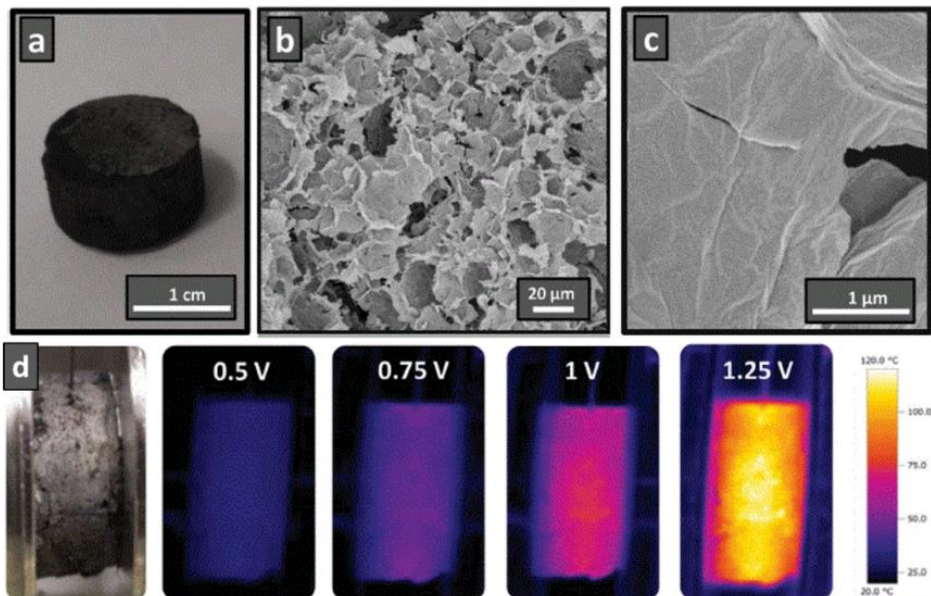


**Figure 1.34** (a) Emulsion-templated rGO aerogel, (b) (c) SEM images of rGO aerogel, (d) Thermal images of surface temperature of rGO aerogel at different voltages (adapted from Ref. 31).

It has also been shown that Joule heating can even be utilised in electrically insulating 3D porous materials, if the materials can be coated with nanocarbons. For example, a commercially available melamine sponge was impregnated and coated with graphene sheets. The graphene-modified sponge was then utilised for the clean-up of crude-oil spillages. Figure 1.35 illustrates the underlying working principle, based on Joule-heating of graphene-coated sponge ( $75\text{ }^{\circ}\text{C}$ ,  $17\text{ V}$ ,  $0.5\text{ W}\cdot\text{cm}^{-3}$ ) to increase crude oil temperature. The increased temperature reduces oil viscosity and thereby enhances the speed of crude-oil uptake into the sponge pores, dramatically improving the efficiency of the overall clean-up process.<sup>209, 210</sup>

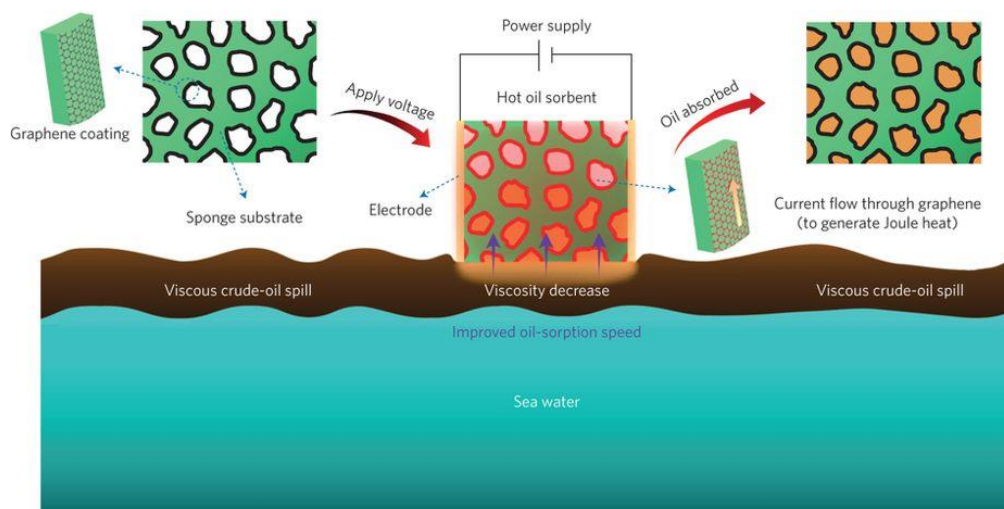


**Figure 1.35** Schematic presentation of Joule-heated graphene wrapped foam for a viscous crude-oil spill cleaning (cited from Ref. 209).

### High temperature Joule heating

Nanocarbon materials can endure ultrahigh working temperature in an inert atmosphere (graphite has a sublimation temperature of around  $3600\text{ }^{\circ}\text{C}$ ) due to their strong C-C bonds.<sup>211</sup> Recent studies have investigated Joule-heating of 3D-printed GO-CNT hybrid nanocarbon papers to very high temperatures ( $T > 1000\text{ }^{\circ}\text{C}$ ). Hybrid nanocarbon papers can be readily printed to different shapes and forms, and exhibit highly flexible mechanical characteristics (Figure 1.36).<sup>212</sup> These nanocarbon papers can be Joule-heated up to  $3320 \pm 50\text{ K}$ , which was measured by the fibre-coupled spectrometer. For example, the 3D-printed GO-CNT papers can be fast Joule-heated to  $2783\text{ K}$  at relatively low power inputs ( $4.10\text{ W}$ ). At these high temperatures, the hybrid nanocarbon papers emit strong black-body radiation, providing promise for new lighting applications in graphene-based light bulbs.<sup>212</sup>

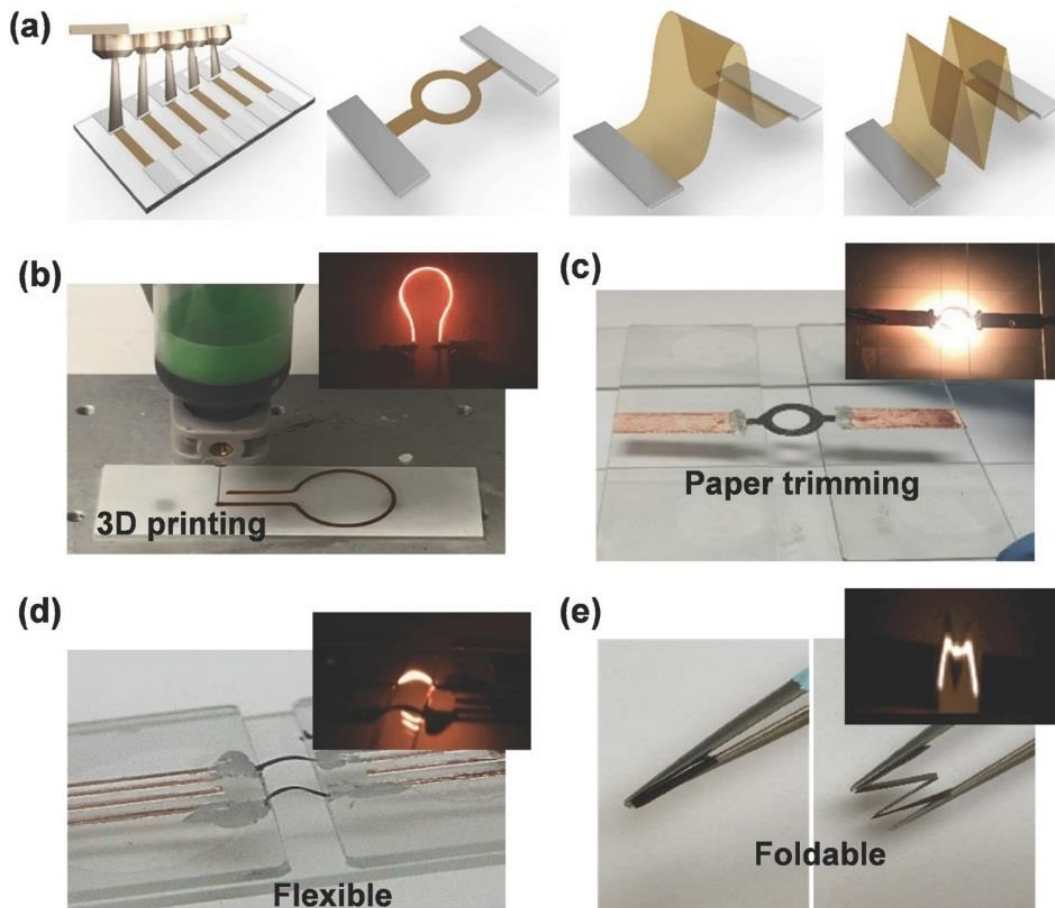


**Figure 1.36** (a) Flexible manufacturing of GO-CNT hybrid nanocarbon papers. (b) 3D printing fo GO-CNT hybrid nanocarbon as a light bulb. (c) Rod-like GO-CNT hybrid nanocarbon paper for a ligh bulb. (d) Flexible GO-CNT nanocarbon paper for lighting. (e) M-like foldable nanocarbon paper for lighting (cited from Ref. 212).

Other studies have explored the durability of nanocarbon films at ultrahigh Joule heating temperature. Studies have shown that Joule heating of rGO films to 3300 K can induce ultrahigh electrical conductivity ( $\sim 4000 \text{ S}\cdot\text{cm}^{-1}$  at 3000 K) owing to the well graphitisation of GO sheets (Figure 1.37).<sup>213</sup> The ultrahigh temperature of rGO film cannot be measured via a traditional thermocouple, therefore a fibre-coupled spectrometer with black-body fitting algorithm is used to detect the emitted light wavelength which is a direct measure of Joule heating temperature (Figure 1.37a and Figure 1.37c). For example in Figure 1.37b, different power intensities cause different light emission profiles, with the colour shift in the emitted light from red to white indicating a significant increase in Joule heating temperature from 1800 K to 3300 K (e.g.  $\sim 2460 \text{ K}$  at 6.3V).<sup>213</sup>

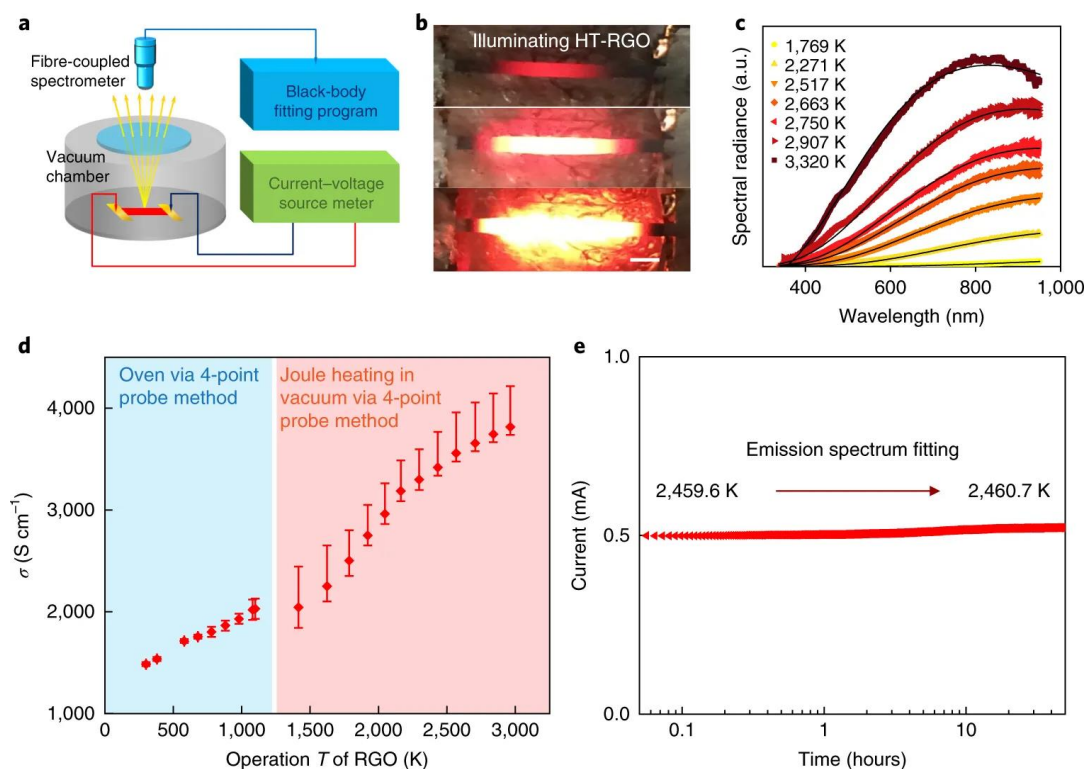


**Figure 1.37** (a) Experimental set-up for measuring the incandescent radiation emission from rGO film. (b) Digital images of rGO films reach to different Joule heating temperatures. (c) The measure emission spectrum fitted by the Planck function. (d) Electrical conductivity versus Joule heating temperature after 3300 K treatment. (e) rGO films working at 6.30 V for 50 h after 3300 K treatment (cited from Ref. 213).

Joule-heating of nanocarbon materials is not limited to applications in light bulbs, thermoelectric materials or heaters. Nanocarbon Joule-heating has also been employed for high-temperature modification of the nanocarbon materials themselves, for example for nanocarbon welding, nanocarbon functionalisation with single atomic sites, and nanocarbon decoration with high-entropy-alloy (HEA) nanoparticles. For example, carbon nanofibers (CNF) can be welded together via ultrahigh temperature Joule heating (reaching up to 2500 K at a heating rate of 200 K·s<sup>-1</sup>). After heating at 2800 K for 10 mins, the CNF show improved graphitic crystallinity and are covalently welded at their junctions, as depicted in Figure 1.38a.<sup>214</sup> Raman spectra and scanning electron microscopy images confirmed that Joule heating is an efficient method to weld CNF (Figure 1.38b-d), with the electrical conductivity significantly increased from pristine 0.01 S·cm<sup>-1</sup> to 381 S·cm<sup>-1</sup>. Due to the high temperature Joule heating, amorphous carbon in the CNF will carbonize and graphitize, while defects in the CNF themselves will be removed and C-C bonds formed at the nanofiber junction.<sup>214</sup>

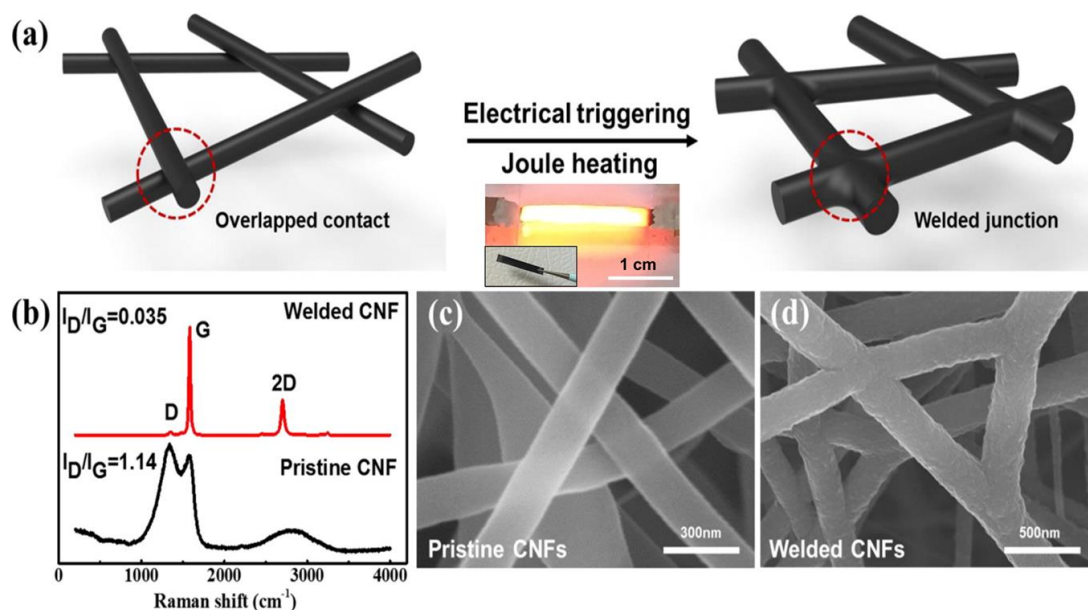


**Figure 1.38** (a) Schematics to describe CNF welding via Joule heating approach. (b) Raman results of CNF before and after Joule heating. SEM images of pristine CNF (c), and the welded CNF (d) (cited from Ref. 214).

The formation and stabilization of well-dispersed single atomic sites on nanocarbon substrates is a highly interesting area of research, with great potential for catalysis and energy storage. Increasing stability of single atomic sites is very challenging to achieve through conventional approaches such as wet chemical synthesis ( $< 500\text{ }^{\circ}\text{C}$ ) or high temperature annealing treatments ( $800 - 900\text{ }^{\circ}\text{C}$ ). However, ‘shock’ Joule heating of nanocarbons to ultrahigh temperatures for very short periods of time is a very promising route to dramatically enhance the stability of single atomic sites. Literature reports show that decoration of metal precursors (ethanol-based  $\text{H}_2\text{PtCl}_6$ ) onto  $\text{CO}_2$ -activated carbon substrates (defective carbon nanofibers), followed by repeated shock (50 ms per cycle) heating to high temperatures (repeated Joule heating to 1500 K for 50 ms), will produce stable single atoms anchored to the nanocarbon surface (Figure 1.39). High temperature Joule heating provides sufficient energy to overcome the high activation energy for the formation of thermodynamically stable single-atomic metal-defect bonds. The very short Joule heating duration (combined with fast natural cooling of graphitic nanomaterials) prevents the aggregation of the formed sites to larger atomic clusters, leading to a very uniform dispersion of single atomic sites.<sup>215</sup>

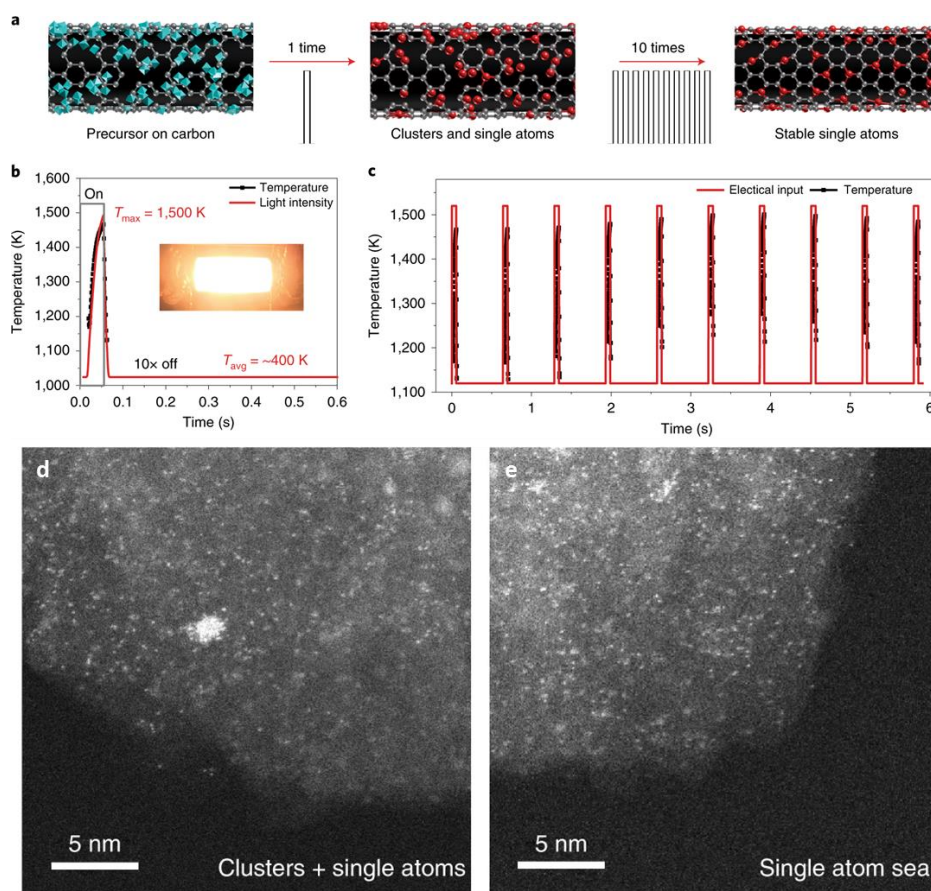


**Figure 1.39** (a) Schematics for description of metal precursor on carbon substrate and in situ high temperature Joule heating shock. (grey: carbon atoms, cyan: metal precursor, red; metallic atoms). (b) Joule heating temperature and a heated CNF film. (c) On/off Joule heating temperature for 10 cycles to make single atoms. TEM images of one-time Joule heating shock (d) and ten-time Joule heating shock (e) (cited from Ref. 215).

Another powerful advantage of using Joule heating of nanocarbon materials is to make high-entropy-alloy (HEA) nanoparticles, which are of importance in catalysis, energy storage and bio imaging. Using conventional methods, it is challenging to mix more than five elements uniformly within individual nanoparticles, due to the elements' hugely different physiochemical properties and slow cooling rate of conventional substrates. As a consequence, adopting conventional approaches to fabricate nanoscale HEA nanoparticles are fairly complex. Nanocarbon Joule-heating however allows for simpler approaches, based on ultrafast, high temperature thermal shock treatments of nanocarbons. For example, well-mixed octonary HEA nanoparticles were formed from a mix of five or more metal precursors deposited onto carbon nanofiber films. Shock Joule heating of the CNF film was then employed to decompose the precursors at 2000 K to form metal liquid nanodroplets ( $MCl_xH_y \rightarrow M(\text{liq}) + \text{gases} \uparrow$ ). When the Joule-heating power is switched off, fast natural cooling occurs (cooling rate  $\sim 10^5 \text{ K}\cdot\text{s}^{-1}$ ), inducing very fast solidification of the metal nanodroplets, inhibiting phase separation effects and resulting in the generation of well-distributed HEA nanoparticles (Figure 1.40).<sup>216</sup>

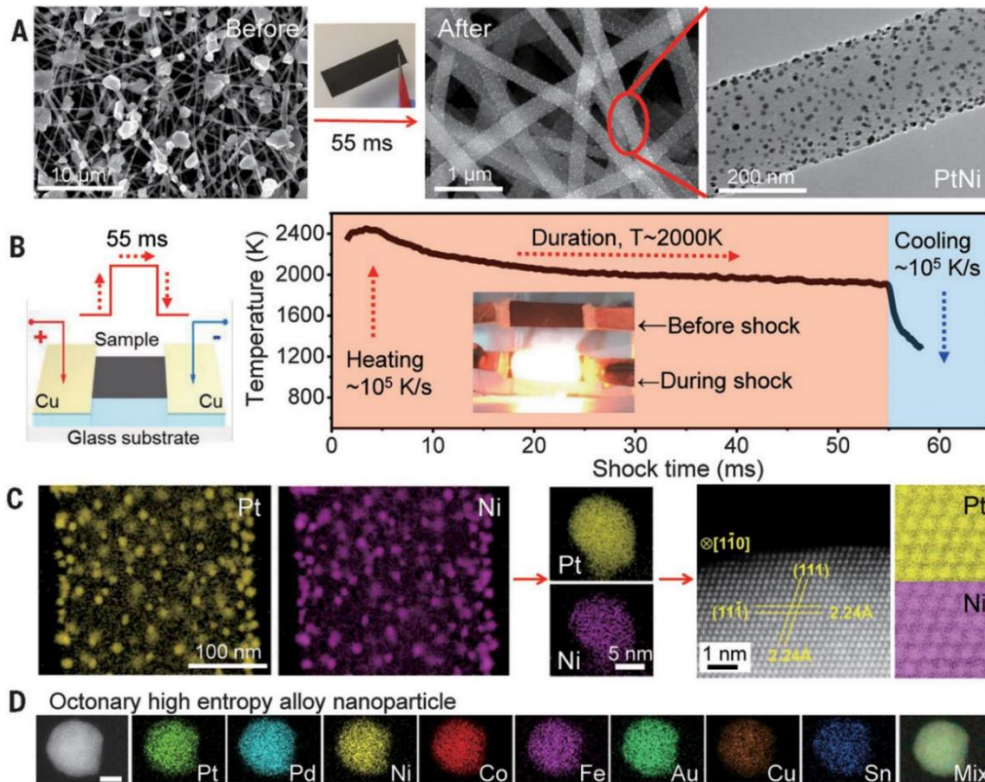


**Figure 1.40** (a) SEM image of CNF films with  $\text{PtCl}_2$  and  $\text{NiCl}_2$  salts, digital image of CNF film with metal salts, and CNF film after 55 ms Joule heating. (b) Schematics of 55 ms Joule heating and temperature changes versus Joule heating time. (c) High resolution microscopy imaging of a binary PtNi alloy. (d) Elemental maps of octonary HEA nanoparticles (cited from Ref. 216).

In summary, Joule-heating of nanocarbon structures has been demonstrated for various applications, including energy-efficient heater, carbon welding, and HEA nanoparticle production. However, most of the reported studies employed nanocarbon films or papers, with almost no reports on using nanocarbon aerogels. Therefore, one of the main areas of investigation for this PhD project will be the study of nanocarbon aerogels' Joule heating. While the Joule-heating characteristics of individual nanocarbon aerogels have been reported, investigations of how Joule-heating behaviour changes as function of nanocarbon aerogel structure have not yet been investigated. This thesis will therefore explore fundamental structure-property relationships of Joule-heated nanocarbon aerogels, as an important requisite to develop new Joule-heating-based applications for nanocarbon aerogels. Then, the Joule-heating characteristics will be exploited in the context of inorganic/nanocarbon hybrid aerogels, specifically in the context of energy efficient thermal regeneration of aerogel-based desulfurisation and  $\text{CO}_2$  adsorbents. Finally, the concept of nanocarbon aerogel Joule-heating will be pushed to more extreme conditions, through studies of ultra-high Joule-heating in the context of nanocarbon welding and nanocarbon aerogel decoration with catalyst nanoparticles, opening new routes for future exploitation of these unique materials.

## Chapter - 2

### Experimental

#### 2.1 Materials

All the materials used in this PhD project are listed in Table 2.1, where material names, sources and specifications are provided. All chemicals were used as received, without further purification.

**Table 2.1** Lists of materials used in this PhD project.

Materials	Sources	Specifications
Graphene oxide ( <b>GO</b> )	William Blythe Limited	Lateral GO sheet dimensions: 0.5-5 $\mu\text{m}$ ; Chem. composition: C( $\sim$ 75%), O( $>$ 18%), N( $<$ 1%), S( $<$ 2%)
Carboxylic acid functionalized, multi-walled carbon nanotube ( <b>oCNT</b> )	Sigma-Aldrich	avg. outer diameter 9.5 nm; avg. length: 1.5 $\mu\text{m}$
Polyvinyl alcohol (PVA)	Sigma-Aldrich	Mw: 85000-124000, soluble in water $>$ 80 $^{\circ}\text{C}$
L-ascorbic acid	Sigma-Aldrich	99% purity
$\text{Mg}(\text{NO}_3)_2 \cdot 6\text{H}_2\text{O}$	Sigma-Aldrich	97% purity
$\text{Al}(\text{NO}_3)_3 \cdot 9\text{H}_2\text{O}$	Sigma-Aldrich	98% purity
$\text{Ni}(\text{NO}_3)_2 \cdot 6\text{H}_2\text{O}$	Sigma-Aldrich	99% purity
$\text{Cu}(\text{NO}_3)_2 \cdot 3\text{H}_2\text{O}$	Sigma-Aldrich	98% purity
Sucrose	Fisher Scientific	n/a
Toluene	Fisher Scientific	n/a
Hydrochloride acid (HCl)	Fisher Scientific	37% purity
HPLC water	Fisher Scientific	n/a
Boron nitride (BN)	Fisher Scientific	n/a
Hexane	Fisher Scientific	n/a
Dodecane	Fisher Scientific	n/a
Chloroform ( $\text{CHCl}_3$ )	Fisher Scientific	n/a
Dichloromethane ( $\text{CH}_2\text{Cl}_2$ )	Fisher Scientific	n/a
1,4-Dichlorobenzene ( $\text{C}_6\text{H}_4\text{Cl}_2$ )	Fisher Scientific	n/a
n-Octane	Fisher Scientific	n/a
Acetonitrile ( $\text{CH}_3\text{CN}$ )	Fisher Scientific	n/a

Sodium hydroxide (NaOH)	Fisher Scientific	n/a
Sodium Carbonate (Na <sub>2</sub> CO <sub>3</sub> )	Fisher Scientific	n/a
tert-Butyl hydroperoxide (TBHP)	Fisher Scientific	n/a
Dibenzothiophene (DBT)	Sigma-Aldrich	n/a
4,6-Dimethyldibenzothiophene (DMDBT)	Sigma-Aldrich	n/a
Biphenyl (BP)	Sigma-Aldrich	n/a
Carbon disulfide (CS <sub>2</sub> )	Sigma-Aldrich	n/a
Thiophene (TP)	Sigma-Aldrich	n/a
2,3-dimethylbenzthiophene (DMBT)	Sigma-Aldrich	n/a
Melamine	Alfa Aesar	n/a
Ethanol	Fisher Scientific	n/a
Boric acid	Sigma-Aldrich	n/a
Methylene blue (MB)	Sigma-Aldrich	n/a
Rhodamine b	Sigma-Aldrich	n/a
Platinum(II) acetylacetonate (Pt(acac) <sub>2</sub> )	Sigma-Aldrich	97% purity
Bis(acetylacetonato)dioxomolybdenum(VI) (MoO <sub>2</sub> (acac) <sub>2</sub> )	Sigma-Aldrich	n/a
Heat shrink tubing	3M	n/a
Nitrogen (N <sub>2</sub> )	BOC	n/a
5% Hydrogen/Nitrogen (5% H <sub>2</sub> /N <sub>2</sub> )	BOC	n/a
Silicon Wafer	Agar Scientific	n/a
Aluminium stub	Agar Scientific	n/a
Carbon adhesive tape	Agar Scientific	n/a

## 2.2 Synthesis of Nanocarbon Aerogels

In this section, the main methods used in this PhD work to fabricate pure nanocarbon aerogels are described. Specific modifications of these general synthetic approaches, e.g. in order to incorporate a desired inorganic particle type into the aerogel structure, are described under the individual result chapter headings. The starting materials for all synthetic approaches were pre-oxidised nanocarbons, specifically graphene oxide (GO) or acid-oxidised multiwalled carbon nanotubes (oCNT). All pre-oxidised nanocarbons were commercially purchased and used without any further purification.

**Templated synthesis of nanocarbon aerogels.** Ice-templated (IT) nanocarbon aerogels were synthesised via a polymer-assisted procedure as shown in Figure 2.1

(top row of schematics).<sup>129</sup> In a typical procedure, 0.0375 g PVA and 0.0375 g sucrose were dissolved in 10 mL HPLC water via tip-probe sonication 10 minutes (30 % of ultrasound power, model HD2200, Bandelin sonopuls). Then, 0.075 g nanocarbons (CNT or GO starting materials) were added into above mixtures and sonicated 4 times to ensure a high degree of nanocarbon exfoliation (each sonication duration 5 minutes). After each sonication, the nanocarbon mixtures were vigorously agitated for at least 3 minutes to uniformly mix the dispersion (3000 rpm/min). After that, 3.5 mL of the mixtures were added into a bespoke PTFE cylindrical module (I.D. 18 mm, O.D. 20 mm, height 20 mm, see Figure 2.2), followed by freezing in liquid nitrogen and freeze-drying for 24 hours (LABCONCO freeze dryer). The obtained non-reduced nanocarbon aerogels were thermally reduced at 1000 °C for 2 hours in H<sub>2</sub>/N<sub>2</sub> (5% H<sub>2</sub>) atmosphere with a heating rate of 5 °C·min<sup>-1</sup> (Carbolite Gero Limited). Then the thermally reduced IT-CNT aerogels were named rIT-CNT aerogels.

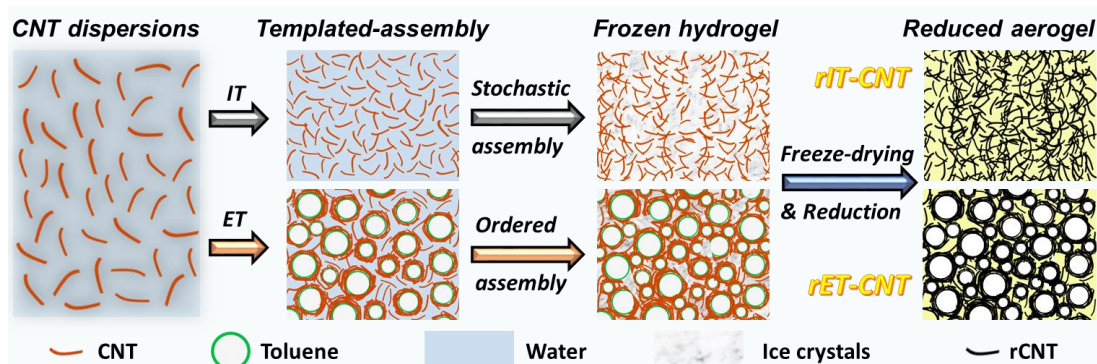


**Figure 2.1** Schematic illustrating the synthesis of CNT aerogels via polymer-assisted ice-templating (rIT-CNT aerogel) and polymer-assisted emulsion-templating (rET-CNT aerogel). The same approach was used to produce the equivalent rIT-GO aerogel samples.

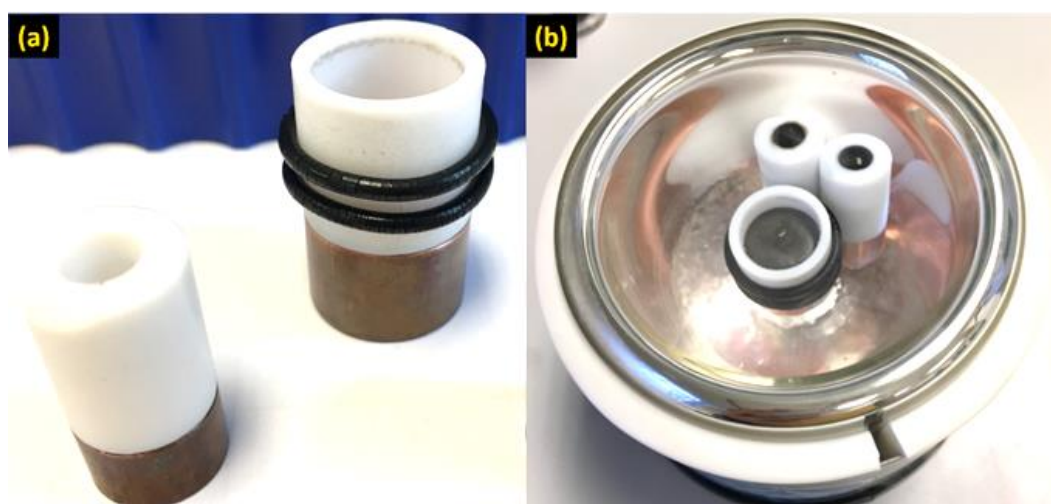


**Figure 2.2** (a) Digital photos of bespoke cylindrical moulds in which the initial aqueous nanocarbon mixtures set into LDH/GO hydrogels. The copper base of the moulds allows for unidirectional heat transfer (cooling) through the bottom of the hydrogel monolith, enabling unidirectional hydrogel freezing. (b) Digital image of moulds emerged via their copper base in a liquid nitrogen bath for unidirectional hydrogel freezing.

A polymer-assisted emulsion-templating (ET) approach was employed to prepare a second type of templated nanocarbon aerogel,<sup>127</sup> with fundamentally different porosity (Figure 2.1 lower row of schematics). In a typical procedure, an initial aqueous oCNT/PVA/sucrose dispersion was prepared using the same synthetic parameters employed for ice-templating procedure. Then, 2.5 mL toluene were added to the aqueous oCNT dispersion, followed by the addition of 1 mL 0.1M HCl under agitation to induce the formation of oCNT-stabilized water/toluene emulsion. The resulting emulsion was then frozen, freeze-dried and thermally reduced, using the same parameters used for the ice-templated nanocarbon aerogels. The thermally reduced ET-CNT aerogels were named rET-CNT aerogels.

**Hydrothermal synthesis of nanocarbon aerogels.** For the hydrothermal (HT) approach (Figure 2.3),<sup>129</sup> ascorbic acid and nanocarbon starting material were dispersed in aqueous solution in a weight ratio 2:1 (Figure 2.3). In a typical procedure, 0.30 g ascorbic acid and 0.15 g GO were mixed into 10 mL HPLC water, followed by tip-probe sonication to ensure good GO dispersion. Then 7 mL of this dispersion were sealed into a sample vial (25 mm diameter, 50 mm height, soda glass with polythene plug), followed by hydrothermal reduction treatment at 80 °C for 4 hours in an oven (Gallenkamp) to form a GO hydrogel. The shape of sample vial gives rise the cylindrical shape of the formed hydrogel monoliths, while dispersion volume and hydrothermal treatment duration determine overall hydrogel dimensions. The GO hydrogel was then freeze-dried and thermally-reduced at 1000 °C, as described in the templated synthesis section, to give the final rGO aerogels (rHT-GO aerogels, see Appendix 1 Figure A1.4 and Table A1.1).

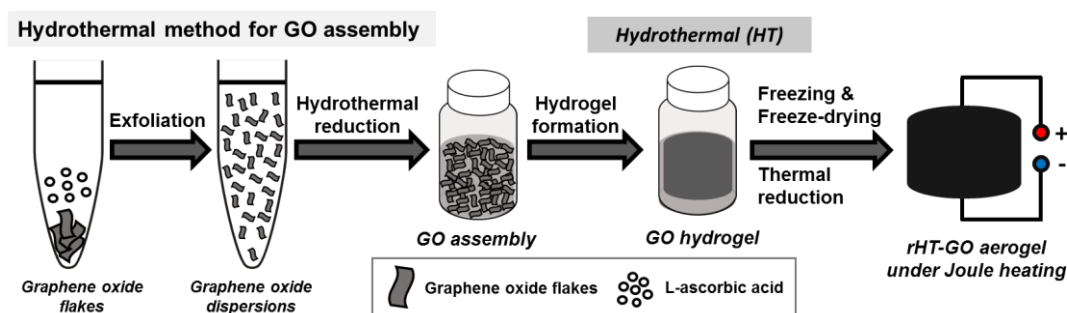


**Figure 2.3** Schematics of thermally reduced hydrothermal GO (rHT-GO) aerogel synthesis for Joule heating.

## 2.3 Materials Characterization

In this section, experimental details are given for the main materials characterisation techniques, employed throughout this PhD work. Where more specialised techniques or unconventional measurement conditions were used, these will be detailed under the relevant result chapter headings.

**Powder X-ray diffraction (XRD)** was conducted on a Bruker D2 Phaser Diffractometer, using  $\text{CuK}\alpha\lambda$  ( $\lambda = 1.54184 \text{ \AA}$ ) at 30 kV, 10 mA, a hold time of 2 s, a step size of  $\theta = 0.01013^\circ$  and the measurement ranging from 5 to  $80^\circ$ . This is a non-destructive technique used to analyse the crystal structure of a material. In this project, XRD was used to identify the crystal phases of the inorganic nanoparticles and to investigate the degree of nanocarbon exfoliation. The data obtained from XRD can be further analysed using the Scherrer equation. This estimates the average crystal domain size of the sample using the full width at half maximum (FWHM) of a defined peak. The equation is as follows:

$$D = \frac{K \lambda}{B \cos \theta}$$

Where:

$D$  = Average crystal domain size                       $K$  = Dimensionless shape factor (0.94)

$\lambda$  = X-ray wavelength                                       $B$  = FWHM of the peak

$\theta$  = The Bragg angle of the peak

**Thermogravimetric analysis (TGA)** was conducted on an SDT Q600 using a  $10 \text{ }^\circ\text{C}\cdot\text{min}^{-1}$  ramping rate from 20 to  $900 \text{ }^\circ\text{C}$  in air atmosphere. This technique is used to estimate the thermal stability of nanocarbon aerogels. For samples containing incombustible inorganic particles, the remaining TGA weight residues after complete nanocarbon combustion at  $900 \text{ }^\circ\text{C}$  were analysed to experimentally determine the particle loadings in the samples.

**Brunauer-Emmett-Teller (BET)** surface area measurements were conducted using a Micromeritics TriStar 3000 instrument. For these measurements, the samples were degassed under  $\text{N}_2$  gas at  $110 \text{ }^\circ\text{C}$  for 3 hours prior to analysis. The  $\text{N}_2$  adsorption and desorption isotherms were collected at 77 K. This technique is used to determine the specific surface area, using BET analysis of the desorption isotherm in the partial pressure range of 0.05-0.2  $p/p_0$ . The size distribution and volume of mesopores (pores between 2-100 nm) were calculated from the desorption isotherm at higher partial pressures, using the Barrett-Joyner-Halenda (BJH) method.

**Scanning electron microscopy (SEM)** was carried out using a Nova NanoSEM 450 with an accelerating voltage of 3 kV. Pure nanoparticle and nanocarbon samples were prepared by dispersing the powders at very low concentrations in water and drop casting onto a silicon wafer. For aerogels samples, small aerogel fragments were sampled from the centre of the aerogel monolith and fixed onto the surface of a conductive adhesive tape. 2 nm Ir conductive layer were coated onto the surface of

all samples before analysis, using a SC 7620 Mini Sputter. SEM imaging is used to visually compare the surface topography and morphology of the materials produced on the nanoscale. It is also used to determine inorganic particle size distributions and to measure average diameters of aerogel macro-pores (large aerogel pores with sizes >100 nm). All SEM images were analysed *via* the software Image J.

**Energy dispersive X-ray spectroscopy (EDX)** was carried out to determine the chemical composition of selected INCA samples. EDX mapping was carried out to visualise the spatial distribution of selected elements on the nanoscale. EDX measurements were performed on the same SEM instrument using an EDX mode detector, typically at an accelerating voltage of 18 kV. EDX samples were prepared as described in SEM section above, but without applying any Ir coating before measurements.

**Transmission electron microscopy (TEM)** images were collected on an electron microscope (Tecnai F30, FEI) at an accelerating voltage of 300 kV. Samples were sonicated in ethanol, followed by drop-casting onto a copper grid coated with a holey carbon film. TEM was carried out to visualise structure of nanocarbon and inorganic particles at greater spatial resolution. For nanoparticles with sizes <20 nm, TEM was used to measure nanoparticle size distributions (measuring the dimensions of at least 100 individual particles). All TEM images were analysed *via* the software Image J. TEM images were taken by Dr Heng Li at Xiamen University, China.

**Raman spectroscopy** was conducted using a Renishaw InVia with an excitation laser wavelength of 532 nm between 100-4000  $\text{cm}^{-1}$ , with an exposure time of 10 s and 3 times of accumulations. This technique is used to analyse the extent of disorder of the nanocarbon material, as well as confirming the presence of nanocarbon in the hybrid materials produced.

**X-ray photoelectron spectroscopy (XPS)** analysis was performed on a K-Alpha<sup>+</sup> X-ray photoelectron spectrometer (Thermo Fisher Scientific), using focused (400  $\mu\text{m}$  spot) monochromatic Al-K $\alpha$  radiation. The binding energies were referenced to the C1s peak of adventitious carbon at 284.8 eV. XPS was used to quantify chemical surface composition of samples and analyse changes in oxidation state. XPS data were measured by Dr Heng Li at Xiamen University, China.

## 2.4 Joule-Heating Measurements

In this section, experimental details are given for typical Joule-heating measurements carried out throughout this work, a major focus of this PhD work. Where more specialised techniques or unconventional measurement conditions were used, these will be detailed under the relevant result chapter headings.

**Joule-heating set-up.** In order to Joule heat aerogels in a highly controlled manner, a custom-made Joule heating set-up was devised. The cylindrical aerogel monoliths were inserted into a custom-made, electrically-contactable sample holder (see below Figure 2.4 and Figure 2.5), consisting two circular, stainless steel electrodes, held by two moveable, heat-resistant alumina holding blocks (allowing for high temperature measurements). The holding blocks are connected to each other through a screw mechanism that allows to put the aerogel between the electrodes under mild compression, important to ensure uniform and stable electrical contact. A DC power supply was then connected to the electrodes and was used to control electrical current through the aerogel sample (Figure 2.6). Multimeters and a dedicated data logger were used to monitor and record electrical voltage and current over time. The current-induced Joule heating of the aerogel was measured using a thin (0.25 mm diameter) K-type thermocouple (TJC 120 Series, TJC120-CASS-IM025U-250-HMPW-M, Omega UK), using a data logger (EL-USB-TC, Lascar Electronics) for continuous temperature read out. For the measurement of the ‘Joule-heating core temperature’,  $T_{core}$ , the thermocouple is inserted into the center of the aerogel monolith. For the measurement of the ‘Joule-heating surface temperature’,  $T_{surf}$ , the thermocouple is fixed so that it firmly touches the outer surface of the aerogel monolith, equidistant to the two electrodes. To further visualize the aerogels’ surface temperature a thermal IR camera (Model: Fluke TiR1) was used in some experiments.

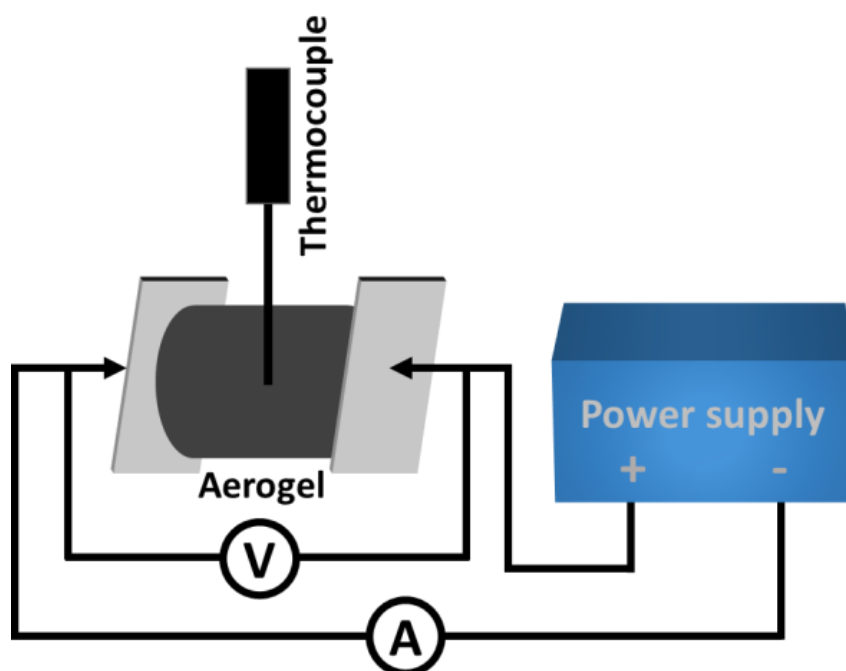


**Figure 2.4** Schematic of a nanocarbon aerogel under Joule heating using a custom-made setup.

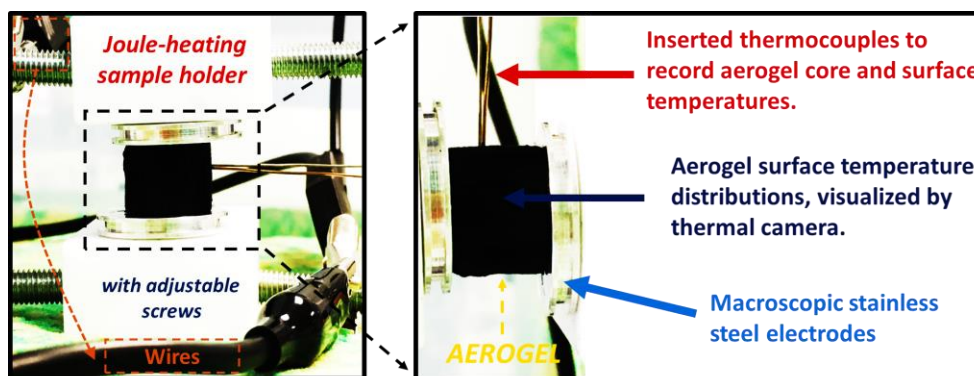


**Figure 2.5** Digital photograph of Joule-heating sample holder.

In order to perform Joule-heating measurements in inert atmosphere conditions, the sample holder was placed into a custom-made air-tight container with fitted gas-inlets and electrical connectors. Inert atmosphere measurements are important for Joule-heating experiments at higher temperatures where nanocarbon oxidation in air needs to be avoided. Figure 2.6a shows the full Joule-heating set-up, including air-tight container, DC supply, and digital multimeters. Figure 2.6b and 2.6c show the corresponding circuit diagram and Joule-heating set-up without air-tight container, respectively.

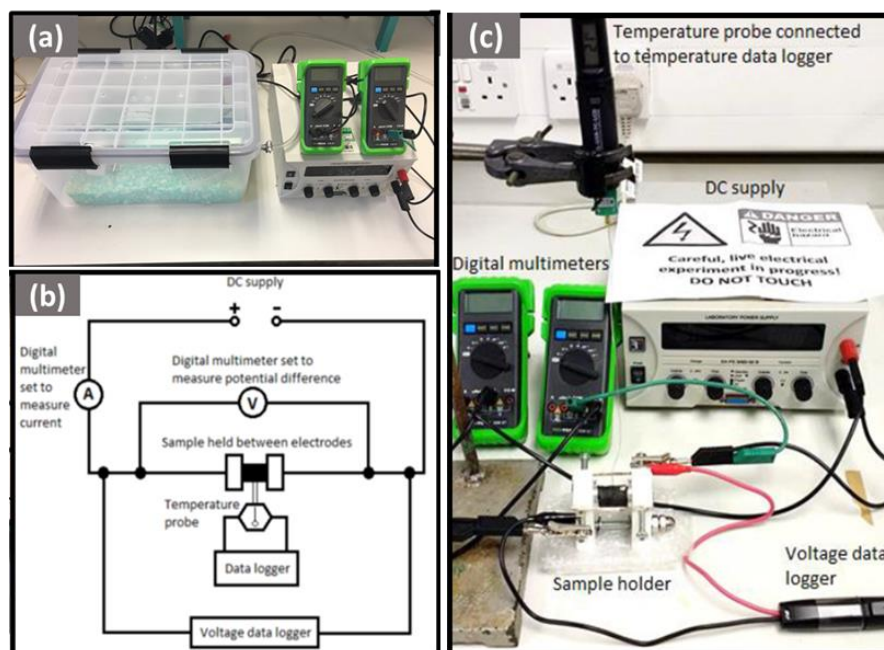


**Figure 2.6** Joule heating setup used to characterize the Joule heating characteristic of the MgAl-MMO/rGO aerogels and to thermally regenerate the hybrid aerogel adsorbent via Joule heating: (a) digital photograph of container with gas inlet/outlets and gas-tight electrical connectors, enabling experiments under inert gas atmospheres, (b) a circuit diagram of Joule-heating set-up; (c) digital photograph of Joule heating setup (outside of gas-tight container for clarity).

**Joule-heating measurements.** All aerogel samples (pure aerogels as well as inorganic/nanocarbon aerogel samples) were preconditioned at a Joule-heating core

temperature of 200 °C for 20 minutes to remove adsorbed water and gases (Figure 2.7a-2.7b). Then a first current-step experiment was carried out by stepwise increasing electrical current and, hence, Joule-heating core temperature of the aerogel samples. Each current was kept constant for 10 minutes before switching to the next current step (Figure 2.7c-2.7d).

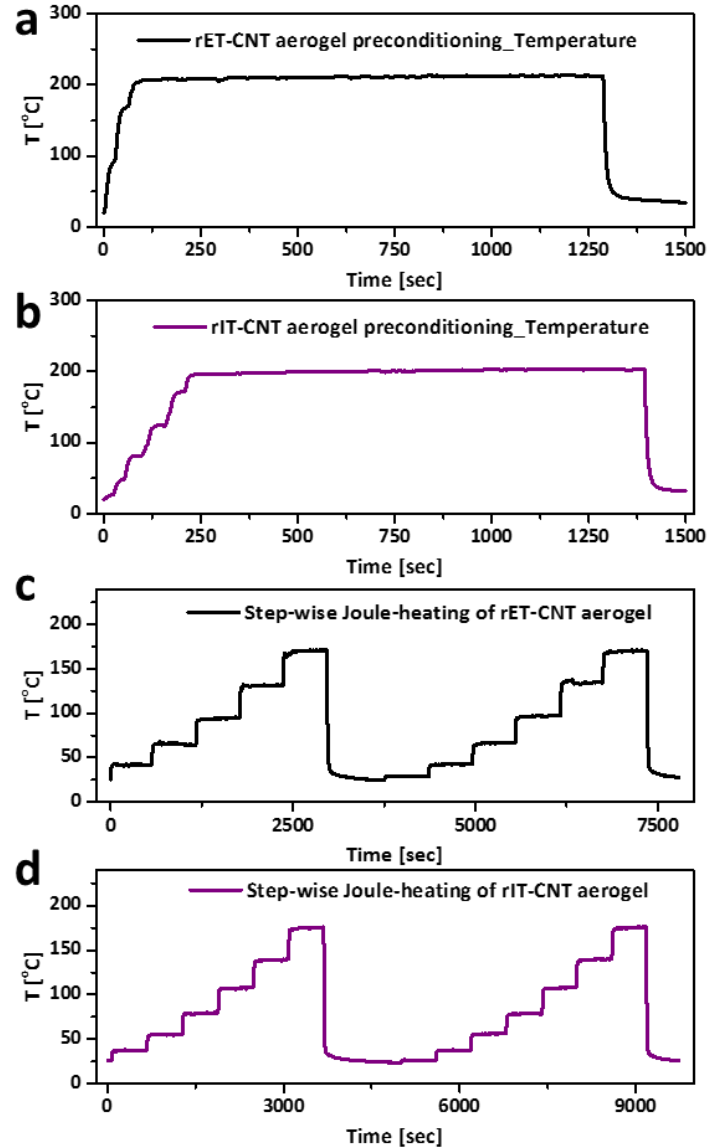


**Figure 2.7** (a-b) Joule-heating preconditioning of emulsion-templated CNT aerogel and ice-templated CNT aerogel at 200 °C for 20 minutes. (c-d) Step-wise Joule-heating of emulsion-templated CNT aerogel and ice-templated CNT aerogel (Each step maintained for 10 min).

During this stepwise current increase, the voltage, current and core temperature values were continuously monitored and recorded through data loggers. The current-step experiments were used to measure the aerogels' current-voltage response (current through aerogel as function of applied voltage) and Joule-heating response (aerogel core temperature as function of electrical power input; power input is determined as product of electrical current and applied voltage).

## Chapter - 3

### Tuning the Heating Properties of Pure Nanocarbon Aerogels through Structural Control

#### 3.1 Introduction

As outlined in Chapter 1, nanocarbon aerogels have shown promise in a wide range of applications, including adsorption, catalysis, sensing, and solar steam evaporation. A highly interesting feature of nanocarbon aerogels, in the context of these applications, is their potential to be directly heated through the application of electrical current (Joule heating)<sup>31</sup> or solar irradiation (solar thermal energy conversion),<sup>217</sup> e.g. in order to activate desired chemical processes at elevated temperatures, to thermally regenerate materials after use, or to accelerate physical processes such as water evaporation.<sup>217</sup>

Joule-heating studies of individual nanocarbon aerogels have shown that the three-dimensional structure of the nanocarbon aerogel framework enables uniform heating throughout the bulk in a fast and energy-efficient manner. For instance, it has been shown that a typical reduced graphene oxide (rGO) aerogel (density 10 mg·cm<sup>-3</sup>) can be accurately and repeatedly Joule-heated to a desired temperature at relatively low electrical potentials (Joule heating to 200 °C at an input potential of 2 V, equivalent to an electrical power input of 4 W).<sup>31</sup> The resulting Joule-heating exhibited great uniformity, very fast heating speeds (600 K·min<sup>-1</sup>) and low energy consumptions (i.e. 200 °C, ~2.5 W·cm<sup>-3</sup>), significantly outperforming external heating approaches (i.e. oven and furnace). The utility of such nanocarbon aerogel Joule-heating has been demonstrated in first applications. For example, direct resistive heating has been utilized to thermally regenerate graphene aerogels used for gas sensing (e.g. 127 °C, 0.125 A), which showed parts-per-million level detection of NH<sub>3</sub> and NO<sub>2</sub> in air.<sup>218</sup> In the context of catalysis, Ag/Co<sub>3</sub>O<sub>4</sub>/Carbon monoliths were employed to catalytically remove formaldehyde via precise Joule-heating temperature control at 90 °C, resulting in increased formaldehyde conversion efficiencies of up to 98 %.<sup>219</sup> As outlined in Chapter 1, Joule-heating has also been applied to graphene-wrapped sponges in order to thermally enhance their performance as clean-up agents for the crude-oil spillage treatments.<sup>209</sup>

Nanocarbon aerogels have also been repeatedly studied as solar thermal conversion materials for solar water evaporation, an emerging technology important in the context of water desalination, liquid-phase separation and sterilization

applications.<sup>217, 220-222</sup> In this context, heat generation is not induced through electrical current but through absorption of solar light. The heat generated upon light absorption can be utilized to promote water evaporation (often also referred to as solar steam generation), important in the context of desalination and water purification technologies.<sup>222</sup> Most solar steam generation methodologies employ porous solar thermal conversion materials that are placed on top of the water surface, so that heat generated from solar irradiation can contribute to water evaporation, overall reducing process duration and lowering energy costs (especially important for large scale desalination applications).<sup>223</sup> Nanocarbon aerogels have been investigated in solar water evaporation due to their efficient light absorption (leading to excellent heat conversion efficiencies), ultra-low density (allowing them to be floated on top of the water reservoir), high porosity (enabling water vapor to escape through the solar thermal conversion materials) and excellent physico-chemical stability (enabling repeated use).<sup>223</sup> For example, GO aerogel membranes, produced via freeze-drying of high-concentration GO dispersions followed by mild photo-reduction, have shown good solar thermal heating performance.<sup>220</sup> The GO aerogel membranes showed high solar irradiation absorption (around 80 % across the wavelength range of 250 to 2500 nm) and could be heated to about 41 °C surface temperature under artificial solar irradiation of 3 sun, i.e. the amount of incoming solar energy tripled. Under this relatively high, artificial irradiation intensity (3 sun), the GO membranes showed thermal conversion efficiencies of around 65 % and good stability over repeated uses.<sup>220</sup> Further improvements were demonstrated for hybrid GO/CNT/alginate hybrid aerogels that have shown even higher solar light absorption (~92 % across 200 - 2500 nm) and high thermal conversion efficiencies, reaching local temperatures of around 42 °C under only one sun irradiation ( $1 \text{ kW}\cdot\text{m}^{-2}$ ), equivalent to 83 % energy transfer efficiency. The resulting aerogel-based solar thermal conversion materials (STCM) showed solar water evaporation rates of up to  $1.622 \text{ kg}\cdot\text{m}^{-2}\cdot\text{h}^{-1}$  under 1 sun irradiation - triple that of pure water under the same irradiation conditions.<sup>217</sup> Similar improvements can be achieved, when using nitrogen doped graphene aerogels which have shown solar thermal conversion efficiencies of up to 90 % and evaporation rates of  $1.558 \text{ kg}\cdot\text{m}^{-2}\cdot\text{h}^{-1}$  at  $1 \text{ kW}\cdot\text{m}^{-2}$  solar irradiation.<sup>222</sup>

While the Joule-heating and solar thermal heating behavior has been studied and optimized for individual nanocarbon aerogel systems,<sup>31</sup> little is known about the more general inter-relationship between nanocarbon aerogel structure and their electrical or solar heating properties. In this chapter, Joule-heating based measurements will be exploited as straightforward and reliable methodology to measure heating properties of a broad range of 3D nanocarbon networks. The initial

focus in this chapter will lie on CNT aerogels, produced by polymer-assisted ice-templating (IT)<sup>224</sup> and emulsion-templating (ET)<sup>127</sup>, to produce two nanocarbon aerogels with fundamentally different microstructure and porosity. The correlation of nanocarbon aerogel structure and heating behavior will then be further explored through the investigation of nanocarbon aerogels that differ in nanocarbon building block, aerogel density and degrees of chemical nanocarbon reduction. We then investigate how the structurally-induced differences impact on the aerogels' thermal conductivity and how this is in turn correlated to the aerogels' functional performance in electrical Joule-heating and solar steam generation.

### 3.2 Results and Discussion

In order to study the impact of microstructure on aerogel heating characteristics, two contrasting CNT aerogels were synthesised via an ice-templating and emulsion-templating fabrication approach, respectively (rIT-CNT aerogel and rET-CNT aerogel, respectively). SEM imaging confirms that the two CNT aerogels exhibited very different internal microstructures (see below Figure 3.1). While the rIT-CNT aerogel presents some larger, micron-sized pockets, likely caused by formation of ice-crystals during aerogel synthesis, its primary structural feature is a comparatively dense, continuous 3D network of highly entangled nanotubes (see below Figure 3.1b). In contrast, the internal microstructure of the rET-CNT aerogels consists of emulsion-templated, hollow CNT microspheres, that are relatively loosely packed with large open gaps and channels between them and with a smaller degree of 3D interconnectivity (see below Figure 3.1a). SEM indicates that the average size of the gaps and pores in the rET-CNT aerogels is about 5.6  $\mu\text{m}$ . In contrast, the predominant pore type in the rIT-CNT aerogels stems from the interstitial spaces in the entangled CNT network, with an average pore size more smaller (around 0.1  $\mu\text{m}$ ) compared to the rET-CNT aerogel (see also pore size distributions, as measured by image analysis in Figure 3.2).

**Table 3.1** Aerogel materials characteristics, reflecting pronounced differences in aerogel microstructure of rET-CNT and rIT-CNT aerogels.

Aerogel	Pore size <sup>a)</sup> [ $\mu\text{m}$ ]	Gas permeability [ $10^{-11} \text{ m}^2$ ]	$\sigma$ <sup>b)</sup> [ $\text{S}\cdot\text{m}^{-1}$ ]	$\kappa$ <sup>c)</sup> [ $\text{W}\cdot\text{m}^{-1}\cdot\text{K}^{-1}$ ]
rET-CNT aerogel	5.6	1.08	0.7	0.174
rIT-CNT aerogel	0.1	0.11	8.0	0.104

<sup>a)</sup> Pore size as obtained from SEM images analysis via Image J; <sup>b)</sup>  $\sigma$  represents aerogel electrical conductivity; <sup>c)</sup>  $\kappa$  represents thermal conductivity collected at a heating power 2W.

The denser, more entangled network microstructure of the rIT-CNT aerogels is further indicated by a high, through-volume electrical conductivity of the aerogel

( $8.0 \text{ S}\cdot\text{m}^{-1}$ , Table 3.1), indicating the presence of a highly interconnected 3D network of high crosslinking density. In contrast, the rET-CNT aerogel exhibits an order-of-magnitude lower through-volume electrical conductivity ( $0.7 \text{ S}\cdot\text{m}^{-1}$ , Table 3.1), suggesting a lower degree of 3D interconnectivity, in line with the more open microstructure of the rET-CNT aerogel observed by SEM.

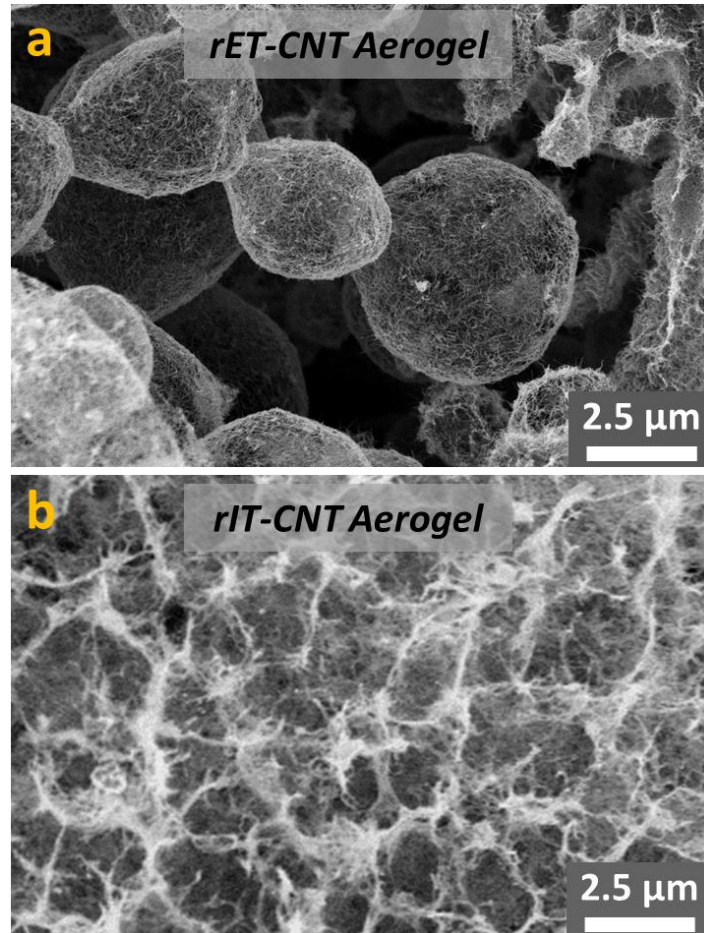


**Figure 3.1** Microstructure of (a) rET-CNT aerogel and (b) rIT-CNT aerogel as imaged by SEM (sampled from the core region of the monolithic aerogel samples).

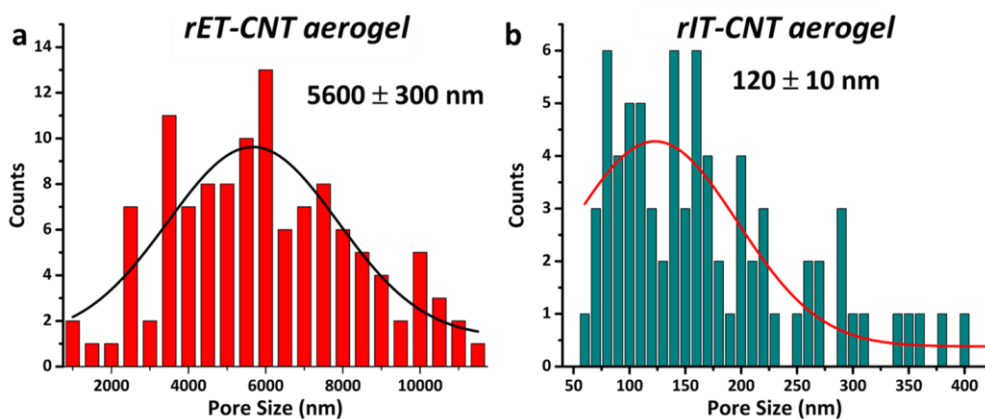


**Figure 3.2** Size distribution of predominant pore type in rIT-CNT aerogels and rET-CNT aerogels, as determined by SEM imaging.

The pronounced difference in microstructure is also reflected in other bulk aerogel properties, such as permeability (Figure 3.3). Through-plane nitrogen flow measurements show highly linear gas velocity-pressure drop correlations (both  $R^2 > 0.999$ , Figure 3.3a) that enable to extract the steady-state gas permeability values for both aerogel types (Figure 3.3b). These measurements reveal a distinct difference in gas permeability between the two aerogels, with the rET-CNT aerogel exhibiting a magnitude-of-order larger nitrogen gas permeability (Figure 3.3b and Table 3.1), consistent with the looser, more open microstructure of the rET-CNT aerogel.

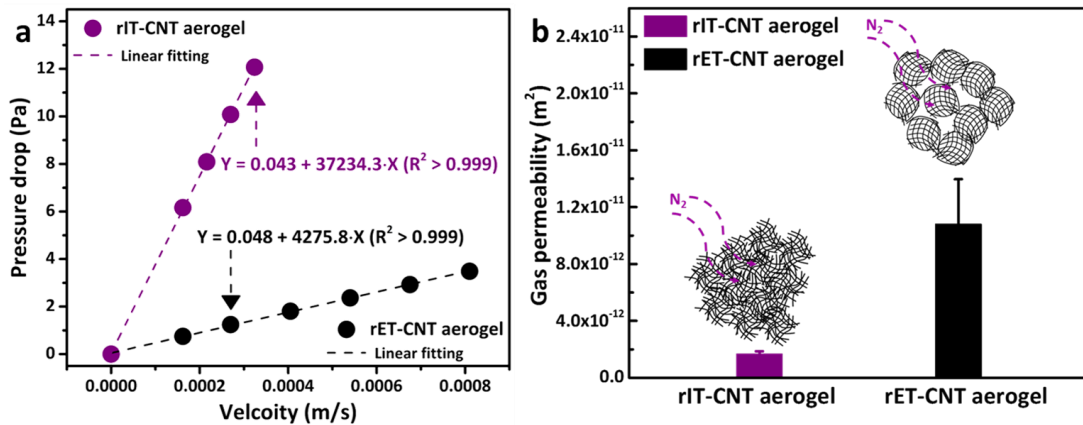


**Figure 3.3** (a) Nitrogen velocity-pressure relationships for extracting gas permeability values in the rIT-CNT aerogel and rET-CNT aerogel. (b) Through-plane gas permeability testing in  $N_2$  atmosphere of the rIT-CNT aerogel and rET-CNT aerogel.

In terms of other structural materials characteristics, the two aerogel samples are however very similar (see below Figure 3.4 and Table 3.2). Both aerogels are formed from the same MWCNT raw material and have been processed, using very similar synthetic parameters (see Experimental). Consequently, both aerogels show very similar, high thermal stability to temperatures up to  $555\text{ }^\circ\text{C}$ ,<sup>225</sup> even in oxidative air atmosphere (an important requisite for many practical thermal applications of nanocarbon aerogels and for the Joule heating studies conducted in this work, see Figure 3.4a and Table 3.2). Raman spectra and XRD patterns of the aerogels confirm very similar graphitic crystallinity and defect concentrations of the CNTs in the aerogels (Figure 3.4c-3.4d and Table 3.2). Nitrogen adsorption measurements show that the specific surface areas are also relatively similar, with the surface area of the rET-CNT aerogel only around 20 % different from the rIT-CNT aerogels (Figure 3.4b, Table 3.2). The main distinguishing feature between the rIT-CNT and rET-CNT aerogels is therefore their highly contrasting internal structure, making the samples an interesting first model system to investigate Joule-heating characteristics as function of nanocarbon aerogel microstructure.

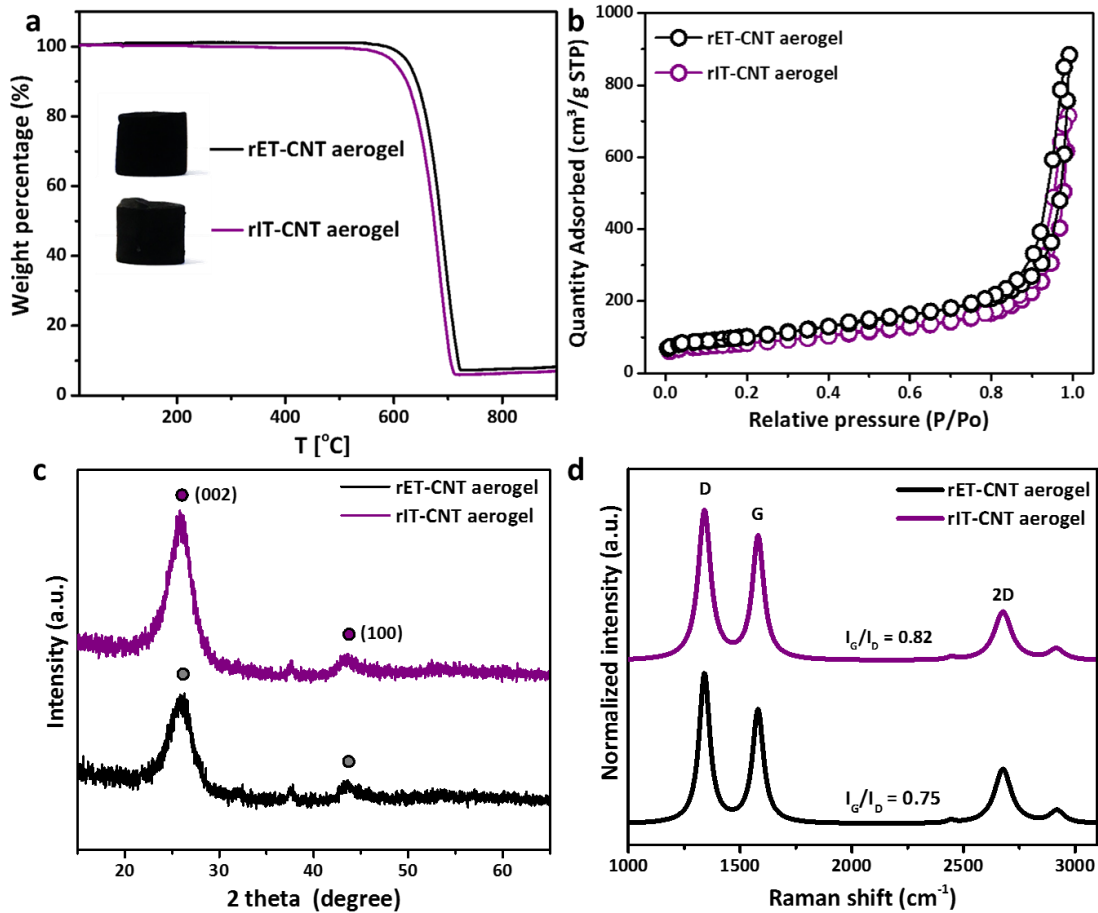


**Figure 3.4** Materials characterization of rET-CNT and rIT-CNT aerogels: (a) TGA in air atmosphere; (b) N<sub>2</sub> adsorption-desorption isotherms; (c) XRD patterns. (d) Raman spectra.

**Table 3.2** Physico-chemical materials characteristics of rET-CNT aerogel and rIT-CNT aerogel.

Aerogel	Nanocarbon type	Envelope Density <sup>a)</sup> [g·cm <sup>-3</sup> ]	TGA combustion temperature [°C]	BET specific surface area <sup>b)</sup> [m <sup>2</sup> ·g <sup>-1</sup> ]	XRD (002) crystal domain size <sup>c)</sup> [nm]	Raman I <sub>D</sub> /I <sub>G</sub> ratio <sup>d)</sup>
rET-CNT aerogel	rCNT	0.006	555 °C	358	2.23	0.75
rIT-CNT aerogel	rCNT	0.009	555 °C	290	2.44	0.82

<sup>a)</sup>  $\rho$  represents aerogel density; <sup>b)</sup> the specific surface area as obtained by BET analysis in Figure 3.4b; <sup>c)</sup> crystal domain size analyzed from (002) peak in Figure 3.4c; <sup>d)</sup> Raman I<sub>D</sub>/I<sub>G</sub> ratio derived from Figure 3.4d.

In order to quantitatively measure Joule-heating characteristics, electrical measurements of the aerogels were carried out using a custom-made Joule-heating set-up (see Chapter 2). All samples were investigated after careful preconditioning at 200 °C to remove adsorbents (water, ambient volatile impurities) from the nanocarbon surfaces, an important requisite to ensure repeatability of the Joule-heating measurements. After preconditioning, both aerogels show highly linear I-V characteristics up to currents of 0.5 A and voltages of 20 V, confirming that the

aerogels behave as traditional Ohmic resistors over the current-voltage range investigated (Figure 3.5a). In the current-voltage range studied here, resistive aerogel Joule-heating to temperature up to 200 °C is observed. Over this temperature range, the aerogels show only relatively minor changes in electrical resistivity (less than 20 % change between room temperature and 200 °C, Figure 3.5b). Interestingly, aerogel resistivity decreases with increasing temperature, indicating a semiconductor-type behavior, in contrast to the metallic nature of individual MWCNTs. This change in electronic behavior between individual CNT building block and macroscopic CNT aerogel is consistently observed in this work for all nanocarbon aerogels investigated and is likely to originate from junction resistance effects in the 3D networks and/or incomplete graphitization during the thermal treatment step.

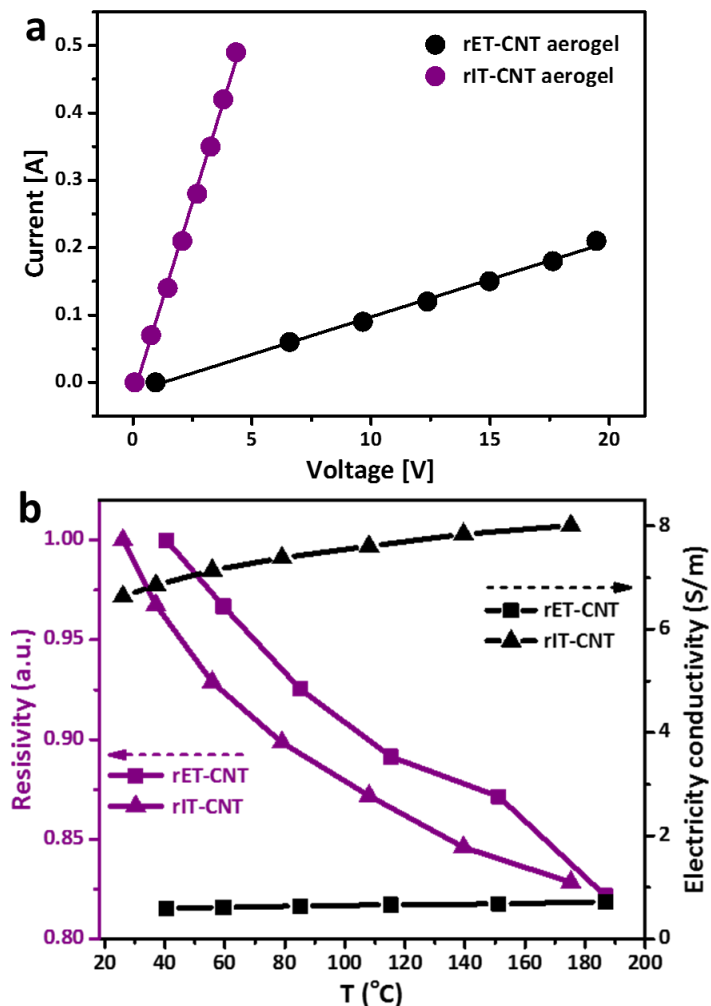


**Figure 3.5** Electrical properties of rET-CNT and rIT-CNT aerogels: (a) I-V curves; (b) Electrical conductivity and relative resistivity as function of Joule-heating temperature.

To assess heating efficiency, the aerogels' steady state Joule-heating temperature was measured at different electrical power inputs ( $P = I \times V$ , Figure 3.6 and Table

3.3). The resulting Joule-heating plots indicate substantial differences in Joule-heating efficiency (here defined as temperature increase per electrical power input,  $dT/dP$ ). Specifically, the rIT-CNT aerogel exhibits a more than 60 % larger Joule-heating efficiency ( $75 \text{ }^\circ\text{C}\cdot\text{W}^{-1}$ ) compared to the rET-CNT aerogel ( $46 \text{ }^\circ\text{C}\cdot\text{W}^{-1}$ ). This efficiency difference is confirmed by Joule-heating experiments carried out at a constant electrical power input. For example, at the same electrical power input of 2 W, the rIT-CNT aerogel reaches a significantly higher Joule-heating core temperature ( $168 \pm 8^\circ\text{C}$ ) compared to the rET-CNT aerogels ( $114 \pm 4^\circ\text{C}$ ).

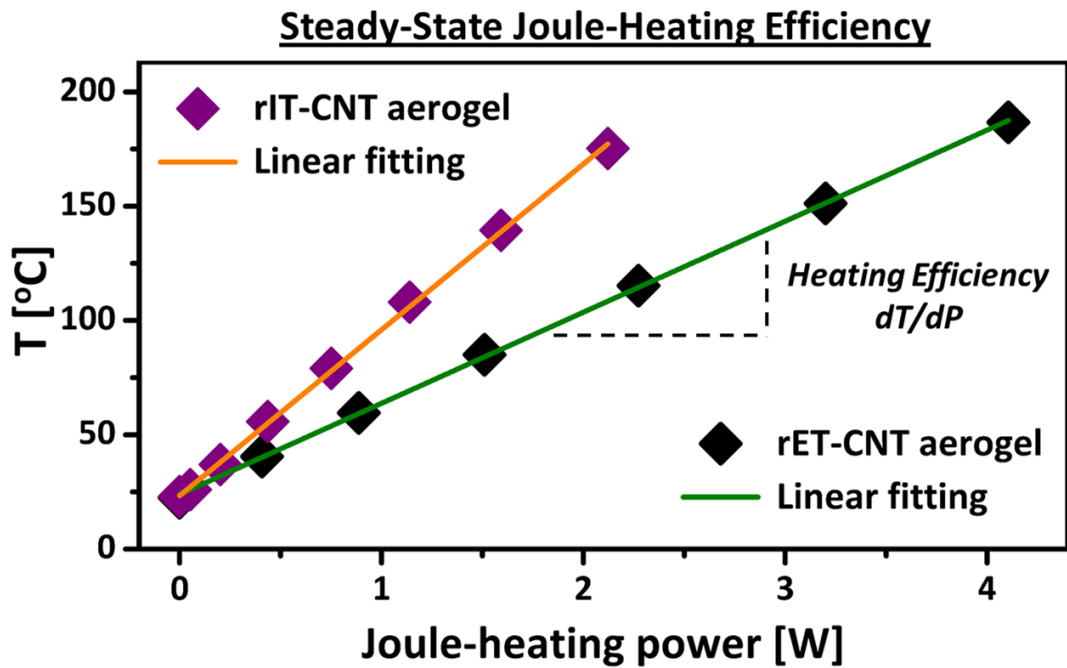


**Figure 3.6** Joule-heating characterisation of rET-CNT and rIT-CNT aerogels via current-step experiments: steady-state Joule-heating core temperature as function of electrical power.

**Table 3.3** Joule-heating characteristics of rET-CNT aerogel and rIT-CNT aerogel (all parameters as measured under steady-state conditions at a power input of 2W).

Aerogel	Core Temperature $T_{\text{core}}$ [°C]	Heating Efficiency $dT/dP$ [°C·W <sup>-1</sup> ]	Heating Rate $dT/dt$ [°C·min <sup>-1</sup> ]	Cooling Rate $-dT/dt$ [°C·min <sup>-1</sup> ]
rET-CNT aerogel	114	46	306	324
rIT-CNT aerogel	168	75	282	264

Differences are also observed in the Joule-heating kinetics of the two aerogel samples. When monitoring Joule-heating temperature over time after ‘switching-on’ electrical current (set to a consistent power input of 2 W), both aerogels show very fast heating kinetics (up to  $5.1 \text{ }^\circ\text{C}\cdot\text{s}^{-1}$ ), with the rET-CNT aerogels showing slightly faster Joule-heating compared to the rIT-CNT aerogels (Figure 3.7a and Table 3.3, see also Appendix 1, Figure A1.1). Due to the excellent thermal conductivity of the

nanocarbon framework, both aerogels also cool down to room temperature very fast once the electrical heating current has been ‘switched-off’ (cooling rates of up to  $5.4\text{ }^{\circ}\text{C}\cdot\text{s}^{-1}$ , Figure 3.7b). Cooling kinetics for the rET-CNT aerogel are about 20 % faster compared to the rIT-CNT aerogel (Table 3.3), potentially caused by the more open internal microstructure, promoting heat loss via improved heat convection during cooling.

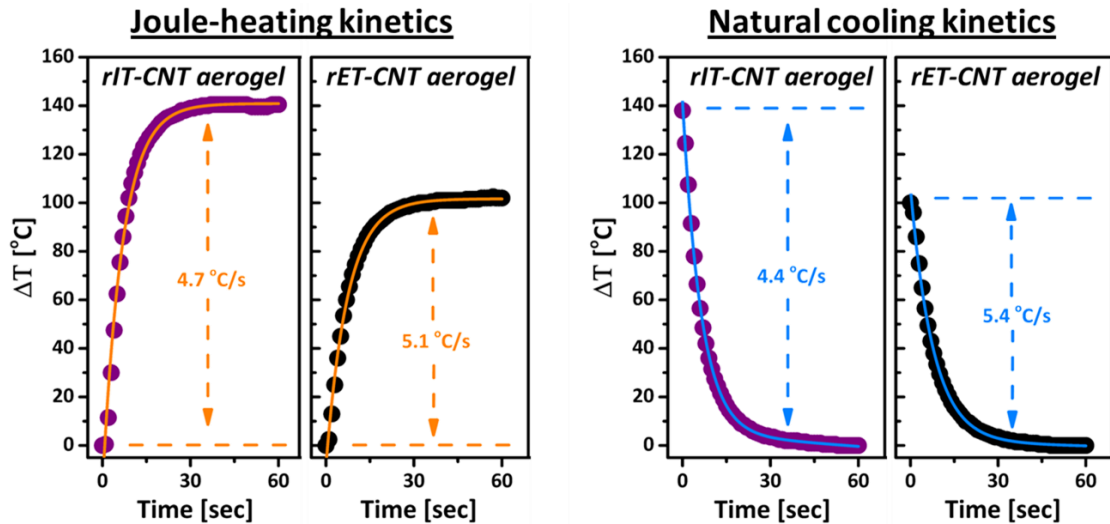


**Figure 3.7** Joule-heating and cooling kinetic of rIT-CNT and rET-CNT aerogels: a) Joule-heating kinetics: increase in core temperature over time after an electrical heating current (electrical power input 2W) has been switched on; (c) Natural cooling kinetics: decrease of core temperature over time after electrical heating current (electrical power input 2W) has been switched off.

The significant differences in efficiency and kinetics clearly demonstrate that aerogel microstructure is a key factor impacting resistive heating behavior. Theoretically, it would be expected that the less electrically conducting rET-CNT aerogel, i.e. the aerogel with higher electrical resistance, would show the higher resistive heating effect. However, our experiments show the opposite trend, indicating that there are a number of additional factors in play, that control Joule-heating characteristics in nanocarbon aerogels.

The most likely alternative factor is the thermal conductivity of the aerogels. Thermal conductivity will control heat losses to the environment and therefore impact on steady-state Joule-heating temperature. To measure thermal conductivity, the radial temperature gradient of the Joule-heated aerogels was analyzed. It has been shown that this Joule-heating-based approach provides values that are in good agreement with thermal conductivity values, determined by other methods, such as thermal diffusivity-based approaches.<sup>31</sup> To measure thermal conductivity, the temperature of a Joule-heated aerogel (electrical power input 2 W) is measured at its core and at defined distances from the core (Figure 3.8, Table 3.1). The resulting radial

temperature gradient can then be analyzed to extract the aerogel's thermal conductivity (see Experimental). Following this approach, the thermal conductivity of the rET-CNT aerogels is found to be about 60 % larger than that of the rIT-CNT aerogel. Due to this substantially larger thermal conductivity, heat conduction to the aerogel surface is more effective in the rET-CNT aerogel, resulting in larger heat losses to the environment, with less of the generated heat remaining 'trapped' in the aerogel, compared to the thermally more conductive rET-CNT aerogel.

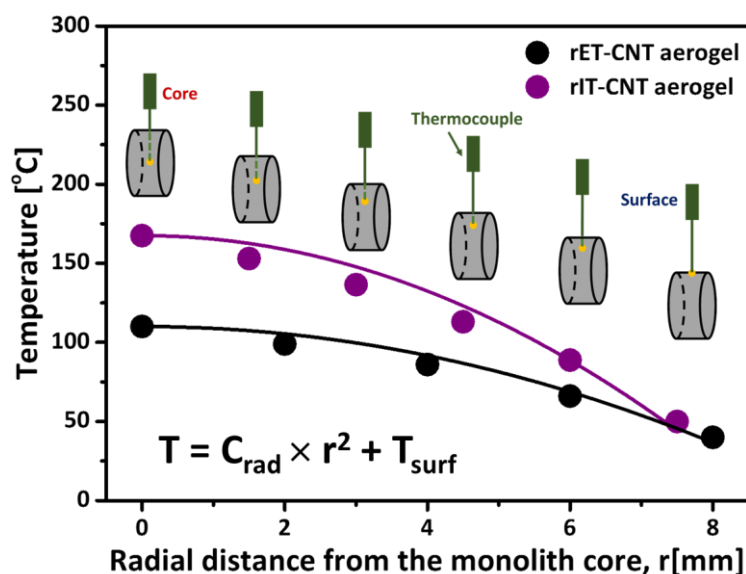


**Figure 3.8** Radial temperature gradient of rET-CNT aerogel and rIT-CNT aerogel, Joule-heated at inputs of electrical power 2W.

To further confirm this effect of thermal conductivity, a series of four additional ice-templated aerogels were synthesised. The ice-templating synthesis was modified by changing nanocarbon building block (CNT replaced by GO, sample labelled rIT-GO aerogel) and thermal reduction treatment (change of reduction atmosphere and reduction temperature; samples labelled as rIT-CNT<sub>N<sub>2</sub></sub> aerogel, rIT-GO<sub>N<sub>2</sub></sub> aerogel and rIT-GO<sub>800</sub> aerogel respectively). All samples were then characterized in terms of envelope density (determined as simple ratio of aerogel weight over aerogel envelope volume). As expected, non-reducing atmosphere (N<sub>2</sub>) and lower reduction temperatures (800 °C) result in nanocarbon aerogels with lower graphitic crystallinity (see Appendix 1, Figure A1.2b), compared to aerogels reduced under standard conditions (5% H<sub>2</sub>/N<sub>2</sub> atmosphere, 1000 °C).<sup>226</sup> The additional aerogels were then also characterized in terms of electrical conductivity, and thermal conductivity (Table 3.4), using the same methodologies, described above.

Joule-heating experiments of the aerogels at an electrical power input of 2W were then used to measure steady-state Joule-heating temperatures and Joule-heating efficiencies.

**Table 3.4** Physical materials parameters of different ice-templated nanocarbon aerogels.

Aerogel	$\rho^a)$ [ $\text{mg}\cdot\text{cm}^{-3}$ ]	$\sigma^b)$ [ $\text{S}\cdot\text{m}^{-1}$ ]	$\kappa^c)$ [ $\text{W}\cdot\text{m}^{-1}\cdot\text{K}^{-1}$ ]	$T_{\text{core}}^d)$ [ $^{\circ}\text{C}$ ]	$dT/dP$ [ $^{\circ}\text{C}\cdot\text{W}^{-1}$ ]
rIT-GO	4.9	8.9	0.152	116	48
rIT-CNT <sub>N2</sub>	9.8	7.3	0.135	136	57
rIT-GO <sub>N2</sub>	6.4	5.7	0.156	113	46
rIT-GO <sub>800</sub>	6.3	9.6	0.125	143	61

<sup>a)</sup>  $\rho$  represents aerogel density; <sup>b)</sup>  $\sigma$  represents electrical conductivity; <sup>c)</sup>  $\kappa$  represents thermal conductivity collected at a heating power 2W; <sup>d)</sup>  $T_{\text{core}}$  obtained from aerogel center at a heating power 2W.

As expected, the four additional samples show clear differences in Joule-heating efficiency. However, their Joule-heating efficiencies do not correlate with key aerogel characteristics, such as electrical conductivity or envelope density (Figure 3.9a, Figure 3.9b).

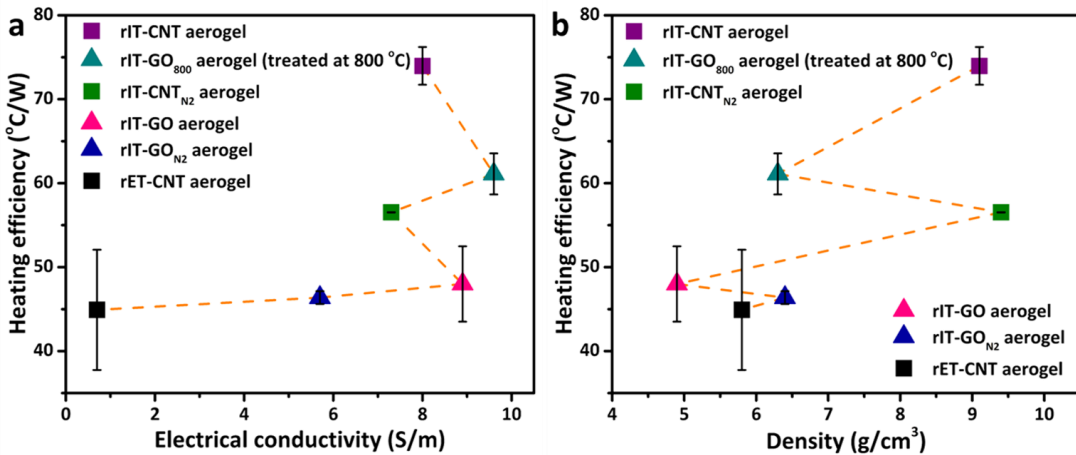


**Figure 3.9** The relationship between Joule-heating efficiency and electrical conductivity (a) and density (b) of different nanocarbon aerogels.

However, a very clear correlation emerges when Joule-heating efficiency is plotted as function of thermal conductivity (Figure 3.10). The inverse relationship between thermal conductivity and Joule-heating efficiency described above is confirmed and can be qualitatively explained by less efficient heat conduction and, therefore, reduced heat dissipation into the environment in aerogels with lower thermal conductivity. The origin for the linear nature of this relationship is not fully clear and requires future investigations. These findings however very clearly demonstrate that thermal conductivity is a key factor in determining Joule-heating characteristics of nanocarbon aerogels. In order to increase Joule-heating efficiency for heating applications (local gas heaters, thermal sorbent regeneration, thermal de-freezing materials), nanocarbon aerogels with relatively low thermal conductivities are required (here observed for aerogels with denser network structure, high crosslinking density and lower degree of graphitic crystallinity). In contrast, for

applications where Joule-heating effects need to be minimized (e.g. catalytic supports in fuels cells, battery materials etc.), nanocarbon materials with relatively high thermal conductivity need to be fabricated (here observed for aerogels with open microstructure, large pore sizes and higher degrees of graphitic crystallinity).

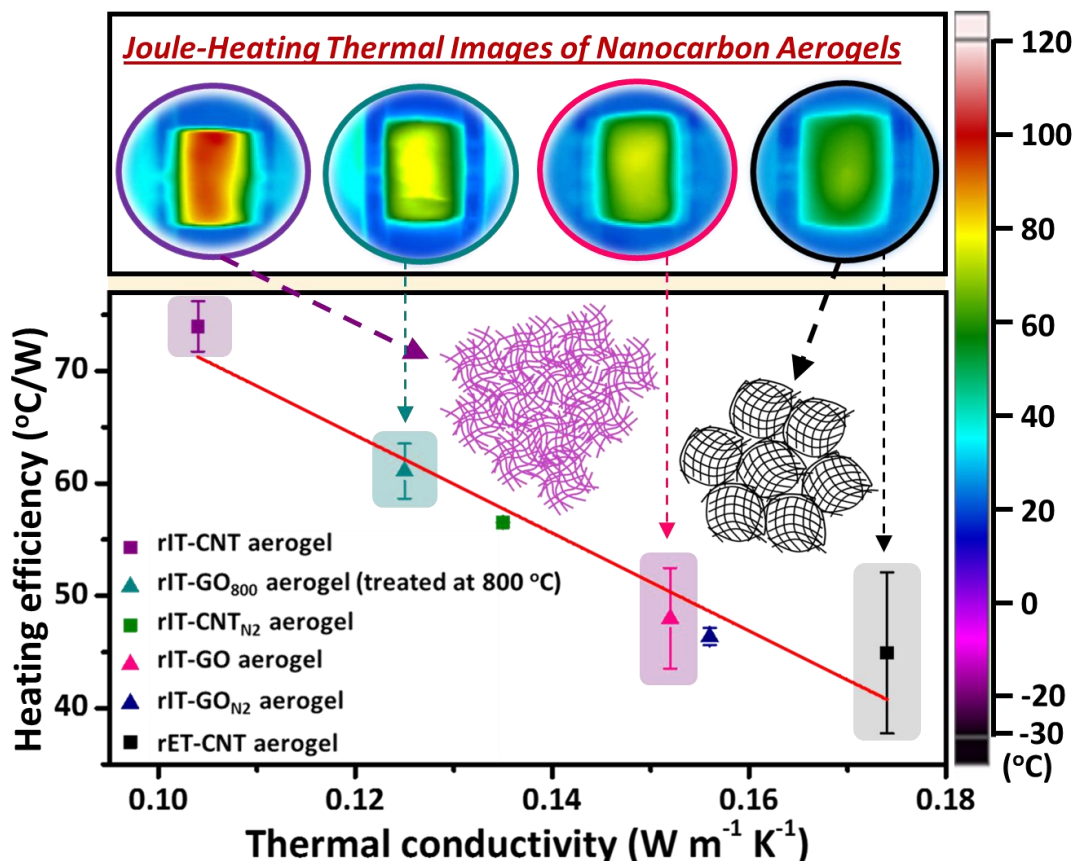


**Figure 3.10** The relationship between Joule-heating efficiency and thermal conductivity of different nanocarbon aerogels. Inserted thermal images were taken at electrical power 2 W.

Differences in thermal aerogel conductivity are also important to tailor functional performance of nanocarbon aerogels in other heating-related applications. As an example, the rET-CNT aerogel and rIT-CNT aerogel were investigated as solar thermal conversion materials (STCM) for solar steam generation applications.<sup>217</sup> Like other nanocarbon aerogels reported in the literature, our rET-CNT and rIT-CNT aerogels exhibit excellent STCM characteristics. Both aerogels show highly efficient light absorption across the whole solar spectrum (more than that 94 % absorbance between 200 nm to 2000 nm), ensuring high solar thermal conversion efficiencies (Figure 3.11a).<sup>217</sup> Contact angle measurements show that water drops placed on the aerogel top surface adopt relatively large contact angles around 140°, indicating an overall hydrophobic surface character (Figure 3.11b).

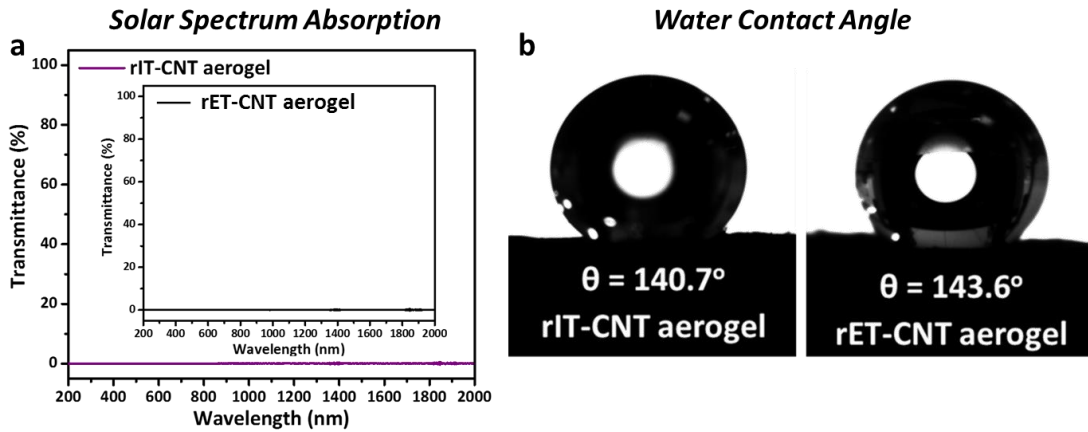


**Figure 3.11** (a) Solar absorption measurements and (b) contact angles of rIT-CNT aerogel and rET-CNT aerogel, respectively.

While light absorption and surface character are very similar in both aerogels (Figure 3.10), they exhibit significantly different thermal conductivities (60 % higher thermal conductivity for the rET-CNT aerogel), as discussed above. To assess the impact of this difference on solar thermal heating, cylindrical rET-CNT and rIT-CNT aerogels were placed on a glass vial and heated through light irradiation from the top (one sun solar simulator, see Figure 3.12).

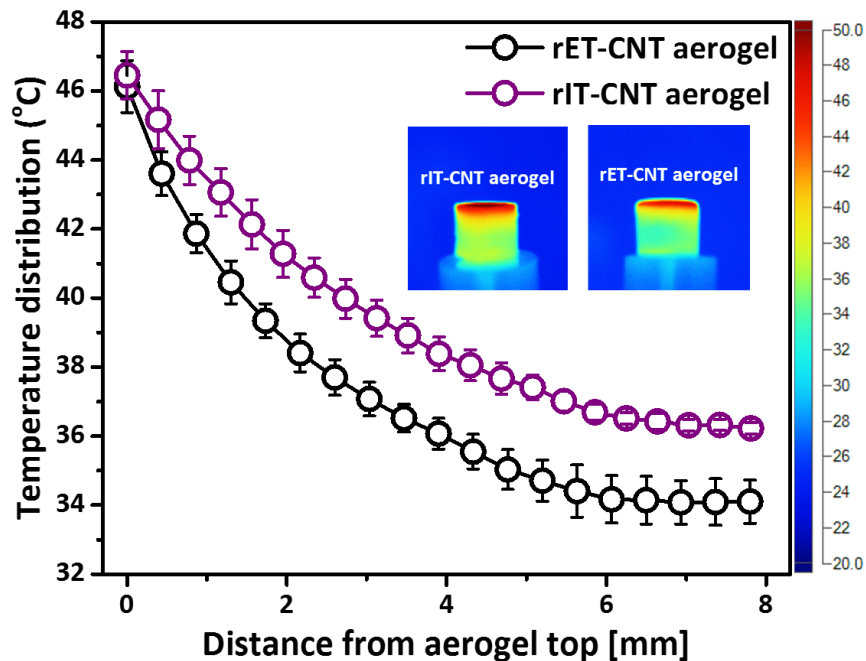


**Figure 3.12** Temperature gradient distributions of the rIT-CNT aerogel and rET-CNT aerogel at shining time 300s (from aerogel top to the middle).

Upon reaching steady state, the temperature of the aerogels was then thermally imaged perpendicular to the irradiation direction (Figure 3.12 inset). The resulting thermal images were analyzed via line scans to plot the temperature gradient between the irradiated aerogel top and the non-irradiated aerogel middle (Figure 3.12). The temperature of the irradiated aerogel top reaches up to 46 °C,

comparable to other nanocarbon based aerogels reported in the literature.<sup>217</sup> The 'vertical' temperature gradient between aerogel top and middle is shallower and plateaus at a higher temperature for the rIT-CNT aerogel. This effect is a direct consequence of the lower thermal conductivity of the rIT-CNT aerogel, with the lower conductivity minimizing heat conduction to the aerogel bottom, and therefore, reducing heat transfer overall enabling the rIT-CNT aerogel to trap light-induced heat more effectively.

To further investigate this effect, the membrane-shaped aerogels were tested for solar steam generation. Membrane-shaped rET-CNT and rIT-CNT aerogels were fabricated using the exact same synthetic parameters as used before, but using smaller volumes of nanocarbon dispersions, which can be defined as aerogels with a high ratio of diameter over height.<sup>227</sup> For the solar steam evaporation experiment, the aerogel membranes were floated on a water reservoir, irradiated from the top (one sun solar simulator), and the resulting weight loss due to water evaporation monitored through a computer-controlled balance (Figure 3.12).

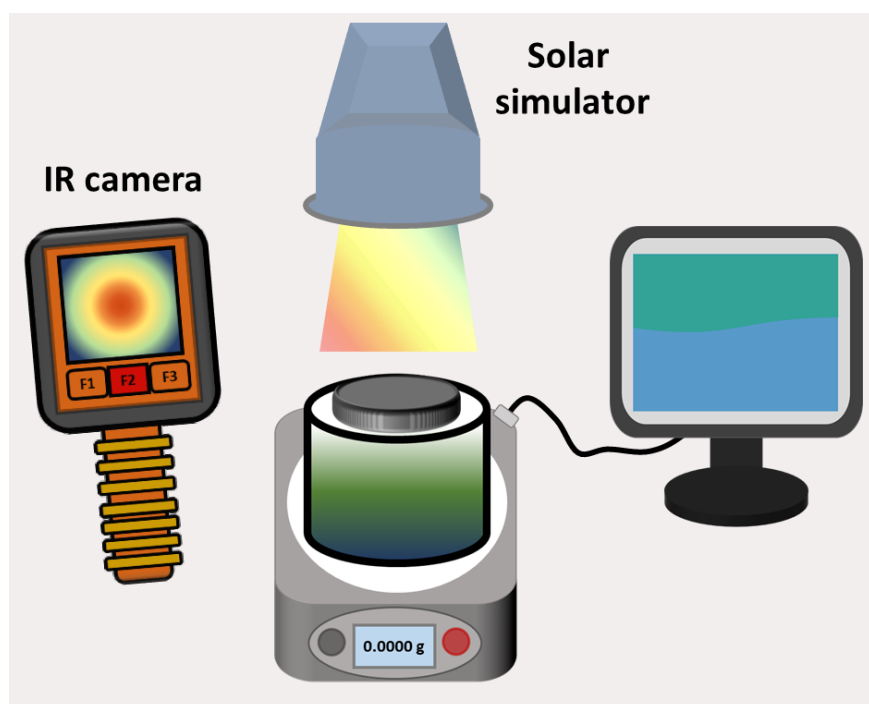


**Figure 3.13** Schematics of rCNT aerogel membranes on top of water for solar steam generation.

Monitoring water evaporation under one sun irradiation shows that the rIT-CNT aerogel exhibits indeed the best solar steam generation performance at a water evaporation rate of  $0.78 \text{ kg}\cdot\text{m}^{-2}\cdot\text{h}^{-1}$ , i.e. 30 % higher water evaporation efficiency than that of the rET-CNT aerogel and three times higher than that of pure water (see below Figure 3.14).

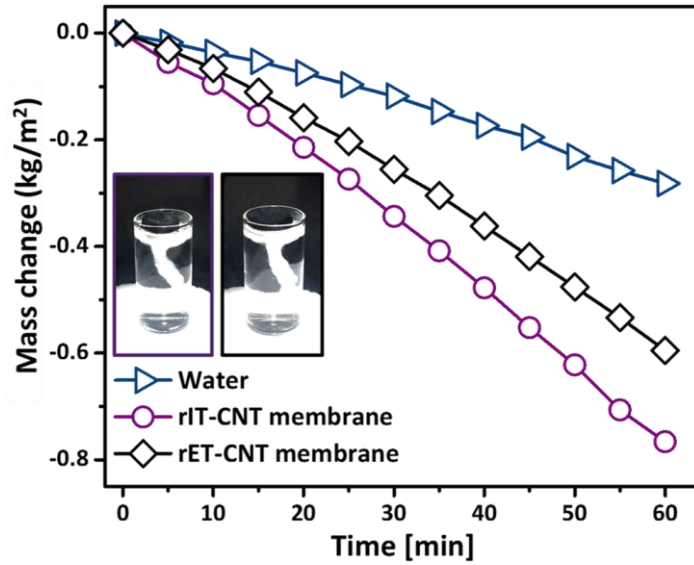


**Figure 3.14** Solar steam generation performance of rET-CNT and rIT-CNT aerogels: Water mass change normalised to water surface area under one sun irradiation over time for pure water, water topped with rIT-CNT aerogel, and water topped with rET-CNT aerogel (Insert shows digital photos of aerogel membranes on top of water).

In terms of absolute values, these evaporation rates are comparable to many carbon-based solar thermal conversion materials reported in the literature (Figure 3.15, Table 3.5).<sup>220, 228-248</sup> Higher water evaporation rates of more than  $1 \text{ kg}\cdot\text{m}^{-2}\cdot\text{h}^{-1}$  (like those mentioned in the introduction) are typically achieved through further chemical functionalisation of the aerogels (e.g. functionalisation with alginate or nitrogen doping) which facilitates the transport of water vapour through the aerogel material. However, our findings clearly show that tailoring the physical microstructure of the aerogel material is an important additional tool to increase solar evaporation efficiencies by at least 30 % as demonstrated here. As observed in the solar steam experiments, the best solar thermal heating efficiencies are observed for the rIT-CNT, i.e. the aerogel with the lower thermal conductivity.

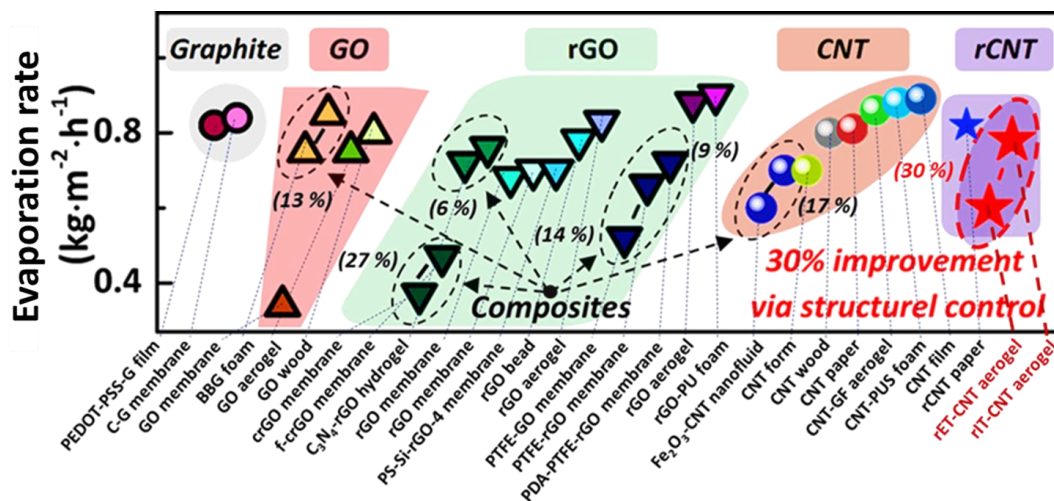


**Figure 3.15** Solar steam water evaporation rates of different nanocarbon-based solar evaporators from literature under one sun illumination (References are listed in Table 3.5).

**Table 3.5** Solar steam generation performance comparison under one sun illumination between nanocarbon-based materials reported from literature and this study.

Solar evaporators	Nanocarbon types	Evaporator Compositions	Water evaporation rate [ $\text{kg}\cdot\text{m}^{-2}\cdot\text{h}^{-1}$ ]	Ref.
PEDOT-PSS-G film	Graphite	poly(3,4-ethylenedioxythiophene)-poly(styrenesulfonate)/Graphite	0.82	228
C-G membrane	Graphite	Semipermeable collodion/Graphite	0.84	229
GO membrane	GO	GO	0.34	230
BBG-0.6 foam	GO	Blue brick/GO	0.75	231
BBG-1.2 foam	GO	Blue brick/GO	0.85	231
GO aerogel	GO	GO	~0.75	220
GO-Wood	GO	GO/Wood	~0.80	232
crGO membrane	rGO	rGO/Hydrazine	0.37	230
f-crGO membrane	rGO	rGO/Hydrazine/Nitric acid	0.47	230
C <sub>3</sub> N <sub>4</sub> -rGO-9 hydrogel	rGO	Graphitic C <sub>3</sub> N <sub>4</sub> /rGO	0.76	233
C <sub>3</sub> N <sub>4</sub> -rGO-1.5 hydrogel	rGO	Graphitic C <sub>3</sub> N <sub>4</sub> /rGO	0.72	233
rGO membrane	rGO	rGO	0.68	246
rGO membrane	rGO	rGO	~0.70	234
PS-Si-rGO-4 membrane	rGO	Polystyrene/rGO	0.7	244
rGO bead	rGO	rGO	0.78	235
rGO aerogel	rGO	rGO	0.83	236
PTFE-GO membrane	GO	Polytetrafluoroethylene/GO	0.52	237
PTFE-rGO membrane	rGO	Polytetrafluoroethylene/rGO	0.66	237
PDA-PTFE-rGO membrane	rGO	Polydopamine/PTFE/rGO	0.72	237
rGO aerogel	rGO	Sodium alginate/rGO	~0.88	238
rGO-PU foam	rGO	rGO/Polyurethane	0.90	239
Fe <sub>3</sub> O <sub>4</sub> /CNT-1 nanofluid	CNT	CNT/Fe <sub>3</sub> O <sub>4</sub>	~0.60	240
Fe <sub>3</sub> O <sub>4</sub> /CNT-10 nanofluid	CNT	CNT/Fe <sub>3</sub> O <sub>4</sub>	~0.70	240
CNT foam	CNT	CNT	~0.70	248
CNT-Wood	CNT	CNT/Wood	~0.80	232
CNT paper	CNT	Filter paper/CNT	0.81	241
CNT-GF aerogel	CNT	Glass fiber/CNT	0.86	247

CNT-PUS foam	CNT	CNT/Polyurethane sponge	0.88	242
CNT film	CNT	CNT	0.89	243
rCNT paper	rCNT	rCNT	0.82	245
rET-CNT aerogel	rCNT	rCNT	0.60	Here
rIT-CNT aerogel	rCNT	rCNT	0.78	Here

### 3.3 Conclusions

In this work, ice-templating (IT) and emulsion-templating (ET) approaches were used to form two types of aerogels consisting of CNT 3D networks (rIT-CNT aerogel and rET-CNT aerogel), which have contrasting internal structures and display very different Joule-heating performance. By tuning aerogel microstructure, porosity, and graphiticity and systematically measuring their Joule-heating characteristics (steady-state core temperatures, Joule-heating kinetics), we show that the Joule-heating efficiencies of the materials are highly correlated with their thermal conductivities. In our systematic set of samples, the lowest thermal conductivity and therefore highest steady-state Joule-heating temperatures (168 °C at 2W power input) were displayed by the rIT-CNT aerogel, structurally based on a combination of a denser, potentially more crosslinked microstructure and relatively small pore size. Specifically, the rIT-CNT aerogels showed a thermal conductivity of  $0.104 \text{ W}\cdot\text{m}^{-1}\cdot\text{K}^{-1}$  while the more open, potentially less crosslinked rET-CNT aerogels exhibited a 67 % higher thermal conductivity. This difference directly translates into a 60 % higher Joule-heating heating efficiency for the rIT-CNT aerogel ( $75 \text{ }^\circ\text{C}\cdot\text{W}^{-1}$ ) compared to its emulsion-templated counterpart ( $46 \text{ }^\circ\text{C}\cdot\text{W}^{-1}$ ). Smaller differences are also overserved for the heating and cooling kinetics, with the cooling rate reaching about  $5.4 \text{ }^\circ\text{C}\cdot\text{s}^{-1}$  (equivalent to  $320 \text{ }^\circ\text{C}\cdot\text{min}^{-1}$ ) for the thermally more conductive rET-CNT aerogel.

Interestingly, similar trends in heating behavior are observed for solar thermal heating. Our samples show excellent solar absorption across a wide wavelength range (96 % across 200 to 2000 nm), resulting in a solar thermal conversion efficiency of 33 %. As observed for Joule-heating, the aerogel with the lowest thermal conductivity (rIT-CNT aerogel) can trap the generated heat more effectively. The differences in thermal conductivity (based on differences in microstructure) give rise to significant differences in solar steam generation performance, with the rIT-CNT aerogel displaying a 30 % higher water evaporation rate than the rET-CNT aerogel under one sun light exposure. While absolute evaporation rates are only moderate for our samples, this work shows the importance of aerogel microstructure and thermal conductivity for this emerging application field. Further

improvements in solar water evaporation performance should be achievable through chemical functionalization with more hydrophilic moieties that will further facilitate capillary water transport to the solar-heated aerogel top. Conversely, control of microstructure and thermal conductivity is likely to be important to boost the performance of other promising solar thermal conversion materials, such as polypyrrole foams.

More generally, we find that both the electrical and solar heating efficiencies of nanocarbon aerogels are best for materials with the lowest thermal conductivities. Further tuning of thermal aerogel conductivity to a desired low value (for applications where high heating efficiencies are required) or a desired high value (for applications where nanocarbon heating needs to be limited) is likely achievable through structural and chemical control, e.g. especially through control of nanocarbon graphiticity and cross-linking density. These principles can therefore guide the design of 3D nanocarbon aerogel networks for a wide range of new applications, including gas heater, clean water generation or temperature activated chemical processes.

### 3.4 Experimental

#### 3.4.1 Materials synthesis

**Aerogel synthesis.** All aerogel samples were produced via the templated aerogel fabrication approaches described in Chapter 2. The two model aerogels (rIT-CNT and rET-CNT aerogel) were produced using the exact synthetic conditions, detailed in Chapter 2. In order to produce aerogels with different degree of chemical reduction, IT-GO aerogels were reduced at temperatures of 800 °C (samples labeled as rIT-GO<sub>800</sub> aerogel) as well as in pure N<sub>2</sub> atmosphere at 1000 °C (labelled as rIT-CNT<sub>N<sub>2</sub></sub> aerogel and rIT-GO<sub>N<sub>2</sub></sub> aerogel) in a tube furnace at a treatment duration of 2 hours. All the IT and ET aerogels were fabricated into the same cylindrical shape and size (diameter ~1.55 cm, height ~ 1.3 cm), important to reduce error in Joule-heating based property measurements.

#### 3.4.2 Materials characterisation

**Gas permeability.** The through-plane gas permeability of nanocarbon aerogels was tested using an in-house built setup with a flow controller (HFC-202, Teledyne Hastings, UK) and a differential pressure sensor (PX653, Omega, UK). Specifically, a circular aerogel sample with a thickness of 3 mm was imbedded into a circular sample holder, then the sample holder was screwed tightly for following nitrogen flow. Subsequently, the nitrogen flow rates were scaled up proportionally to record

applied voltages to obtain the pressure drop (Pa) and velocity ( $\text{m}\cdot\text{s}^{-1}$ ) data (see above Figure 3.3a), which were then linear fitted to extract the slope value ( $S$ ,  $\text{Pa}\cdot\text{s}\cdot\text{m}^{-1}$ ). Then the gas permeability value ( $K$ ) of the measured aerogel sample was calculated using Equation 3.1.

$$\text{Gas permeability, } K = \frac{\mu \times m}{S} \quad (\text{Equation 3.1})$$

Where  $K$  is the gas permeability ( $\text{m}^2$ ),  $\mu$  is the dynamic viscosity value of nitrogen ( $1.80 \times 10^{-5} \text{ Pa}\cdot\text{s}$ ) and  $m$  is the thickness of samples. Dr Mohamed Ismai helped and trained me how to measure gas permeability at The University of Sheffield, UK.

**Solar steam generation** was measured using a solar simulator (Newport Co.) under one sun solar radiation, accompanying with a digital balance (uncertainty of  $\pm 0.001 \text{ g}$ , Ohaus, Mettler Toledo) to measure the mass change over time. In general, the nanocarbon aerogel was put on top of water which was poured in a glass vial with a diameter of 25 mm and a height of 50 mm at room temperature. The water evaporation rates ( $WER$ ,  $m_{\text{evap}}$ ,  $\text{kg}\cdot\text{m}^{-2}\cdot\text{h}^{-1}$ ) and solar steam conversion efficiencies ( $\eta_{\text{evap}}$ , %) were calculated from Equation 3.2 and Equation 3.3 respectively, the corresponding mathematical equation are shown below:

$$WER = \frac{m_{\text{evap}}}{t} \quad (\text{Equation 3.2})$$

$$\eta_{\text{evap}} = \frac{m_{\text{evap}} \times h_{\text{vap}}}{Q_s} \quad (\text{Equation 3.3})$$

Where  $\Delta m$  is the water mass loss ( $\text{kg}\cdot\text{m}^{-2}\cdot\text{h}^{-1}$ ),  $t$  is the illuminating time (h),  $\eta_{\text{evap}}$  defines solar steam conversion efficiencies,  $h_{\text{vap}}$  represents the total enthalpy of liquid-vapor phase change (sensible heat and potential heat) and  $Q_s$  is the solar illuminating intensity ( $\text{kW}\cdot\text{m}^{-2}$ ).

**Contact angles** of aerogel materials were tested using a drop-shape analysis device (OCA 25, Dataphysics UK). Specifically, a sessile drop of water was squeezed onto the surface of aerogel sample waiting 30 seconds for stabilization. Then the picture was captured for contact angle value analysis via software. Generally, the contact angle between liquid and solid surface is defined by the Young equation:

$$\cos \theta_{\text{Young}} = \frac{\gamma_{\text{sv}} - \gamma_{\text{sl}}}{\gamma} \quad (\text{Equation 3.4})$$

Where  $\theta_{\text{Young}}$  is the contact angle,  $\gamma_{\text{sv}}$  and  $\gamma_{\text{sl}}$  are the solid-vapour and solid-liquid interfacial tensions, respectively, and  $\gamma$  is the surface tension of the liquid.

**Thermal images** were taken using Fluke TiR1 thermal camera, and were analysed via Fluke Connect software.

**UV/VIS/NIR spectrometer** was used to measure the light transmittance with the wavelength range from 200 nm to 2000 nm on Lambda 950, PerkinElmer.

### 3.4.3 Joule-heating measurements

**Joule-heating characterisation of nanocarbon aerogels.** All Joule-heating measurements were carried out in air atmosphere, using the electrical set-up described in Chapter 2 and measuring Joule-heating temperatures at the aerogel core through an inserted thermocouple. All samples were pre-conditioned via Joule-heating at 200 °C for 20 min before measuring their steady state Joule-heating behaviour. Steady-state Joule heating temperature as function of power input (as displayed in Figure 2.7) was measured through the current step experiment described in Chapter 2. Heating kinetics were determined by switching on an electrical current (equivalent to an electrical power input of 2 W) and logging aerogel core temperature over time. Cooling kinetics (in ambient air) were measured by switching off the 2W heating current and monitoring aerogel core temperature over time. Heating and cooling rates,  $k$ , are approximated as

$$k = \frac{\Delta T}{\Delta t} \quad (\text{Equation 3.5})$$

where  $\Delta T$  is the temperature difference between temperature of an unheated aerogel (here consistently taken as 20 °C) and the equilibrium temperature of the aerogel under Joule-heating at 2 W power input. For the Joule-heating heating kinetics,  $\Delta t$  is the time difference between switching on the heating current and reaching steady-state Joule-heating temperature. For the natural cooling kinetics,  $\Delta t$  is the time difference between switching off the heating current and the aerogel core reaching ambient temperature (here consistently taken as 20 °C).

#### **Measurement of aerogel thermal conductivity through Joule-heating experiments:**

At constant electrical current input, the Joule-heating temperature of an aerogel at the aerogel core will be considerably higher than at the aerogel surface due to constant heat loss at the aerogel surface. The difference between the monolith core and surface temperature (i.e. the degree of heat loss) is crucially dependent on the thermal conductivity of the aerogel. It has been shown for nanocarbon aerogels, that the radial core-to-surface temperature gradient is well fitted by a quadratic function (see Ref. 31 and Figure 3.8 for representative data from this work).

Therefore, the radial temperature gradient across a Joule-heated nanocarbon aerogel can be analyzed by a simplified model for one-dimensional heat conduction in cylinders with homogeneous, internal energy generation:<sup>31</sup>

$$T = C_{rad}r^2 + T_{surf} \quad (\text{Equation 3.6})$$

$$k = \frac{q}{4C_{rad}} \quad (\text{Equation 3.7})$$

Where  $r$  is the distance from the aerogel core (mm);  $T$  is the measured temperature at distance  $r$  ( $^{\circ}\text{C}$ );  $q$  is the Joule heating energy density ( $\text{W}\cdot\text{m}^{-3}$ );  $T_{surf}$  is the surface temperature;  $C_{rad}$  is the corresponding quadratic fit parameters ( $\text{K}\cdot\text{m}^{-3}$ );  $k$  is the thermal conductivity of the aerogel ( $\text{W}\cdot\text{m}^{-1}\cdot\text{K}^{-1}$ ).

To determine aerogel thermal conductivity in this work, radial Joule-heating gradients of cylindrical aerogels (diameter  $\sim 1.55$  cm, height  $\sim 1.3$  cm) were determined at an electrical power input of 2 W, measuring Joule-heating temperatures at different radial distances from the aerogel core via a thermal couple. Thermal conductivity values were extracted from the resulting temperature gradient plots through quadratic fitting (Equation 3.6). Thermal conductivity was then calculated from the quadratic fitting parameter (Equation 3.7), with the Joule heating energy density,  $q$ , estimated as ratio of electrical power input over aerogel monolith volume. All Joule-heating experiments were carried out at least three times and exhibited high reproducibility.

## **Chapter - 4**

### **Electrically-Heatable Graphene Aerogels as Nanoparticle Supports in Adsorptive Desulfurisation and High-Pressure CO<sub>2</sub> Capture**

As outlined in Chapter 1, integrating inorganic nanoparticles (metal-oxides,<sup>249</sup> metallic nanoparticles,<sup>50</sup> clays,<sup>250</sup> other 2D materials<sup>251</sup> etc.) into nanocarbon aerogels has proven an extremely successful strategy to substantially boost the performance of nanocarbon aerogels in established technologies (e.g. energy storage, sensors)<sup>252, 253</sup> as well as to open up completely new application routes (e.g. in heterogeneous catalysis or piezoelectronics).<sup>250, 254</sup> This chapter will therefore focus on the decoration of nanocarbon aerogels (specifically rGO aerogels) with a class of technologically important nanoparticles, namely LDH-derived mixed metal oxide. The resulting hybrid aerogel systems will be characterised in terms of both liquid-phase and gas-phase adsorption performance, using the commercially important application examples of organosulfur sorption from liquid hydrocarbons and high-pressure, elevated-temperature CO<sub>2</sub> adsorption. In this context, the utility of Joule-heating will be investigated in terms of fast and energy-efficient thermal sorbent regeneration.

#### **4.1 Introduction**

As outlined in Chapter 1, wet-chemical nanoparticle assembly approaches have proven particularly popular for the fabrication of inorganic/graphene hybrid aerogels, due to their intrinsic capability for straightforward tuning of crucial macroscopic material characteristics (surface area, porosity, crosslinking density etc.)<sup>255</sup> and intrinsic compatibility with solution-based inorganic nanoparticle synthesis.<sup>252</sup> Wet-chemical aerogel fabrication of graphene-based aerogels typically utilizes GO in hydrothermal or polymer-assisted approaches,<sup>256</sup> followed by lyophilisation and reduction treatments to produce the final rGO aerogels with (partially) restored graphitic properties.<sup>31, 257, 258</sup> To embed inorganic nanoparticles within the 3D network of rGO aerogels, a variety of solution-based synthetic approaches has been explored, as outlined in Chapter 1.<sup>259</sup> The resulting nanoparticle/rGO hybrid aerogels have shown enhanced functional activity and stability in catalytic, sensing and structural applications, mainly based on the support function of the high-surface-area rGO aerogel network. Examples include Pt/rGO aerogels with excellent electro-catalytic performance in the oxygen reduction

reaction,<sup>260</sup> Fe<sub>3</sub>O<sub>4</sub>/rGO aerogels for ultralight, magnetic actuators,<sup>261</sup> MXene/rGO aerogels for fast and highly-sensitive piezoresistive sensors,<sup>262</sup> and complex hybrid Pt/C<sub>3</sub>N<sub>4</sub>/rGO aerogel catalysts for efficient methanol oxidation.<sup>263</sup>

Recently, graphene-based aerogels have also been successfully hybridised with hydrotalcite-like LDH particles for applications in solar-driven photo-electrochemical water oxidation (NiFe-LDH/GO aerogels),<sup>264</sup> sodium-ion batteries (NiCo-LDH/GO aerogels)<sup>265</sup> and water treatment (MgAl-LDH/GO aerogels).<sup>61</sup> Due to their flexible chemical composition and excellent atomic metal dispersion, LDH particles provide ideal precursors for other classes of functional inorganic nanoparticles. LDH-derived mixed metal oxide (MMO) nanoparticles can be easily synthesised through straightforward, scalable calcination or annealing treatments of the LDH parent materials.<sup>57</sup> Under highly-reductive, thermal annealing conditions, noble metal ions in the LDH precursor materials can also be fully reduced to their metallic state, leading to the formation of LDH-derived metal nanoparticles (MNP).

Unsupported LDH-derived MMO materials have been widely studied for the adsorptive removal of inorganic and organic pollutants from liquids and gases. For example, LDH-derived MMO have shown promise for the adsorptive desulfurisation of fuels, often studied via adsorption of model organosulfur compounds (such as dibenzothiophene, DBT) from hydrocarbon solutions. In terms of organosulfur sorption capacity, LDH-derived MMO nanoparticle systems show only moderate activity (around 1 mg·S/g ads for MgAl-MMO) compared to other porous sorbents (activated carbons, MOFs, zeolites etc.).<sup>169, 266, 267</sup> However, they outperform other solid sorbent systems in a number of other practically-important sorption characteristics, making them overall viable, selective and regenerable sorbents for desulfurisation applications.<sup>268</sup> The additional benefits of MMO-based sorbents include, non-reactive organosulfur binding (enabling sorbent regeneration via relatively mild temperature- or pressure-swing), good thermal and chemical stability, very good performance in the presence of common, competing adsorbate species (e.g. water), and high selectivity for challenging, sterically-hindered organosulfurs.<sup>57</sup>

LDH-derived MMO materials are also particularly interesting sorbents for pre-combustion CO<sub>2</sub> capture and hydrogen generation. Hydrotalcite-derived MMO nanoparticles are particularly promising chemisorbents for sorption enhanced reaction (SER) technologies (see also Chapter 1) as they show their highest CO<sub>2</sub> sorption performance at the relevant high operating temperatures (200-500 °C) and high CO<sub>2</sub> pressures (1-30 bar), typically employed in practical SER processes. Under elevated-temperature conditions, CO<sub>2</sub> physisorbents (e.g. zeolites and activated carbons) have relatively low capacities and selectivities, while other CO<sub>2</sub>

chemisorbents (e.g. lithium zirconates and calcium oxides) exhibit slow adsorption kinetics or require high energy to be regenerated.<sup>269</sup>

Despite the positive sorption characteristics of LDH-derived MMO materials for desulfurisation and SER, their overall multicycle performance in terms of capacity, kinetics and stability needs to be further improved before they can be successfully used commercially. The sorption performance of MMO nanoparticles can be significantly limited by particle sintering when they are exposed to successive adsorption and desorption cycles, resulting in significantly reduced sorption capacities and loss of accessible sorption sites over time. In addition, the energy efficiency of these sorption systems needs to be further improved so they can be environmentally and economically feasible compared to more mature technologies.<sup>198, 270</sup>

It has been reported that significant performance enhancements of LDH-derived MMOs in both organosulfur and CO<sub>2</sub> sorption can be obtained by dispersing them on high surface area materials, such as carbons.<sup>57, 58, 270</sup> It has also been shown that graphene-based powders provide particularly suitable supports due to matching morphology and surface charge between LDH and GO support.<sup>57, 58</sup> However, there are no studies assessing the benefits of 3D-structured macroscopic graphene supports, such as rGO aerogels, on the MMO performance in these important sorption applications. In addition, the electrical conductivity of rGO aerogels provides a unique opportunity for direct electrical heating (as investigated in detail in Chapter 2), with great potential to substantially improve energy efficiency of thermally-driven MMO processes and applications. While electrical heating has been demonstrated for pure rGO aerogels,<sup>209</sup> this valuable additional functionality of the rGO aerogels has not yet been explored for the technologically-important MMO nanoparticle systems. Finally, there is also a substantial lack of sorption data for carbon-supported MMO materials under realistic commercial SER operating sorption conditions. While some CO<sub>2</sub> sorption studies have been carried out at the relevant high temperatures (T= 200-500 °C),<sup>271-274</sup> there are no studies investigating the sorption characteristics of carbon-supported MMO sorbents at high CO<sub>2</sub> pressures ( $p_{\text{CO}_2} > 1$  bar).

This study addresses these research gaps by investigating rGO aerogels as stabilising and electrically-responsive supports for LDH-derived nanoparticles to create multifunctional porous materials that combine substantially enhanced performance (across different sorption applications) with the novel capability for energy-efficient, resistive sorbent heating. These principles are investigated by decorating rGO aerogels with very high loading fractions of LDH-derived mixed metal sorbent

nanoparticles (MgAl-MMO, CuAl-MNP, NiAl-MNP). The chemical and structural properties of the resulting hybrid aerogel sorbents are carefully assessed and linked to their fundamental sorption characteristics (capacity enhancement, sorption kinetics, regeneration stability, selectivity), as assessed via liquid-phase organosulfur sorption measurements. The additional functionality of the hybrid aerogels sorbents is demonstrated by exploiting electrical heating of the rGO aerogel framework for rapid thermal MMO sorbent recycling via energy-efficient Joule heating (a practically important process enabled by the hybrid aerogel form, and not possible for MMO sorbents in powder form). To demonstrate the benefits of rGO aerogel support for gas-phase sorption applications, a typical MgAl-MMO/rGO hybrid aerogel sorbent is also investigated for CO<sub>2</sub> sorption under high-pressure ( $p_{\text{CO}_2} = 1\text{-}10$  bar), high-temperature ( $T = 300$  °C) conditions relevant to SER processes, and its performance data assessed against an equivalent unsupported MMO-powder sorbent and literature data on other high-pressure, high-temperature CO<sub>2</sub> sorbents.

## 4.2 Results and Discussion

### 4.2.1 Hybrid aerogel synthesis

In order to support MMO sorbent nanoparticles within the framework of rGO aerogels at high loadings, hybrid aerogels were produced through an adapted ice-templating aerogel synthesis (see Chapter 2). The key change to the standard ice-templating process is the addition of pre-formed LDH particles to the initial GO dispersion. Addition of LDH at this relatively early stage of aerogel fabrication process was chosen to attach the particles to the GO sheets prior to assembly into gels. This approach avoids potential diffusion-related issues associated with more conventional aerogel decoration methods (i.e. impregnation of pre-assembled aerogel monoliths), and, thereby, ensures uniform and high particle loading throughout the entire aerogel.

Specifically, hybrid aerogels were synthesised through a facile three-stage fabrication process (Figure 4.1). In Step 1, pre-synthesised LDH particles are thoroughly dispersed within an aqueous GO/polymer dispersion. LDH particles are introduced in form of a wet-paste (rather than a dried powder) in order to aid complete LDH nanoparticle dispersion and individualisation. In this LDH/GO mixture, the positively-charged LDH nanoparticles electrostatically attach to the negatively-charged GO sheets, aiding the formation of LDH-decorated GO sheets in solution. The aqueous mixtures are then cast into cylindrical moulds where, assisted by the polymer additive, the LDH-decorated GO sheets assemble into a stochastic 3D network, resulting in the formation of hydrogels (LDH/GO hydrogel). In Step 2, the LDH/GO

hydrogels are frozen, adopting a unidirectional freezing approach (Figure 4.1) to induce ice-templated macro-porosity within the final aerogel monoliths. Subsequent freeze-drying yields cylindrical LDH/GO aerogel monoliths. In Step 3, high-temperature annealing in a reducing atmosphere was employed to produce the final nanoparticle/rGO hybrid aerogel in the form of cylindrical monoliths. The annealing treatment is required to remove the polymer additive from the final products and to promote covalent nanocarbon crosslinking (enhancing the hybrid aerogels' structural stability, important for their practical application as sorbents). The high-temperature treatment also results in the conversion of the supported LDH particle into MMO or MNP, depending on the chemical composition of the initial LDH particles. Crucially, the annealing treatment also restores the graphitic crystallinity of the nanocarbon framework, rendering the final hybrid aerogel sorbents electrically-conducting and, hence, electrically-heatable.

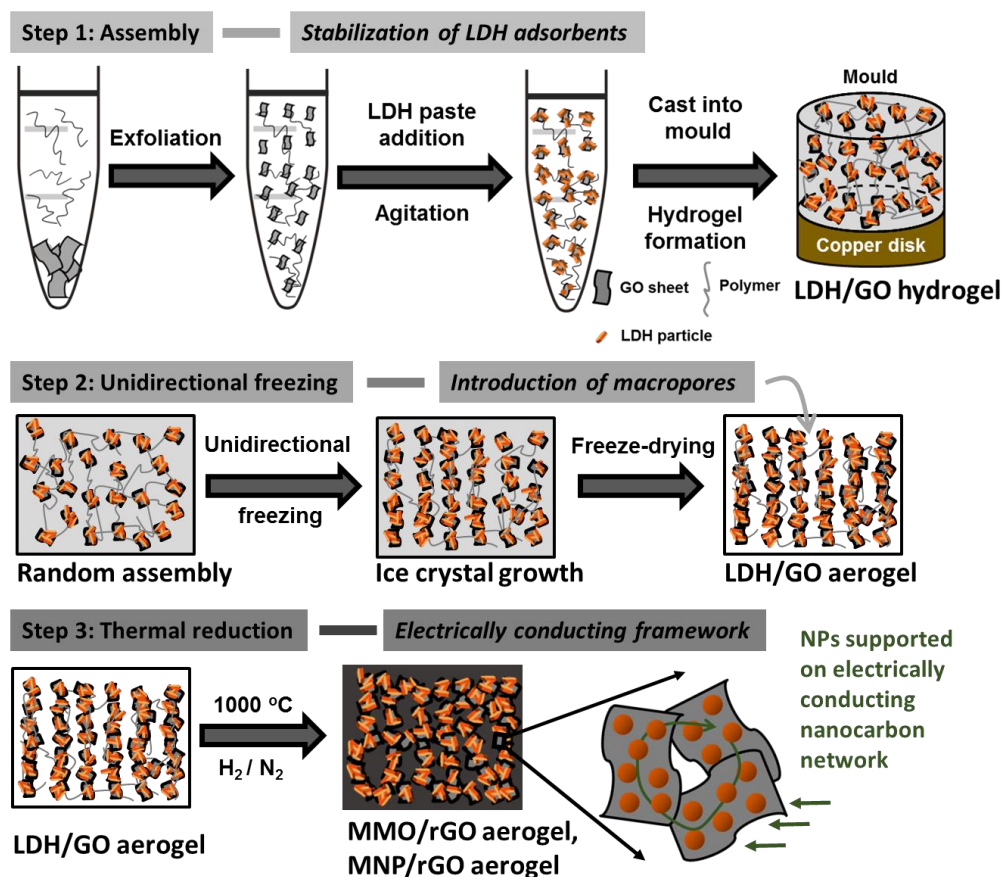


**Figure 4.1** Synthetic procedure for the fabrication of electrically-conducting, high-weight loading sorbent-nanoparticle/rGO hybrid aerogel. MMO = mixed-metal-oxide; MNP = metal nanoparticle.

#### 4.2.2 Hybrid aerogel characterisation

As an important model system, MgAl-MMO/rGO hybrid aerogels were synthesised from MgAl-LDH (atomic Mg:Al ratio 2:1) and GO. Zeta-potential

measurements confirm that the initial MgAl-LDH particles and GO sheets carry substantial, opposite surface charge (at pH = 7,  $\zeta_{\text{LDH}} = +41.8$  mV;  $\zeta_{\text{GO}} = -31.1$  mV, Figure 4.2). The resulting electrostatic attraction drives efficient and strong particle attachment onto the GO sheets in Step 1 and contributes to the firm anchoring and stabilisation of the functional nanoparticles within the final rGO aerogels.<sup>275</sup>

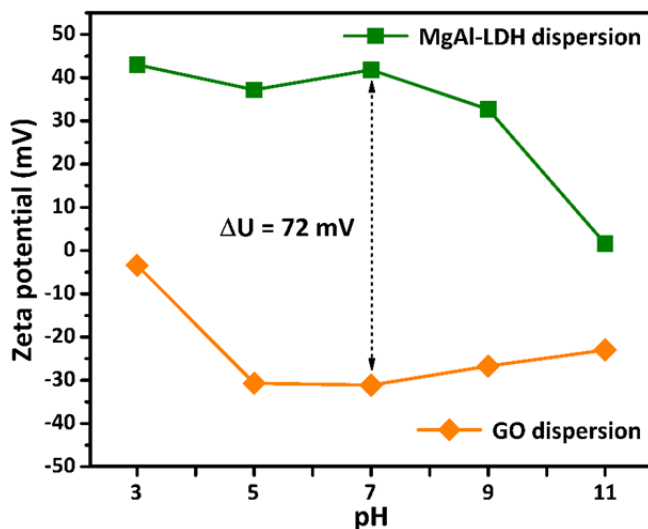


**Figure 4.2** Zeta potential of the initial MgAl-LDH and GO suspensions at different pH values.

The maximum nanoparticle loading within the rGO aerogels achievable through our synthetic approach was exceptionally high at 78 wt% (as measured by TGA, Figure 4.3). Hybrid aerogels with lower nanoparticle loadings can also be easily synthesised (see Appendix 2, Figure A2.1). However, high nanoparticle weight loadings are highly beneficial for sorption applications (as the ‘parasitic’ weight of the support framework is minimised),<sup>276</sup> and are difficult to achieve by other synthetic strategies (such as aerogel monolith impregnation).<sup>199</sup>

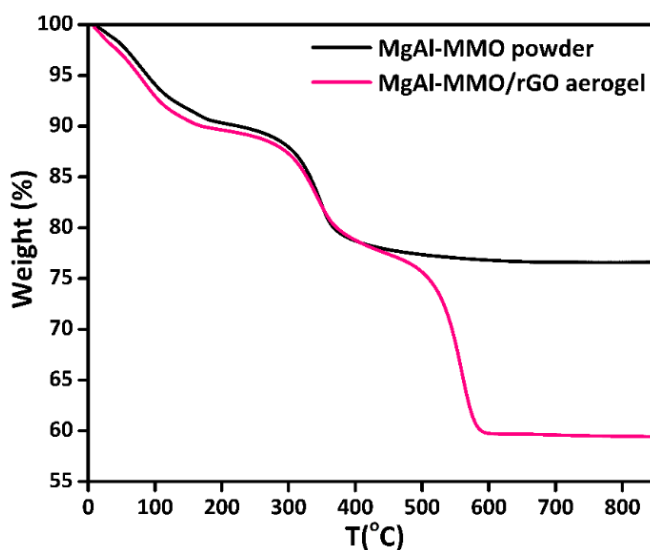


**Figure 4.3** TGA of MgAl-MMO powder and MgAl-MMO/rGO aerogel in air.

In order to visualise particle distribution in the aerogels, fragments of LDH/GO and MMO/rGO aerogels were imaged by SEM. Figure 4.4 presents SEM images of MgAl-LDH/GO aerogels (prior to thermal annealing).

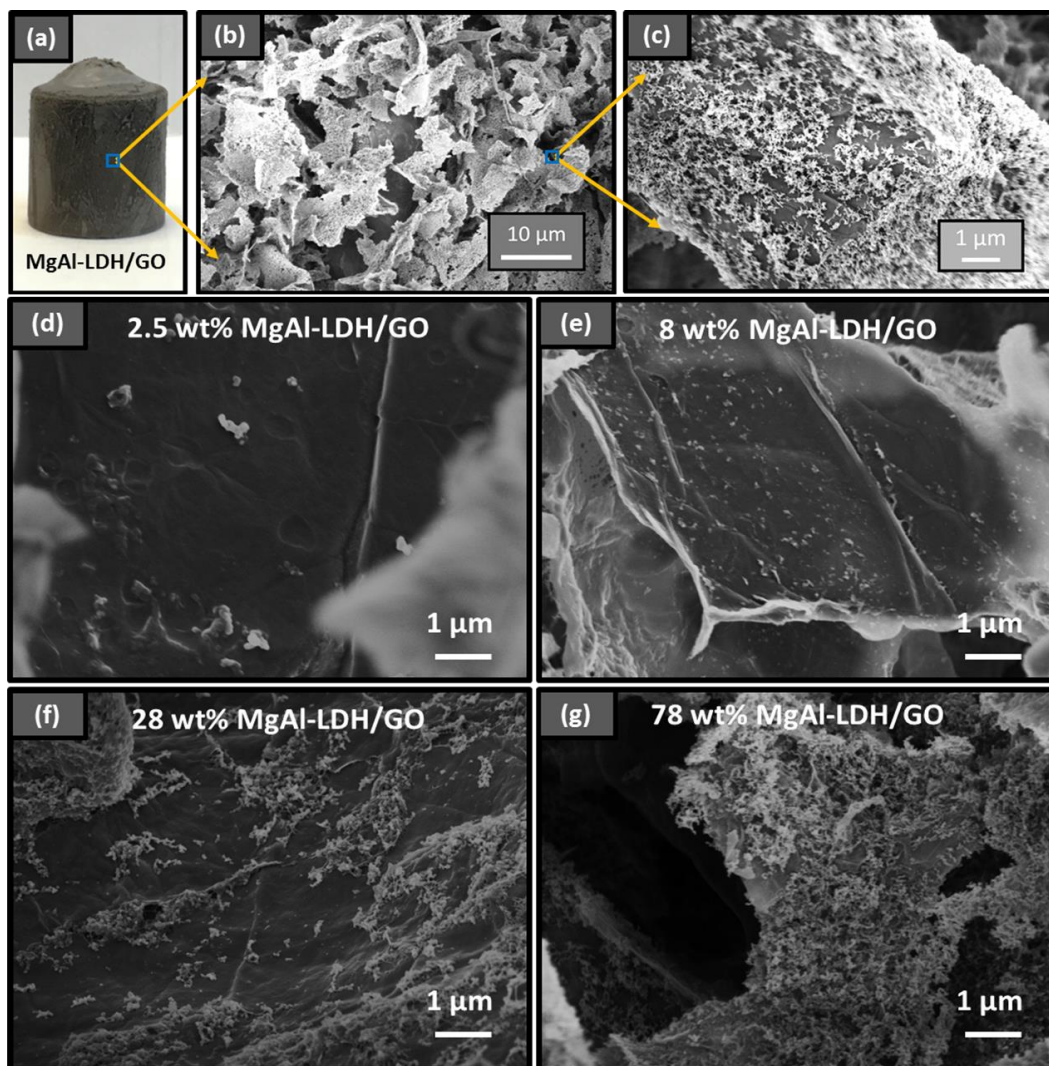


**Figure 4.4** (a) Digital image of an MgAl-LDH/GO aerogel monolith (78 wt% LDH loading) before thermal treatment. (b) - (c) SEM images of the internal microstructure and LDH-decorated GO surfaces for the same MgAl-LDH/GO aerogel (78 wt%). (d) - (g) SEM images showing MgAl-LDH nanoparticle decoration for MgAl-LDH/GO aerogels produced at different LDH loadings.

The LDH precursor particles are uniformly distributed onto the surface of GO sheets across the entire aerogel. As shown in Figure 4.4d-g, the spacing of the particles across the GO aerogel surfaces can be controlled through LDH loading. At 78 wt% LDH loadings the whole GO surface is fully covered with particles while some small spacings between particles remains. Due to this combination of high particle loading and good particle spacing, the 78 wt% MgAl-MMO/rGO aerogel was taken forward for further materials characterisation and the adsorption measurements, described in the rest of this chapter.

After high temperature thermal treatment, SEM imaging confirmed that the original microstructural morphology in the MgAl-LDH/GO aerogel (78 wt%) is well maintained (Figure 4.5). The SEM of the MgAl-MMO/rGO aerogel showed smaller particles ( $\sim 70$  nm, Figure 4.5c, Appendix 2 Figure A2.3), evenly distributed across the rGO surface at relatively high density. Lower magnification SEM showed larger internal pores of around  $30\ \mu\text{m}$  diameter (Figure 4.5b, Appendix 2 Figure A2.3). These macropores are due to ice-crystal growth induced by unidirectional freezing during fabrication and are likely to be beneficial for adsorption application, by aiding adsorbate diffusion to active sorption sites within the aerogel interior. TEM images of the hybrid aerogels show that the MgAl-MMO particles observed in SEM are clusters of smaller primary nanoparticles (10 - 20 nm, similar in size to the crystallite domain sizes observed via XRD) (see below Figure 4.5d-4.5f). TEM also visualises the relatively thin rGO sheets (Figure 4.5d), difficult to observe by SEM.

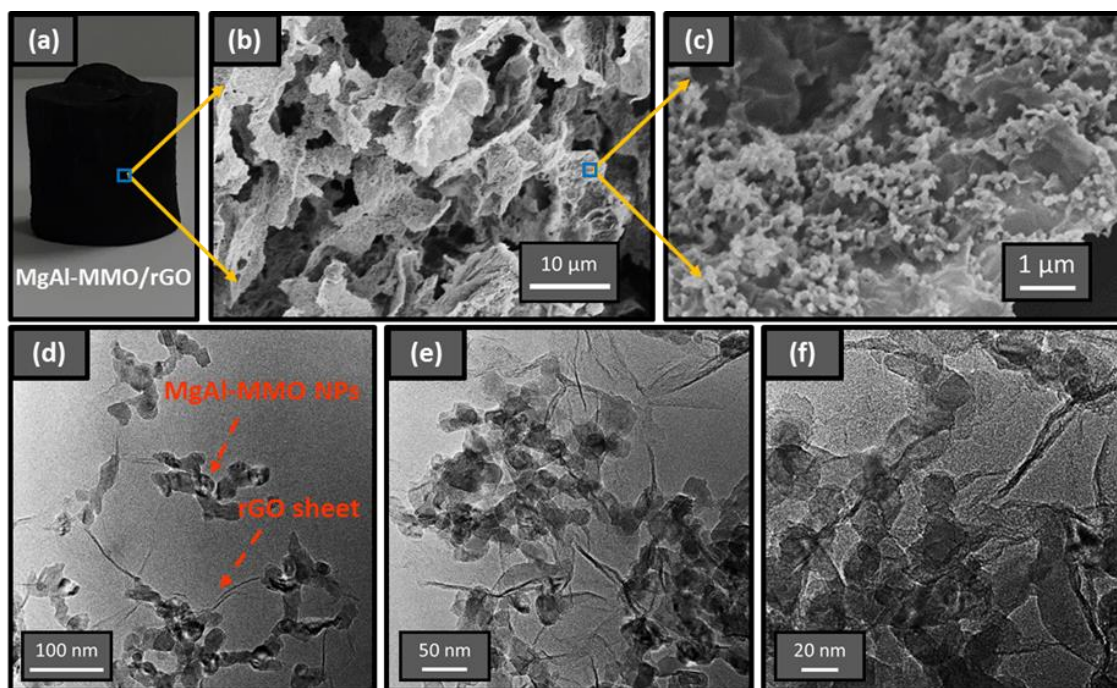


**Figure 4.5** (a) Digital image of a MgAl-MMO/rGO aerogel monolith. (b) and (c) SEM images of MgAl-MMO/rGO aerogel. (d) – (f) TEM images of the MgAl-MMO/rGO aerogel at different magnifications.

The nominal Mg:Al ratio (2:1) is controlled by the stoichiometry of the Mg and Al salts used during LDH synthesis. EDX line scanning and EDX mapping were used to experimentally measure atomic ratio of the final MgAl-MMO/rGO aerogels (see below Figure 4.6). The two EDX scanning techniques indicate an experimental atomic Mg:Al ratio of 1.8 and 1.9, respectively, close to the nominal ratio of 2:1. The EDX mapping also shows that Mg and Al are co-located and uniformly distributed across

the aerogel flake, further confirming uniform MgAl-MMO particle distribution (see below Figure 4.6a and Figure 4.6b).

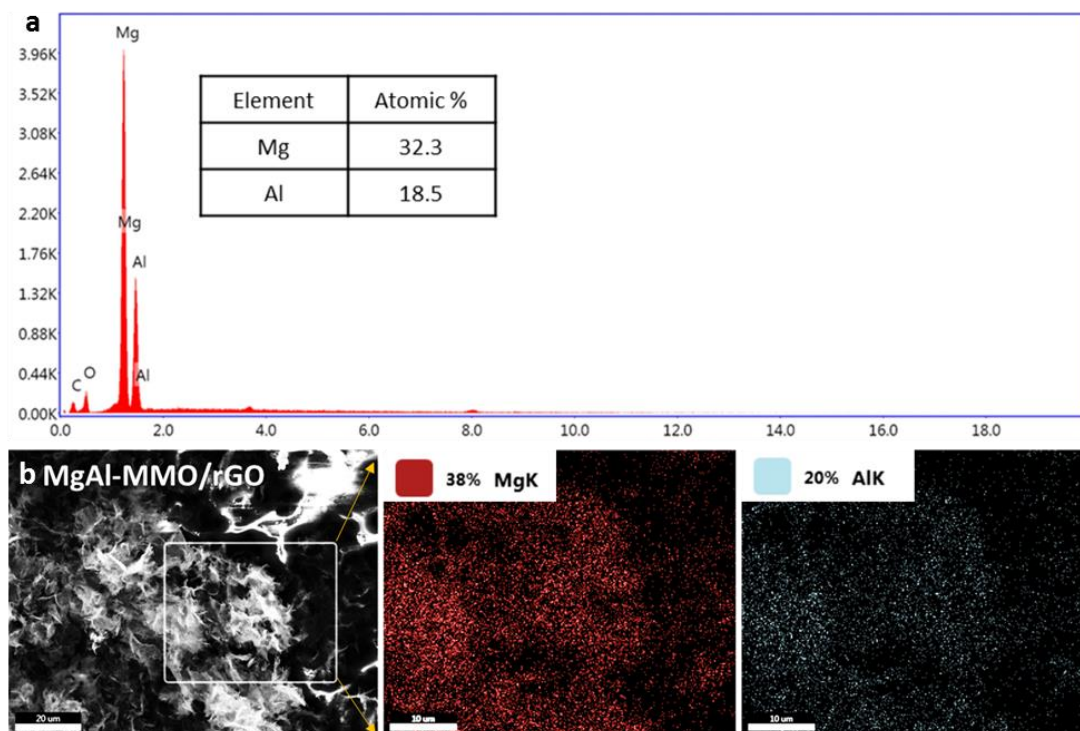


**Figure 4.6** (a) EDX line scan spectrum of MgAl-MMO/rGO aerogel. (b) EDX mapping of MgAl-MMO/rGO aerogel. The experimental atomic Mg:Al ratio is close to the nominal ratio of 2:1.

Formation of MgAl-LDH particles in Step 1 of our synthetic procedure is confirmed by XRD. As observed in Figure 4.7a, the XRD pattern of MgAl-LDH reference powder exhibits prominent hydroxalcite characteristic peaks at  $11.5^\circ$ ,  $23.2^\circ$ ,  $34.5^\circ$ ,  $38.4^\circ$ ,  $45.5^\circ$ ,  $60.6^\circ$  and  $61.9^\circ$  respectively, corresponding to (003), (006), (009), (015), (018), (110) and (113) crystal planes, consistent with reported studies and confirming successful formation of LDH particles.<sup>190</sup> The presence of the same peaks in the XRD pattern of MgAl-LDH/GO aerogel confirms that phase-pure LDH particles were successfully integrated into the GO aerogel.

Conversion of MgAl-LDH into MgAl-MMO particles upon thermal annealing in Step 3 can also be confirmed by XRD (Figure 4.7b). Specifically, a mixture of MgO and MgAl<sub>2</sub>O<sub>4</sub> is formed after thermal annealing, as evidenced by sets of characteristic periclase (MgO) and spinel (MgAl<sub>2</sub>O<sub>4</sub>) peaks, in line with well-known MgAl-LDH annealing transformations.<sup>190</sup>

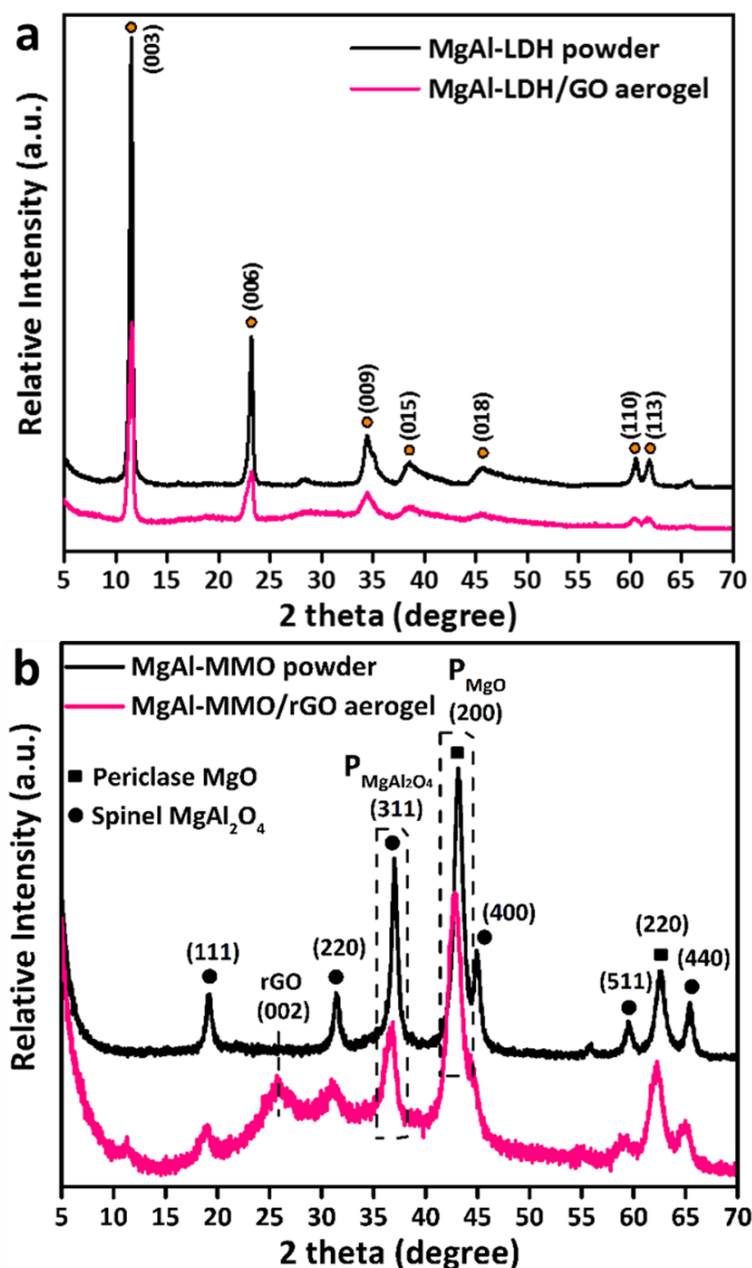


**Figure 4.7** (a) XRD patterns of MgAl-LDH powder and MgAl-LDH/GO aerogel. (b) XRD pattern of the MgAl-MMO powder and MgAl-MMO/rGO aerogel.

Scherrer analysis of the XRD peak widths indicates that the aerogel-supported nanoparticles exhibit almost 50 % smaller crystallite domain sizes compared to unsupported nanoparticles (7.4 nm vs 12.9 nm, see below Table 4.1), confirming that nanoparticle anchoring within the graphitic aerogel is strong and effectively inhibits sintering during annealing.

Interestingly, XPS analysis (Figure 4.8) also indicates strong interactions between the graphitic aerogel framework and the MMO nanoparticles. While the MgAl-MMO powder exhibits Mg1s and Al2p peaks at 1032.5 eV and 74.6 eV (characteristic for Mg and Al oxides),<sup>277, 278</sup> the MgAl-MMO/rGO aerogels exhibit noticeably shifted

peaks, suggesting charge transfer between the rGO surfaces and the MgAl-MMO particles.

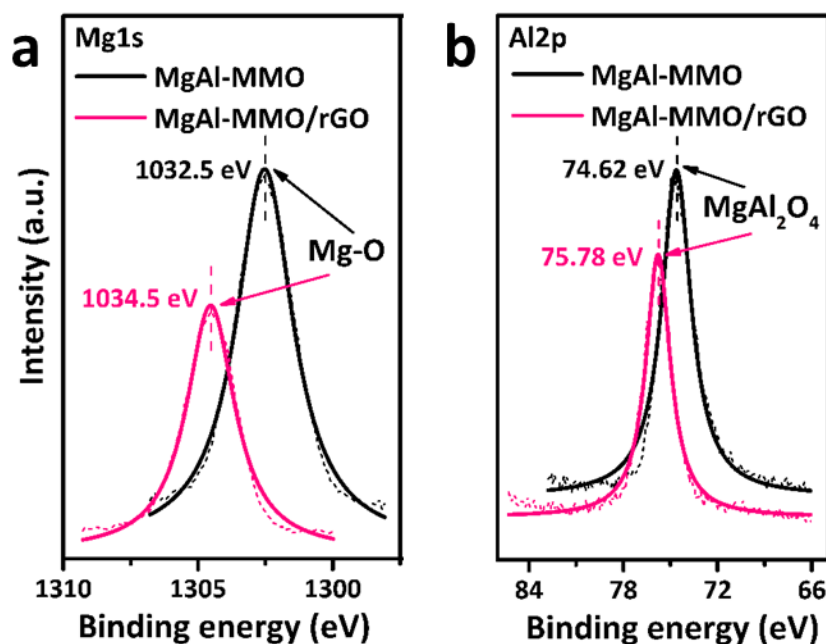


**Figure 4.8** High-resolution Mg1s (a) and Al2p (b) XPS spectra of MgAl-MMO powder and MgAl-MMO/rGO aerogel.

**Table 4.1** Materials characteristics of MgAl-MMO powder (pure, unsupported MgAl-MMO nanoparticles) and MgAl-MMO/rGO hybrid aerogel (MgAl-MMO nanoparticles supported within rGO aerogels at a weight loading of 78 wt%).

Sorbent	Density (mg·cm <sup>-3</sup> )	Conductivity (S·m <sup>-1</sup> )	MMO size (XRD) <sup>a)</sup> (nm)	MMO size (SEM) <sup>b)</sup> (nm)	SSA (BET) (m <sup>2</sup> ·g <sup>-1</sup> )	Mesopore size <sup>c)</sup> (nm)
MgAl-MMO powder	756.5	0	12.9	131	49.7	30
MgAl-MMO/rGO aerogel	18.3	15	7.4	68	96.8	52

<sup>a)</sup>Crystallite domain sizes, as derived from the (311) MgAl<sub>2</sub>O<sub>4</sub> XRD peak widths (Figure 4.7b); <sup>b)</sup>Average size of MMO particles, as measured by SEM (Appendix 2, Figure A2.3 and A2.4); <sup>c)</sup>Average mesopore diameters, as derived from the BJH mesopore size distributions (Figure 4.10b).

The thermal annealing treatment also successfully re-graphitises GO into an interconnected, electrically conducting rGO framework. The successful formation of rGO is indicated by the characteristic (002) reflection at 26.3° in the XRD pattern of the final hybrid aerogel (Figure 4.7b). Scherrer analysis suggests that the rGO aerogel support framework consists of few-layer rGO (five rGO sheets per average stack, see Appendix 2 Figure A2.2).<sup>279</sup> Significant increase in the graphiticity of the graphene oxide support framework is confirmed by Raman spectroscopy, as indicated by a marked increase in *I<sub>D</sub>*/*I<sub>G</sub>* ratio from 0.98 to 1.42 (Figure 4.9); consistent with Raman studies of thermally-treated GO in the literature.<sup>226, 280, 281</sup> Importantly, re-graphitisation upon thermal treatment results in the restoration of electrical

conductivity. Even at very high contents of (electrically-insulating) MgAl-MMO, the hybrid aerogel exhibits excellent electrical conductivity of up to  $15 \text{ S}\cdot\text{m}^{-1}$ , thereby opening up routes for framework-mediated electrical stimulation and electrical-heating of the supported nanoparticles.

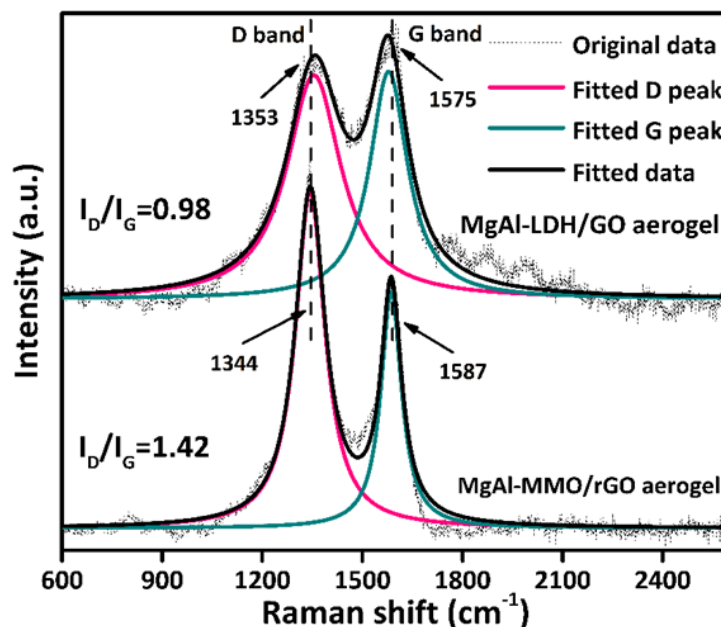


**Figure 4.9** Raman spectra of initial MgAl-LDH/GO aerogel (product of Step 2) and final MgAl-MMO/rGO aerogel (Product of Step 3).

BET measurements (as shown in Figure 4.10a) suggest excellent nanoparticle dispersion on the 3D rGO network and minimised particle aggregation, even at high MMO loadings, as indicated by an almost 100 % larger specific surface area of the aerogel-supported MgAl-MMO particles compared to the unsupported powder. The MgAl-MMO/rGO aerogel also exhibits a considerably broader mesopore distribution (Figure 4.10b) with a larger mean mesopore size ( $d_{mesopore} \sim 50 \text{ nm}$ ), compared to the unsupported powder adsorbents ( $d_{mesopore} \sim 30 \text{ nm}$ , see above Table 4.1), indicative of a more spaced, less aggregated nanoparticle morphology in the hybrid aerogels.

These materials characterisation measurements show that the rGO aerogel provide a number of important structural improvements for the supported MMO particles, including larger specific surface area, smaller particle size and larger porosity (see above Table 4.1), confirming the excellent stabilising support function of the rGO aerogels (important for the sorption applications explored in the next section).

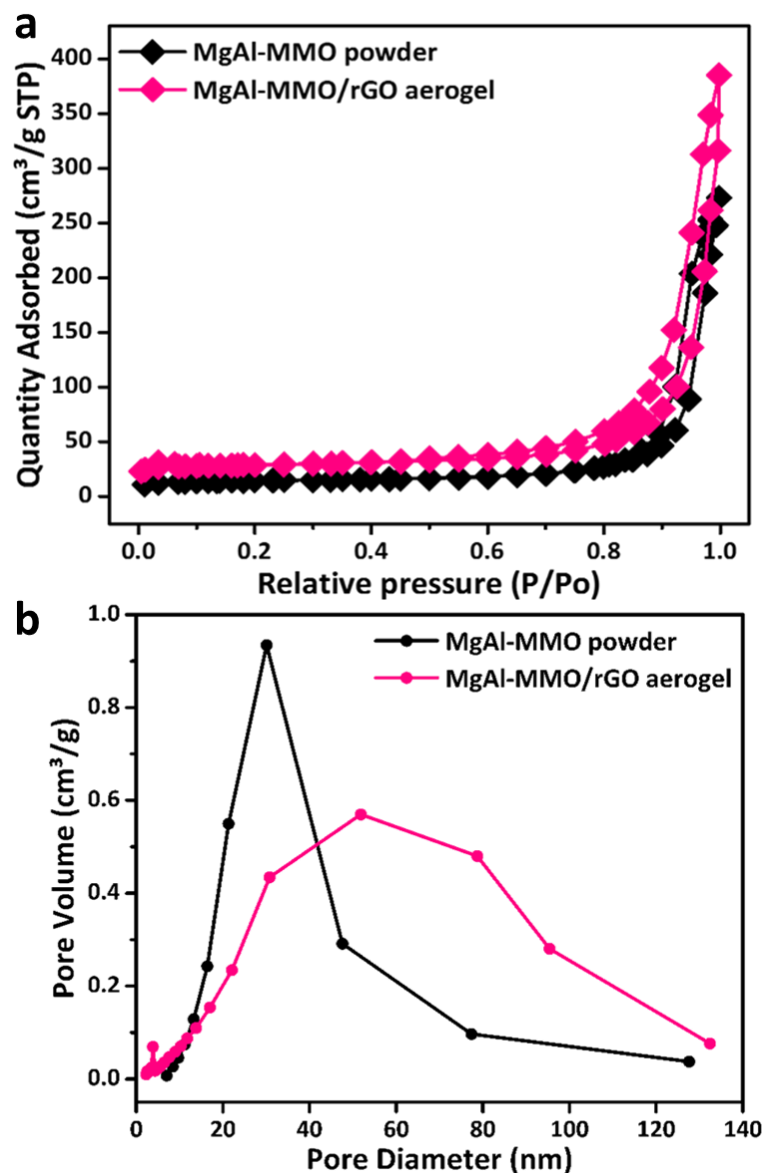


**Figure 4.10** (a) BET  $N_2$  adsorption-desorption isotherms of the MgAl-MMO powder and the MgAl-MMO/rGO aerogel. (b) corresponding BJH pore-size distributions.

Importantly, the synthetic methodology used to introduce MgAl-MMO can be easily adapted to introduce other types of nanoparticles, such as MNP, which have a wide range of applications beyond sorption, including as heterogeneous catalyst systems and supercapacitor electrodes. CuAl-MNP and NiAl-MNP systems were also synthesised from their respective LDH precursor particles. Thermal treatment in Step 3 results in the complete reduction of the LDH precursor particles into copper and nickel metal nanoparticles (as confirmed by XRD, see Figure 4.11) under the thermal treatment conditions. (Reduction of the aluminium is unlikely under these conditions and is potentially present as amorphous aluminium oxide.)<sup>282</sup> As observed for the MgAl-based particle system, the obtained Cu and Ni MNP crystal domain sizes (as determined via Scherrer analysis of the corresponding XRD peak widths) are also

considerably smaller in the aerogels compared to MNP powders (Table 4.2 and Table 4.3), confirming that rGO aerogels are also suitable to decrease the sizes of other nanoparticle types.

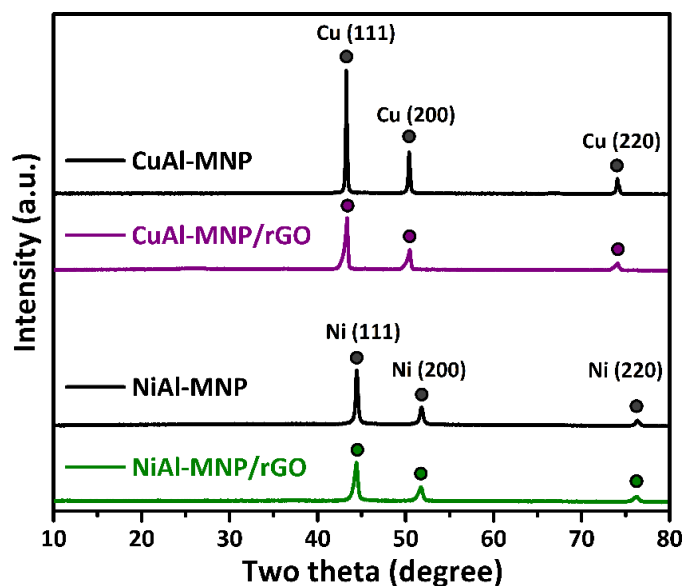


**Figure 4.11** XRD of CuAl-MNP powder and NiAl-MNP powder, and the corresponded rGO hybrid aerogels.

**Table 4.2** Materials characteristics of CuAl-MNP/rGO aerogels (78 wt% CuAl-MNP loading) and NiAl-MNP/rGO aerogel (88 wt% NiAl-MNP loading).

Hybrid Aerogel	Density (mg·cm <sup>-3</sup> )	Conductivity (S·m <sup>-1</sup> )	MNP size (XRD) <sup>a</sup> (nm)	SSA aerogel (m <sup>2</sup> ·g <sup>-1</sup> )	Mesopore size <sup>b</sup> (nm)
CuAl-MNP/rGO aerogel	35.2	7.7	24.2	65.9	40
NiAl-MNP/rGO aerogel	44.3	0.2	19.9	52.6	12

<sup>a</sup>) Crystal domain sizes, as derived from the (111) fcc XRD peak widths (Figure 4.11); <sup>b</sup>) Average mesopore diameters, as derived from the BJH mesopore size distributions (see Appendix 2, Figure A2.5)

**Table 4.3** Structural characterisation and organosulfur sorption capacities of LDH-derived metal nanoparticles (MNP) in their pure and aerogel-supported form.

LDH derivatives	MNP surface area <sup>a</sup> (m <sup>2</sup> ·g <sup>-1</sup> )	MNP crystal domain size <sup>b</sup> (nm)	MNP loading in rGO aerogel <sup>c</sup> (wt %)	DBT Uptake MNP Powder <sup>d</sup> (mg·S·g <sup>-1</sup> MNP)	DBT Uptake MNP/rGO Aerogel <sup>d</sup> (mg·S·g <sup>-1</sup> MNP)	Uptake increase (%)
NiAl-MNP	48.1	31.2	88	0.45	0.61	36
CuAl-MNP	23.3	51.7	78	0.17	0.83	388

<sup>a</sup>) Specific Surface Area as determined by BET measurements of the MNP powder. <sup>b</sup>) Crystal domain size, as determined via Scherrer analysis of the (111) XRD peak. <sup>c</sup>) as determined from TGA measurements of MNP/rGO aerogels in oxidative atmosphere. <sup>d</sup>) as determined via batch DBT sorption measurements (uptake from 500 ppm DBT in n-octane solution).

The metallic Cu and Ni nanoparticles can also be supported at high weight loadings within the rGO aerogels (78 wt% and 88 wt%, as indicated by TGA, Appendix 2 Figure A2.6). As with the MgAl-MMO particles, the Cu and Ni nanoparticles are uniformly distributed across the aerogel as indicated by SEM imaging and EDX mapping of aerogel flakes sampled from the core of the respective aerogel monoliths (see below Figure 4.12).

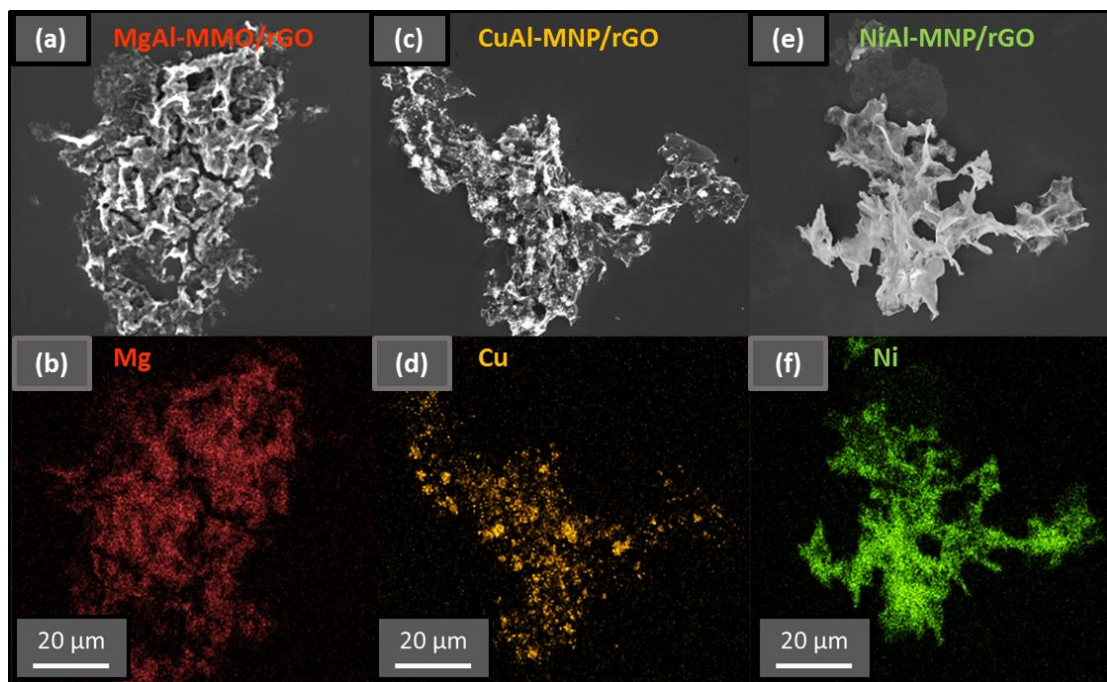


**Figure 4.12** SEM images of the aerogel flakes sampled from the cores of (a) MgAl-MMO/rGO aerogel, (c) CuAl-MNP/rGO aerogel, and (e) NiAl-MNP/rGO aerogel, and EDX mapping of the corresponding (b) Mg, (d) Cu, and (f) Ni distributions.

Both the CuAl-MNP/rGO and NiAl-MNP/rGO aerogels exhibit excellent electrical conductivity ( $7.7 \text{ S}\cdot\text{m}^{-1}$  and  $0.2 \text{ S}\cdot\text{m}^{-1}$ , see above Table 4.2) and repeatable I-V characteristics (Figure 4.13a), highlighting the suitability and stability of the hybrid aerogel systems for electrical heating applications. Interestingly, the NiAl-MNP/rGO aerogels also showed clear magnetic properties (Figure 4.13b), a unique additional functionality of the Ni-based hybrid aerogel systems, that could be highly beneficial in sorption application (e.g. by enabling simple magnetic recovery of spent aerogel sorbents). These findings demonstrate the general applicability of our synthetic approach to produce a wide range of electrically-conducting (and hence electrically-heatable) aerogel-supported nanoparticle systems for different applications.

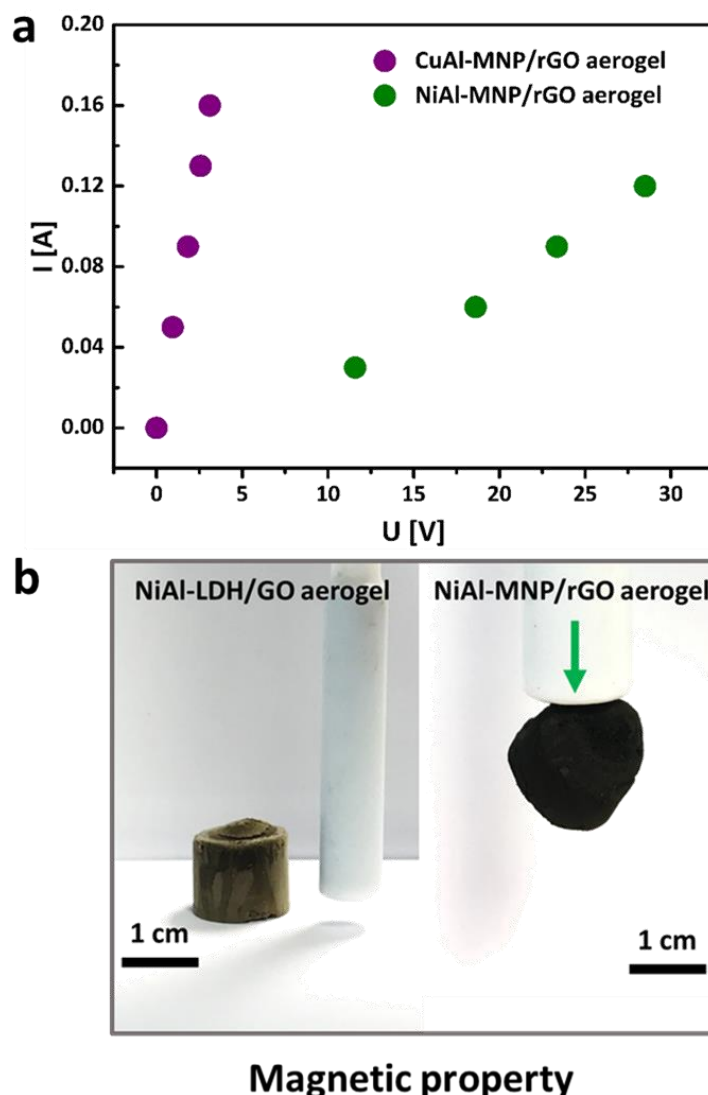


**Figure 4.13** (a) I-V characteristics of the CuAl-MNP/rGO aerogel and the NiAl-MNP/rGO aerogel. (b) Digital images of the initial NiAl-LDH/GO aerogel and the final NiAl-MNP/rGO aerogel next to a magnet.

### 4.2.3 Liquid-phase organosulfur sorption

In a first set of experiments, the MgAl-MMO/rGO hybrid aerogels were assessed via liquid-phase organosulfur sorption experiments, specifically, the adsorption of DBT from n-octane solution. DBT sorption provides an excellent model system to assess sorption-related benefits imparted by rGO aerogel supports on inorganic nanoparticles across a broad spectrum of important sorption characteristics, including uptake capacities, sorption kinetics, sorption isotherms, selectivity and sorbent re-cycling.

In terms of equilibrium capacity (at 500 ppm initial organosulfur concentration), the DBT uptake of the aerogel-supported MgAl-MMO was more than double compared to the unsupported nanoparticles (Figure 4.14, see below Table 4.4), in line with the

larger surface area and improved particle dispersion of the hybrid aerogel samples. The isotherms for DBT adsorption onto the MgAl-MMO powder and MgAl-MMO/rGO aerogel adsorbents both show an excellent fit with the Langmuir model, indicating DBT monolayer formation, in line with a cation- $\pi$  interaction mechanism between the aromatic organosulfur and the MMO nanoparticles (as shown in Figure 4.14). The corresponding maximum DBT uptake capacity of MgAl-MMO/rGO aerogel is around  $1.7 \text{ mg}\cdot\text{S}\cdot\text{g}^{-1} \text{ MMO}$  (Appendix 2 Table A2.2), which is around 130 % higher compared to that of the unsupported MgAl-MMO. In contrast, the Langmuir fitting parameter  $K_L$  (related to the sorption energy) has a similar value for both adsorbents, confirming that the introduction of rGO aerogel supports has no significant effect on DBT sorption strength or mechanism. These findings suggest that improvements in DBT uptake are mainly due to a higher concentration of accessible sorption sites for the rGO supported nanoparticles, in line with the improved nanoparticle dispersion observed in the aerogel-based sorbent samples.

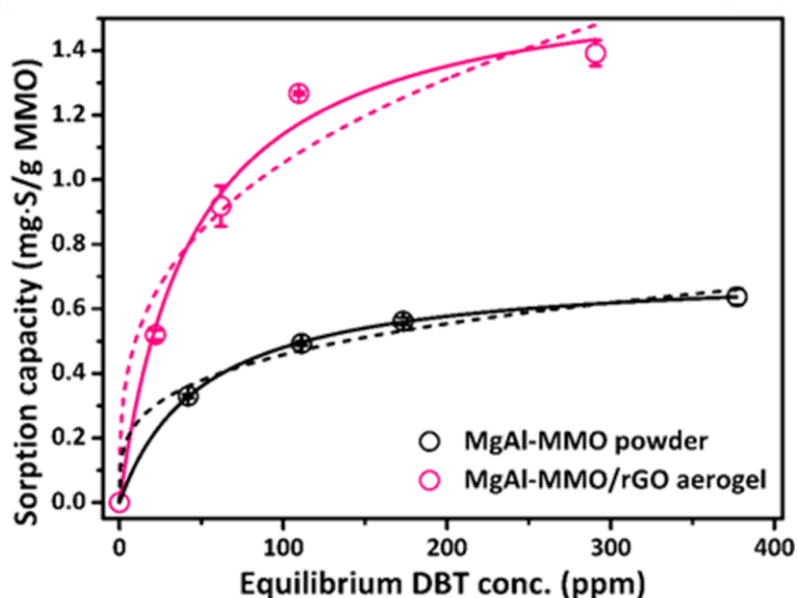


**Figure 4.14** Uptake isotherms for sorption of DBT from n-octane (initial concentrations tested at 100 ppm, 200 ppm, 300 ppm and 500 ppm, respectively). The dash line is fitted via Freundlich model and the solid line is fitted via Langmuir model.

Interestingly, a large increase in equilibrium capacity (123 % increase) is also observed for the uptake of 4,6-dimethyldibenzothiophene (4,6-DMDBT) (see Figure 4.15), a sterically hindered organosulfur that is particularly difficult to remove via conventional desulfurisation processes.<sup>57</sup> It is worth noting that pure rGO aerogels (i.e. rGO aerogels without any nanoparticle loading) exhibited no measurable DBT or DMDBT uptake, i.e. there is no significant organosulfur sorption onto the rGO framework itself. The observed improvements in adsorption performance therefore exclusively stem from improved particle dispersion on the open, high-surface-area

nanocarbon framework and the resulting higher concentration of accessible MMO sorption sites.

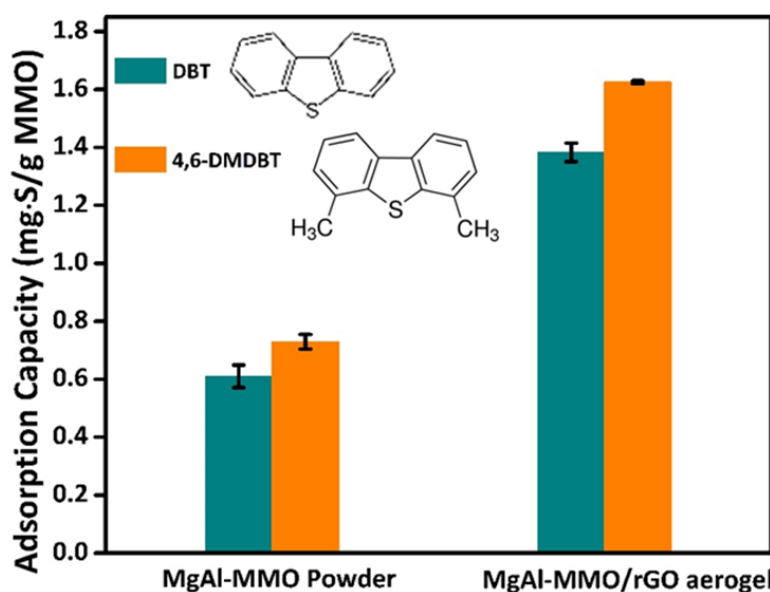


**Figure 4.15** Liquid-phase organosulfur sorption characteristics of MgAl-MMO/rGO aerogels, compared to MgAl-MMO powders: Equilibrium uptake capacities for sorption of DBT and DMDBT from n-octane (initial concentration 500 ppm).

**Table 4.4** Relative enhancements in liquid-sorption characteristics of MgAl-MMO/rGO aerogels (sorbent nanoparticles supported within rGO aerogels, loading fraction 78 wt%) compared to MgAl-MMO powder (unsupported sorbent nanoparticles), as measured via DBT uptake from n-octane solution (500 ppm DBT, 20 °C).

Sorbent	CAPACITY	KINETICS	SELECTIVITY	RECYCLABILITY
	DBT equilibrium uptake <sup>a</sup> (mg·S·g <sup>-1</sup> MMO)	DBT sorption rate constant <sup>b</sup> (10 <sup>-3</sup> g·mg <sup>-1</sup> ·h <sup>-1</sup> )	DBT Selectivity against BP <sup>c</sup> (%)	Capacity retention after 3 regeneration cycles <sup>d</sup> (%)
MgAl-MMO powder	0.64	6	84%	16%
MgAl-MMO/rGO aerogel	1.39	195	87%	95%
RELATIVE ENHANCEMENT	Capacity increase by 117%	Kinetics accelerated by a factor of 32	Selectivity remains high	Regeneration stability improved by a factor of 6

<sup>(a)</sup> DBT uptake from n-octane after 120 h (see Figure 4.15); <sup>(b)</sup> rate constant of adsorption kinetics fitted to pseudo-second-order model (see Figure 4.16); <sup>(c)</sup> as determined from competitive sorption of DBT/BP mixtures from n-octane (see Figure 4.17b; selectivity = molar DBT uptake relative to combined molar uptake of DBT and BP); <sup>(d)</sup> as determined from repeated sorbent re-use after thermal regeneration at 250 °C via Joule heating (see Figure 4.23, capacity retention = DBT uptake after 3 regeneration cycles relative to initial DBT uptake).

Beyond these marked improvements in capacity, the rGO aerogels also induce substantial improvements in other important sorption characteristics, such as

kinetics and recycling stability, without diminishing the high organosulfur selectivity of the MgAl-MMO system. In terms of sorption kinetics, the MgAl-MMO/rGO aerogel sorbents show a remarkable acceleration in organosulfur uptake, more than 30 times faster compared to the unsupported powder (as determined from the pseudo-second-order fit of the uptake kinetics, Figure 4.16, see above Table 4.4). This dramatic acceleration is likely caused by significantly improved diffusion of the organosulfur adsorbates into the MMO/rGO aerogel adsorbents, due to a combination of large, open macroporosity (as observed by SEM) and an increased average mesopore size (as observed by BET), facilitating mass transfer both on the macro- and micro-scale.

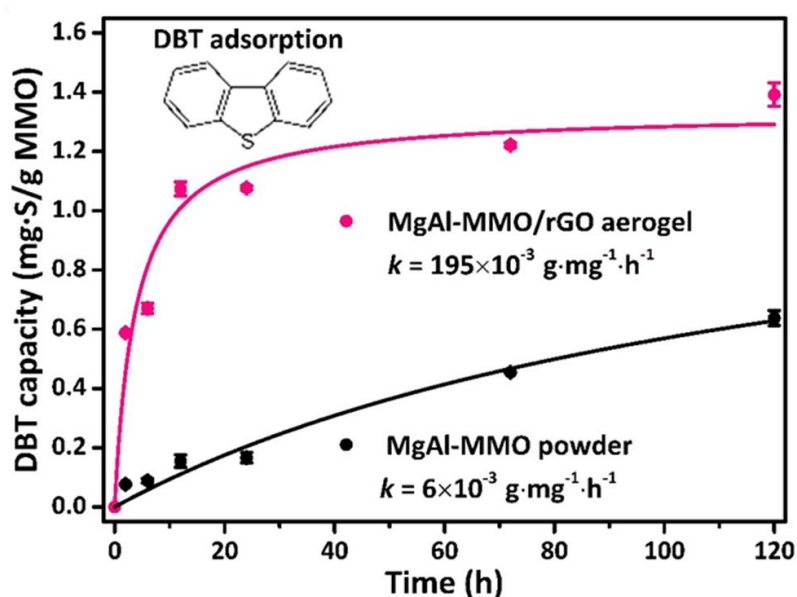


**Figure 4.16** Uptake kinetics for sorption of DBT from n-octane (initial concentration 500 ppm).

In terms of practically very important organosulfur selectivity, competitive adsorption experiments, using DBT/biphenyl mixtures (molar ratio 1:1), were tested. Biphenyl (BP), a common hydrocarbon impurity, was tested as a competitive adsorbate to DBT to provide first evidence that our MgAl-MMO/rGO aerogel materials show preferential binding to aromatic sulfur compounds, important for practical applications of desulfurisation sorbents in complex hydrocarbon mixtures and fuels. The BP competitor has been carefully chosen in that it is structurally very similar to DBT: the biphenyl structure can be thought of as the DBT structure without the sulfur atom (Figure 4.17a). In addition, BP is practically important as it is a common aromatic impurity in light fuels. When studying MgAl-MMO/rGO aerogel sorbents in hydrocarbon solution of DBT/BP mixtures, strongly preferential DBT sorption is observed, namely the presence of sulfur-free aromatics does not interfere with the efficient and selective uptake of DBT (Figure 4.17b, see above Table 4.4).

This is in strong contrast to sorption from binary mixtures of organosulfurs (e.g. DBT/DMDBT mixtures) where strong sorption of both organosulfurs are observed (see above Figure 4.15). This provides first evidence for practically-important, high organosulfur selectivity in the hybrid aerogel materials.

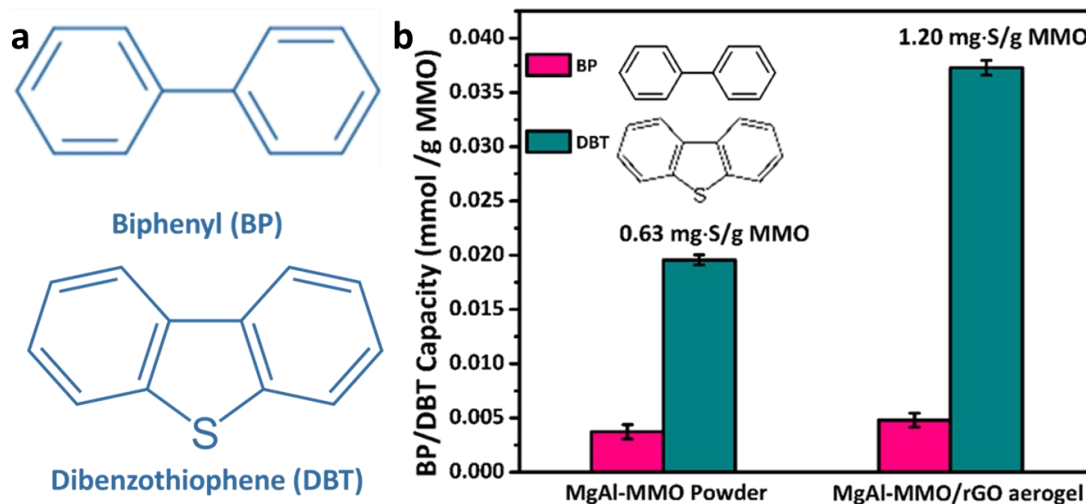


**Figure 4.17** (a) Molecular structures of biphenyl and dibenzothiophene. (b) Organosulfur selectivity: DBT uptake capacities from *n*-octane (initial concentration 500 ppm) in the presence of biphenyl (initial concentration 500 ppm).

In terms of sorbent recycling, the stabilising effect of the rGO framework allows for highly-effective thermal (temperature-swing) regeneration of the MMO nanoparticles. The recycled MgAl-MMO/rGO aerogel sorbents show excellent, high retention of DBT uptake capacity upon thermal regeneration at 250 °C via Joule heating (retention of almost 95 % of the original DBT capacity after three regeneration cycles), in contrast to the poor capacity retention (only 16 %) of the unsupported MgAl-MMO powders (see above Table 4.4). In addition, the monolithic shape of the hybrid aerogels also allows for easy recovery of the spent sorbent from solution, another benefit for liquid-phase sorption application due to the avoidance of lengthy or energy-intensive separation methods.

It is worth mentioning, that improvements are also observed for the CuAl-MNP/rGO aerogel and NiAl-MNP/rGO aerogels (see above Table 4.3). In terms of DBT sorption capacity, significant uptake increases by up to 390 % were observed when supporting these nanoparticle types within rGO aerogels. Further characterisation of sorption characteristics (kinetics, selectivity, regenerability) were not carried out as the absolute capacity values are relatively low (as expected due to the absence of metal cations in these metallic nanoparticles). However, the consistently observed enhancement in sorption capacity across different particle systems clearly confirms the generic benefits of supporting LDH-derived nanoparticles within rGO aerogels in terms of improved sorption-site accessibility and stabilisation against nanoparticle

deactivation, relevant to other important applications beyond sorption such as catalysis or energy storage.

### 4.2.3 Thermal sorbent regeneration via electrical framework heating

Apart from its stabilising function, the rGO aerogel supports also provide important additional functionality, including the capability for electrical nanoparticle heating. Electrical heating is enabled by the excellent electrical conductivity of the interconnected 3D rGO support framework (even at high particle loadings) as well as the aerogels' defined monolithic shape and robust mechanical properties (allowing easy contacting with macroscopic electrodes, Figure 4.18a).

Using the electrode setup described in Chapter 2, a model hybrid aerogel (MgAl-MMO/rGO aerogel) was electrically heated up to 400 °C in N<sub>2</sub> atmosphere (Figure 4.18).

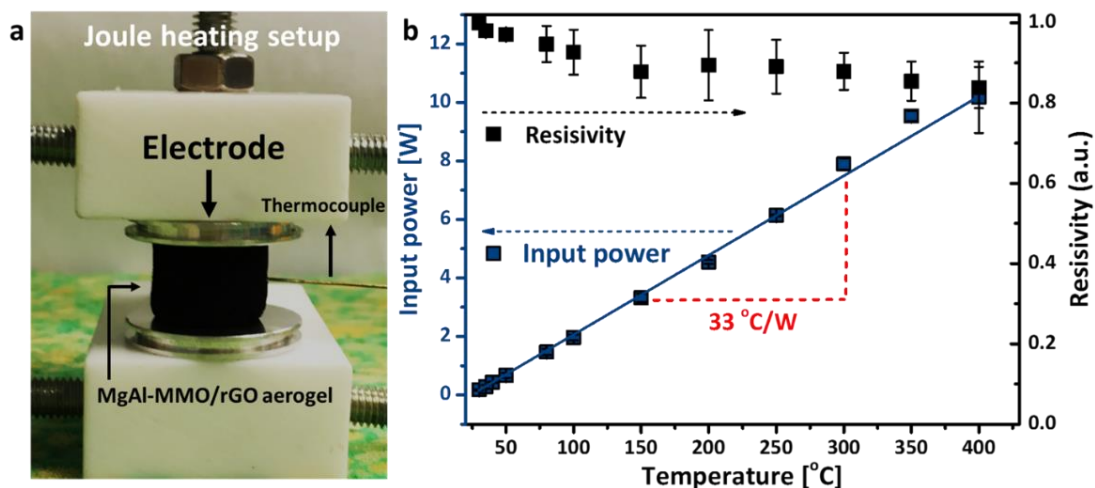


**Figure 4.18** Digital images of an MgAl-MMO/rGO aerogel (78 wt% nanoparticle loading) in a Joule heating set-up. (b) Relationship between electrical input power and aerogel Joule-heating temperature (measured at the aerogel surface); the right-hand y-axis shows the relative electrical through-volume resistivity of the aerogels at different Joule-heating temperatures.

The Joule-heating temperature of the MgAl-MMO/rGO aerogels scales linearly with electrical power input, enabling repeatable and accurate nanoparticle temperature control over a wide temperature range through simple adjustment of power input (Figure 4.18b). The Joule-heating efficiency for the MgAl-MMO/rGO aerogels, as indicated by the gradual change of temperature with electrical power input,  $dT/dP$ , is high at 33 °C·W<sup>-1</sup> (52 °C·W<sup>-1</sup> for the pure rGO aerogel in Chapter 3), which is on the same order of magnitude as observed for the Joule-heating of pure, nanoparticle-free rGO films and aerogels of similar dimensions.<sup>31, 283</sup> Small, reversible changes in electrical resistivity (reduction by about 20 % at 400 °C) are observed at higher

temperatures (Figure 4.18b) and suggest minor structural changes in the hybrid aerogels upon heating (thermal expansion, desorption of ambient impurities etc.). However, these resistivity changes are fully reversible upon cooling and do not impact on the repeatability of the linear Joule heating behaviour.

The thermal conductivity (determined via radial temperature measurements described in Chapter 3) show only minor variation over the Joule heating temperature range investigated here (25-400 °C, Figure 4.19a), further evidencing that the MgAl-MMO/rGO aerogel is an electrically and thermally stable system. Once a set temperature is reached (often within seconds, see also Figure 4.19b), the Joule heating temperature remains extremely stable. To demonstrate this temperature stability, MgAl-MMO/rGO aerogels were electrically-heated to 300 °C and 400 °C (application-relevant temperatures, linked to the thermal activation of CO<sub>2</sub> adsorption and CO<sub>2</sub> desorption on MgAl-MMO, as mentioned below) over repeated long periods of up to one hour (Figure 4.19c). The resulting temperature profile shows that the aerogels can reliably be heated to very stable temperatures, rendering temperature control via framework Joule heating highly feasible for practical applications (Figure 4.19).

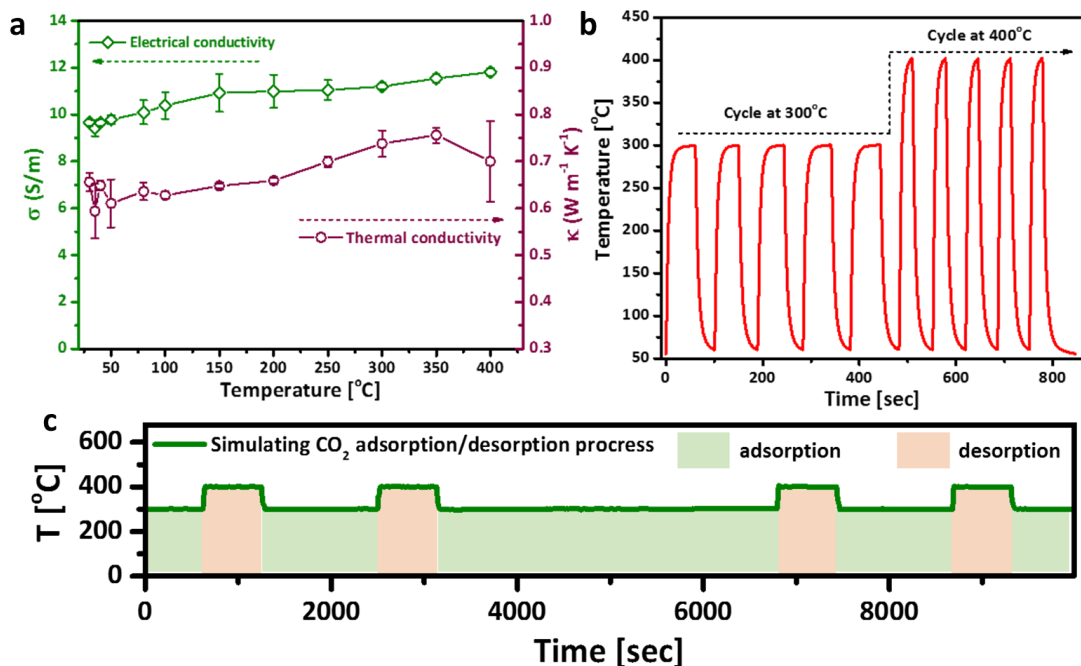


**Figure 4.19** Joule-heating related characteristics of MgAl-MMO/rGO aerogels: (a) Electrical conductivity ( $\sigma$ ) and thermal conductivity ( $\kappa$ ) of the MgAl-MMO aerogel at different Joule heating temperatures and, (b) Rapid thermal cycling of MgAl-MMO/rGO aerogel between 300 °C and 400 °C via Joule heating. (c) Joule-heating temperature stability of MgAl-MMO/rGO aerogel over extended time periods at temperatures relevant to MMO applications in pre-combustion CO<sub>2</sub> capture.

In order to demonstrate practical utility, Joule heating was employed to thermally regenerate MgAl-MMO/rGO aerogel sorbents after DBT adsorption (Figure 4.20). Conventionally, solid organosulfur sorbents are regenerated via washing at elevated temperatures (consuming large volumes of organic solvents) or through external sorbent heating in a furnace (consuming large amounts of energy). Here, Joule heating of the rGO aerogel framework (not possible for unsupported, electrically-insulating metal oxide sorbents) was exploited as an alternative regeneration approach with much lower energy cost.

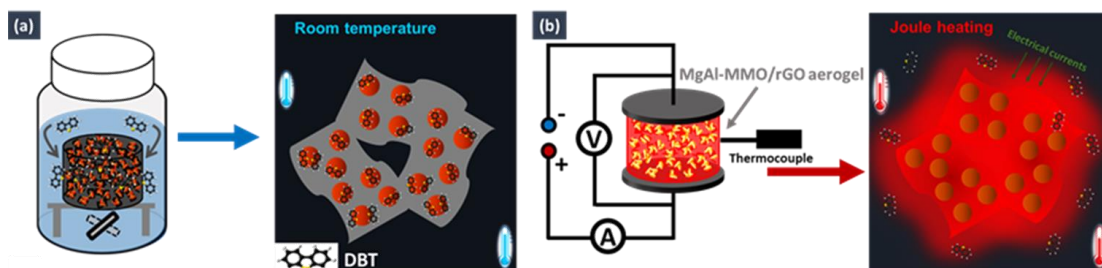


**Figure 4.20** (a) Schematic description of liquid-phase DBT adsorption onto a hybrid aerogel monolith; (b) Schematic representation of Joule-heating regeneration of a hybrid aerogel sorbent after DBT adsorption.

Joule heating of post-sorption MgAl-MMO/rGO aerogel sorbents to 250 °C (electrical current input 1 A) resulted in a very successful sorbent regeneration (purple curve in Figure 4.21).

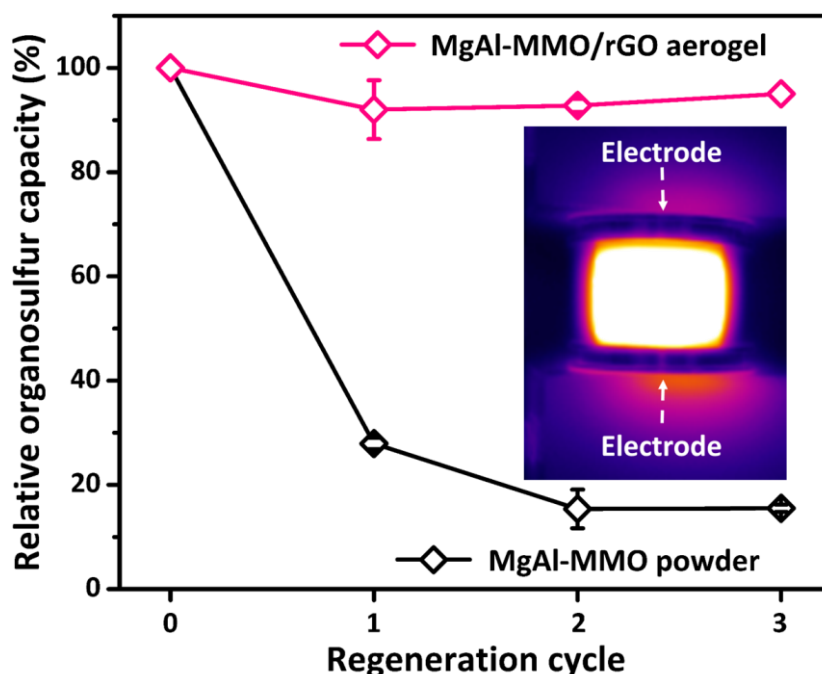


**Figure 4.21** Joule heating regeneration of exhausted MgAl-MMO/rGO hybrid aerogel sorbents. Thermal regeneration stability of MgAl-MMO powder (regenerated in a Muffle furnace, black curve), and MgAl-MMO/rGO aerogel (regenerated via Joule-heating, purple curve); insert: thermal image of the Joule-heated MgAl-MMO/rGO aerogel.

XPS analysis confirms complete removal of the organosulfur adsorbates after Joule-heating as indicated by the disappearance of a characteristic, DBT-related peak in the XPS C1s spectrum (Figure 4.22a). The regenerated MgAl-MMO/rGO aerogel sorbents can be readily re-used in new adsorptive DBT removal experiments. Importantly, the organosulfur capacity remains very high (around 90 % of the initial capacity) over repeated Joule heating regeneration cycles (Figure 4.21), highly beneficial for real-life applications.

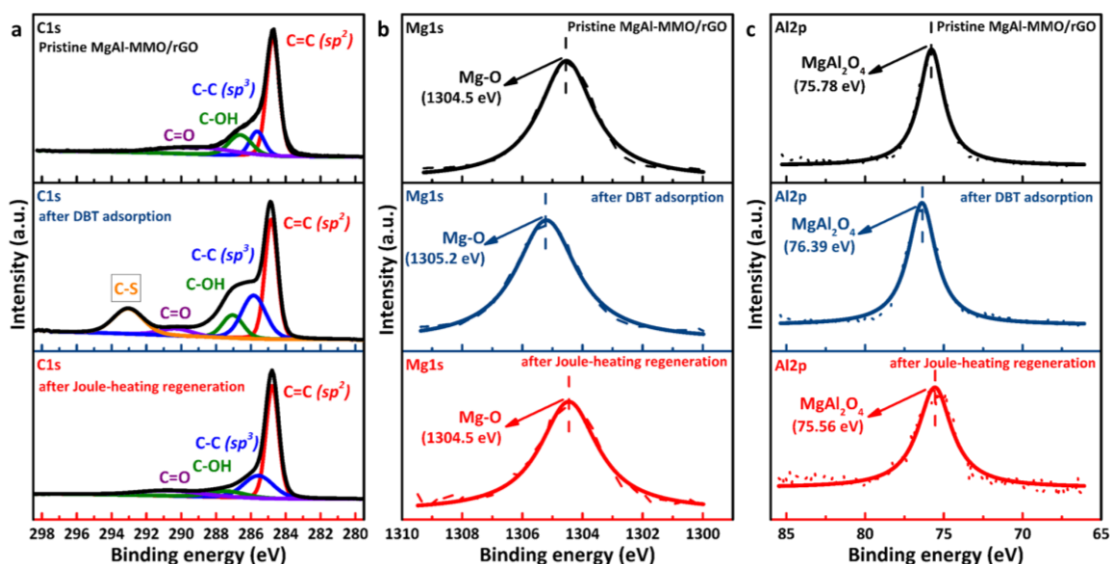


**Figure 4.22** XPS analysis of the MgAl-MMO/rGO aerogel sorbent in its pristine state (as-synthesised sorbent), post-sorption state (i.e. sorbent after maximum adsorptive DBT uptake from n-octane), and post-regeneration state (i.e. after Joule-heating regeneration of the post-sorption sorbent): a) C1s, b) Mg1s and c) Al2p high-resolution XPS spectra.

XPS analysis of the hybrid MgAl-MMO/rGO aerogel before and after regeneration confirms that Joule heating regeneration can be carried out without degradation of the sorbent system. For example, a shift of the Mg1s and Al2p XPS peaks observed after DBT adsorption (likely due to adsorbate-induced charge transfer) is fully reversed upon Joule heating regeneration, suggesting that the MMO particles are restored to their original (pre-sorption) chemical state (Figures 4.22b and 4.22c). Similarly, XPS and Raman analyses confirm that Joule heating regeneration does not cause any oxidative damage to the rGO aerogel support framework, as indicated by an unchanged fraction of  $sp^2$  carbon (XPS, Figure 4.22a and see Appendix 2, Table A2.5)<sup>284</sup> and an unchanged  $I_D/I_G$  ratio (Raman, Appendix 2 Figure A2.9) before and after regeneration. Importantly, direct electrical heating ( $\sim 0.9$  W·h) also allows for sorbent nanoparticle regeneration at much lower energy cost, compared to conventional, furnace-based regeneration at the same temperature ( $\sim 350$  W·h, Appendix 2 Table A2.4). The reduction in energy consumption is mainly due to the local nature of the resistive heating process, allowing to directly heat nanoparticles

on their support framework, without the need for any wasteful external heating processes.

A significant additional factor is that electrical framework heating also enables extremely fast heating of the supported nanoparticles. Through Joule heating, regeneration-relevant temperatures can be reached within seconds (in contrast to relatively slow external heating processes), further reducing the energy costs of the sorbent regeneration process. Specifically, the investigated MgAl-MMO/rGO hybrid aerogels exhibited heating rates of up to  $720 \text{ K}\cdot\text{min}^{-1}$  (reaching  $250 \text{ }^\circ\text{C}$  in less than 20 s, Figure 4.23a). Interestingly, the high thermal conductivity and large porosity of the rGO aerogel supports also gives rise to very fast thermal energy dissipation once electrical heating is switched off, enabling extremely fast cooling (cooling rates around  $420 \text{ K}\cdot\text{min}^{-1}$ , Figure 4.23b). The combination of fast heating and cooling kinetics allows for very rapid temperature cycling of the supported nanoparticles which might be exploited for energy-efficient cycling of fast adsorption or catalytic processes in the future. These findings highlight the broad range of advantages of framework-mediated direct, electrical heating of functional nanoparticles compared to conventional thermal approaches, in terms of reduced energy consumption, temperature stability and rapid thermal cycling kinetics.

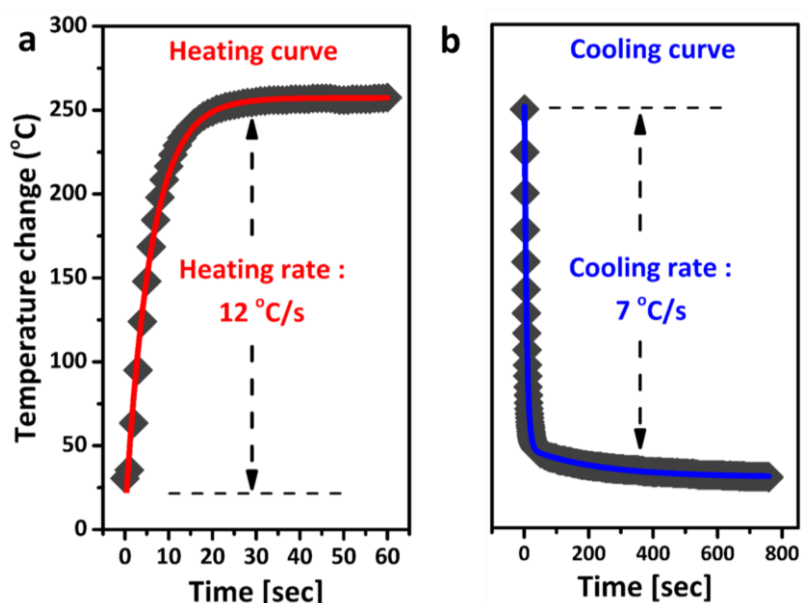


**Figure 4.23** a) Joule-heating kinetics of MgAl-MMO/rGO aerogel and, b) Natural cooling kinetics of MgAl-MMO/rGO aerogel.

#### 4.2.4 High-pressure, elevated-temperature CO<sub>2</sub> adsorption

The rGO aerogel support also gives rise to substantial improvements in functional nanoparticle performance in gas-phase sorption systems. As an important model application, CO<sub>2</sub> sorption at elevated temperatures ( $T = 300 \text{ }^\circ\text{C}$ ) was

investigated. Importantly, in this study, elevated-temperature CO<sub>2</sub> sorption was studied at technically-challenging, but practically-important high CO<sub>2</sub> pressure conditions (up to 10 bar total CO<sub>2</sub> pressure, Figure 4.24a). In fact, this study presents a first example of investigating inorganic/graphene hybrid aerogels for CO<sub>2</sub> sorption at elevated temperatures ( $T = 300\text{ }^{\circ}\text{C}$ ) and high-CO<sub>2</sub>-pressures ( $p_{\text{CO}_2} > 1\text{ bar}$ ) - crucial operating conditions for pre-combustion carbon capture technologies.

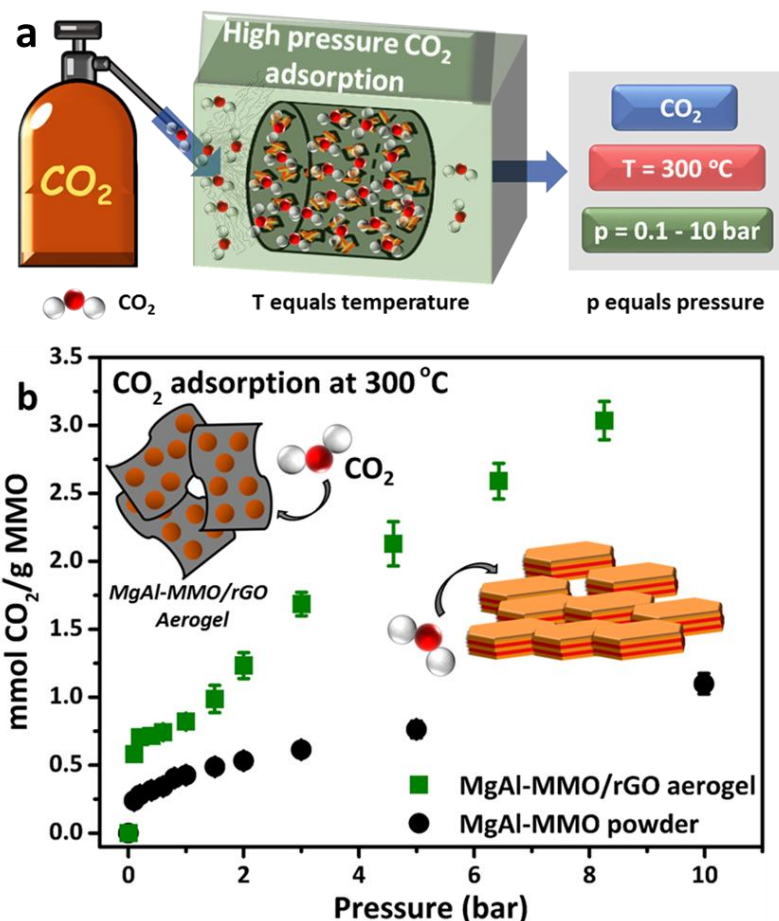


**Figure 4.24** (a) Schematics of high-pressure pre-combustion CO<sub>2</sub> adsorption on MgAl-MMO/rGO aerogels. (b) CO<sub>2</sub> adsorption isotherms onto MgAl-MMO powder and MgAl-MMO/rGO aerogel at 300 °C across CO<sub>2</sub> pressure range of 0.2-10 bar, capacities shown with standard errors.

At these challenging conditions ( $T = 300\text{ }^{\circ}\text{C}$ ,  $p_{\text{CO}_2} = 8\text{ bar}$ ), the MgAl-MMO/rGO aerogel exhibits an excellent intrinsic CO<sub>2</sub> capacity of  $3.02\text{ mmol}\cdot\text{CO}_2\cdot\text{g}^{-1}\text{ MMO}$  (Figure 4.24b, Table 4.5), which corresponds to a high total CO<sub>2</sub> capacity value of  $2.36\text{ mmol}\cdot\text{CO}_2\cdot\text{g}^{-1}\text{ ads}$ . Both intrinsic and total CO<sub>2</sub> capacities of the MgAl-MMO/rGO aerogels markedly outperform other solid-state CO<sub>2</sub> sorbents (e.g. activated carbons, commercial MOFs, metal-oxides, zeolites), assessed under comparable elevated-temperature, high-CO<sub>2</sub>-pressure conditions (see below Figure 4.25b, Table 4.6, and Appendix 2 Table A2.6-A2.7).<sup>271-274</sup> The MgAl-MMO/rGO aerogel shows markedly improved intrinsic CO<sub>2</sub>-capacity, compared to the unsupported MMO powder, over a

wide CO<sub>2</sub> pressure range ( $p_{\text{CO}_2} = 0.2\text{-}10$  bar), as shown in the high-pressure CO<sub>2</sub> sorption isotherm (Figure 4.24b). This CO<sub>2</sub> capacity enhancement, induced by the rGO aerogel support, is particularly pronounced under high pressure conditions: at 8 bar, the intrinsic CO<sub>2</sub> uptake capacity of the MgAl-MMO/rGO aerogel is over 230 % higher than that of the already well-performing unsupported MgAl-MMO powder (Figure 4.24b, Table 4.5). This remarkable enhancement stems to a large extent from the improved nanoparticle dispersion and excellent MMO accessibility on the aerogel support framework. An important secondary effect is very likely related to the aerogels' broader and more stable porosity, with the crosslinked rGO aerogel framework helping to prevent porosity collapse (and hence loss of active surface area for CO<sub>2</sub> sorption) under high pressure conditions (while loose powder sorbents are more likely to lose porosity and surface area at high gas pressures due to compaction). The unusual isotherm shape of MgAl-MMO/rGO aerogel reflects this broader, more complex porosity in the aerogels at higher pressures, compared to powder sorbents.

**Table 4.5** CO<sub>2</sub> uptake of MgAl-MMO powder and MgAl-MMO/rGO aerogel at different pressures (300 °C working temperature)

CO <sub>2</sub> Pressure	Intrinsic CO <sub>2</sub> capacity (mmol CO <sub>2</sub> ·g <sup>-1</sup> MMO)			Total CO <sub>2</sub> capacity (mmol CO <sub>2</sub> ·g <sup>-1</sup> ads)		
	MgAl-MMO Powder	MgAl-MMO/rGO Aerogel	Capacity increase	MgAl-MMO Powder	MgAl-MMO/rGO Aerogel	Capacity increase
<b>0.2 bar</b>	0.28	0.71	154 %	0.28	0.55	96 %
<b>1.0 bar</b>	0.43	0.82	49 %	0.43	0.64	49 %
<b>8.0 bar</b>	0.91	3.02	236 %	0.91	2.36	159 %

It is worth mentioning that the MgAl-MMO/rGO aerogel also perform better than equivalent hybrid powders, such as MMO/rGO powders and MMO/CNT powders. Carbon-supported powder sorbents have been investigated for elevated CO<sub>2</sub> sorption application in the literature, albeit only at low and atmospheric CO<sub>2</sub> pressures ( $p_{\text{CO}_2} = 0.05\text{-}1$  bar).<sup>58, 285-287</sup> When compared under these lower-pressure conditions, the MgAl-MMO/rGO aerogels show markedly higher intrinsic CO<sub>2</sub> adsorption capacity than equivalent MgAl-MMO/nanocarbon powders (see Appendix 2 Table A2.6), confirming the benefits of the robust, 3D-structured nanocarbon aerogel supports over loose nanocarbon powder supports in terms of improved nanoparticle stabilisation and larger, more stable porosity.

**Table 4.6** High-pressure CO<sub>2</sub> sorption capacities ( $p_{\text{CO}_2}$ = 8-10 bar) at high temperatures (T=300 °C) of different solid-state sorbent systems, reported in the literature, compared against MgAl-MMO powders and MgAl-MMO/rGO aerogel sorbent prepared in this work.

CO <sub>2</sub> adsorbents	CO <sub>2</sub> uptake capacity (mmol CO <sub>2</sub> ·g <sup>-1</sup> ads)	Temp (°C)	Pressure (bar)	Ref.
13X [a commercial zeolite]	1.27	300	10	271
AC [activated carbon]	0.29	300	10	271
A100 [a commercial MOF, Basolite MIL-53-Al]	0.42	300	10	271
MgAl-MMO [a commercial hydroxalite after calcination]	0.59	300	10	271
MgAl-MMO [a commercial hydroxalite after calcination]	0.50	300	1*	272
MgAl-MMO [as-synthesised after calcination]	1.00	300	10	273
MgAl-MMO [a commercial hydroxalite after calcination] K-promoted	1.16	300	4*	288
MgAl-MMO [a commercial hydroxalite after calcination], K-promoted, presence of water	1.10	400	10	274
Ni-MO-5 [5% Ni oxides decorated HTC]	1.03	300	10	271
Co-MO-5 [5% Co oxides decorated HTC]	0.35	300	10	271
Fe-MO-5 [5% Fe oxides decorated HTC]	0.33	300	10	271
MgAl-MMO powder [this work]	0.91	300	8	[This Work]
MgAl-MMO/rGO aerogel [this work]	2.36	300	8	[This Work]

\* Included for reference of data reported for MMOs at relatively low  $p_{\text{CO}_2}$  and high temperature

In addition to their excellent CO<sub>2</sub> adsorption capacity, the MgAl-MMO/rGO aerogels also exhibit outstanding thermal regeneration stability for CO<sub>2</sub> sorption applications, similar to their organosulfur regeneration performance. After five regeneration cycles, the CO<sub>2</sub> uptake of the MMO/rGO aerogel remains practically constant, retaining more than 90 % of its original capacity (at low, intermediate and high CO<sub>2</sub> pressures, Figure 4.25a). The stability obtained for the MgAl-MMO/rGO aerogel was found to be significantly higher compared to that of MMO adsorbents supported on rGO powder support, that retain less than 60 % of initial uptake under the same multicycle conditions.<sup>285, 287</sup> At high-CO<sub>2</sub>-pressure conditions, previous studies of unsupported MMO sorbents have reported mechanical stability issues.<sup>287</sup> In contrast, the MgAl-MMO/rGO aerogel exhibits excellent regeneration stability at high CO<sub>2</sub> pressures of up to 8 bar (Figure 4.25a).

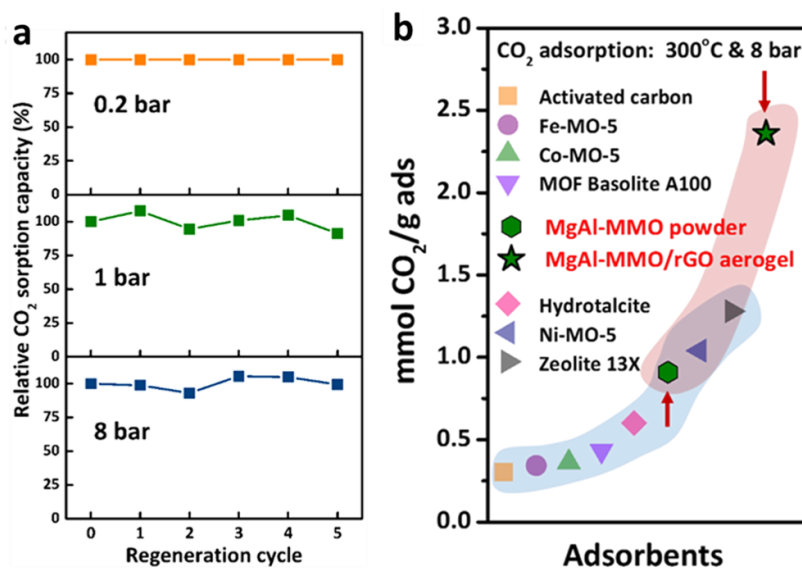


**Figure 4.25** (a) Relative CO<sub>2</sub> capacity retention of the MgAl-MMO/rGO aerogel over five thermal regeneration cycles at 400 °C at 0.2, 1, and 8 bar CO<sub>2</sub> pressure. (b) High-pressure CO<sub>2</sub> sorption capacities (8 bar, 300 °C) of the MgAl-MMO powder and MgAl-MMO/rGO aerogel sorbents prepared in this work, compared against different solid-state sorbent systems, reported in the literature (see above Table 4.6).

The combination of high capacity and excellent regeneration stability makes the MgAl-MMO/rGO aerogels very promising candidates for pre-combustion CO<sub>2</sub> capture conditions. To the best of our knowledge, this work provides the first study characterising carbon-supported MMO sorbents at both high-CO<sub>2</sub>-pressures *and* elevated temperatures ( $p_{\text{CO}_2} = 8 \text{ bar}$ ,  $T = 300 \text{ °C}$ ). This work therefore provides valuable first materials systems and performance data for future studies (structure-function relationships, predictive modelling etc.) on the utilisation of supported MMOs for technologically-important high-pressure, elevated-temperature CO<sub>2</sub> sorption. Moreover, the electrical conductivity of the rGO aerogel support opens up new routes towards energy-efficient and uniform temperature control of the MMO-based CO<sub>2</sub> sorbents, with great future potential for rapid switching between CO<sub>2</sub> capture (thermally-activated CO<sub>2</sub> sorption) and sorbent regeneration (thermally-induced CO<sub>2</sub> desorption) via framework-mediated electrical heating (see above Figure 4.18).

### 4.3 Conclusions

This study introduces a facile route to uniformly support functional, LDH-derived nanoparticles within nanocarbon aerogels at high weight loading in order to boost their functional performance in both gas-phase and liquid-phase sorption applications. Specifically, polymer-assisted assembly of LDH-decorated GO sheets was successfully adopted to support metal oxide and metal nanoparticles (MgAl-MMO, NiAl-MNP, CuAl-MNP) within the electrically-conducting framework of porous

rGO aerogel supports at loading fractions of up to 88 wt%. Supporting the LDH-derived nanoparticles within open, macroporous aerogels results in outstanding improvements in their organosulfur adsorption characteristics, including markedly increased organosulfur uptake capacities (both for simple and sterically-hindered aromatic organosulfurs), 30 times accelerated adsorption kinetics, excellent organosulfur selectivity and significantly improved sorbent regeneration stability. This work also provides first data for the sorption of CO<sub>2</sub> onto supported MMO nanoparticles at high-pressure, elevated-temperature conditions ( $p_{\text{CO}_2} = 8 \text{ bar}$ ,  $T = 300 \text{ }^\circ\text{C}$ ), relevant to pre-combustion carbon capture technologies. Under these conditions, the MgAl-MMO/rGO aerogel sorbents exhibit excellent total CO<sub>2</sub> sorption capacities of up to 2.36 mmol CO<sub>2</sub>·g<sup>-1</sup> ads (equivalent to 3.02 mmol CO<sub>2</sub>·g<sup>-1</sup> MMO). This uptake value constitutes a 160 % increase in total CO<sub>2</sub> capacity (compared to the unsupported MgAl-MMO), and is higher than that reported for other solid-state sorbents previously tested under comparable conditions. The excellent performance of the aerogel-supported MgAl-MMO in two independent sorption applications clearly evidences the excellent stabilising support function of rGO aerogels. Nanoparticle sintering and deactivation during sorbent use and sorbent regeneration is efficiently inhibited due to strong anchoring of the LDH-derived nanoparticles within the rGO aerogel framework, while nanoparticle accessibility is markedly improved due to the large and robust porosity of the aerogel support. Future studies are likely to explore structure-function relationships in more detail (e.g. investigating impact of nanocarbon type, nanoparticle loading fraction, crosslinking density).

Further, our study demonstrates additional functionality enabled by the electrical conductivity of the rGO aerogel support, specifically direct electrical framework heating of the supported sorbent nanoparticles for thermal regeneration purposes. Sorbent regeneration via Joule heating allows for regeneration of exhausted organosulfur sorbents at considerably lower energy cost (>350 times less energy consumption than furnace heating) and shorter time scales (heating rates of > 720 K·min<sup>-1</sup>) compared to conventional regeneration via external heating. In the future, such electrical framework heating could be explored for applications beyond thermal regeneration, for example for energy efficient temperature control in SER technologies or other temperature-sensitive reaction processes. The macroscopic and monolithic form of the aerogels and their well-controlled micro- and nano-scale porosity also provides new opportunities to exploit aerogel-induced performance enhancement and energy-efficient electrical heating in continuous flow processes to further push process efficiency and compatibility with existing technological infrastructure. More generally, these findings will help to further unlock the potential of nanoparticle/nanocarbon aerogel hybrids in a wide range of

applications, including pre-combustion CO<sub>2</sub> capture, heterogeneous catalysis, electro-catalysis and sensing.

## 4.4 Experimental

### 4.4.1 Materials synthesis

**Synthesis of LDH decorated GO aerogels.** All aerogels are produced through a modified version of the ice-templated aerogel synthesis approach, described in Chapter 2. Typically, 75 mg GO and 75 mg organic additives (PVA and sucrose in a 1:1 weight ratio) were sonicated in 10 mL HPLC water to produce a well-dispersed GO suspension. To this GO dispersion, a pre-fabricated wet-paste of MgAl-LDH (containing about 210 mg MgAl-LDH, see below) was added, followed by dilution with HPLC water to a total suspension volume of 10 mL. Then, 3.5 mL of the obtained suspension was cast into bespoke cylindrical moulds for unidirectional freezing in liquid nitrogen for 10 minutes. Finally, the MgAl-LDH/GO aerogel was obtained by freeze-drying overnight using a freeze-dryer (LABCONCO). The as-prepared aerogel was thermally reduced at 1000 °C, for 2 h, under N<sub>2</sub>/H<sub>2</sub> atmosphere (5% H<sub>2</sub>), using a tube furnace (Carbolite Gero Limited) to obtain a MgAl-Mixed-Metal-Oxide/GO aerogel (MgAl-MMO/rGO aerogel) with an inorganic adsorbent loading of around 78%. MgAl-MMO/rGO aerogels within different loadings were also fabricated for specific Joule heating studies. Typical dimensions of the cylindrical hybrid aerogel monoliths were 1.5 cm × 1.3 cm (cylinder diameter × cylinder height).

**Synthesis of LDH wet paste.** All LDH wet pastes were produced through co-precipitation of high concentration mixed metal salt solutions under alkaline conditions. For the synthesis of MgAl-LDH wet-paste, a liquid solution (4.5 mL) containing 0.5 M Mg(NO<sub>3</sub>)<sub>2</sub>·6H<sub>2</sub>O and 0.25 M Al(NO<sub>3</sub>)<sub>3</sub>·9H<sub>2</sub>O was added dropwise (2 min) into an alkaline solution (5 mL) of 4.7 M NaOH and 1.2 M Na<sub>2</sub>CO<sub>3</sub>. The as-prepared white suspension was aged under vigorous stirring at 60 °C for 16 h. The obtained white precipitate was washed with HPLC water to neutrality. The washed LDH particles were recovered as wet paste (i.e. avoiding drying out at any stage of the washing or recovery process) and used immediately in the aerogel synthesis in order to minimise irreversible particle aggregation. Using MgAl-LDH paste produced under the above conditions directly in the aerogel synthesis resulted in an LDH loading of 78 wt% in the final hybrid aerogel; other loading fractions were achieved by reducing the volumes of the initial metal salt and alkaline solutions.

**Synthesis of pre-formed NiAl-LDH and CuAl-LDH nanoparticles.** To produce the NiAl-LDH wet paste, a peristaltic pump was used to add a liquid solution (50 mL) containing Ni(NO<sub>3</sub>)<sub>2</sub> (0.075 M) and Al(NO<sub>3</sub>)<sub>3</sub> (0.025 M) slowly into an alkaline solution

(50 mL) of 0.2 M NaOH and 0.05 M Na<sub>2</sub>CO<sub>3</sub> at 60 °C. The pH of the resulting mixture was adjusted to pH of 10.5 through continuous addition of a NaOH solution (0.2 M) via a second peristaltic pump. To keep the pH constant at 10.5 ± 0.2 throughout the reaction (crucial to favour formation of NiAl-LDH over formation of nickel and aluminium oxides at higher pH values), the pH was constantly monitored via a pH probe and the NaOH addition rate was continuously adjusted through manual adjustment of the NaOH solution pumping rate. After complete addition of the metal salt solution, the resulting suspension was aged for 18 h at 60 °C. Finally, the obtained green precipitate was washed with HPLC water to neutrality. For aerogel fabrication, the washed LDH particles were recovered as wet paste. To obtain the pure NiAl-MNP powder sample, the obtained green precipitate was dried at 50 °C overnight in an oven, and then was thermally reduced at 1000 °C, for 2 h, under N<sub>2</sub>/H<sub>2</sub> atmosphere (5% H<sub>2</sub>), using a tube furnace (Carbolite Gero Limited).

To produce the CuAl-LDH wet paste, a synthetic co-precipitation approach equivalent to the one used for NiAl-LDH synthesis was employed, again using two peristaltic pumps and a pH probe to carry out synthesis at constant pH conditions. Specifically, an aqueous metal salt solution (24 mL, 0.67 M Cu(NO<sub>3</sub>)<sub>2</sub> and 0.33 M Al(NO<sub>3</sub>)<sub>3</sub>) was slowly added into an aqueous reservoir (100 mL, 0.01 M NaOH, pH 12) at 50 °C, maintaining a constant pH of 10 through continuous addition of an aqueous base solution (1 M NaOH, 1 M Na<sub>2</sub>CO<sub>3</sub>). The resulting blue suspension was aged at 50 °C for 20 h under stirring. The product was filtered and washed using HPLC water several times until the final pH reached 7. For aerogel fabrication, the washed LDH particles were recovered as wet paste. To obtain the pure CuAl-MNP powder sample, the obtained blue precipitate was dried at 80 °C overnight in an oven, and then was thermally reduced.

**Synthesis of NiAl-MNP/rGO and CuAl-MNP/rGO aerogels.** For the synthesis of NiAl-MNP/rGO aerogel and CuAl-MNP/rGO aerogel, the synthetic procedure was the same for the MgAl-MMO/rGO aerogel, described in the main text (Figure 4.1). Notably, the weight of organic additives and GO sheets used to fabricate NiAl-MNP/rGO aerogel and CuAl-MNP/rGO aerogel were adjusted to the yield of pre-formed NiAl-LDH and CuAl-LDH nanoparticles.

#### 4.4.2 Materials characterisation

**Zeta potential** values were measured using a Malvern Zetasizer-Nano ZS model (Malvern Instruments Ltd., UK). The pH values of the different solutions were adjusted by adding 0.1 M HCl and 0.1 M of NaOH solutions, respectively.

### 4.4.3 Adsorption measurements

**Organosulfur sorption.** The adsorbent (60 mg) was added to a DBT solution in *n*-octane (initial DBT concentration 500 ppm) and stirred at 20 °C for 120 h (*n*-octane is a major component of gasoline with high organosulfur solubility and therefore frequently used as model fuel). Aerogel adsorbents were placed onto a bespoke porous sample holder within the DBT solution in order to avoid damage to the aerogel monolith through the stirrer bar (Figure 4.26).

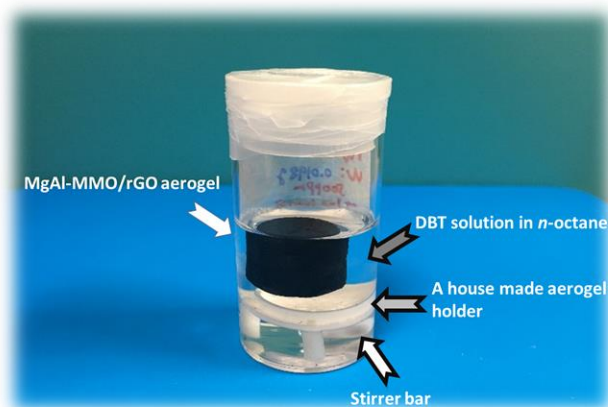


**Figure 4.26** Digital photo of an MgAl-MMO/rGO aerogel monolith for DBT adsorption.

Each sample was accompanied by a pure DBT reference solution in order to account for potential non-adsorbent-related variations in DBT concentration. To determine DBT equilibrium uptake values, aliquots of DBT solution were sampled after 120 h, centrifuged to sediment potential particle impurities, and then measured via gas chromatography (GC, Agilent 7890B GC system with an HP-5 column). The reduction in organosulfur GC peak area relative to the pure DBT reference was then used to calculate the quantity of adsorbed DBT. The intrinsic DBT uptake values of the adsorbents (in “mg·S·g<sup>-1</sup> MMO” units) are obtained from the ratio of adsorbed DBT quantity (in “mg·S” units) and the mass of MMO in the adsorbent (as determined by TGA). For the DMDBT experiments, an initial concentration of 500 ppm DMDBT in *n*-octane was used.

For the measurement of sorption kinetics, aliquots were sampled at defined time intervals (2 h, 6 h, 12 h, 24 h, 72 h, 120 h). The corresponding DBT take values (in “mg·S·g<sup>-1</sup> MMO” units) were plotted against time and fitted according to the pseudo-second-order model to obtain the DBT sorption rate constant  $k_2$  (in “g·mg<sup>-1</sup>·h<sup>-1</sup>”, where “g” relates to gram MMO in the adsorbent and “mg” relates to milligram sulfur in the adsorbate).

$$\frac{t}{q_t} - \frac{t}{q_e} = \frac{1}{k_2 q_e^2} \quad (\text{Pseudo-Second-Order Model, Equation 4.1})$$

where  $q_e$  and  $q_t$  are the amount of organosulfur compound absorbed ( $\text{mg}\cdot\text{g}^{-1}$ ) at equilibrium and at contact time  $t$  (h), respectively.

The DBT sorption isotherms of the MgAl-MMO powder and the MgAl-MMO/rGO aerogel were analysed using the Freundlich model and Langmuir model:

$$q_e = K_F C_e^{1-n} \quad (\text{Freundlich Model, Equation 4.2})$$

$$q_e = \frac{q_m C_e K_L}{1 + C_e K_L} \quad (\text{Langmuir Model, Equation 4.3})$$

where  $q_e$  is the adsorbed DBT at equilibrium ( $\text{mg}\cdot\text{g}^{-1}$ ),  $C_e$  is the DBT concentration at equilibrium ( $\text{mg}\cdot\text{g}^{-1}$ ),  $K_F$  is the Freundlich constant ( $\text{mg}^{1-n}\text{L}^n\cdot\text{g}^{-1}$ ) related to the sorption capacity, and  $n$  is the factor representing adsorption intensity,  $q_m$  is the maximum organosulfur uptake capacity ( $\text{mg}\cdot\text{g}^{-1}$ ), and  $K_L$  is related to the energy of adsorption ( $\text{L}\cdot\text{mg}^{-1}$ ).

For the testing of adsorbent selectivity, mixed BP and DBT solutions in n-octane (500 ppm BP and 500 ppm DBT) were used. The selectivity was quantified as ratio of molar DBT uptake relative to combined molar uptake of DBT and BP.

For the regeneration experiments described above, sorbents were removed from DBT solution (500 ppm DBT) after 120 h, thermally regenerated in a Muffle furnace at 250 °C, and then re-used in a fresh DBT solution (500 ppm DBT). The capacity retention values were determined by taking the ratio of the DBT uptake value after 3 regeneration cycles relative to the initial DBT uptake value of the as-synthesised sorbent. All experiments were carried out multiple times and exhibited high reproducibility.

**High-pressure, high-temperature CO<sub>2</sub> sorption.** All CO<sub>2</sub> sorption experiments were carried out by Dr Iruretagoyena at the Department of Chemical Engineering at Imperial College. An Intelligent Gravimetric Analyser (Hiden Isochema, IGA 002, software HIsorp 2016) operating up to 20 bars was used to obtain adsorption isotherms under dry conditions. The samples (~10-50 mg) were pre-conditioned in situ under vacuum at 400 °C for 3 h using a standard furnace (operating up to 500 °C). The temperature was then decreased from 400 to 300 °C at 5 K·min<sup>-1</sup> and held for 1 h. Adsorption isotherms were performed by switching the feed gas to pure CO<sub>2</sub>. First contact adsorption isotherms at 300 °C were obtained by increasing CO<sub>2</sub> pressure from ~0.01 bar to ~10 bar using different pressure step sizes (step sizes between 0.5 bar to 5 bar), with a minimum step duration of 60 min. The stability of the adsorbents was measured by multicycle tests in which after the adsorption step, a desorption isotherm was carried out from ~10 bar to ~200 mbar keeping the

temperature at 300 °C. Then the sample was degassed under vacuum at 400 °C for 1h. This procedure was repeated for 5 consecutive cycles. The multicycle experiments conducted are a combination of pressure and temperature swing regeneration. The data of each adsorption step are reported in this work. The adsorption capacity of the materials was determined from the change in mass during the adsorption steps.

#### 4.4.4 Joule-heating measurements

**Joule-heating of hybrid aerogels.** Joule heating characterisation of the MgAl-MMO/rGO aerogel and thermal aerogel regeneration post organosulfur adsorption were conducted using the customized Joule-heating setup, described in Chapter 2.

For the Joule-heating regeneration experiments, the MMO/rGO aerogel monolith was recovered from DBT solution after 120 h, mildly dried at room temperature and then placed within the Joule heating setup. The electrical current through the aerogel was then slowly increased until the aerogel surface temperature reached 250 °C (measured by thermocouple) and kept at this temperature for 60 min. After Joule heating regeneration, the intact aerogel was immersed into fresh DBT solution and the Joule heating procedure was repeated for three regeneration cycles. As comparison, thermal regeneration of pure MMO powders and MMO/rGO aerogels after DBT adsorption was also carried out in a Muffle furnace (250 °C, 5 °C·min<sup>-1</sup> ramping rate, Figure 4.27).

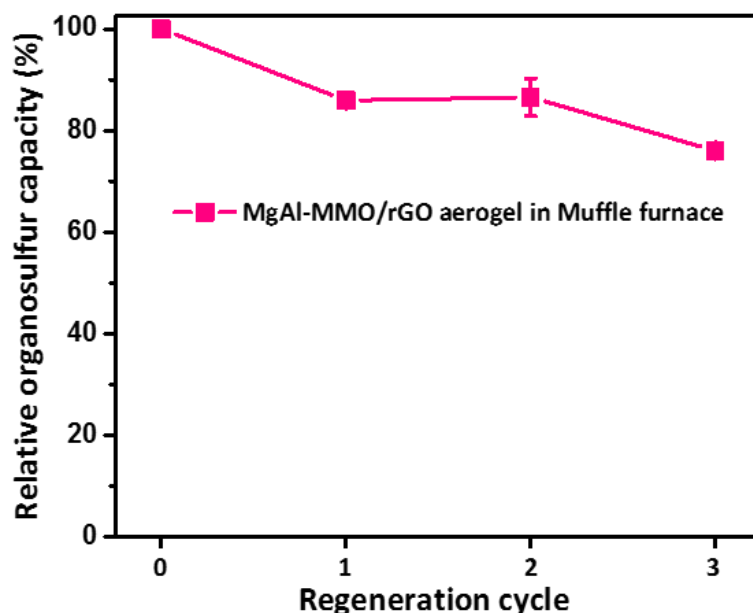


**Figure 4.27** Conventional thermal regeneration of MgAl-MMO/rGO aerogel via external heating: DBT adsorption performance of MgAl-MMO/rGO aerogel over three cycles of DBT adsorption and thermal regeneration in a muffle furnace at 250 °C (same DBT sorption conditions and temperature as in sorbent Joule-heating regeneration experiments, described in the main text, see above Figure 4.21).

## Chapter - 5

### Boron-Nitride/Carbon-Nanotube Hybrid Aerogels as Multifunctional Desulfurisation Agents

In Chapter 4, the as-measured MgAl-MMO/rGO hybrid aerogels exhibit remarkable CO<sub>2</sub> capture capacities that have outperformed many reported high-pressure CO<sub>2</sub> solid state sorbents. However, their total organosulfur adsorption capacities are relatively low compared to existing, commercial products. Hence, this chapter develops the work presented in Chapter 4 by exploring a different class of inorganic nanoparticles (here BN) and different nanocarbon type (here CNT) to produce aerogel-based hybrid sorbents (BN/rCNT aerogels) with much higher organosulfur capacities. In addition, the work in this chapter also expands the previous study by including organosulfur compounds beyond DBT and DMDBT, with aerogel sorbent capacities also assessed for other organosulfurs (such as carbon disulfide, thiophene and 2,3-dimethylbenzthiophene) with great relevance to adsorptive desulfurisation applications. Finally, this chapter extends the Joule-heating principles presented in Chapter 4 to much higher temperatures of up to 700 °C.

#### 5.1 Brief introduction

Boron nitride materials have attracted increasing attention over recent years due to a combination of unique features, including excellent mechanical properties,<sup>289</sup> high thermal conductivity and stability,<sup>290</sup> high resistance to oxidation,<sup>291</sup> and interesting catalytic properties.<sup>292</sup> BN in different material forms (powders, nanotubes, nanosheets, films, membranes) are intensely investigated for a wide range of applications,<sup>293</sup> including field emitters,<sup>294</sup> optoelectronic nanodevices,<sup>295</sup> water treatment,<sup>296</sup> and catalysis.<sup>297</sup> It has been shown that combining BN with nanocarbons, such as graphene or carbon nanotubes (CNT), produces interesting heterostructures, that can be utilised, for example, as highly efficient BN/nanocarbon hybrid electrodes in supercapacitors<sup>298</sup> and Li-S batteries.<sup>299</sup> However, the study of BN/nanocarbon hybrids has been mainly restricted to powders and films, so far. The incorporation of BN into nanocarbon aerogels is investigated rarely and has so far been restricted to studies of mechanical and electro-thermal properties. Examples include the decoration of graphene oxide aerogels with exfoliated commercial BN for enhanced thermal conductivity,<sup>300</sup> the reinforcement of CNT aerogels with thin BN nanosheets to enhance the mechanical

strength of aerogels,<sup>301</sup> and the fabrication of BN/rGO hybrid aerogels for thermo-electric energy conversion applications.<sup>125</sup>

This study will focus on the synthesis of electrically-conducting BN/nanocarbon hybrid aerogels for application in adsorption desulfurisation (ADS). A variety of materials have been shown to exhibit good adsorption desulfurisation performance, including BN,<sup>302</sup> Y-zeolite,<sup>303</sup> Cu<sub>2</sub>O,<sup>304</sup> Cu-based MOFs,<sup>305</sup> and nickel-based adsorbents.<sup>306</sup> Porous carbon materials, such as activated carbons, MOF derived carbons and N-doped porous carbons, have also shown excellent organosulfur capacities,<sup>307-309</sup> however BN powders typically exhibit more selective and faster organosulfur uptake. BN desulfurisation adsorbents are typically synthesised via high-temperature reaction of boric acid with organic, nitrogen-rich precursors (e.g. melamine, dicyandiamide, urea).<sup>195</sup> Examples include urea-derived BN powders consisting of few-layers BN nanosheets (high DBT adsorption capacity, good reusability)<sup>196</sup> and melamine-derived mesoporous BN powder adsorbents with very high surface areas.<sup>195</sup> For many commercial ADS applications, the ability to regenerate exhausted desulfurisation adsorbents is crucial.<sup>310</sup> BN-based ADS studies commonly employ solvent-based regeneration strategies (adsorbent washing with hot organic solvents),<sup>196</sup> which are slow, energy-intensive and produce large amounts of organic solvent waste. Alternative thermal regeneration (adsorbent heating in air or inert atmosphere) is in principle a greener approach with greater compatibility with existing technologies.<sup>311</sup> However, traditional thermal regeneration depends on external adsorbent heating, e.g. in an oven or muffle furnace, associated with high energy consumption and large thermal gradients.<sup>312</sup>

This study will explore how hybridising BN with nanocarbon aerogels can be exploited to enhance the desulfurisation performance of BN, while also adding new functionality, such as electrical conductivity, not available in pure BN materials (which are electrical insulators). As mentioned throughout this work, it has been repeatedly shown that the functional performance of catalytic and adsorbent nanoparticles (metal, metal oxide etc.) can be improved by supporting them within nanocarbon aerogels.<sup>50, 53, 313</sup> However, similar investigations on supporting functional BN particles within nanocarbon aerogels have not yet been reported. Our study will introduce a facile synthetic approach for the in-situ formation of BN within carbon nanotube aerogels, followed by detailed materials characterisation and assessment of adsorptive desulfurisation performance (organosulfur uptake capacity, selectivity, regenerability). The electrical conductivity of the hybrid materials (not available in the pure, electrically-insulating BN adsorbents) will be utilised for energy efficient BN regeneration post-adsorption at high temperatures.

## 5.2 Results and Discussion

### 5.2.1 BN/rCNT aerogel synthesis and characterisation

BN/rCNT hybrid aerogels were produced from a dispersion of commercially-available, acid-oxidised multi-walled carbon nanotubes (oCNT) in a solution of simple molecular BN precursors (boric acid and melamine in a nominal molar ratio 1:2), as shown in Figure 5.1. As solvent a 1:1 water/ethanol mixture was used to ensure solubility of the molecular precursors while maintaining a high solvent polarity, crucial for the exfoliation of the oCNT. At the relatively high precursor and oCNT concentrations used, thorough dispersion results in the formation of an oCNT network infused with the BN precursors. The resulting wet-gel withstands lyophilisation to form a stable oCNT/boric-acid/melamine aerogel. Subsequent high-temperature treatment in inert atmosphere is used to convert the molecular precursors into BN and to thermally reduce the oCNT into electrically-conducting reduced CNT (rCNT), forming monolithic BN/rCNT aerogels (Figure 5.1).

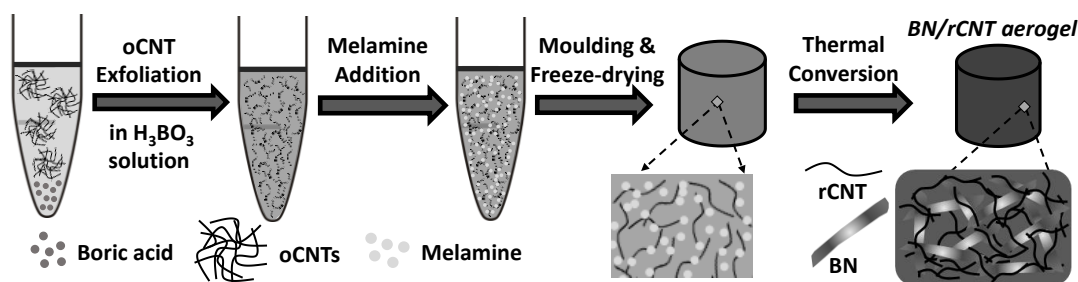


**Figure 5.1** Synthesis of BN/rCNT aerogels via high-temperature conversion of B- and N-containing precursors supported within a CNT aerogel network.

Initial optimisation studies focused on the variation of the BN:CNT ratio to improve the structural integrity of the final hybrid aerogels, a crucial prerequisite for the practical application of the aerogel materials. Hybrid aerogels with different nominal BN weight percentage were produced. While BN weight ratios of 2.5 wt% and 10 wt% yielded free-standing aerogel monoliths, their structure was relatively fragile (Figure 5.2b). However, aerogels consisting of 40 wt% BN and 60 wt% rCNT showed excellent mechanical robustness (able to support about 4000 times their own weight, see Figure 5.2a) and were taken forward for subsequent materials characterisation and desulfurisation testing. It is worth noting that BN weight ratios larger than 40 wt% could not be accessed in our synthetic approach due to solubility limitations of the molecular BN precursors.

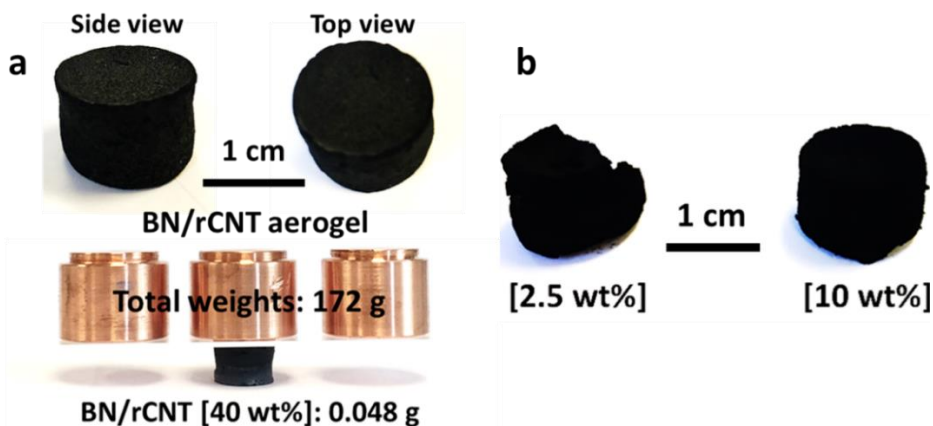


**Figure 5.2** (a) Digital images of BN/rCNT aerogels (40 wt% BN); (b) Digital images of BN/rCNT aerogel adsorbents with 2.5 wt% and 10 wt% BN loading.

The hybrid aerogels with a nominal BN weight ratio of 40 wt% (for the remainder of the paper referred to as BN/rCNT aerogels for simplicity) were characterised and tested in more detail. The actual BN weight ratio in the hybrid aerogel was estimated by TGA to be 39 wt% (Figure 5.3a), very close to the intended nominal weight ratio, indicating full precursor conversion and efficient removal of any by-products during the thermal conversion treatment. Raman spectroscopy confirmed graphitisation of the CNT network after the thermal treatment, as indicated by a significant increase of the  $I_G/I_D$  ratio from 0.68 to 0.87 (Figure 5.3b).

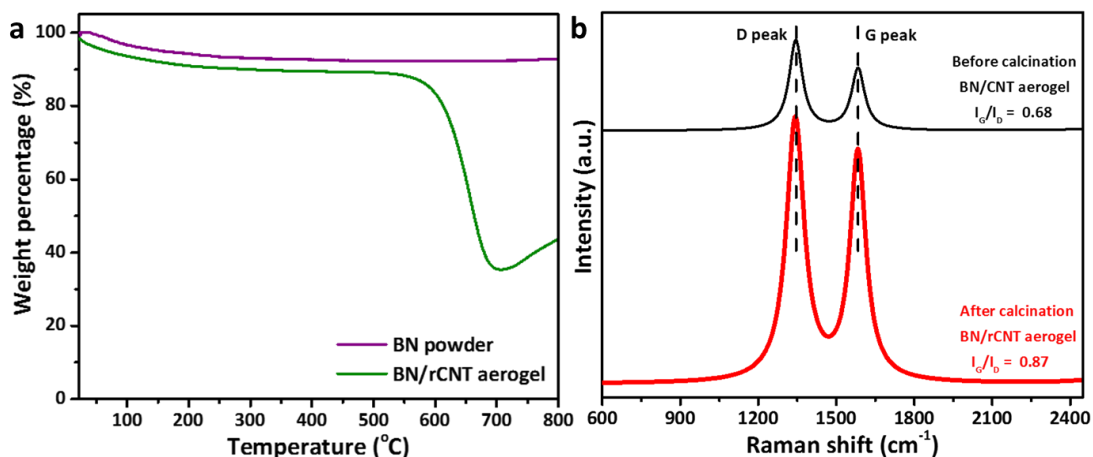


**Figure 5.3** (a) TGA of the BN powder adsorbent and the BN/rCNT aerogel adsorbent. (b) Raman spectra of BN/CNT aerogel adsorbent before and after thermal reduction.

In order to confirm the formation of BN during thermal treatment, the BN/rCNT aerogels as well as a pure BN powder control sample were characterised by XRD, IR and XPS spectroscopy. The XRD pattern of the BN powder showed two broad diffraction peaks at  $26^\circ$  and  $43^\circ$  (Figure 5.4a), corresponding to the (002) and (100) lattice planes of BN and consistent with the formation of turbostratic and/or amorphous BN.<sup>167, 314</sup> For the BN/rCNT aerogel, the strong graphitic (002) diffraction of the rCNT,<sup>315</sup> potentially obscures the BN peak at  $26^\circ$ . Therefore, IR spectroscopy

was used to further confirm BN formation (Figure 5.4b). Both BN powder as well as BN/rCNT aerogel exhibit two characteristic IR bands at around  $1370\text{ cm}^{-1}$  and  $801\text{ cm}^{-1}$ , corresponding to the in-plane B–N stretching vibrations and out-of-plane B–N–B bending vibrations, respectively,<sup>316</sup> providing clear evidence for the formation of BN in both samples.

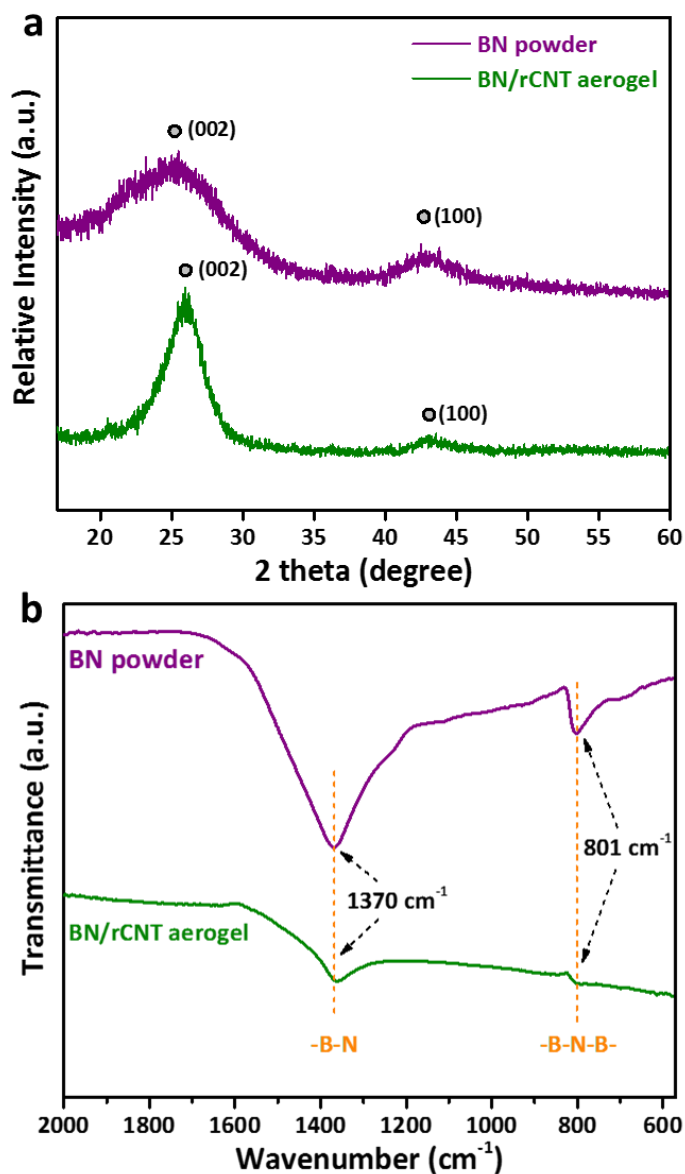


**Figure 5.4** (a) Powder XRD patterns of BN powder and BN/rCNT aerogel. (b) IR spectra of BN and BN/rCNT aerogel.

X-ray photoelectron spectroscopy (XPS) was carried out to quantify elemental composition and chemical binding state (Figure 5.5). XPS survey spectra confirmed the presence of B and N, further confirming successful precursor conversion into BN. XPS also indicates the presence of carbon and oxygen defects in the BN powder sample (Figure 5.5a-5.5b), consistent with reported studies.<sup>167, 302, 316</sup> This observation suggests that our synthetic approach generates carbon-doped BN (with

some of the carbon associated with residual oxygen), which has been repeatedly observed in the literature when forming BN from melamine precursors under conditions comparable to ours.<sup>302, 317</sup> In fact, carbon-doped BN samples have been shown to be outstanding adsorbents, rendering the synthesised hybrid aerogels highly promising for adsorptive desulfurisation applications.<sup>302</sup>

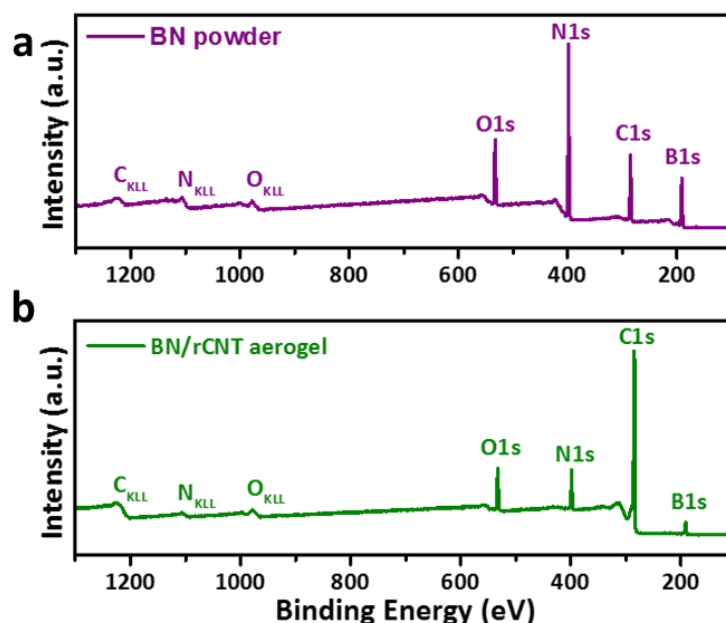


**Figure 5.5** XPS full spectra of BN powder (a) and BN/CNT aerogel (b) adsorbents.

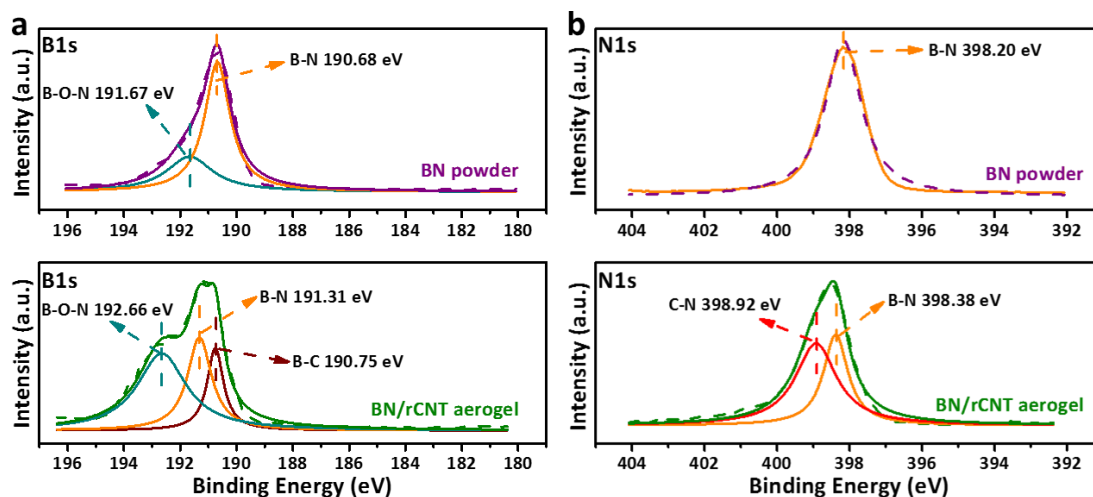


**Figure 5.6** (a-b) XPS analysis (B1s high-resolution scan; N1s high-resolution scan) of BN powder and BN/rCNT aerogel.

High-resolution XPS scans in the B1s region and N1s regions give further insight into changes in chemical binding state of BN. For the un-hybridised BN powder (Figure 5.6a), the high-resolution B1s spectrum exhibits two characteristic peaks, related to B-N (190.68 eV) and B-O-N (191.67 eV), consistent with literature findings on doped BN.<sup>317, 318</sup> In the BN/rCNT aerogel, these B-N (191.31 eV) and B-O-N (192.66 eV) binding energies shift to higher energies indicating charge transfer between rCNT

and BN.<sup>167, 319</sup> Further a new peak emerges, which is assigned to B-C binding, suggesting a degree of covalent binding between BN and rCNT. The high-resolution N1s spectra show a very similar behaviour (Figure 5.6b). For the BN powder only the characteristic B-N peak (398.20 eV) is observed.<sup>319</sup> For the BN/rCNT aerogel however, an additional shoulder (398.92 eV) emerges, attributable to C-N binding.<sup>316</sup> These XPS findings provide clear evidence that BN and rCNTs are in intimate contact within the hybrid aerogels and that some degree of covalent cross-linking between the BN and rCNT structures has occurred during the high-temperature synthesis.

Scanning electron microscopy (SEM) and energy dispersive X-ray (EDX) mapping were performed to visualise the internal structure and elemental distribution of the synthesised materials (Figure 5.7). The BN powder consists of micrometer-sized whisker-like particles (Figure 5.7a), in line with melamine-derived BN adsorbents previously described in the literature.<sup>167, 314</sup> The BN particles in the CNT-free BN powder are heavily aggregated, due to sintering during the high-temperature conversion process. EDX mapping confirms that the BN structures are carbon-doped, showing a uniform distribution of boron, nitrogen and carbon throughout the BN rod structures (Figure 5.7a<sub>1</sub>-a<sub>4</sub>).

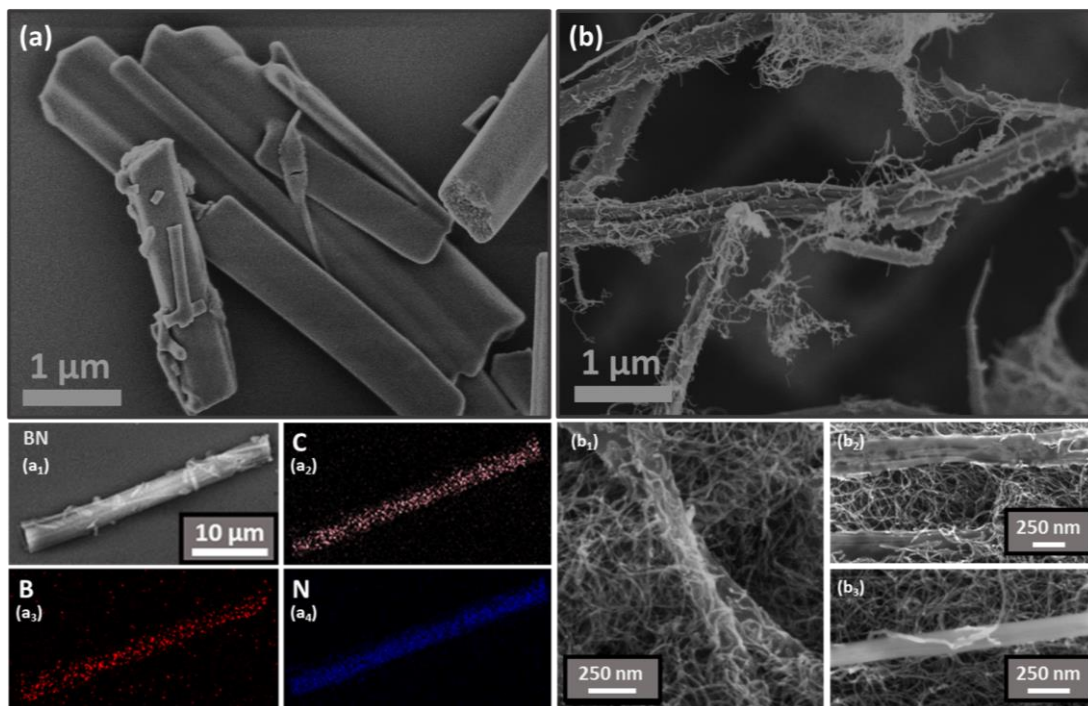


**Figure 5.7** (a) SEM image of BN powder adsorbent. (a<sub>1</sub> - a<sub>4</sub>) EDX mapping of C, B and N distribution across an individual in-hybridised BN structure. (b) SEM image of BN/rCNT aerogel adsorbent. (b<sub>1</sub> - b<sub>3</sub>) High magnification SEM of BN/rCNT aerogel internal structure.

TEM of the corrugated edges of some thinner BN structures (Figure 5.8) indicate the presence of very small pores (< 5 nm) within the BN structures. For BN/rCNT aerogels, SEM imaging shows BN particles of similar elongated morphology as in the

BN powder but with smaller diameter and considerably less aggregated (Figure 5.7b). SEM also shows that the BN structures are in intimate contact with the rCNT (Figure 5.7b) and well embedded within the CNT network (Figure 5.7b<sub>1</sub>-b<sub>3</sub>). In addition, EDX mapping of BN/rCNT aerogel also confirms the uniform distribution of boron, nitrogen and carbon components in a separated aerogel structure (see Appendix 3 Figure A3.1), suggesting even distributions of active sites. TEM images of the BN/rCNT aerogel fragments (as observed in Figure 5.9) further confirm that the BN structures are fully embedded within a porous, mesh-like network of multi-walled CNT.

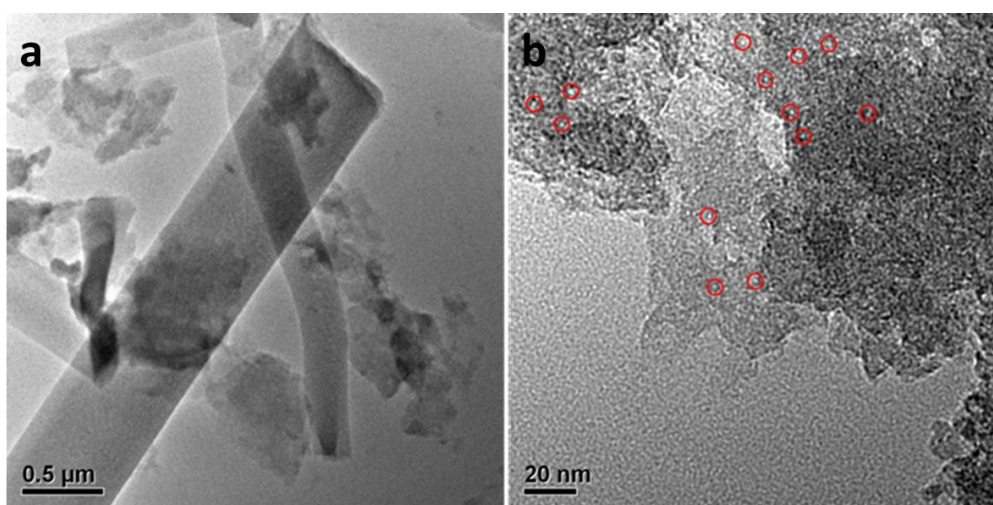


**Figure 5.8** TEM images of un-hybridised BN mesostructures: (a) low-resolution TEM image of a thin BN structure; (b) higher-resolution TEM of a thin corrugated edge of one of the nanostructures. Red circles indicate pores with diameters < 5nm.

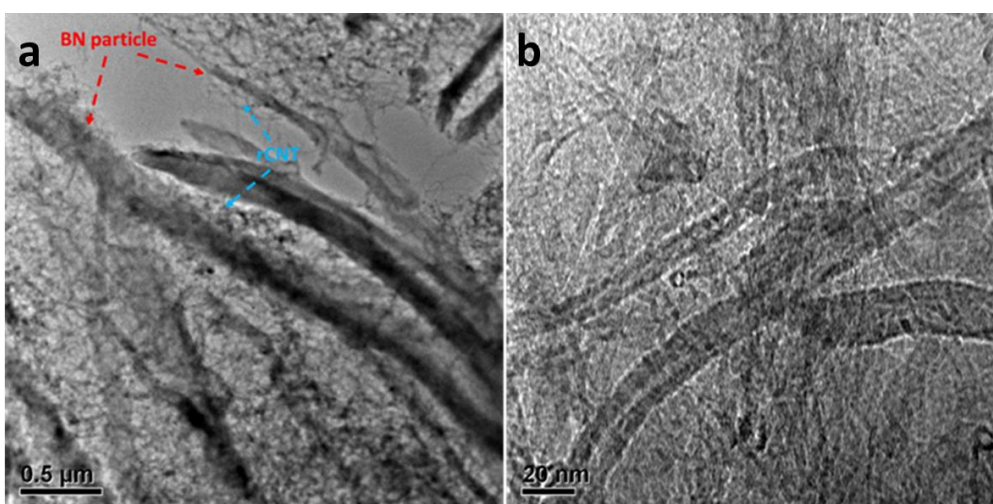


**Figure 5.9** TEM images of BN/rCNT aerogel fragment. (a) Low-resolution TEM image. The red arrows indicate the BN mesostructures, the blue arrows indicate the rCNT network. (b) Higher resolution TEM image of the rCNT network.

Bulk characterisation of the materials via BET measurements (Figure 5.10a and 5.10b) is fully consistent with the sorbent microstructures observed by electron

microscopy. For the pure BN powders, the shape of nitrogen isotherm (Figure 5.10a) exhibits combined characteristics of Type I and Type IV isotherms, indicating the presence of hierarchical porosity, i.e. indicating the presence of both micro-pores and meso-pores. Meso-porosity likely arises from the interstitial spaces between BN structures, while the micro-porosity observed is consistent with the very small, internal BN pores, observed by TEM (Figure 5.8b). The high specific surface area of the pure BN ( $1000 \text{ m}^2\cdot\text{g}^{-1}$ , Table 5.1) further confirms the presence of significant amount of micro-porosity within the BN structures. These results are in line with literature observations on melamine-derived BN structures.<sup>314</sup> For the BN/rCNT aerogels, the shape of the nitrogen isotherm is closer to a pure Type IV form. This shape indicates a significant increase in mesopore volume compared to the pure BN powder, likely to be associated with the mesh-like morphology of the CNT network and the less aggregated morphology of the BN structures in the aerogels, as observed by SEM (Figure 5.7b).

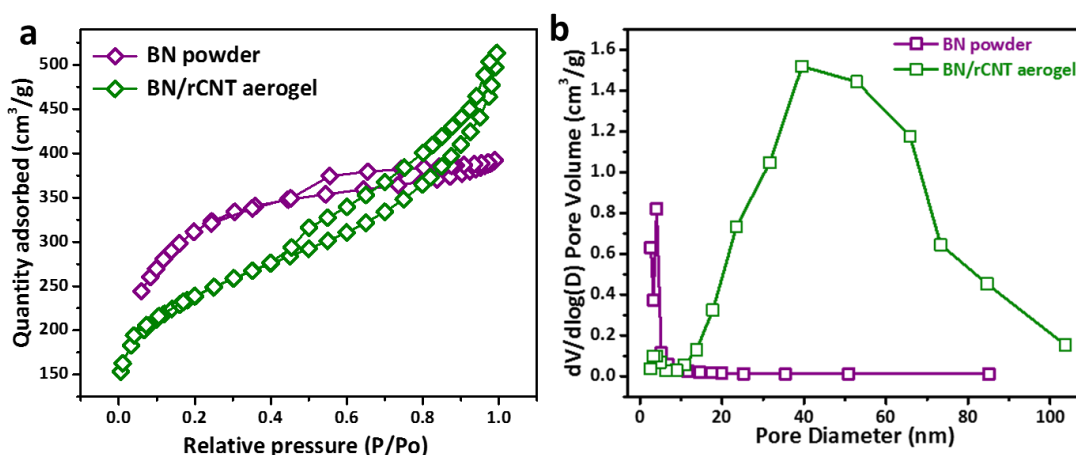


**Figure 5.10** (a)  $\text{N}_2$  adsorption isotherms and (e) BJH pore distributions of BN powder and BN/rCNT aerogel.

**Table 5.1** Organosulfur Uptake and materials characterisation of BN powder and BN/rCNT aerogel.

Adsorbent	DBT Uptake	Surface Area	Meso-Porosity		Conductivity
	$q_m^a$ ( $\text{mg}\cdot\text{S}\cdot\text{g}^{-1}$ BN)	$S_{\text{BET}}^b$ ( $\text{m}^2\cdot\text{g}^{-1}$ )	$V_p^c$ ( $\text{cm}^3\cdot\text{g}^{-1}$ )	$D_p^d$ (nm)	$\sigma^e$ ( $\text{S}\cdot\text{m}^{-1}$ )
BN powder	29.6	1004	0.04	4	non-conducting
BN/rCNT aerogel	45.2	840	0.62	40	5.92

<sup>a</sup> Maximum DBT adsorption capacities as extrapolated from Langmuir model (see Figure 5.13);

<sup>b</sup> BET specific surface area; <sup>c</sup> BJH meso-pore volume; <sup>d</sup> Average meso-pore size from BJH analysis (see Figure 5.10b); <sup>e</sup> Electrical conductivity.

In fact, BJH analysis (Figure 5.10b) shows that the BN/rCNT aerogel sorbents have very large meso-pore volume ( $V_{\text{meso}} = 0.62 \text{ cm}^3\cdot\text{g}^{-1}$ ) and a relatively large, average meso-pore size ( $d_{\text{meso}} = 40 \text{ nm}$ ) – more than one order of magnitude increased,

compared to the pure, unhybridized BN sorbents (Table 5.1). The specific surface area of the BN/rCNT aerogels is however slightly lower compared to the pure BN powder (Table 5.1), which might be related to a somewhat reduced micro-porosity. However, the dramatic improvements in meso-porosity substantially outweigh this slight surface area decrease, resulting in significantly improved organosulfur uptake in the highly mesoporous BN/rCNT aerogel sorbents, compared to the more aggregated, pure BN materials (Table 5.1).

The hybridisation of BN with CNT aerogels also impacts on other important materials properties. The interpenetration of the nanoscale rCNT network with larger, robust BN structures imparts the BN/rCNT aerogels with considerably enhanced electrical, thermal and mechanical properties, highly beneficial for sorption (and other) applications. Importantly, our hybrid BN/rCNT aerogels are electrically conducting ( $\sigma = 5.3 \text{ S}\cdot\text{m}^{-1}$  at rt, Table 5.1), in contrast to conventional BN sorbents that are electrically insulating. The ability to conduct electricity confirms that the rCNT network remains interconnected throughout the whole aerogel volume in the presence of the BN structures. The I-V characteristics of the BN/rCNT aerogel (Figure 5.11a) show non-linear behaviour with a clear drop in electrical resistance at higher currents related to Joule heating and typical for hybridisation of electrical insulators (BN) with conductors (rCNT).<sup>320</sup>

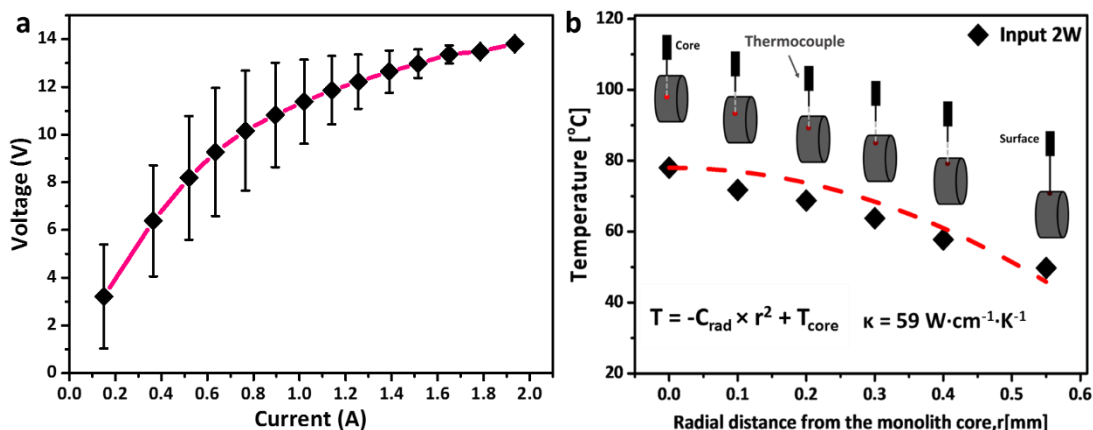


**Figure 5.11** (a) I-V curve of BN/rCNT aerogel. (b) Radial thermal gradient of an uninsulated BN/rCNT aerogel (Joule-heated at 2W), used for the calculation of the thermal conductivity,  $\kappa$ , of the hybrid aerogel.

Further, the BN/rCNT aerogels exhibit excellent thermal conductivity ( $\kappa = 0.59 \text{ W}\cdot\text{m}^{-1}\cdot\text{K}^{-1}$ ), considerably higher than conventional porous sorbent materials (Figure 5.11b, e.g. the pure rCNT aerogel exhibits a thermal conductivity of  $0.104 \text{ W}\cdot\text{m}^{-1}\cdot\text{K}^{-1}$  in Chapter 3). High thermal conductivity results in fast heat dissipation which can be highly beneficial for sorption and catalytic applications, enabling efficient natural

cooling as well as rapid temperature cycling, e.g. during thermal material regeneration.

The BN/rCNT aerogels also show good mechanical properties (Figure 5.12). Preliminary mechanical compressibility tests show that the BN/rCNT aerogels have significantly larger compressive strength compared to an analogous aerogel made from only rCNT. While more detailed measurements and analysis of the mechanical properties of the hybrid aerogels are required, these preliminary results suggest that the BN structures act as mechanical reinforcements in the rCNT network, likely aided by a degree of covalent crosslinking between BN and CNT as indicated by XPS. The improved mechanical strength is a crucial prerequisite for applications, providing durable aerogel monoliths that are able to maintain structural integrity during operation and subsequent regeneration.

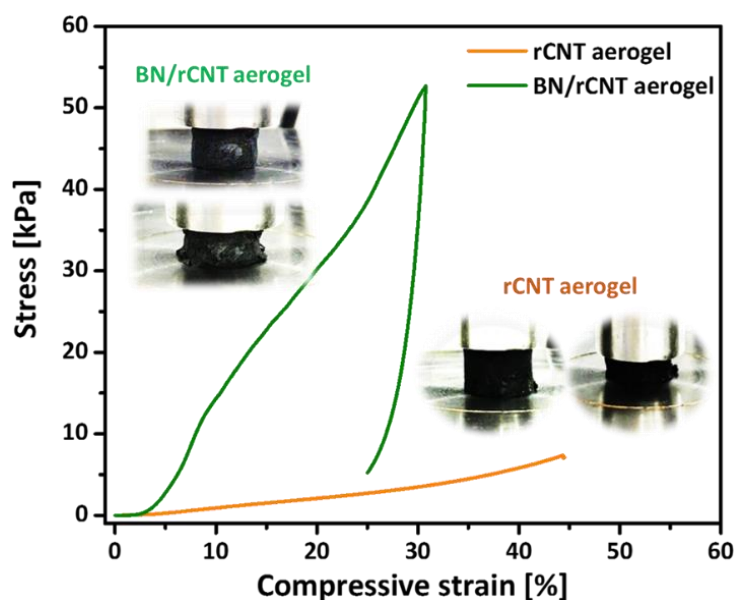
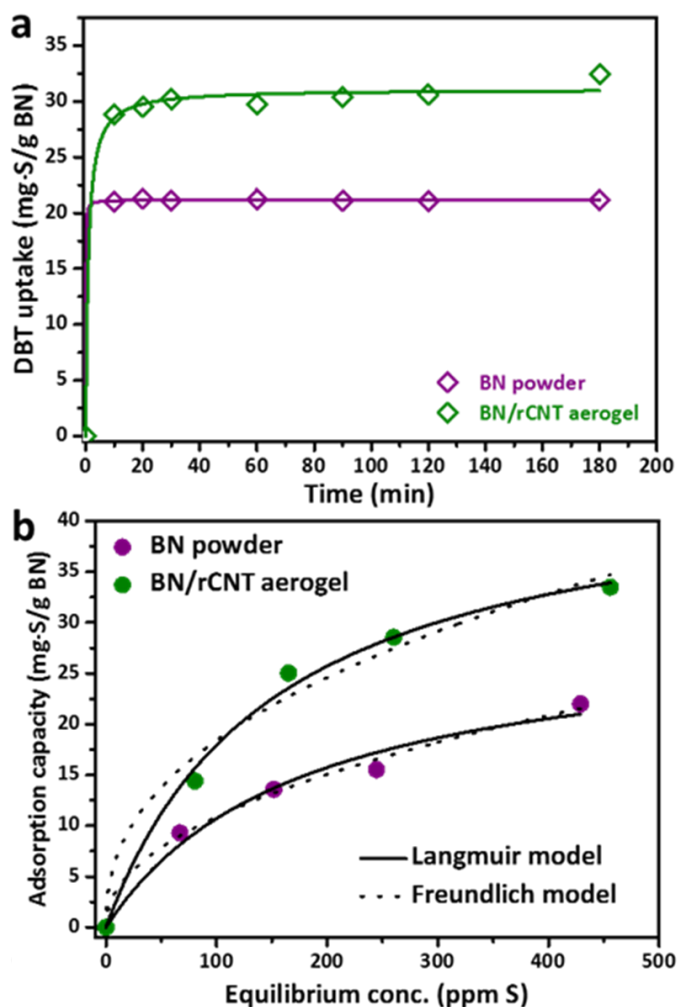


Figure 5.12 Compressibility measurements of BN/rCNT aerogel and pure rCNT aerogel.

### 5.2.2 Adsorptive desulfurisation

Dibenzothiophene (DBT) adsorption from n-octane solution onto the BN/rCNT aerogels and pure BN powders was investigated to assess the adsorptive desulfurisation performance (Figure 5.13a and 5.13b). Temperature-dependent sorption studies showed a significant drop in DBT uptake at elevated temperatures (Appendix 3 Figure A3.2), indicating that DBT sorption onto BN is exothermic, as previously reported.<sup>196</sup> Consequently, all desulfurisation tests were carried out at room temperature. Organosulfur uptake kinetics onto pure and hybridised BN are relatively fast, reaching equilibrium in less than 30 min (Figure 5.13a). The DBT adsorption isotherms show that, for all initial DBT concentrations tested, organosulfur uptake onto the BN/rCNT aerogels is greater than onto pure BN (Figure

5.13b). For example, an initial DBT concentration of 500 ppm S, the BN/rCNT aerogels show a 50 % increase in DBT uptake ( $32 \text{ mg}\cdot\text{S}\cdot\text{g}^{-1}\text{BN}$ ) compared to the BN powder ( $21 \text{ mg}\cdot\text{S}\cdot\text{g}^{-1}\text{BN}$ ). Importantly, control experiments using pure (i.e. BN-free) rCNT aerogels confirmed that the rCNT framework itself does not significantly contribute to this increase (see Appendix 3 Figure A3.2), indicating that the capacity improvement is purely due to changes in BN morphology, including improved dispersion of BN structures and substantially increased meso-porosity in the BN/rCNT aerogels. As to the BN/rCNT aerogels obtained from different thermal treatment temperatures ( $800 \text{ }^\circ\text{C}$  and  $1000 \text{ }^\circ\text{C}$ ), the lowering of the thermal conversion temperature during materials synthesis leads to a significant decrease in desulfurisation capacity (see below Table 5.3). This might be related to incomplete BN precursor conversion and/or changes in aerogel porosity.



**Figure 5.13** (a) DBT adsorption kinetics of BN powder and BN/rCNT aerogel (DBT, 500 ppm S, n-octane). (b) DBT adsorption isotherms of BN powder and BN/rCNT aerogel (100 ppm S, 200 ppm S, 300 ppm S and 500 ppm S DBT in n-octane).

Both isotherms fitted very well a conventional Langmuir model ( $R^2 > 0.97$ , Table 5.2), suggesting the presence of a relatively homogeneous surface and the formation of a

saturated monolayer. The maximum DBT uptake capacity ( $q_m$ , Table 5.2) of the BN/rCNT aerogels is again about 50 % higher compared pure BN, further confirming the substantial improvement in organosulfur uptake in the hybrid materials. The second Langmuir fitting parameter,  $K_L$  (related to the sorption energy) is also slightly larger (around 15 %) for the BN/rCNT aerogel, which might indicate a slight increase in DBT-BN binding strength in the aerogels, potentially related to the charge transfer effects discussed earlier.

**Table 5.2** Isotherm fitting parameters for DBT sorption onto BN powder and BN/rCNT aerogel

Sample	Langmuir model		
	$q_m$ ( $\text{mg}\cdot\text{S}\cdot\text{g}^{-1}$ )	$K_L$ ( $\text{L}\cdot\text{mg}^{-1}$ )	$R^2$
BN powder	29.6	$5.7 \times 10^{-3}$	0.974
BN/rCNT aerogel	45.2	$6.6 \times 10^{-3}$	0.993

The DBT removal capacity of our BN/rCNT aerogels reach commercially relevant levels (in line with previous BN desulfurisation studies),<sup>167, 195, 196</sup> showing similar or higher performance compared to many other desulfurisation sorbents (Table 5.3),<sup>57, 307, 308, 309, 321, 322</sup> such as  $\text{Cu}_2\text{O}$  powder,<sup>304</sup> Ni nanoparticles decorated activated carbon beads (Ni-ACB)<sup>323</sup> and commercial metal-organic frameworks (Cu-BTC).<sup>305</sup> It is worth noting that the desulfurisation sorbents listed in Table 5.3 (including the high-capacity N-doped porous carbon) are powders, while our BN/rCNT hybrids are monolithic aerogels. The monolithic form of our sorbent allows for much easier recovery from liquid solution, while the integrated interconnected CNT network enables direct electrical heating (not possible in loose powders), which will be studied in detail in the next section. Our BN/rCNT aerogel sorbents show also excellent desulfurisation performance for other typical organosulfur impurities, including carbon disulphide, thiophene, 3,5-dimethylbenzthiophene and 4,6-dimethyldibenzothiophene, with uptake capacities (from n-octane solution) between 18-49  $\text{mg}\cdot\text{S}\cdot\text{g}^{-1}$  BN, depending on the sulfur compound (Figure 5.14).

**Table 5.3** Organosulfur uptake of various ADS adsorbents.

Adsorbents	S concentration (ppm)	Sorption capacity ( $\text{mg}\cdot\text{S}\cdot\text{g}^{-1}$ ads)	Ref.
MgAl-MMO <sup>a</sup>	50 ppm	1.5	57
$\text{Cu}^+$ /MIL-(Fe) <sup>b</sup>	50 ppm	11	308
N-doped C	115 ppm	93	307

AC <sup>c</sup>	300 ppm	7	321
Cu <sub>2</sub> O	550 ppm	11	304
NaY <sup>d</sup>	500 ppm	13	309
ZnY	500 ppm	15	309
Ag/Fe@SiO <sub>2</sub>	663 ppm	5	322
Ni-ACB <sup>e</sup>	800 ppm	27	323
Cu-BTC <sup>f</sup>	630 ppm	32	305
BN/rCNT	500 ppm	32	Here

<sup>a</sup> MMO = mixed metal oxides; <sup>b</sup> Cu<sup>+</sup>/MIL = Cu<sup>+</sup> in MOF; <sup>c</sup> AC = activated carbon; <sup>d</sup> NaY = Na-Y zeolite; <sup>e</sup> ACB = activated carbon beads; <sup>f</sup> Cu-BTC = copper-benzenetricarboxylate MOF.

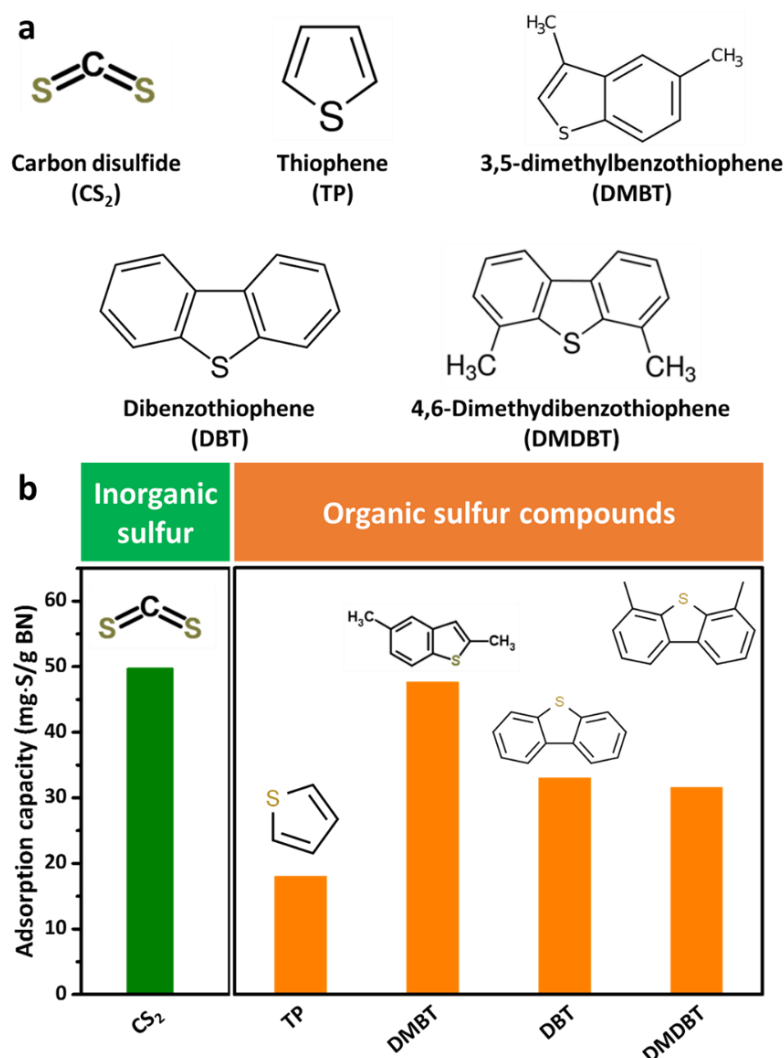


**Figure 5.14** (a) Chemical structures and abbreviation of inorganic sulfur compound and organic aromatic sulfur compounds. (b) Adsorption desulfurisation performance of various sulfur-containing onto BN/rCNT aerogels (sorption from n-octane; initial concentration for all compounds 500 ppm S).

In addition, our sorbents have pronounced selectivity towards organosulfurs. To provide first evidence for this, the uptake of DBT from n-octane solution was tested in the presence of dissolved biphenyl (Figure 5.15a).<sup>57</sup> Competitive sorption experiments using a mixture of DBT and BP in n-octane (Figure 5.15a) showed only very small BP uptake while DBT uptake remains undiminishedly high (31 mg·S·g<sup>-1</sup> BN, Figure 5.15a). However, when competitive sorption measurements were conducted using a mixture of two organosulfur compounds (mixture of DBT and DMDBT in n-octane, Figure 5.15b) both organosulfur compounds were adsorbed strongly, reaching a high total (combined) organosulfur uptake of 43 mg·S·g<sup>-1</sup> BN in the BN/rCNT aerogels (Figure 5.15b). The combination of excellent selectivity towards organosulfurs and high uptake across a broad variety of sulfur compounds renders out BN/rCNT aerogels highly promising for real-life adsorptive desulfurisation applications across a range of fuel types.

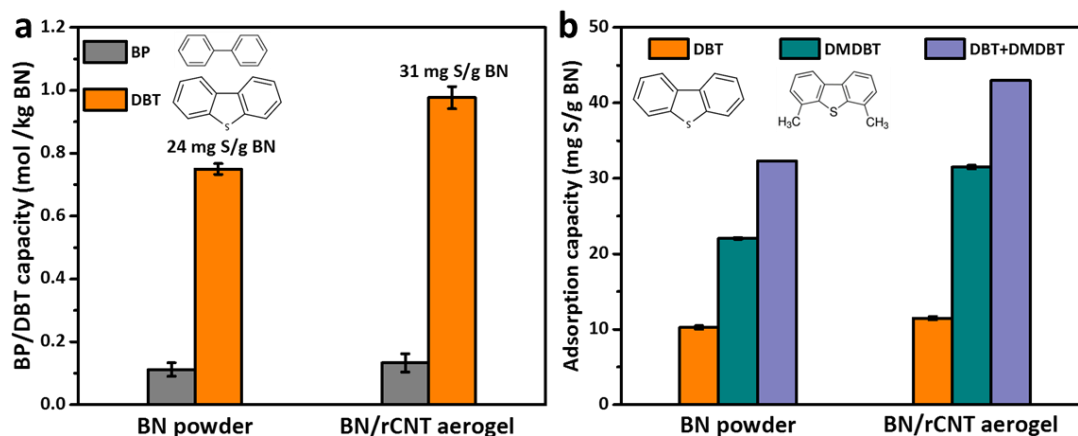


**Figure 5.15** (a) Selectivity: Adsorption capacities of BN powder and BN/rCNT aerogel as measured in BP/DBT mixtures (2873 ppm BP, 500ppm S DBT in n-octane). (b) DMDBT adsorption performance of BN powder and BN/rCNT aerogel in the presence of DBT (250 ppm S DMDBT and 250 ppm S DBT in n-octane).

To rationalise the affinity of our BN materials towards organosulfurs, post-sorption analysis of the aerogel and powder adsorbents via IR and XPS was carried out to gain further insight into the underpinning sorption process. To this end, sorbents were left to equilibrate in DBT solution, then washed with n-octane at room temperature and dried. The IR spectra of the post-sorption samples showed a new characteristic band, clearly indicating the presence of firmly bound DBT molecules (Figure 5.16a). XPS of post-sorption BN and BN/rCNT aerogel further confirmed the presence of sulfur (Figure 5.16b). Comparison between the high-resolution S2p spectrum of the post-sorption sorbents and pristine DBT powder indicates strong interactions between DBT and BN. Both post-sorption adsorbents showed an additional large shoulder in the high-resolution S2p peak that we attribute to S···B=N- binding.<sup>324</sup>

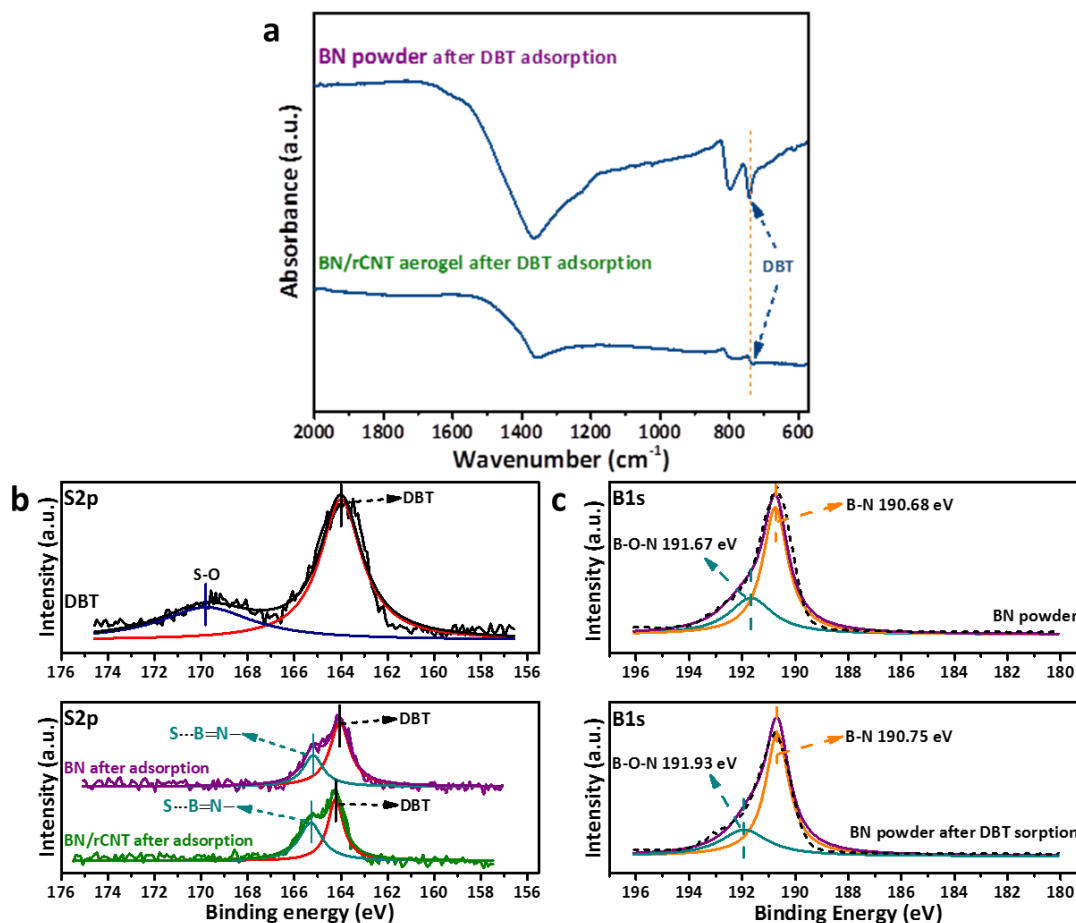


**Figure 5.16** (a) IR spectra of BN and BN/rCNT aerogel adsorbents after DBT adsorption. Post-sorption XPS analysis: (b) S2p XPS peaks of DBT powder, BN powder after DBT adsorption and BN/rCNT aerogel after DBT adsorption; (c) B1s XPS peak of BN powder before and after DBT sorption.

A small shift is also observed in the B1s peaks post-sorption (Figure 5.16c). However, no significant peak shifts are observed for the N1s XPS peaks or the C1s peaks of the carbon dopant (see Appendix 3 Figure A3.3). This observation indicates charge transfer from the lone pairs of the DBT sulfur atoms (Lewis base) to empty acceptor orbitals located at the boron atoms of BN adsorbent (Lewis acid).<sup>167, 196</sup> The underpinning sorption process is therefore based on strong Lewis acid-base interactions between organosulfur and BN sorbent, with the electron-rich sulfur-containing impurities binding through their lone pairs to the electron-deficient boron atoms in the BN structure. These findings are consistent with recent theoretical studies, investigating the binding of DBT to BN via DFT simulations.<sup>196</sup> Organosulfur sorption based on Lewis interactions is also consistent with the very low DBT uptake observed for the rCNT network, evidencing poor interactions between the electron-rich graphitic surfaces and the electron lone pairs at the DBT sulfur. The higher affinity of BN towards DMDBT compared to DBT (Figure 5.16b) further confirms a Lewis acid base sorption mechanism (leading to stronger interactions between BN

and DMDBT due to the increased Lewis basicity of alkyl-substituted benzothiophenes).<sup>196, 325</sup>

### 5.2.3 Joule-heating of BN/rCNT aerogel for sorbent regeneration

The electrical conductivity of the BN/rCNT aerogel enables direct electrical heating (Joule-heating) of the rCNT network and thereby fast and energy-efficient heating of the embedded BN desulfurisation sorbents (Figure 5.17a). The BN/rCNT aerogels can be readily heated to up to 700 °C (27 W, in inert atmosphere, using the electrical setup described in Chapter 2) without any damage or degradation to the aerogel. The Joule-heating temperature of the BN/rCNT aerogel is linearly dependent on the electrical power input ( $25\text{ °C}\cdot\text{W}^{-1}$ , Figure 5.17a,  $75\text{ °C}\cdot\text{W}^{-1}$  for the pure rCNT aerogel in Chapter 3), enabling to set any desired temperature by simply adjusting electrical voltage or current. Importantly, Joule-heating occurs very rapidly, exhibiting heating rates of up to  $74\text{ K}\cdot\text{s}^{-1}$  and reaching 700 °C in less than 10 s. Once the Joule-heating current is switched off, the BN/rCNT aerogels also exhibit very fast cooling rates (up to  $73\text{ K}\cdot\text{s}^{-1}$ ), enabled by their excellent thermal conductivity and associated heat dissipation properties (Figure 5.17b). These heating and cooling kinetics are considerably faster than those of the MMO/rGO aerogels discussed in Chapter 4, likely due to the higher power inputs applied here as well as the larger thermal conductivity of BN, compared to MMO. The hybrid BN/rCNT aerogels also show excellent Joule heating performance in air atmosphere where they can be heated to up to 320 °C without damage to the carbon network (see Appendix 3 Figure A3.6).

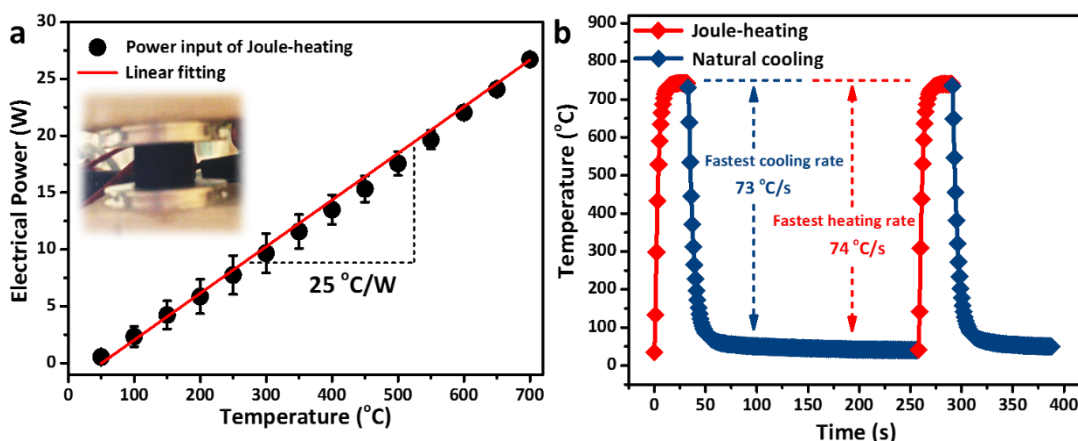


**Figure 5.17** (a) Electrical power versus Joule-heating temperature. (b) Heating and cooling curves of the Joule-heated BN/rCNT aerogel.

Regenerability and reusability of exhausted desulfurisation adsorbents are crucial factors for the viability of commercial desulfurisation agents. As mentioned previously, the monolithic form of the BN/rCNT aerogels allows very easy recovery of

the exhausted sorbents from hydrocarbon solution. The post-sorption hybrid aerogels remain electrically-conducting and can be easily regenerated via Joule heating (Figure 5.18a). To this end, exhausted BN/rCNT aerogels were Joule heated to 400 °C (Figure 5.18b) to induce thermal DBT desorption.

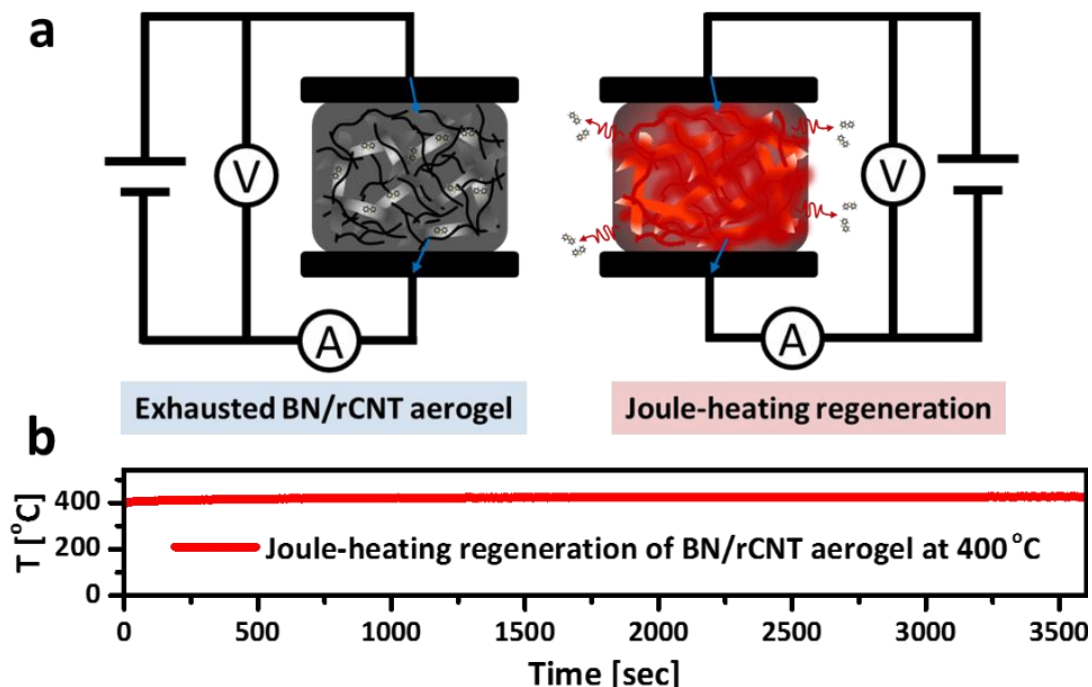


**Figure 5.18** (a) Joule-heating regeneration of an exhausted BN/rCNT aerogel adsorbent via thermal DBT desorption under Joule-heating. (b) Temperature stability over 1 h of Joule-heating regeneration.

The corresponding Joule heating temperature over five thermal cycles is shown in Appendix 3 Figure A3.4. Each thermal cycle shows good thermal stability, suggesting the rCNT aerogels are promising support frameworks for functional sorbents. Additionally, the high thermal conductivities of BN/rCNT aerogels are well-inherited even after five times cycles, as evidenced by the ultrafast cooling kinetics in Appendix 3 Figure A3.4b.

The regenerated hybrid aerogels were re-used in batch DBT adsorption measurements and repeatedly regenerated. The regeneration efficiency remains close to 90 % of the initial uptake capacity over five regeneration cycles (Figure 5.19). The slight decrease in regeneration capacity after the fourth cycle is attributed to a marginal loss of sorbent material during repeated use and manual handling of the aerogel sorbents.

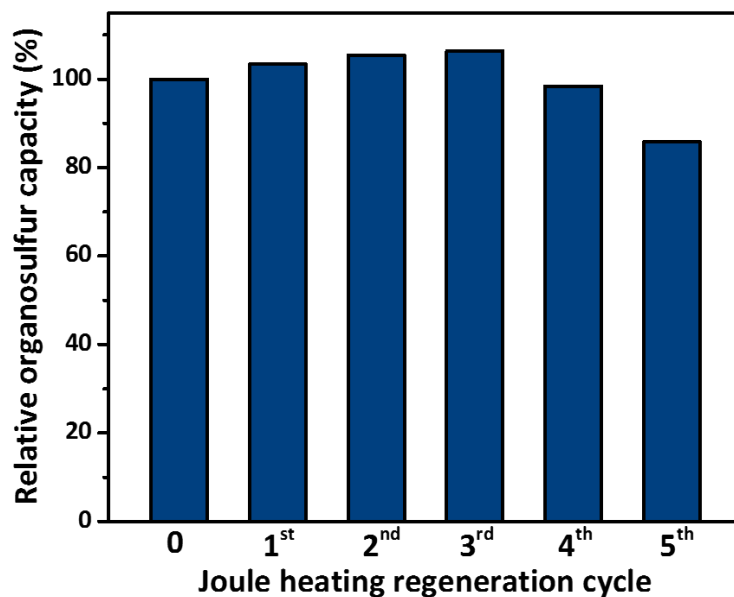


**Figure 5.19** Regeneration stability of BN/rCNT aerogel adsorbent: Organosulfur uptake (relative to initial organosulfur capacity) over five Joule-heating regeneration cycles.

The average energy consumption for each Joule-heating regeneration cycle was only 0.018 kW·h (see Appendix 3 Table A3.1), which is considerably lower than traditional thermal regeneration of the same sorbent through external heating in an oven or furnace. For 1 kg sorbent, the energy consumption for fast, high-temperature regeneration (Joule heating 700 °C, 1 min as depicted in Figure 5.17a) is estimated to be around 9 kW·h·kg<sup>-1</sup> sorbent. The use of BN/rCNT aerogel adsorbents therefore enables highly efficient and repeatable thermal sorbent recycling at minimal energy costs via direct resistive framework heating.

#### 5.2.4 BN/rCNT aerogels fabrication at lower temperatures

The BN/rCNT aerogels discussed here have all been produced through precursor conversion at 1000 °C as discussed in section 5.2.1 (see above Figure 5.1). It is worth noting that BN/rCNT aerogels can also be produced at lower conversion temperatures but that the resulting hybrid aerogels exhibit reduced organosulfur sorption and Joule-heating regeneration performance (see Table 5.4 and Figure 5.20). The lowering of the thermal conversion temperature leads to significant decrease in electrical conductivity of the hybrid aerogels (Table 5.3). As a consequence, the Joule heating regeneration process becomes less efficient. Specifically, the BN/rCNT aerogels produced at 800 °C require larger electrical power input compared to the materials produced at 1000 °C to reach the same Joule heating temperature (Figure 5.20a). Both reduced electrical conductivity and reduced Joule heating efficiency are likely associated with the lower degree of CNT graphiticity of the sample produced at the lower temperature. This is confirmed by

Raman spectroscopy which shows a clear reduction in  $I_G/I_D$  ratio for the material produced at 800 °C (Figure 5.20b)

**Table 5.4** Density, electrical conductivity and DBT sorption capacity of BN/rCNT aerogel under 800 °C and 1000 °C treatments.

Sample name	Temp (°C)	Density (mg·cm <sup>-3</sup> )	Heating efficiency (°C·W <sup>-1</sup> )	Electrical conductivity (S·m <sup>-1</sup> )	$I_G/I_D$	DBT capacity (mg·S·g <sup>-1</sup> BN)
BN/rCNT aerogel	800	25.43	15	1.47	0.78	13.4
BN/rCNT aerogel	1000	15.85	25	5.92	0.86	32

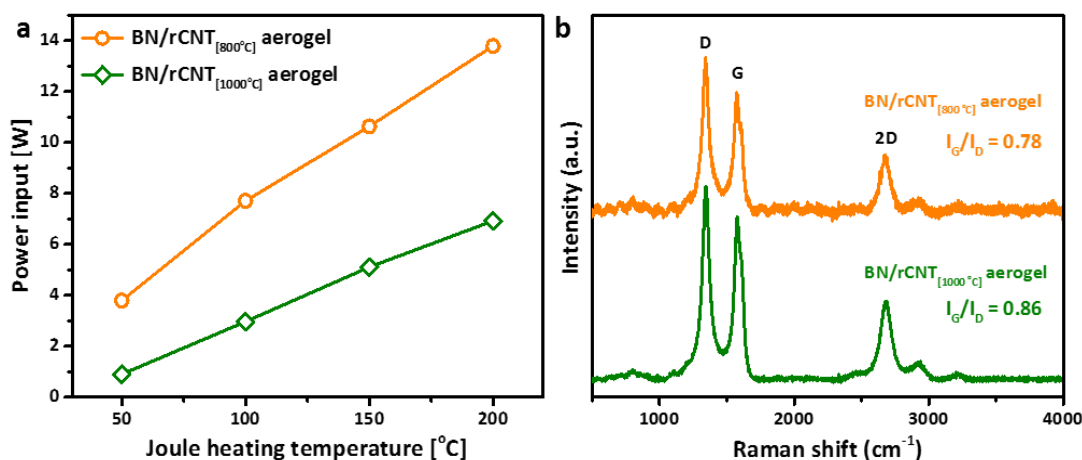


**Figure 5.20** (a) Joule heating performance and (b) Raman spectra of BN/rCNT thermally treated at 800 °C and 1000 °C.

### 5.3 Conclusions

In summary, our study reports the fabrication of electrically-heatable, highly-porous BN/rCNT aerogel materials, produced via facile thermal conversion of molecular precursors within a 3D CNT network. The BN/rCNT aerogels exhibit outstanding desulfurisation properties, including large, commercially-relevant organosulfur uptake capacities, excellent organosulfur selectivity, fast uptake kinetics and high recycling stability. Detailed materials characterisation of the BN/rCNT aerogels showed reduced BN particle sintering and increased mesoporosity compared to pure BN powder adsorbents, underpinning the improved organosulfur uptake in the hybrid aerogels. XPS measurements provided clear evidence for strong Lewis acid-base interactions between the BN adsorbent and the organosulfur adsorbates, likely giving rise to the excellent organosulfur selectivity of BN, confirming recent theoretical predictions. Joule-heating of the BN/rCNT aerogels (not possible in pure BN powders or pure BN aerogels) enabled temperature control to high temperatures (up to 700 °C) at very high heating rates (up to 74 °C·s<sup>-1</sup>) and low energy consumption. Electrical framework heating was successfully exploited for

the thermal regeneration of BN, with less than 10 % loss in organosulfur capacity over five regeneration cycles.

More generally, our study demonstrates how to produce highly efficient BN sorbents with commercially relevant performance parameters (capacity, selectivity, recyclability), likely to inform other BN sorption applications, such as water treatment or carbon capture. The concept of direct electrical framework heating is highly interesting for rapid and energy-efficient temperature control for other BN applications (e.g. temperature-activated sorption or catalysis). Moreover, the hybridisation of electrically-insulating materials with electrically-conducting 3D nanocarbon networks can be extended to introduce other new functionalities, such as electrical stimulation, actuation or control of electrical potential. Our synthetic strategy is readily transferable to other 3D nanocarbon frameworks (graphene aerogels, carbon fibre foams) as well as to inorganic materials, produced via high-temperature reactions (e.g. dichalcogenides, carbides, nitrides), opening up routes to a range of new functional porous materials that combine electrical conductivity, thermal stability and mechanical robustness.

## **5.4 Experimental**

### **5.4.1 BN/rCNT aerogel synthesis**

The BN/rCNT hybrid aerogels were synthesised as depicted in Figure 5.1. Typically, commercial oxidised CNT (oCNT, 0.075 g) were dispersed in 10 mL water/ethanol solution via ultrasonic probe sonication (4 × 5 min, 30 % of ultrasound power, model HD 2200, Bandelin sonopuls). Then boric acid (0.1315 g, 0.0021 mole) was added to the oCNT dispersion and sonicated, followed by the addition of melamine (0.5365 g, 0.0042 mole). The resulting mixture was probe sonicated for 4 × 5 min. The resulting boric-acid/melamine/oCNT mixture was frozen and freeze-dried for 24 h within bespoke cylindrical moulds. Freeze-drying yielded a freestanding, cylindrical boric-acid/melamine/oCNT aerogel monolith that was thermally treated in a tube furnace (Carbolite Gero Limited) at 1000 °C for 2 h under a nitrogen atmosphere at a heating rate of 5 °C·min<sup>-1</sup> to convert the small molecule precursors into BN. The resulting hybrid aerogel (BN/rCNT aerogel) had a nominal BN weight loading of 40 wt%. Other aerogels with BN loadings of 2.5 wt% and 10 wt%, were prepared by adjusting the boric acid and melamine concentrations in the procedure above. To produce a pure BN reference sample ('BN powder'), the BN precursors, boric acid (0.619 g, 0.01 mole) and melamine (2.53 g, 0.02 mole), were dissolved in 40 mL water/ethanol solution (volume ratio 1:1) and heated at 50 °C to dryness. The resulting solid boric-

acid/melamine mixture was ground into a fine powder and then thermally treated under conditions described above.

#### 5.4.2 Materials characterisation

**Infrared spectroscopy** (IR) was carried using a PerkinElmer Spectrum One IR Spectrometer, with the scanning range between 550 and 4000  $\text{cm}^{-1}$ .

**Thermal conductivity** was determined from the thermal temperature gradient of Joule heated aerogels under the same conditions as described in Chapter 3.

**Compressibility measurement.** The mechanical compressibility was tested using an Instron 5566 serials mechanical testing machine at a loading speed 1  $\text{mm}\cdot\text{min}^{-1}$ . Specifically, an intact aerogel sample was located at the centre between the support substrate and a suitable load, followed by adjusting the load height to reach the aerogel surface. After that, the compression data was recorded via starting measurements. This measurement was trained and helped by Dr Umair Zafar at University of Leeds, UK.

#### 5.4.3 Adsorption measurements

The adsorbents were tested via batch adsorption experiments. All model fuels were prepared by dissolving a desired amount of organosulfur in pure n-octane. Unless otherwise stated, standard experiments were carried out at room temperature, using DBT as a model organosulfur compound at a concentration of 500 ppm sulfur. For a standard adsorption experiment, the adsorbent (0.05 g) was added to the DBT solution and agitated at room temperature for 3 h, using a magnetic stirrer bar or an orbital shaker (Stuart SSL1, UK, 120  $\text{rpm}\cdot\text{min}^{-1}$ ). Each adsorption measurement was accompanied by a pure reference solution to account for potential non-adsorbent-related variations in DBT concentration. All sampled DBT solutions were centrifuged to sediment potential particle impurities. The DBT concentration was then measured via gas chromatography using an Agilent 7890B GC system with a HP-5 column (0.32 m diameter, film thickness of 0.25  $\mu\text{m}$ , 30 m in length, working temperature from 25 to 300  $^{\circ}\text{C}$ ). The amount of adsorbed DBT was calculated from the reduction in organosulfur GC peak area relative to the pure DBT reference. The effect of temperature on DBT sorption was tested at 25  $^{\circ}\text{C}$ , 50  $^{\circ}\text{C}$ , and 80  $^{\circ}\text{C}$  respectively. To determine adsorption kinetics, samples were agitated for 3 h and solution aliquots (0.6 mL) were sampled at defined time intervals. Curves were fitted according to the pseudo-second order model, given in Chapter 4 (Equation 4.1). For the adsorption isotherms, DBT sorption was tested, using a range of initial DBT concentrations (100, 200, 300, and 500 ppm S). Curves were fitted according to the Langmuir model, given

in Chapter 4 (Equation 4.3). Organosulfur selectivity testing was carried out using mixtures of DBT and BP in n-octane (500 ppm sulfur DBT, 2873 ppm BP). The simultaneous adsorption of DBT and DMDBT was measured at a total sulfur concentration of 500 ppm sulfur (i.e. using a mixture of 250 ppm sulfur DBT and 250 ppm sulfur DMDBT). Additional experiments were carried out to explore the uptake of other organosulfur compounds, including carbon disulfide, thiophene and 2,3-dimethylbenzthiophene. These experiments were carried using the respective pure organosulfur compound in n-octane solution at an initial concentration of 500 ppm S.

#### **5.4.4 Joule-heating of aerogel adsorbents**

To protect the samples during high-temperature Joule-heating (i.e. during heating above 320 °C), the set-up, described in Chapter 2, was placed in a custom-made airtight container that allowed connection to an external power source and constant flow of inert nitrogen gas (100 mL·min<sup>-1</sup>) during the heating experiments. Using this setup, BN/rCNT aerogels were electrically heated between 50-750 °C. To measure accurate Joule-heating characteristics, the electrical current through the aerogel was adjusted until a set temperature was reached. The sample was then left to equilibrate, before recording voltage and current. This procedure was repeated to heat the aerogel in 50 °C steps. Prior to a measurement series, the aerogel samples were preconditioned (Joule-heating to 200 °C for 20 min) in order to desorb any undesired impurities (e.g. water, CO<sub>2</sub> etc, see Appendix 3 Figure A3.5-A3.7) and obtain stable Joule-heating readings. For thermal aerogel regeneration post-adsorption, the BN/rCNT aerogels were removed from the organosulfur solution and mildly dried at 50 °C to remove residual n-octane. The BN/rCNT aerogels were then electrically heated to 400 °C for 1 h. After Joule heating regeneration, the intact aerogel was immersed into fresh DBT solution and the Joule heating procedure was repeated for five regeneration cycles.

## Chapter - 6

### High-Temperature Joule-Heating of Graphene Oxide Aerogels

In the previous chapters, Joule-heating of nanocarbon aerogels was systemically investigated in terms of structure-property relationships and was shown to be of great utility in gas-phase and liquid-phase adsorption applications. In the investigations so far, Joule-heating in intermediate temperature range between 100 - 700 °C has been exploited. However, the thermal stability of graphitic materials in inert conditions (sublimation temperature of graphite 3300 °C) allows in principle to reach (ultra-)high temperatures, i.e. temperatures above 1000 °C, via local electrical heating at higher electrical power inputs. The ultra-high temperature range is very challenging to achieve with conventional external heating technologies, such as standard furnaces. Joule-heating based high-temperature heating therefore offers great potential to open up a completely new range of Joule heating applications. This chapter will explore high-temperature Joule-heating and provide some first proof-of-principle evidence for its exploitation in a range of new applications, including nanocarbon graphitisation, nanocarbon welding and nanoparticle synthesis.

#### 6.1 Brief introduction

High-temperature heating of graphitic materials is of great practical importance. For example, high-temperature annealing treatments are essential to improve and tune graphitic crystallinity (graphitisation) of graphitic materials, e.g. in carbon-based high-performance aircraft brakes.<sup>326</sup> High-temperature furnaces (using in fact often graphite as external heating element) exist for such annealing treatments but are challenging to operate and have extremely high energy consumptions.<sup>127</sup> More direct electrical heating has proven a practically viable alternative to external heating. Of great practical importance for ceramics processing is spark plasma sintering (also known as pulsed electric current sintering), based on ultrafast, electrical heating of a graphite to very high temperatures in order to sinter and densify ceramic powders.<sup>327</sup> Direct high-temperature Joule-heating has also been explored to enhance properties of functional nanocarbon materials. For example, high-temperature Joule-heating (~2450 °C) at heating rate of 200 K·min<sup>-1</sup> has been exploited to induce covalent cross-linking in carbon nanofibers, resulting in considerable enhancements in mechanical strength, modulus and conductivities of the fibers.<sup>214</sup> Direct Joule-heating was also used to heat silica-coated carbon nanofiber frameworks to very high temperatures (~2000 K for 10 min) in order to

form sub-micron SiC particles (average size  $\sim 182$  nm), uniformly distributed across the surface of carbon fibers.<sup>328</sup> Joule-heating to extremely high temperatures of 3000 K has also been demonstrated for graphene films.<sup>213</sup> High temperature Joule heating ( $\sim 2000$  K, 55 ms) of carbon nanofiber films impregnated with metal salt mixtures was used to prepare high-entropy-alloy nanoparticles with excellent catalytic performance in ammonia oxidation.<sup>216</sup> Very high temperature Joule heating ( $>2800$  K, 30 min,  $\sim 20$  W) was also utilised for the ‘welding’ carbon nanotube in CNT films with the resulting materials showing improved performance as aqueous battery current collectors.<sup>329</sup>

These first application examples have mostly focused on nanocarbon films (carbon nanofiber, CNT, graphene etc). However high-temperature Joule-heating ( $>1000$  °C) of nanocarbon aerogels has not yet been demonstrated. This chapter will provide some first proof of principle data, exploring high-temperature Joule-heating for the example of hydrothermally synthesised GO aerogels. As outlined in Chapter 2, GO aerogels show excellent performance in adsorption, catalysis, energy storage, water treatment, and sensing. For many of these applications, the initial GO aerogels need to be thermally annealed in order to crosslink the aerogel network and (partially) restore graphitic properties (especially thermal and electrical conductivities as well as mechanical properties).<sup>300</sup> High-temperature thermal treatments are also important for the further chemical modification of the aerogels, for example through functional nanoparticle decoration (often achieved through thermal decomposition of precursor compounds on the aerogel framework).<sup>199</sup> Most reported studies have utilised thermal furnace treatment at temperatures  $<1000$  °C in these contexts, due to furnace limitations and high energy-consumption. In this work, direct high-temperature Joule-heating of hydrothermal GO aerogels will be explored for a range of diverse purposes, including graphitisation of the GO aerogels, fast sorbent regeneration, nanocarbon welding, and nanoparticle decoration (Figure 6.1).

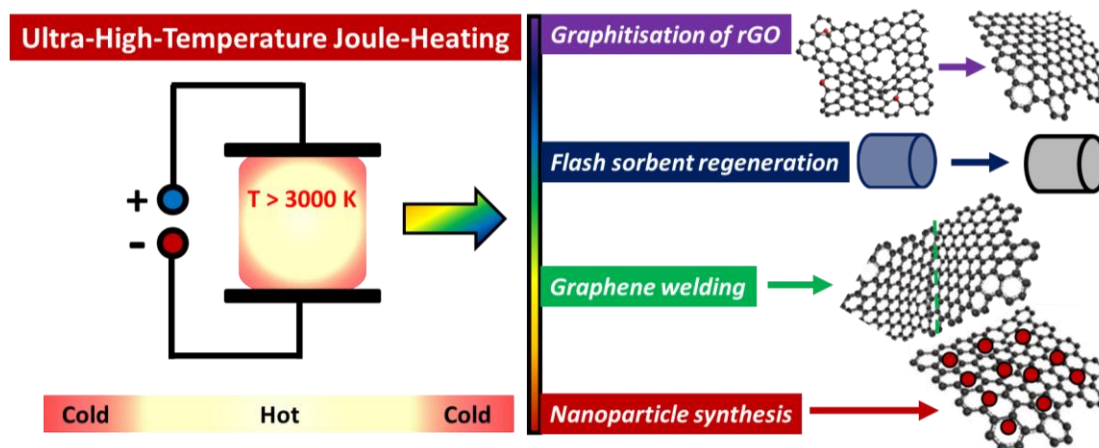


**Figure 6.1** High-temperature Joule-heating studies of GO-based aerogels in this chapter.

## 6.2 Results and Discussion

### 6.2.1 High-temperature Joule-heating of reduced GO aerogels

For the high-temperature studies, all aerogels were produced through a conventional hydrothermal synthesis approach at 50 °C, using ascorbic acid as chemical reducing agent (see Experimental). While hydrothermal synthesis leads to some degree of chemical reduction, the resulting GO aerogels (labelled GO[HT] aerogels for the remainder of this chapter) have relatively low electrical conductivity and show overall unstable electrical and electrical-heating behaviour (see Appendix 4, Figure A4.1). This electrical instability is most likely due to incomplete reduction under the relatively mild hydrothermal reaction conditions, leading to structural changes upon Joule-heating (further GO reduction, removal of remaining ascorbic acid impurities etc.) even under relatively moderately electrical heating currents. In order to obtain stable samples for our fundamental high-temperature studies, the GO[HT] aerogels were therefore thermally reduced via a conventional furnace treatment in H<sub>2</sub>/N<sub>2</sub> atmosphere at 1000 °C for 2 hours. These furnace-reduced samples are labelled rGO[HT] aerogels for the remainder of the chapter. The rGO[HT] aerogels possess excellent electrical and thermal conductivities as well as good structural stability, enabling to study electrical heating characteristic under high current and high temperature conditions.

The electrical heating behaviour of the rGO[HT] aerogel at high power inputs (>10 W) was then characterised within our custom-made electrical setup in inert nitrogen atmosphere. Specifically, Joule-heating of the rGO[HT] aerogel was measured at a high electrical current of 10.12 A in nitrogen. Under these high current conditions, the rGO[HT] showed a striking orange-white glow, indicating that very high temperatures are reached (Figure 6.2a).<sup>213</sup> This glow is stable over at least 60 sec in which the electrical current also remains stable (see Figure 6.2b). This stability indicates that the glow is not connected to nanocarbon combustion, but heat radiation, so called black body radiation.<sup>213</sup> The emission of orange-white radiation indicates that the temperature of the heated object near its surface is extremely hot. In fact, the aerogel core reaches such high temperatures that it cannot be measured by a conventional thermocouple which melted when inserted into the heated aerogel. The surface temperature could however be estimated via a surface temperature-power input correlation, reaching a high steady-state value of ~2030 °C under the applied high current conditions ( $I = 10.12$  A,  $V = 9$  V,  $P = 90$  W, Figure 6.3).

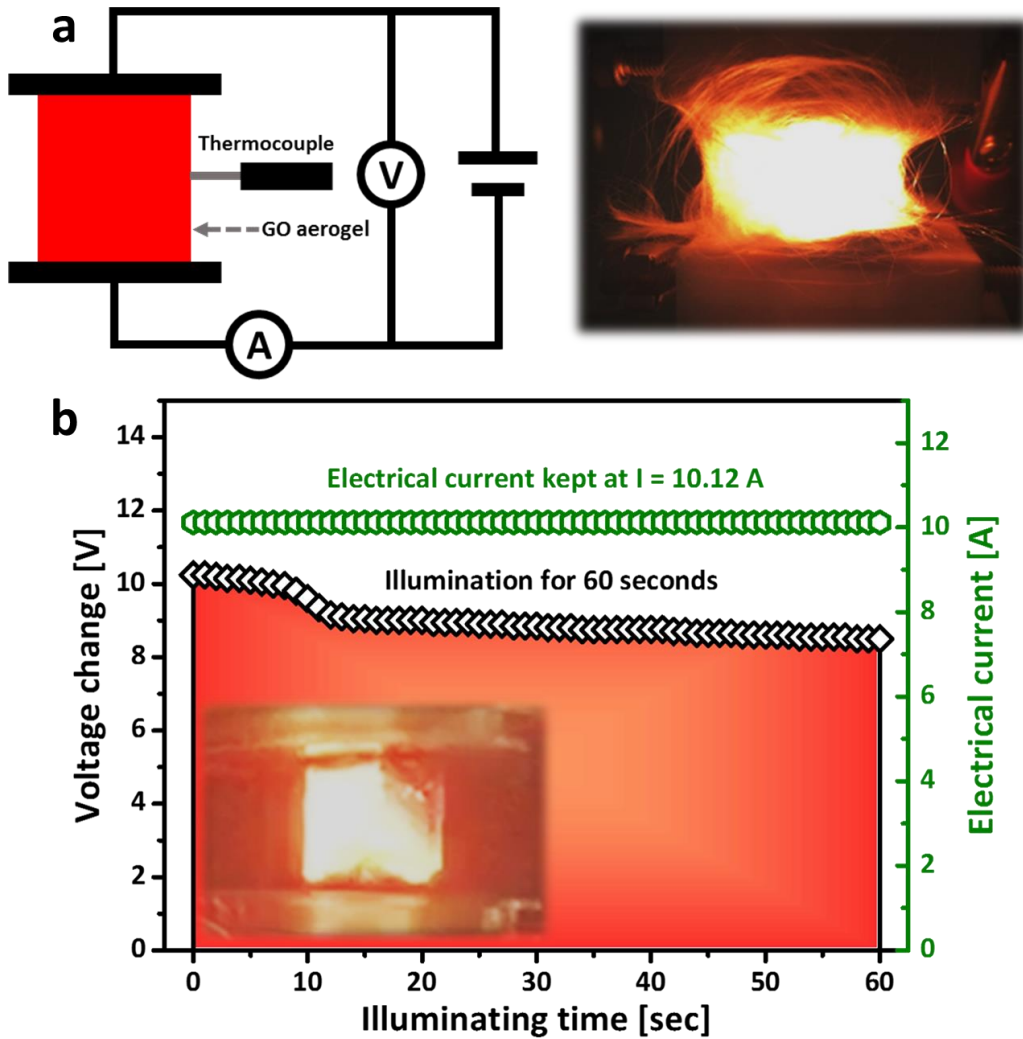


**Figure 6.2** (a) Schematic of an aerogel under flash Joule-heating and a digital picture of rGO[HT] aerogel under Joule-heating covered by glass wool. (b) Voltage and current for an rGO[HT] aerogel experienced 60 seconds long Joule-heating. Inset shows the black-body radiation.

As mentioned above the electrical current remains stable over the entire high-temperature heating period. At the same time, a 20 % reduction in voltage is observed, indicating that the resistivity of the rGO[HT] reduces over the heating period. This observation suggests that the high temperature heating leads to structural aerogel changes that give rise to an overall increase in the aerogel's electrical conductivity. The most likely origin for this change is that high temperature Joule-heating leads to additional nanocarbon reduction, impurity removal and crosslinking of the furnace-reduced rGO[HT] aerogel. The resulting 'double-reduced' sample (a furnace-reduced aerogel, additionally reduced through Joule-heating at a power input of 90 W for 60 seconds) was therefore labelled rrGO[HT] aerogel.

To explore the high-temperature Joule-heating more systematically, the aerogel surface temperatures were measured at slightly lower electrical power inputs

between 2 - 50 W for a fresh rGO[HT] and a rrGO[HT] aerogel (Figure 6.3). For both samples, Joule-heating temperature shows the same linear dependency on electrical power input. Heating efficiencies ( $dT_{\text{surface}}/dP$ ) are around  $22\text{ }^{\circ}\text{C}\cdot\text{W}^{-1}$ . It is worth noting that these efficiencies are lower than in the previous chapters, the aerogel measured here were produced at higher densities and show different crosslinking chemistry (based on reduction by ascorbic acid during hydrothermal aerogel synthesis rather than carbonised polymer residues as in the templated aerogel synthesis). The linear correlation between power input and Joule-heating temperature is slightly better for the doubly reduced rrGO[HT] aerogel (as indicated by the  $R^2$  correlation coefficients,  $R^2 > 0.990$  for the rGO[HT] aerogel,  $R^2 > 0.999$  for the rrGO[HT] aerogel), again suggesting additional reduction improved graphiticity. The increased graphitic crystallinity after high-temperature Joule-heating is also indicated by changes in electrical conductivity (Figure 6.3) for the rrGO[HT] aerogel sample which shows overall higher electrical conductivity (almost 4 times higher at room temperature),<sup>213</sup> compared to the furnace-reduced rGO[HT] aerogel sample. Raman and XPS measurements confirm the marked changes in nanocarbon reduction level and graphiticity of the rGO[HT] and rrGO[HT] samples.

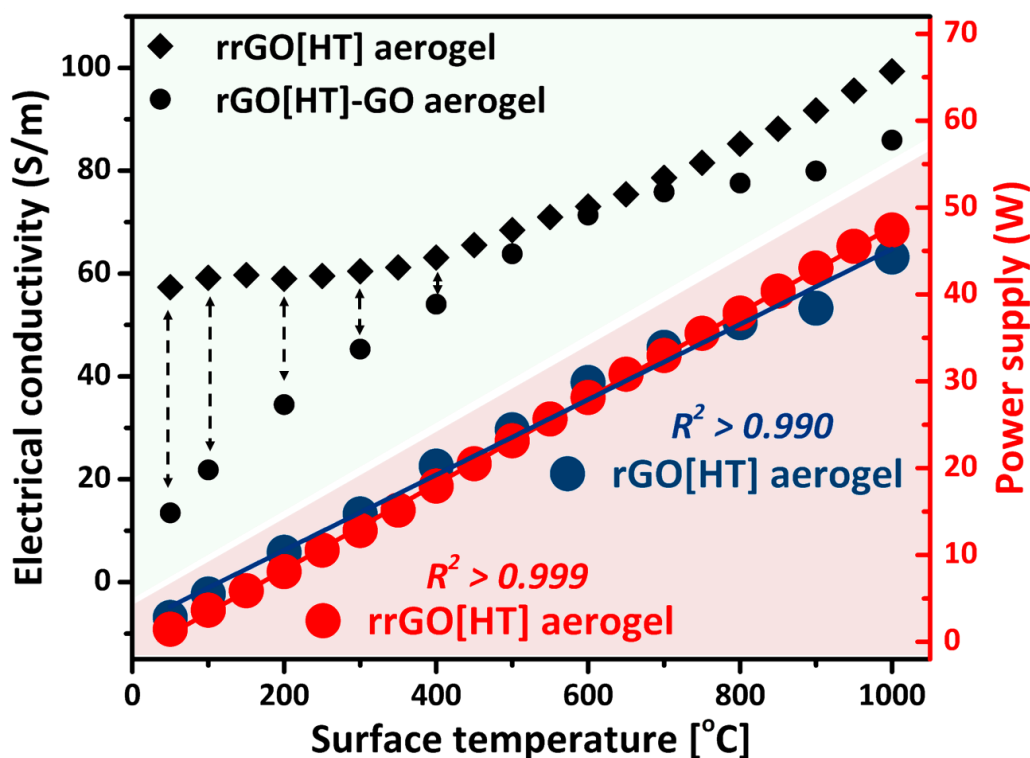


**Figure 6.3** Electrical conductivity and electrical power input versus Joule-heating temperature of rGO aerogel and rrGO aerogel.

XPS (Figure 6.4a, see Appendix 4, Figure A4.3) suggests that the furnace-reduced sample (rGO[HT] aerogel) has an already low oxygen content of around 2.0 at%, which can however be almost halved again to 1.1 at% after Joule-heating at 10.12 A

(rrGO[HT] aerogel). Raman indicates (Figure 6.4b) an even more dramatic change with a complete reversal in peak intensity (accompanied by a marked reduction in peak width) for the characteristic graphitic D and G peaks, confirming a significant increase in graphitic crystallinity induced by high-temperature Joule-heating at 10.12 A.<sup>213</sup> Due to its excellent graphiticity, the rrGO[HT] was taken forward for further studies, including Joule-heating kinetics and Joule-heating stability.

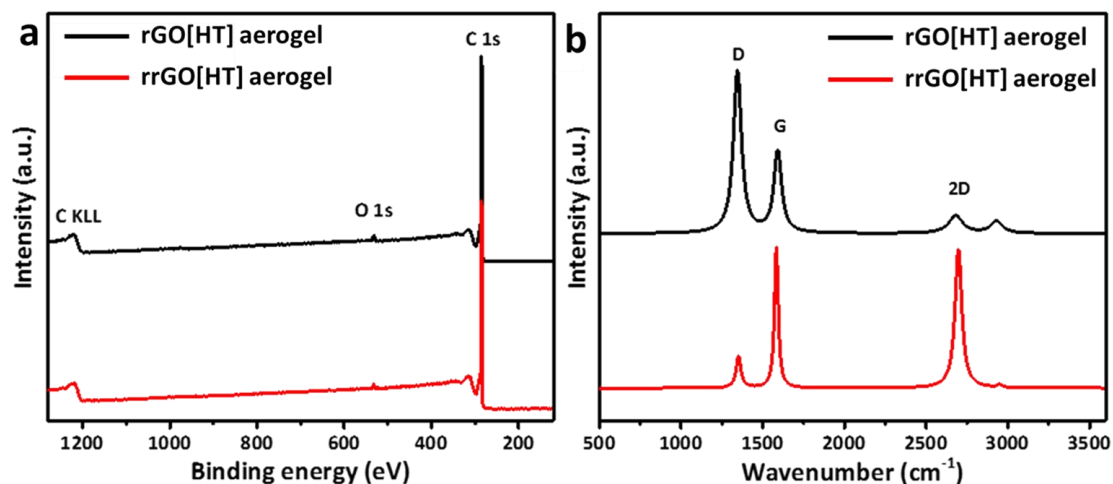


**Figure 6.4** (a) Raman spectra and (b) XPS full spectra of the rGO[HT] aerogel and rrGO[HT] aerogel.

Heating and cooling kinetics of the rrGO[HT] aerogel were measured as described in the previous chapters. A high heating current (here a power input of 46.85 W) was suddenly switched on to trigger instantaneous Joule-heating, with the aerogel surface temperature monitored by a thermocouple (Figure 6.5). Under these conditions, the rrGO[HT] aerogel reached its steady state temperature of 1050 °C within less than 10 seconds at an extremely fast heating rate of 120 °C·s<sup>-1</sup> (equivalent to 7200 °C·min<sup>-1</sup>). Cooling kinetics from 1050 °C in nitrogen atmosphere were measured by switching of the heating current and monitoring temperature decrease. In contrast to observations in the previous chapters, cooling kinetics are significantly slower than the observed heating kinetics. Cooling from 1050 °C to about 100 °C (a temperature sufficiently low to arrest many high-temperature processes, such as thermally-induced graphitisation) occurs at an estimated heating rate of about 24 °C·s<sup>-1</sup> (equivalent to about 1450 °C·min<sup>-1</sup>). While still very fast (in fact faster than the cooling rates observed in the previous chapters), the cooling rates are an order of magnitude lower than the heating rates. The most likely reason is that the metallic electrodes holding the aerogel act as heat sinks during the experiments. During the high-temperature heating experiment the electrodes take up and store a large amount of heat. Once the heating current is switched off, the highly porous, thermally conductive aerogel is likely to cool down faster than the dense solid

electrodes, resulting in some heat transfer back from the hot electrodes into the cooling aerogels, thereby slowing the aerogel's cooling kinetics.

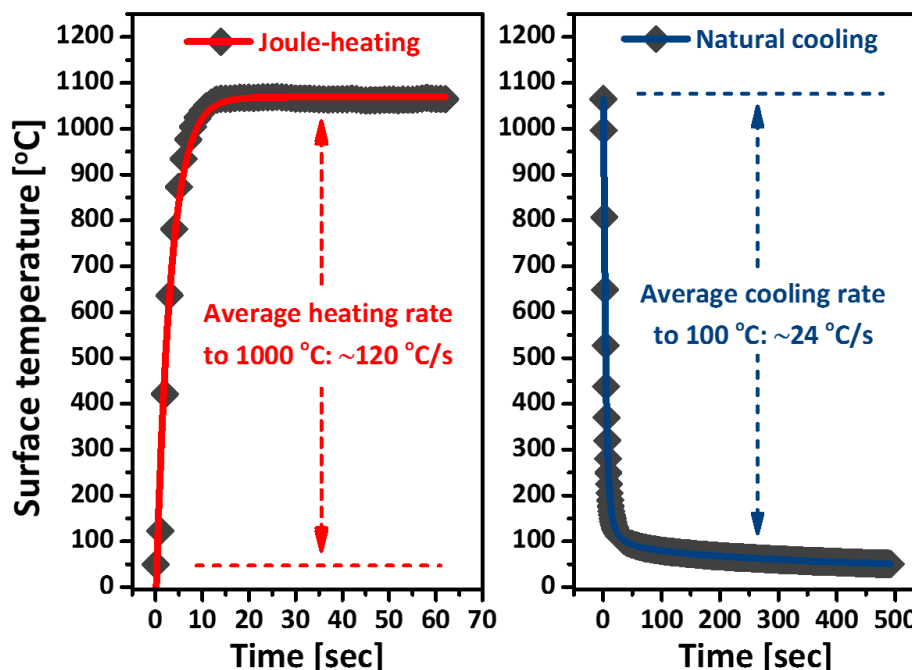


**Figure 6.5** Surface temperature Joule-heating kinetics of the rrGO[HT] aerogel at 46.85 W electrical power input and corresponding cooling curves.

Aerogel surface temperatures above 1000 °C are also easily achieved through Joule-heating. The temperature of the aerogel surface can be readily and repeatedly controlled between 1000 °C and 1200 °C by selection of the electrical power input (Figure 6.6), with the rrGO[HT] aerogel reaching a temperature of 1200 °C at a power input of around 57 W.

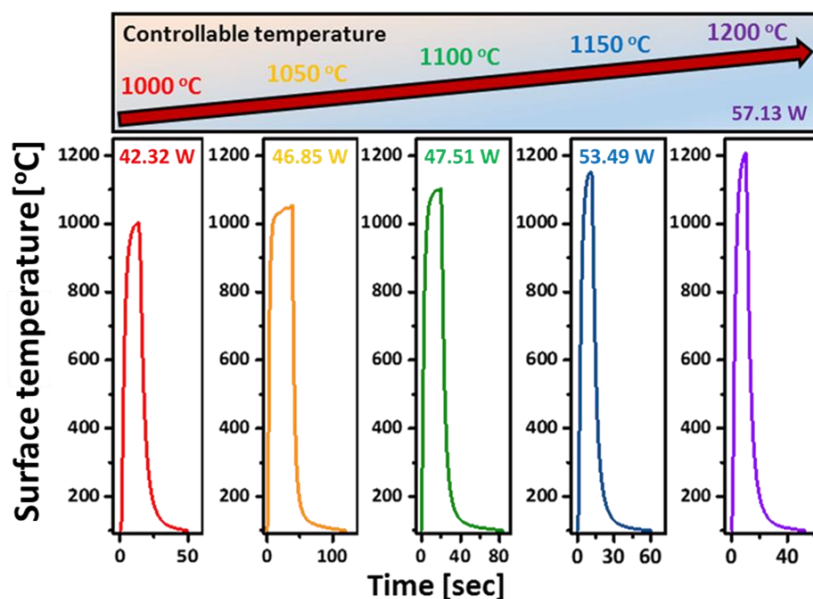


**Figure 6.6** Controlled high-temperature Joule-heating from 1000 °C to 1200 °C at 50 °C increments controlled through electrical power input.

Importantly, these high temperatures can be reached in a reliable and repeatable manner. For example, the aerogel can be accurately heated to 1200 °C more than 10 times in a row (Figure 6.7a). In addition, the fast heating and cooling kinetics enable rapid high-temperature cycling of the aerogels. One cycle of heating to 1200 °C and cooling down to ambient temperature can be completed in less than 1 minute (Figure 6.7a), an extremely short duration not accessible through external heating technologies. Even faster cycling kinetics are potentially possible, but would require a redesign of the electrodes (e.g. thinner, mesh-like electrodes) in order to minimise issues with heat transfer back into the electrodes.

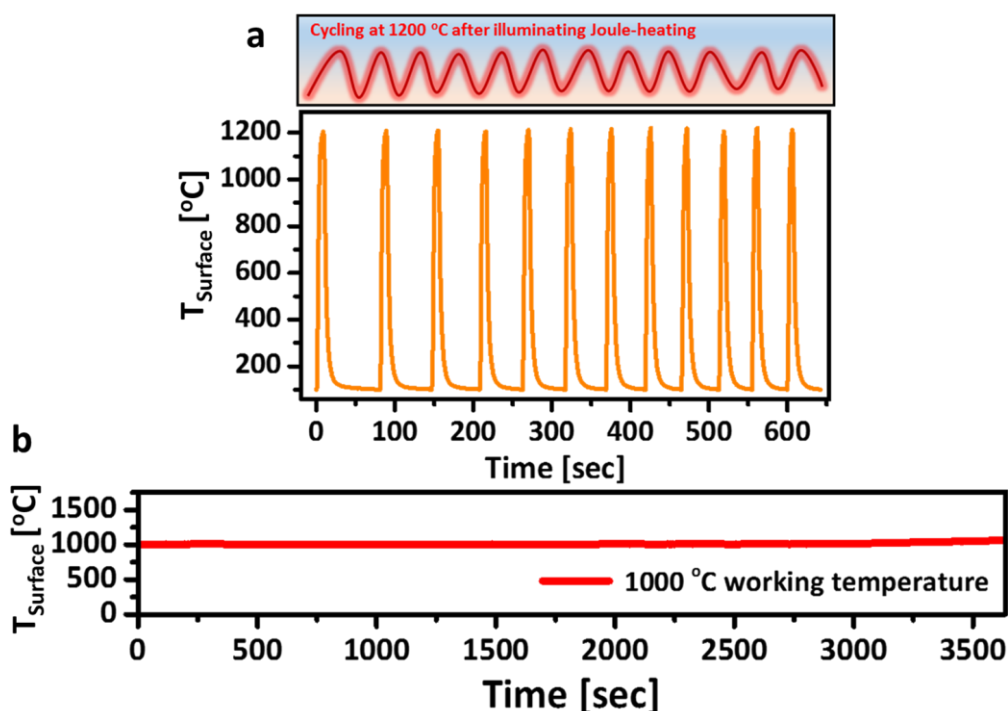


**Figure 6.7** (a) Rapid thermal cycling between room temperature and 1200 °C of the rrGO aerogel. (b) Long-term (1 hour) Joule-heating stability of the rrGO aerogel at 1000 °C.

Importantly, high-temperature Joule-heating can also be reliably carried out over long time periods if required. For example, the rrGO[HT] aerogel can be kept at a constant working temperature for an hour and longer (Figure 6.7b). This excellent stability of high-temperature aerogel heating, both on very short and very long time scales, opens up a number of routes for high-temperature applications, some of which will be explored in the following sections of this chapter.

## 6.2.2 High-temperature Joule heating of un-reduced GO[HT] aerogels

Importantly, high-temperature Joule-heating can be directly utilised for the high-temperature annealing step of the GO[HT] aerogel synthesis procedure, without the need for any conventional furnace treatment. All samples investigated so far had

been pre-annealed in a furnace at 1000 °C to obtain stable samples for our initial high-temperature investigations. In a new study, a freshly synthesised GO[HT] aerogel (not pre-annealed) was investigated in our Joule-heating setup in nitrogen atmosphere. As mentioned above, the un-annealed GO[HT] aerogels exhibit relatively low electrical conductivity due to incomplete reduction during the hydrothermal synthesis and ascorbic acid residues remaining within the aerogel interior.<sup>129</sup> These features make the un-annealed aerogels relatively unstable in conventional current step experiments (carried out in previous chapters to pre-condition samples and collect Joule-heating responses). In fact, when slowly increasing current and, therefore, Joule-heating temperature of the aerogels tended to completely break down at 400 °C (see Appendix 4, Figure A4.1), most likely due to melting of ascorbic acid residues within the aerogel interior, leading to violent sparking and structural collapse.

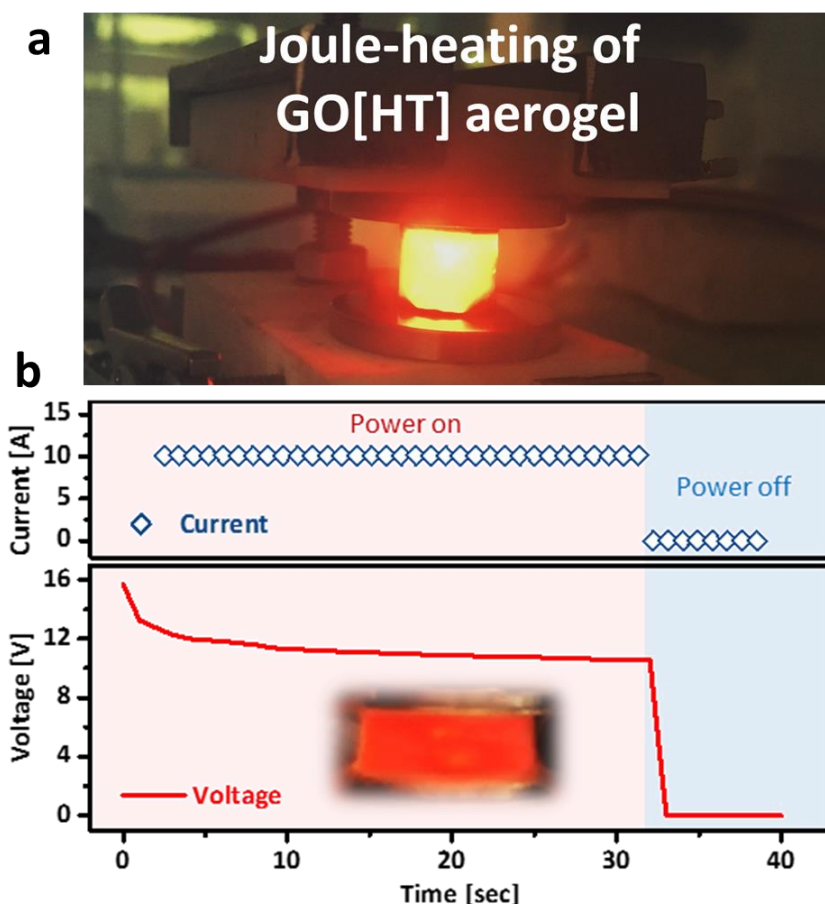


**Figure 6.8** (a) Digital photo of a GO[HT] aerogel under flash Joule-heating at  $I = 10.12$  A. (B) The electrical current and voltage curves of a GO[HT] aerogel under 30 seconds Joule-heating with strong black-body irradiation. The resulting aerogel is referred to as GO[30sec] aerogel for the rest of this section.

However, the GO[HT] aerogels can be annealed through application of large current for relatively short time ('Flash Joule-Heating'). Specifically, the GO[HT] aerogel was

treated at an electrical power input of  $P = 120 \text{ W}$  for 30 seconds (Figure 6.8). As before, a characteristic black body radiation (strong orange glow) is observed, indicating that high-temperature Joule heating is successful (reaching again a surface temperature of around  $1253 \text{ }^\circ\text{C}$ , Figure 6.8a). Over the heating period, electrical current remains stable while a clear 30 % decrease in applied voltage is observed, indicating that annealing/graphitisation is successful (Figure 6.8b).

The resulting, flash-heated aerogel (referred to as GO[30sec] aerogel in this section) showed substantially increased electrical conductivities ( $\sigma = 84 \text{ S}\cdot\text{m}^{-1}$  at ambient temperature), more than an order of magnitude higher than that of the original GO[HT] aerogel ( $\sigma = 1.6 \text{ S}\cdot\text{m}^{-1}$ , Figure 6.9, Table 6.1). Additionally, the electrical conductivity of the GO[30sec] aerogel is gradually increasing with Joule-heating temperature arising as shown in Figure 6.9, confirming its semiconducting behaviours. In fact, temperature dependent measurements of conductivity indicate that the rGO bandgap has significantly decreased from 0.09 eV in the GO[HT] aerogel to only 0.01 eV in the GO[30sec] aerogel (see Appendix 4, Figure A4.4).<sup>213</sup> Importantly, the resulting electrical conductivity of the 30-seconds flash Joule-heated aerogel is comparable to the furnace-annealed rGO[HT] aerogels, produced via conventional external heating treatment at  $1000 \text{ }^\circ\text{C}$  for 2 hours. In other words, flash Joule-heating for 30 seconds gives comparable annealing results to the much longer (15,000 times longer) conventional furnace treatment, dramatically reducing process duration and energy consumption.

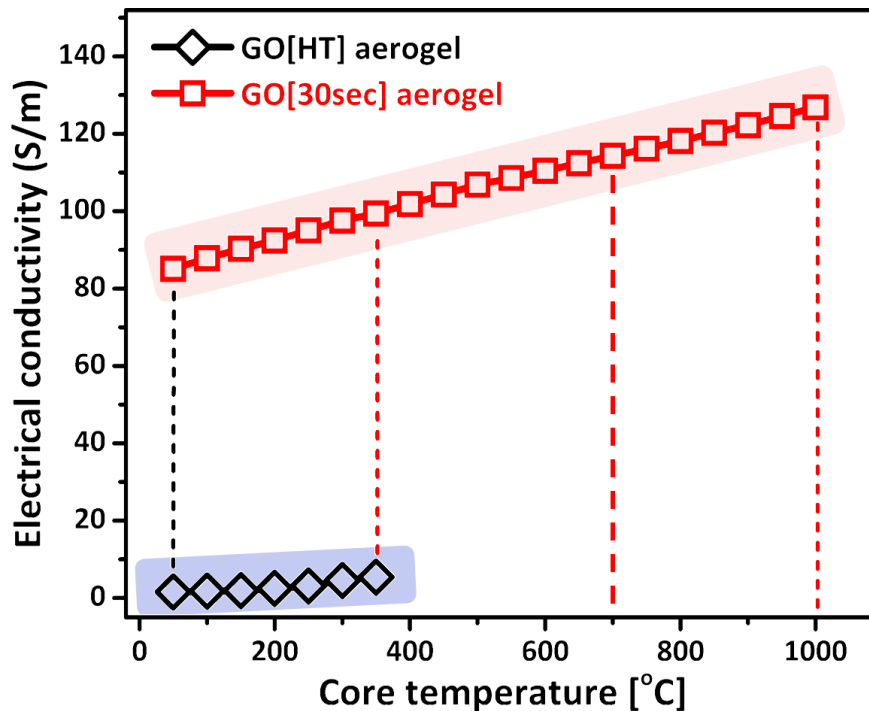


**Figure 6.9** Electrical conductivity/density of GO[HT], GO[HT] after preconditioning and GO[30sec] aerogels as function of Joule-heating core temperature.

**Table 6.1** Parameters of GO[HT] aerogel and GO[30sec] aerogel, including electrical conductivity ( $\sigma$ ), specific surface area (SSA), Volume of meso-porosity ( $V_{\text{Meso-porosity}}$ ), micro-pore volume ( $V_{\text{micro}}$ ) and average pore size ( $D_p$ ).

Name	$\sigma$ ( $\text{S}\cdot\text{m}^{-1}$ )	SSA ( $\text{m}^2\cdot\text{g}^{-1}$ )	$V_{\text{Meso-porosity}}$ ( $\text{cm}^3\cdot\text{g}^{-1}$ )	$V_{\text{micro}}$ ( $\text{cm}^3\cdot\text{g}^{-1}$ )	$D_p$ (nm)
GO[HT] aerogel	84	68.1	0.34	0.0018	68.4
GO[30sec] aerogel	1.6	634.3	1.93	0.0224	39.7

The success of aerogel annealing after only 30 second heat treatment manifest itself also in a number of other, dramatically changed aerogel materials characteristics (Figure 6.10, Table 6.1). For example, the surface characteristics of the aerogel are completely reversed, as indicated by water contact angle measurements (Figure 6.10a-6.10b). While the original GO[HT] aerogel is completely hydrophilic ( $\theta = 0^\circ$ ), the flash-annealed sample shows pronounced hydrophobic character with a water contact angle of  $\theta = 143^\circ$ . The flash heating treatment also results in substantial increases in specific surface area, meso-pore volume and micro-pore volume of the aerogels (as determined from the liquid nitrogen adsorption isotherms, Figure 6.10c-6.10d) by an order of magnitude in each case (Table 6.1). These large increases are most likely due the removal of ascorbic acid residues (which are extremely difficult to remove through washing procedures), that had blocked surface area and pores in the un-annealed samples.

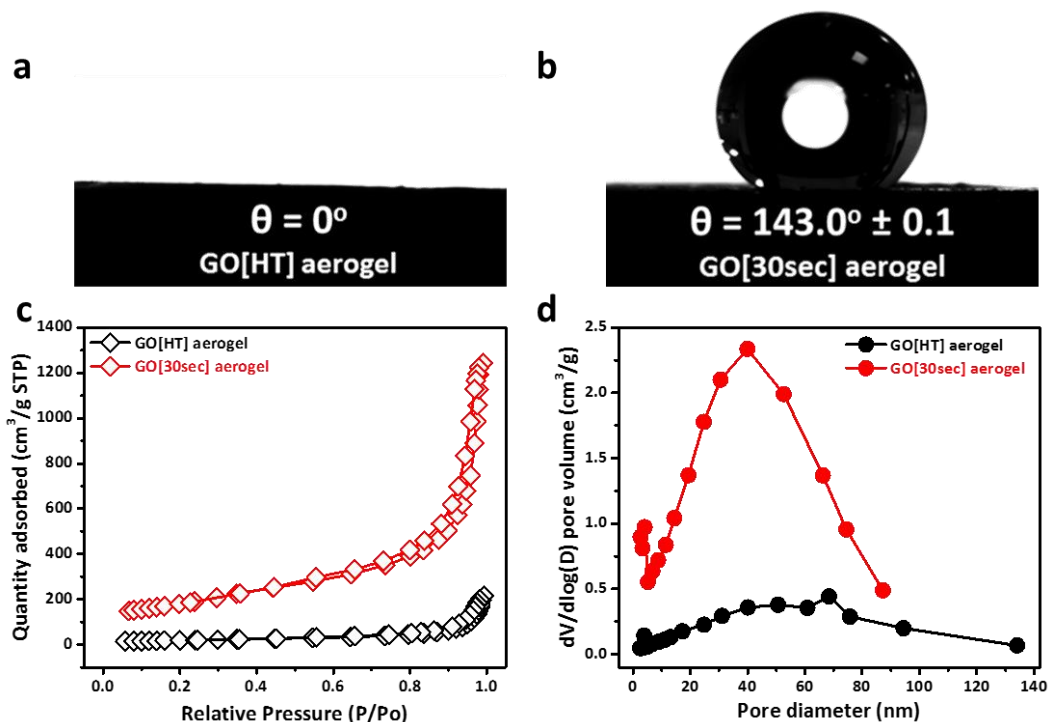


**Figure 6.10** (a-b) Contact angles of GO[HT] aerogel and GO[30sec] aerogel. (c-d) Nitrogen adsorption-desorption curves and pore size distributions of GO[HT] aerogel and GO[30sec] aerogel.

In terms of Joule-heating characteristics, the flash-annealed GO[30sec] aerogel shows also excellent performance (Figure 6.11), comparable to the furnace-annealed rGO[HT] aerogels (Figure 6.3 and 6.9, see Appendix 4, Figure A4.2).

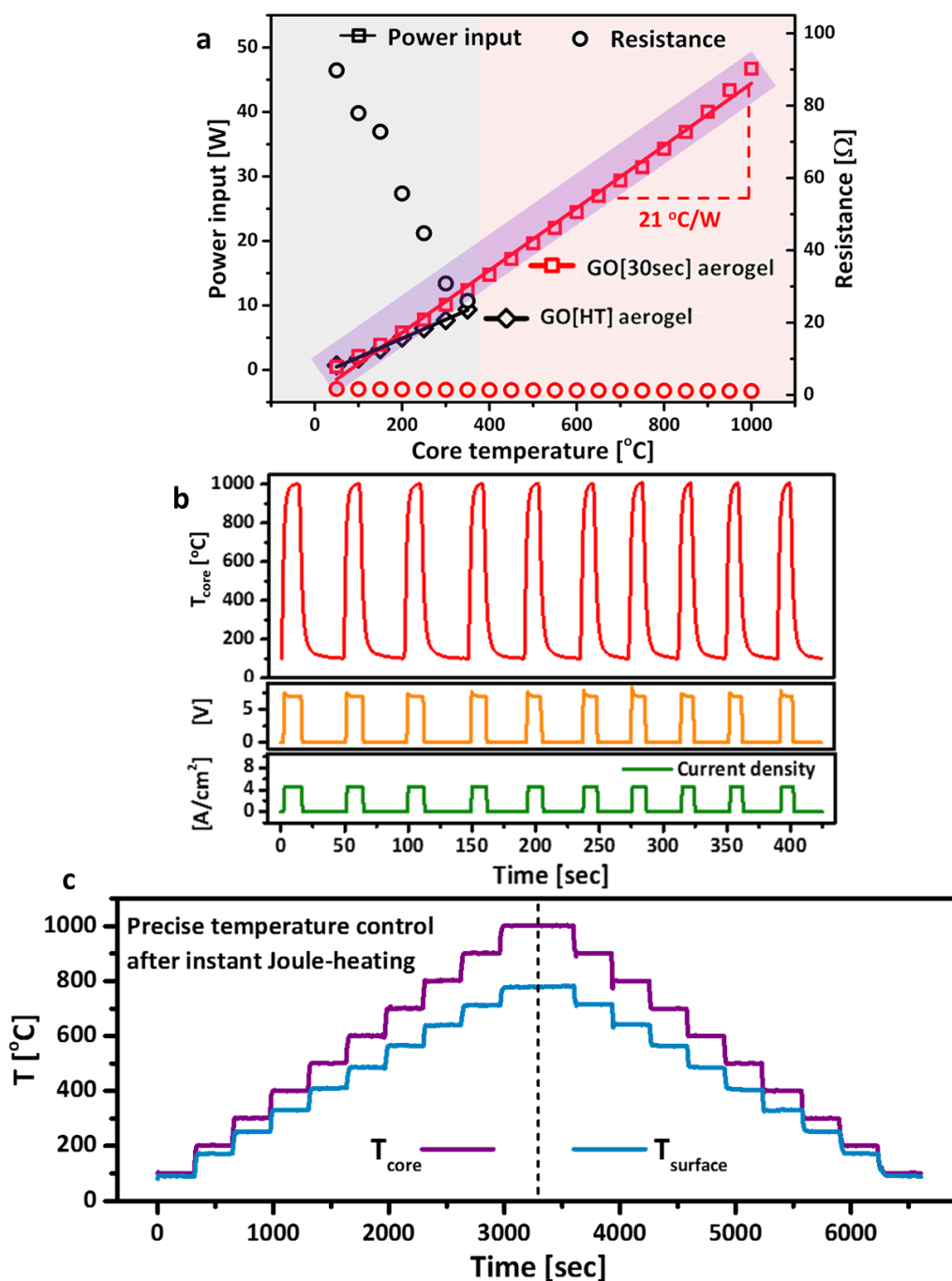


**Figure 6.11** (a) Joule-heating core temperature versus electrical power input and resistance of GO[HT] aerogel (black), GO[HT] aerogel after preconditioning (blue) and GO[30sec] aerogel (red). (b) Joule-heating cycling of GO[30sec] aerogel at core temperature  $1000\text{ }^{\circ}\text{C}$ . (c) Precise Joule-heating temperature control of GO[30sec] aerogel.

The GO[30sec] aerogels show a linear relationship between electrical input power and Joule-heating core temperature (Figure 6.11a), with a heating efficiency of  $dT_{\text{core}}/dP = 21\text{ }^{\circ}\text{C}\cdot\text{W}^{-1}$ . The flash annealed aerogels also show fast cooling and heating

kinetics that enable rapid thermal cycling between room temperature and 1000 °C (Figure 6.11b). Importantly, the flash-annealed GO[30sec] aerogels can be reliably Joule-heated to any given temperature up to 1000 °C with excellent temperature stability over heating periods of 1 hour or more across the whole temperature range (Figure 6.11c).

### **6.2.3 Joule-heating annealing of GO[HT] aerogels at prolonged heating duration**

The Joule-heating experiments described in Figure 6.9 and Figure 6.11 were carried out at high power inputs of up to 50 W. However, the GO[30sec] aerogels can be readily heated at even higher power inputs > 100 W. At these power inputs, core temperatures become too hot to be measured by a thermocouple. However, a simple estimate of the core temperature under these high power inputs can be obtained from the linear correlation between power input and Joule-heating core temperature, observed for the GO[30sec] aerogel in Figure 6.11a. The corresponding heating efficiency value of  $dT_{\text{core}}/dP = 21 \text{ } ^\circ\text{C}\cdot\text{W}^{-1}$  suggests that an extremely high core temperature of  $\sim 2520 \text{ } ^\circ\text{C}$  is reached at an electrical power input of 120 W (the power input used to produce the GO[30 sec] sample in the first place). While this estimate is only very approximate (as it does not take into account the change in electrical and thermal conductivity with increasing temperature), it clearly shows that under these conditions ultrahigh temperatures are reached in the aerogel core (in fact temperatures that would be challenging to obtain with conventional external heating methods). To study how the graphitic structure of the aerogels evolves at prolonged exposure to such ultrahigh temperatures, a set of three different GO aerogels were prepared. The first sample studied is the as-synthesised GO[HT] aerogel (before any annealing has been carried out), acting as a control sample. The second sample is the GO[30sec] aerogel discussed in the previous section, i.e. a GO[HT] aerogel that was Joule-heating annealed for 30 seconds at 120 W (aerogel core temperature at least 2500 °C). The third sample is the GO[300sec] aerogel, i.e. a GO[HT] sample that was Joule-heating annealed at 120 W ( $T_{\text{core}} > 2500 \text{ } ^\circ\text{C}$ ) for 300 seconds (10 times longer than the GO[30sec] aerogel), to assess impact of prolonged exposure to such high heating temperatures.

As expected, the GO[HT], GO[30sec] and GO[300sec] aerogels showed significant differences in their graphitic structure, as indicated for example by characterisation of their combustion behaviour in air via TGA (Figure 6.12). For the un-annealed GO[HT] aerogel, the TGA profile shows three distinct weight loss stages (which are more clearly seen in the corresponding differential TGA profiles): 1) weight loss at around 80 °C due to evaporation of residue water; 2) weight loss at around 250 °C

associated with the combustion of ascorbic acid residues and loss of GO oxygen groups; 3) weight loss at around 570 °C due to combustion of remaining GO (Figure 6.16a). For the flash-Joule heated GO[30sec] aerogel (Figure 6.16b), TGA indicates that there are no water and ascorbic acid residues left, consistent with the discussions above. However, GO combustion occurs in two distinct phases, with a smaller weight loss at around 570 °C and a major weight loss at 710 °C. The first phase likely relates to some small amount of not fully reduced GO (containing more defects and therefore combusting at lower temperatures). The second stage occurs at relatively high combustion temperature, indicating the presence of highly annealed and very crystalline rGO. For the GO[300sec] aerogel (Figure 6.16c), combustion only occurs at this higher temperature of 710 °C, indicating that resulting material shows excellent graphitic crystallinity, with no partially reduced GO remaining. The corresponding heat-flow profiles confirm these observations with two distinct exothermic events (i.e. combustion events) observed for the GO[30sec] aerogel while the GO[300sec] aerogel only shows one pronounced heat-flow peak at high temperature.

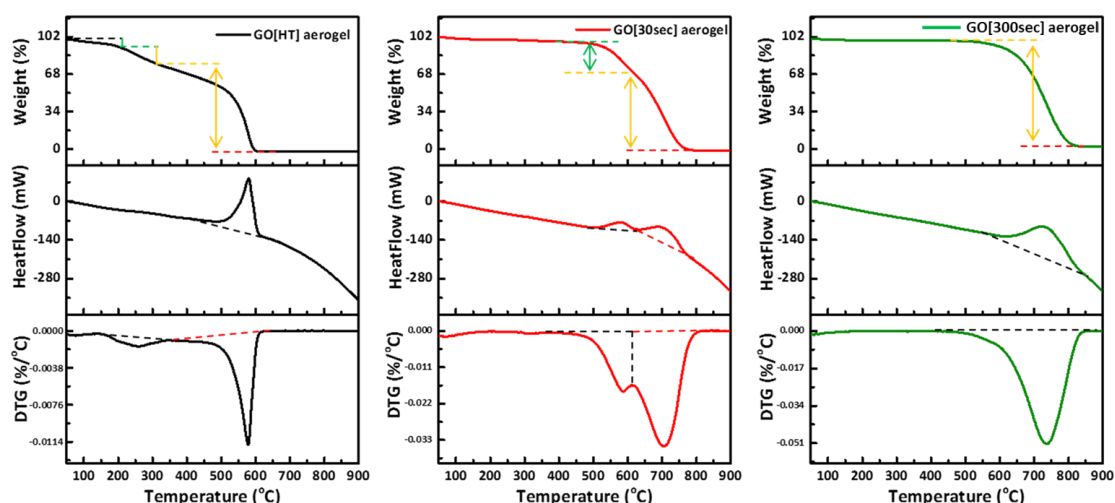


**Figure 6.12** TGA, heat-flow profiles and DTGA traces of GO[HT] aerogel (a), GO[30sec] aerogel (b) and GO[300sec] aerogel (c).

TGA-FTIR measurements of the same three samples in air further confirm these observations. The TGA-FTIR technique analyses the gases that evolve during TGA via IR spectroscopy (Figure 6.13). The gases evolved from all samples show the two prominent IR peaks at  $\sim 650\text{ cm}^{-1}$  and  $\sim 2350\text{ cm}^{-1}$ , confirming that only  $\text{CO}_2$  is generated during aerogel combustion,<sup>330</sup> in line with presence of (reduced) GO and minor organic impurities. As observed in the TGA profiles, the evolution of  $\text{CO}_2$  is observed at later times (i.e. at higher TGA temperatures) for GO[300sec] aerogel samples, confirming a high degree of graphitisation in this sample.

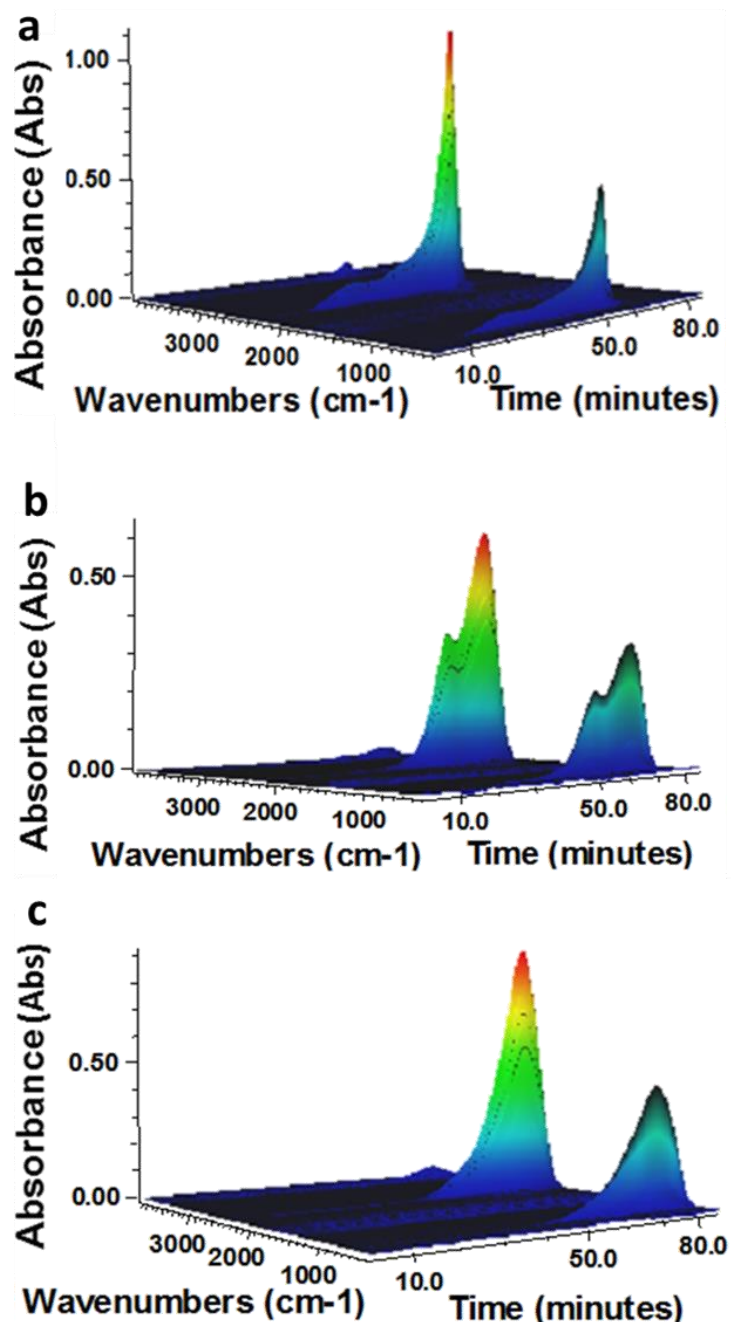


**Figure 6.13** TGA-FTIR of (a) GO[HT] aerogel, (b) GO[30sec] aerogel and (c) GO[melted] aerogel in air. The time axis relates to the TGA temperature (0 min equivalent to a TGA temperature of 20 °C, 80 min equivalent to a TGA temperature of 800 °C). The wavenumber and absorbance axis relate to the IR spectroscopic analysis of the gases evolved at different TGA temperatures.

Striking differences are also indicated by Raman mapping of aerogel fragments, sampled from the aerogel cores. The Raman maps in Figure 6.14 visualise the intensity ratio of the 2D peak to the G peak ( $I_{2D}/I_G$ ) across a 50  $\mu\text{m}$  x 50  $\mu\text{m}$  aerogel flake area. The  $I_{2D}/I_G$  ratio is related to the defectiveness of graphitic materials, with a high ratio (indicated by yellow and green colours in Figure 6.17) indicating high low concentrations in the graphitic sheets, while small values (indicated by blue colour)

indicate very low defect concentrations and large domains of perfect  $sp^2$  hybridisation within the graphene sheets.<sup>331</sup> The Raman maps confirm a high level of graphitic defects within the original GO[HT] aerogel. In contrast, the Joule-heating annealed samples show clearly improved graphiticity, with the longer heating duration of 300 seconds particularly effective. It is worth noting that not only the average defect level is reduced at the prolonged Joule-heating annealing, but that the longer treatment also results in a structurally more homogeneous sample (as indicated by a more uniform colour distribution in the Raman map of the GO[300sec] aerogel). Overall, these results confirm that high-temperature Joule-heating for prolonged time is extremely effective in producing graphene-based materials with excellent graphitic crystallinity.

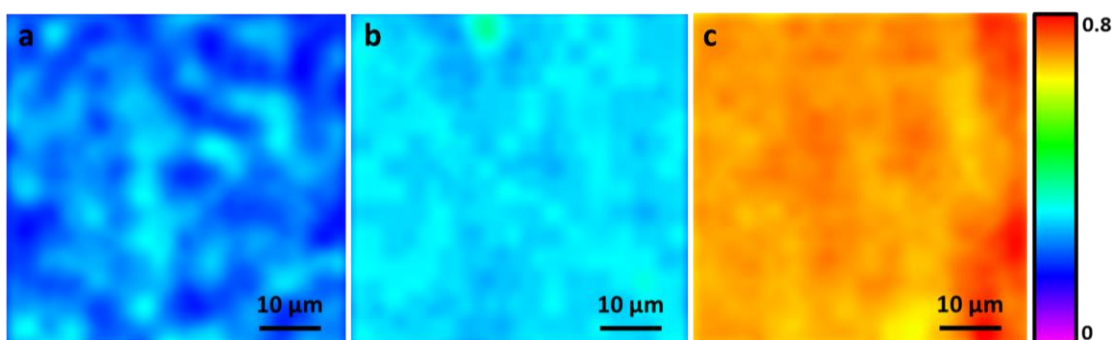


**Figure 6.14** Raman maps of the intensity ratio of the 2D peak to the G peak ( $I_{2D}/I_G$ ) for the GO[HT] aerogel, GO[30sec] aerogel and GO[300sec] aerogel, accordingly.

Further indications that prolonged Joule-heating induces pronounced changes in graphitic nanostructure are indicated by TEM imaging of aerogel fragments. For the GO[HT] (Figure 6.15a), TEM imaging shows graphene-layer stacks with a thickness of  $\sim 4.7$  nm. This stack thickness is equivalent to about 14 stacked graphene layers, indicating that the hydrothermally produced aerogels consist of ‘nano-graphite’ sheets (rather than mono-layer or few-layer graphene sheets). It is worth noting that for this sample contrast is relatively poor, with lattice planes almost not distinguishable, suggesting a high degree of defectiveness in this material, in line with the discussions above. Upon 30 second Joule-heating, the stack thickness increases to  $\sim 6.4$  nm (Figure 6.15b), likely due to thermally induced re-stacking of sheets. This effect is even more pronounced in the GO[300sec] aerogel, where the graphene layers substantially increased to  $\sim 19.5$  nm, potentially due to stacking of two graphene layer stacks together (Figure 6.15c).<sup>214</sup> In the GO[300sec] sample, graphitic lattice planes show a very clearly visible at strong contrast, further confirming highly efficient annealing to produce a highly crystalline material. In the two Joule-heated samples, there are also some first suggestions that graphene sheets have been welded together due to the ultrahigh Joule-heating temperatures reached during the annealing treatment.<sup>214</sup> While most graphene stacks in the TEM

images overlap, there are some preliminary indications for some welded junctions in the TEM images of the GO[30sec] and GO[300sec] aerogels (see Figure 6.15b-6.15d, and see Appendix 4 Figure A4.5-A4.7 for more discussion from SEM, XRD, Raman, TEM and XPS). However, more detailed high-resolution TEM imaging is required to confirm these preliminary indications.

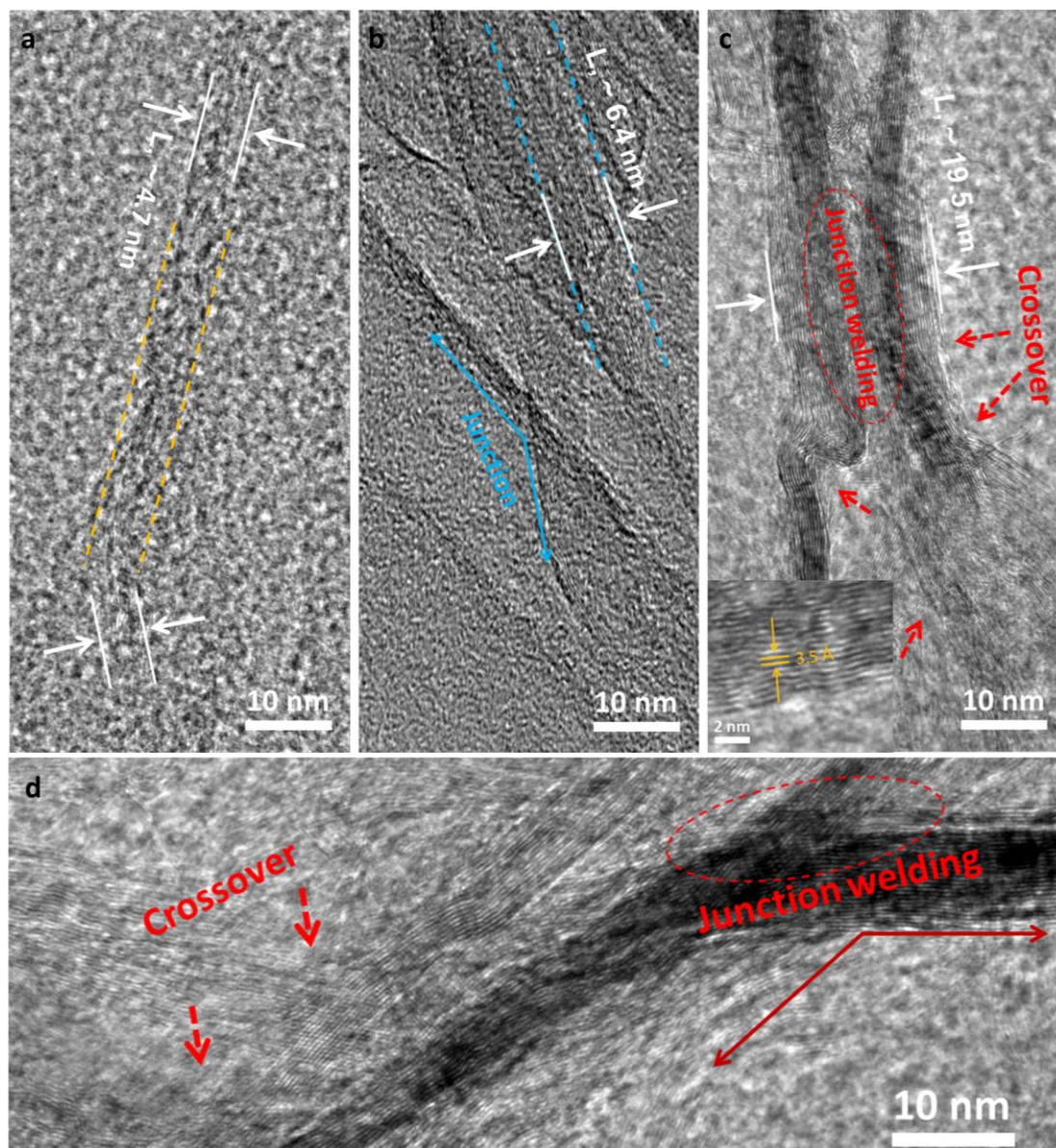


**Figure 6.15** High resolution TEM images of GO[HT] aerogel (a) and GO[30sec] aerogel (b). High resolution TEM images of GO[300sec] aerogel with observed graphene sheet welding, such as increased graphene sizes and crossover areas (c-d).

The combination of TGA, Raman mapping and TEM characterisation very clearly shows that the ultrahigh temperature Joule-heating is extremely effective in graphene annealing, enabling to produce high quality rGO aerogels with extremely high graphitic crystallinity, difficult to achieve through other annealing approaches.

### 6.2.4 Flash sorbent regeneration

To demonstrate another exploitation route for high-temperature Joule-heating, the ultrafast regeneration of rGO aerogel sorbents was studied. As mentioned in Chapters 4 and 5, pure rGO aerogels are not efficient in adsorbents for CO<sub>2</sub> or organosulfurs in their pure, unfunctionalized form. However, GO-based materials show excellent performance for the adsorption of many commercially important dyes from aqueous solution, an important challenge for the water treatment of dye effluents in the textile industry.<sup>332</sup>

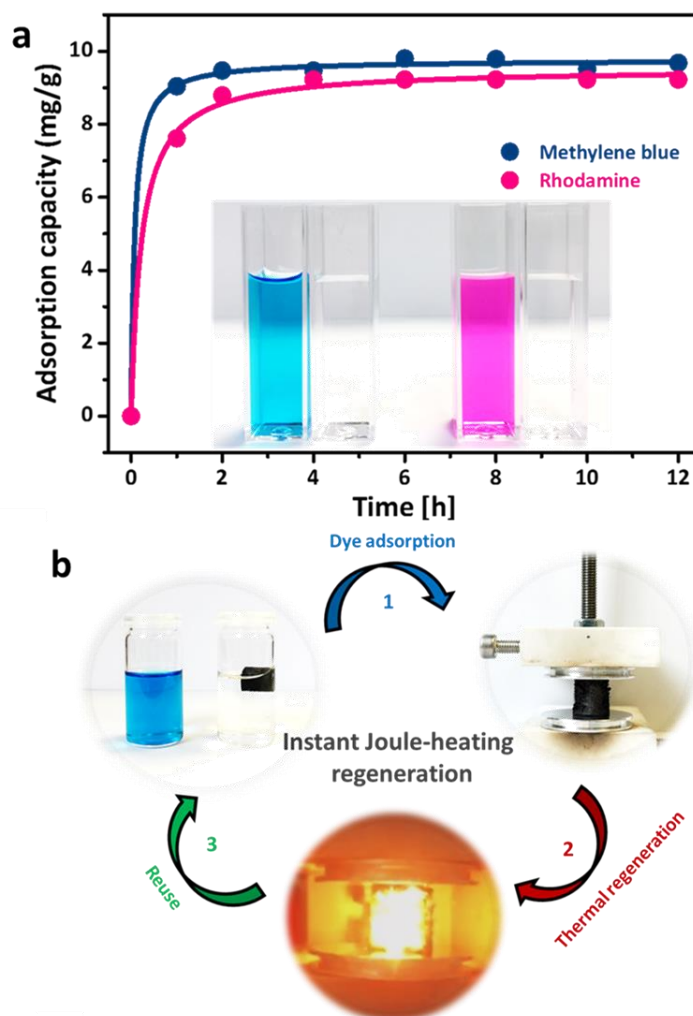


**Figure 6.16** (a) Adsorption kinetics of methylene blue and rhodamine onto rGO aerogels. (b) Schematics of flash Joule-heating regeneration of dye-saturated rGO aerogels.

Here, the rGO[HT] aerogels (here referred to as rGO aerogels for simplicity) were used to adsorb two different dyes, e.g. methylene blue (MB) and Rhodamine B, from water (Figure 6.16a). At the concentrations explored, the rGO aerogels showed excellent dye uptake, leading to complete removal of the dyes from aqueous solution after two hours (see Figure 6.16a). The post-sorption rGO aerogels were then heated in inert atmosphere within our Joule heating set-up (Figure 6.16b).

Specifically, the exhausted rGO aerogel was Joule heated at a power input of 120 W for 30 seconds (similar to the conditions used for the flash annealing of the GO[HT] aerogels). As before, an intense yellow-white glow indicated that ultrahigh temperatures ( $T_{\text{core}} > 2500\text{ }^{\circ}\text{C}$ ) were reached. At these temperatures, any adsorbed dye molecules are immediately and completely decomposed. The digital photo of an rGO aerogel emitting black body radiation in Figure 6.16b clearly visualize the thermal regeneration process.

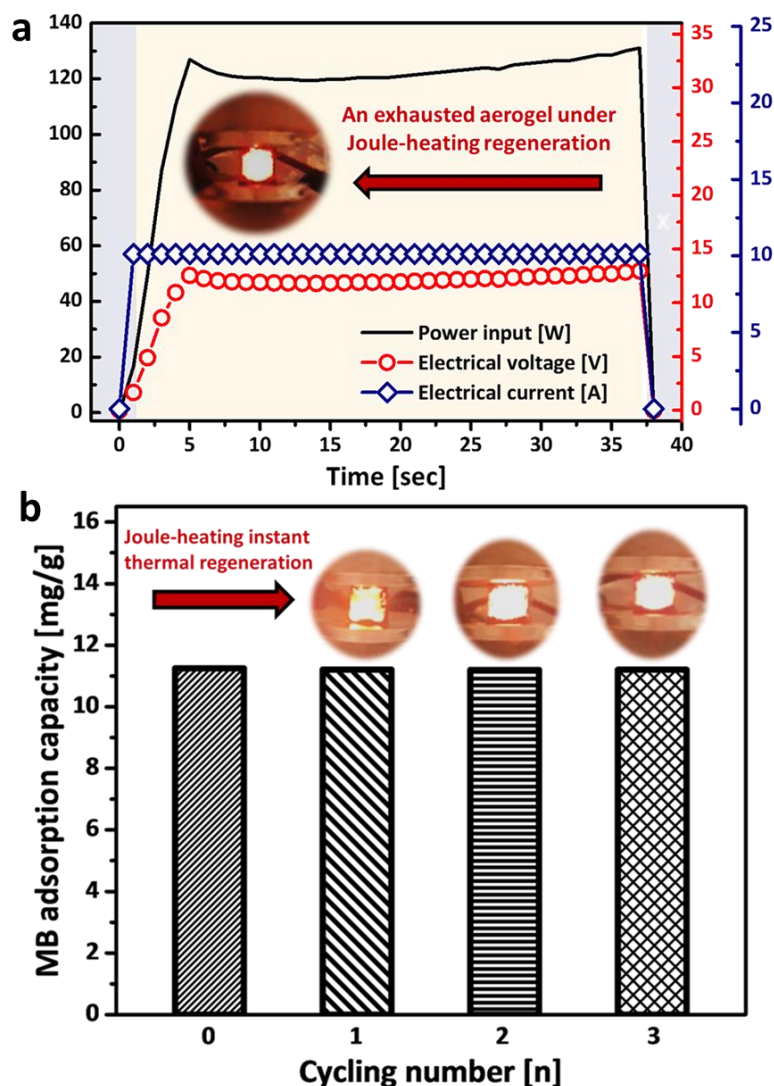


**Figure 6.17** (a) 30 second flash Joule-heating regeneration of post-sorption rGO aerogels at electrical power input of  $P = 120\text{ W}$ , and corresponding voltage and current evolution over time. The digital photo shows rGO[HT] aerogel under ultrahigh Joule-heating conditions, emitting black body radiation. (b) Dye uptake of rGO[HT] aerogels after flash Joule-heating regeneration over three re-use cycles.

The corresponding electrical parameters over the 30 second flash regeneration period were monitored via data loggers (Figure 6.17), showing that applied voltage current and power input remain relatively stable. Even though the electrical power input is very high at 120 W, the very short Joule-heating duration (30 seconds)

results in a regeneration process that is overall very energy-efficient. It is estimated that one flash regeneration cycle consumes only  $\sim 0.001$  kW·h energy, which is more energy-efficient than many other reported regeneration methods (see Appendix 4, Figure A4.8).

The success of sorbent regeneration by flash Joule-heating is verified by multicycle dye sorption tests. The regenerated rGO aerogels were reused for new dye adsorption measurements, where their adsorptive capacities, remained high and unchanged over three successive 3 regeneration cycles (Figure 6.17b).

### **6.2.5 Joule-heating-based synthesis of metallic nanoparticles**

Joule-heating of GO aerogels can also be exploited for synthetic purposes, for example in order to chemically modify the aerogels through decoration with functional particles. As demonstrated in Chapter 5, a highly effective route towards functionalisation is the thermal conversion of precursor compounds, deposited within the aerogel framework, into inorganic particles. This conversion process is usually carried out through thermal treatment in a tube furnace or through other external methods. In this section, it will be explored how aerogel Joule-heating can be exploited for thermal precursor conversion, using the nanocarbon aerogels in effect as ultrahigh-temperature nanoscale furnaces.<sup>216</sup>

As a first example, the synthesis of Cu nanoparticles (important chemical and electrochemical catalysts) is investigated (Figure 6.18). To this end, pre-fabricated rGO aerogels were impregnated with a Cu nanoparticle precursor solution ( $\text{Cu}(\text{acac})_2$  in chloroform) for 24 hours, with the pronounced hydrophobicity of the rGO aerogel facilitating solution uptake and precursor adsorption. Upon removal from the solution, the chloroform readily evaporates, leaving the precursor compound deposited within the aerogel (see  $\text{Pt}(\text{acac})_2$  decorated rGO aerogel as described in below Figure 6.18). The precursor decorated aerogel is then Joule-flash heated in inert atmosphere using our electrical setup. Flash heating is carried out again at  $\sim 100$  W power input, to create the ultrahigh temperatures ( $>2000$  °C) discussed above, that allow for full precursor decomposition and conversion into nanoparticles in an almost instantaneous fashion.<sup>216</sup> An additional, highly beneficial feature of the Joule-heating approach is that heating times can be minimised to only seconds. This again reduces energy costs of this synthetic process substantially.

Importantly, short heating durations (especially at the high temperatures investigated here) are also important to ensure the formation of smaller nanoparticles, based on limiting thermally-activated migration of nanoparticles and nanoparticle sintering at longer heating times.<sup>333</sup> To confirm this point, Joule-heating

precursor conversion (at  $\sim 100$  W) was carried out for 1 second, 10 seconds, and 30 seconds, respectively (Figure 6.18a-6.18c). SEM imaging confirms that Cu particles have indeed formed (Figure 6.18d-6.18f), and are relatively uniformly distributed across the aerogel surfaces. A clear difference in particle size is observed, depending on the Joule-heating duration, with large micron-sized Cu particles observed for the 30-second-heating sample, while significantly smaller particles are observed for shorter heating durations. It is worth noting that there are likely very small nanoparticles formed in the 1-second-heating sample, that cannot be observed by SEM due to its spatial resolution restrictions. Further investigation would require TEM studies. However, Cu-based precursors tend to form overall relatively large particles and are also difficult to visualise due to relatively low contrast in electron microscopy.

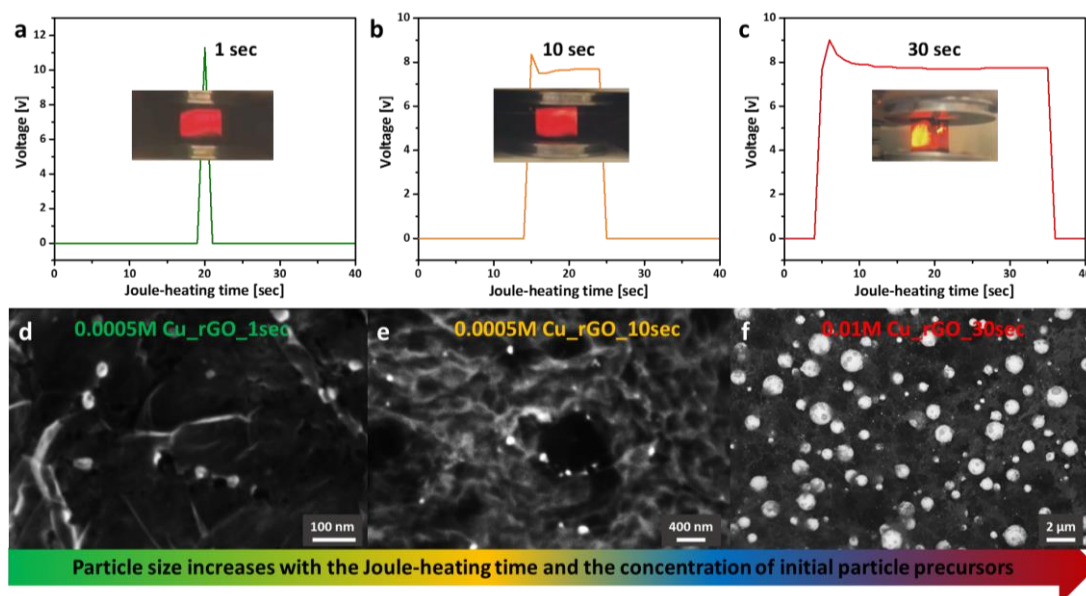


**Figure 6.18** (a-c) Joule-heating time versus voltage of Cu NP/rGO aerogels. Digital photos to display strong black-body radiations of rGO aerogels. (d-f) SEM images of various initial concentrations of  $\text{Cu}(\text{acca})_2$  in chloroform to make Cu NP/rGO aerogels using different time Joule heating.

Therefore, equivalent experiments (aerogel precursor decoration, followed by Joule-heating precursor conversion) were carried out for Pt nanoparticles, using  $\text{Pt}(\text{acac})_2$  in chloroform as precursor solution (Figure 6.19a). Flash Joule-heating of the  $\text{Pt}(\text{acac})_2$  decorated rGO aerogels was carried out again at 120 W for 10 seconds and 1 second, respectively (Figure 6.19b).

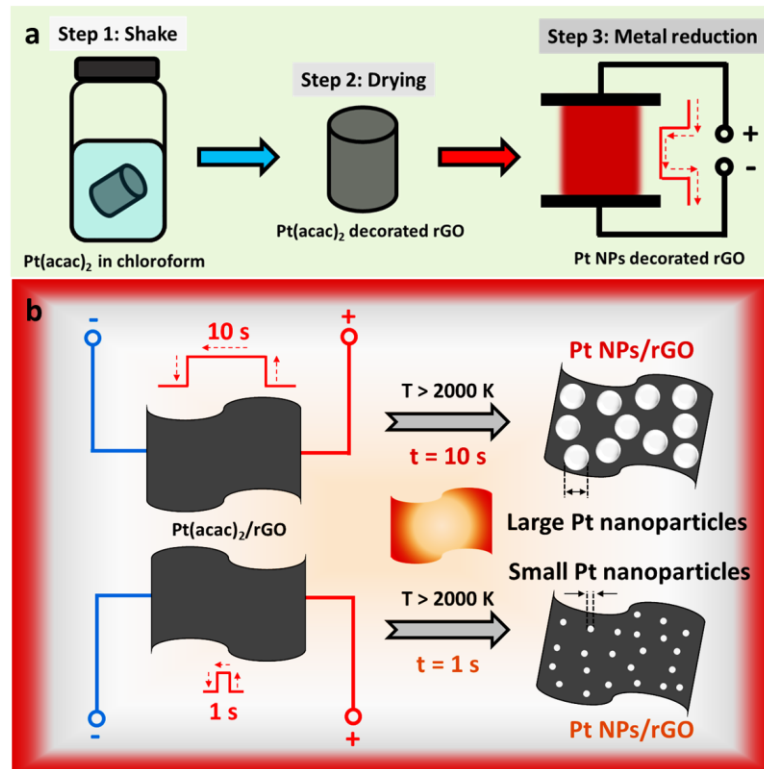


**Figure 6.19** (a) Schematics of producing Pt nanoparticles via flash Joule-heating using rGO[HT] aerogel as nanoscale furnace. (b) Schematics for describing long time flash Joule-heating leads to large Pt nanoparticles.

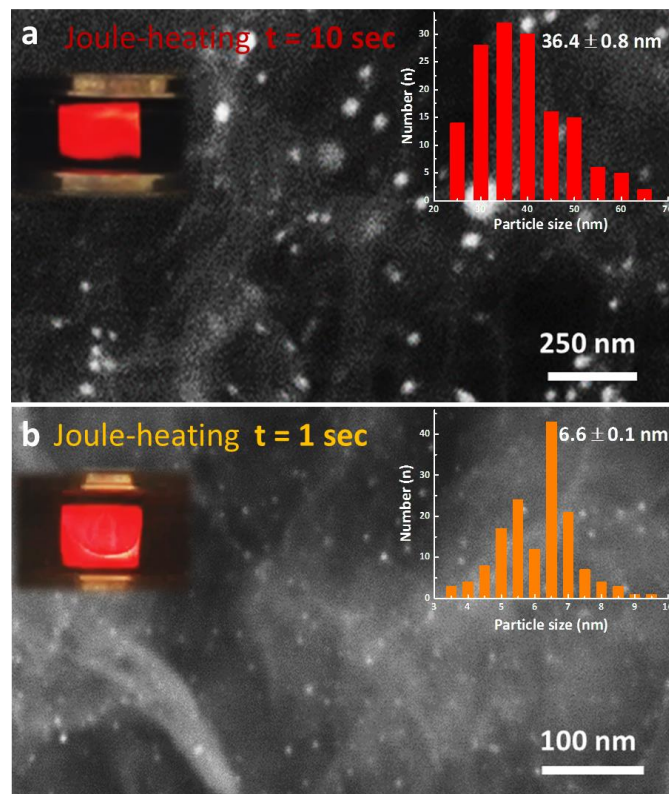


**Figure 6.20** (a) SEM image of Pt-NP/rGO aerogel using 10 second Joule-heating duration and (b) Pt-NP/rGO aerogel using 1-second Joule heating. The inserts show corresponding digital photos of the Joule-heated precursor-decorated rGO[HT] aerogels and Pt nanoparticle diameter distributions, obtained from SEM image analysis.

SEM imaging reveals that Pt nanoparticles have been successfully formed (even at the very short heating time of 1 second) and are dispersed well across the aerogel framework. Particle size distributions clearly show that the average size of the formed nanoparticles can be reduced from  $\sim 36$  nm to  $\sim 7$  nm when reducing Joule-heating conversion time from 10 seconds to 1 second (Figure 6.20).

High-resolution TEM images was then carried out to check if even smaller nanoparticles have formed under the outlined Joule-heating conditions (Figure 6.21). TEM images clearly show that a second set of very small Pt nanoparticles (sub 5 nm) are formed (which cannot be observed by SEM). TEM-EDX mapping verifies that C, O and Pt elements are uniformly distributed in both the rGO aerogels (Figure 6.21d and Figure 6.21h). Particle size distribution were obtained from these TEM images and showed there are also significant size differences for these smaller Pt nanoparticles, with an average particle diameter of  $\sim 4.0$  nm for the 10-seconds-heated sample and an extremely small size of only  $\sim 1.5$  nm for the 1-second-heated sample (Figure 6.21). High resolution TEM images reveal that both materials exhibit classic Pt(111) lattice spacings of  $\sim 0.23$  nm (as observed in Figure 6.21c and 6.21g).<sup>333</sup>

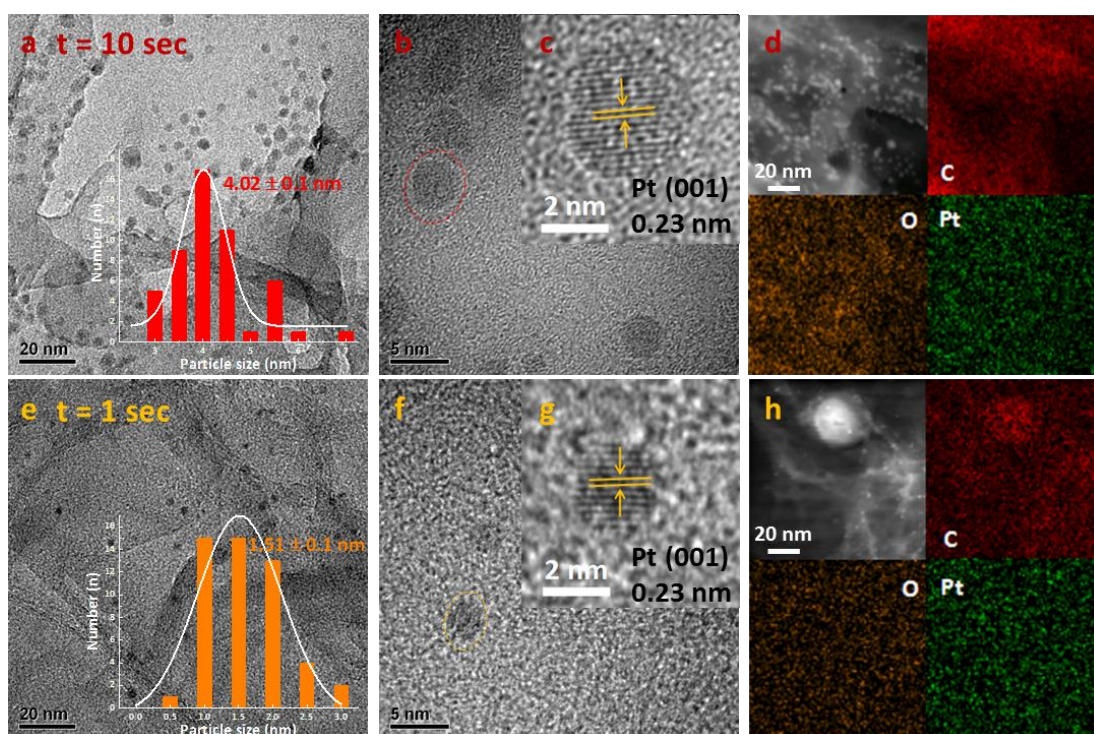


**Figure 6.21** TEM images/particle size distributions of 10 seconds (a) and 1 second (e) flash Joule-heating of Pt/rGO aerogel. High resolution TEM images/lattice distance images for 10 seconds (b-c) and 1 second (f-g) flash Joule heating Pt/rGO aerogel. EDX mapping of 10 seconds (d) and 1 second (h) flash Joule heating Pt/rGO aerogel.

Raman spectra, XPS spectra and XRD patterns show clear structural changes between the original rGO aerogel and the 1-second-heated Pt NP/rGO aerogel (Figure 6.22 and Appendix 4 Figure A4.9). The strong G peak in Pt NP/rGO aerogel

confirms improved graphitic crystallinity of the rGO framework after only 1 second flash Joule-heating (Figure 6.22a). XPS overview spectra (Figure 6.22b) verify the presence of the Pt NPs within the aerogel. Analysis of the high-resolution Pt 4f peak confirms that metallic Pt<sup>0</sup> is the predominant species present, confirming that high-temperature Joule-heating conversion from Pt<sup>2+</sup> (precursor) to Pt<sup>0</sup> (metallic nanoparticles) was successful at the short 1-second heating duration (Figure 6.22c, Appendix 4 Figure A4.9).<sup>333</sup>

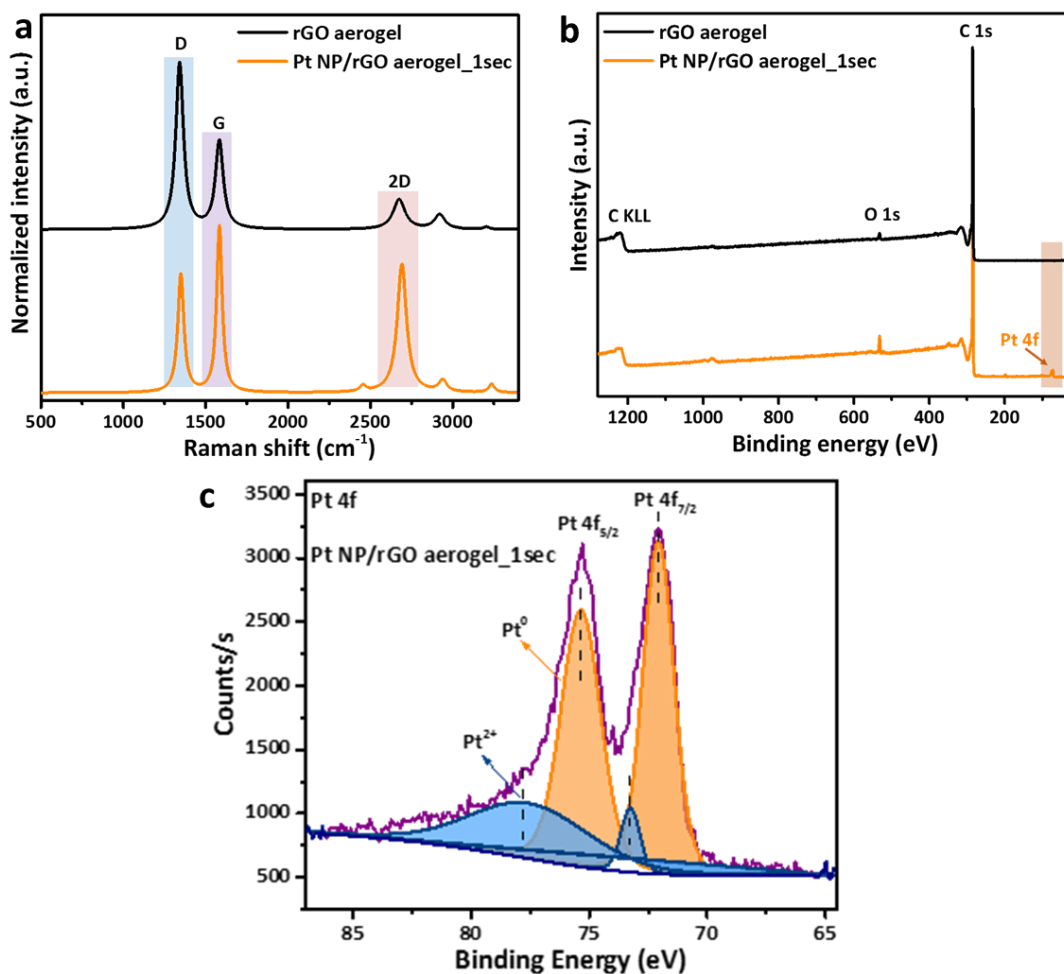


**Figure 6.22** Raman spectra (a)/XPS full spectra (b) of 10 seconds and 1 second flash Joule-heating of Pt/rGO aerogel. (c) Pt 4f peak analysis of 1 second flash Joule-heating of Pt NP/rGO aerogel.

As mentioned above, the very short Joule-heating durations also help to inhibit particle clustering and sintering. Lower magnification of the 10-second-heated sample confirm excellent distribution of the particles across larger viewing area, confirming that flash Joule-heating precursor conversion is successful in producing samples of remarkable uniformity and very small nanoparticle sizes (Figure 6.23).

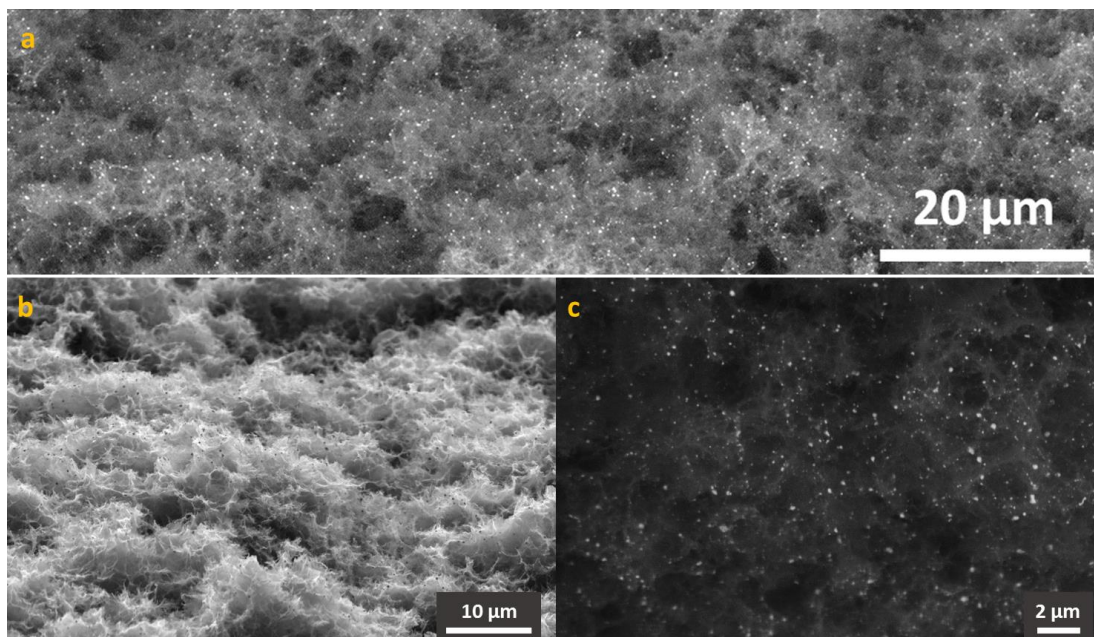


**Figure 6.23** (a-c) SEM images of Pt NPs/rGO aerogel with 10 seconds long flash Joule heating using 0.001M Pt(acac)<sub>2</sub> precursors in chloroform solution.

### 6.2.6 Joule-heating-based synthesis of metal-oxide nano-catalysts

Joule-heating based particle synthesis is not only limited to metallic nanoparticles, but can also be employed for the synthesis of metal oxide nanoparticles. To demonstrate this point, flash Joule heating was utilised to fabricate MoO<sub>2</sub> NPs which are industry-relevant oxidative desulfurisation catalysts, important for fuel purification applications.<sup>334</sup> Following the synthetic approach of the previous section, the GO[30sec] aerogel was soaked a MoO<sub>2</sub>(acac)<sub>2</sub> solution to deposit the nanoparticle precursor, followed by 1-second flash Joule-heating to produce a hybrid MoO<sub>2</sub>/GO[30sec] aerogel.

As observed by SEM (Figure 6.24b), MoO<sub>2</sub> NPs of about 10 nm particle diameter are successfully formed and very uniformly distributed on the surface of rGO sheets. Comparison with the un-treated GO[30sec] aerogel (Figure 6.24a) shows a similar overall aerogel morphology, evidencing that the Joule-heating treatment does not cause any major changes in aerogel microstructure or macro-porosity. Higher magnification SEM images (Figure 6.24c and Figure 6.24d) further indicate that MoO<sub>2</sub> NPs are compactly attached on the surface of rGO sheets. EDX mapping demonstrate that C, Mo and O elements are evenly distributed in the porous graphene aerogel bulk (Figure 6.24e).

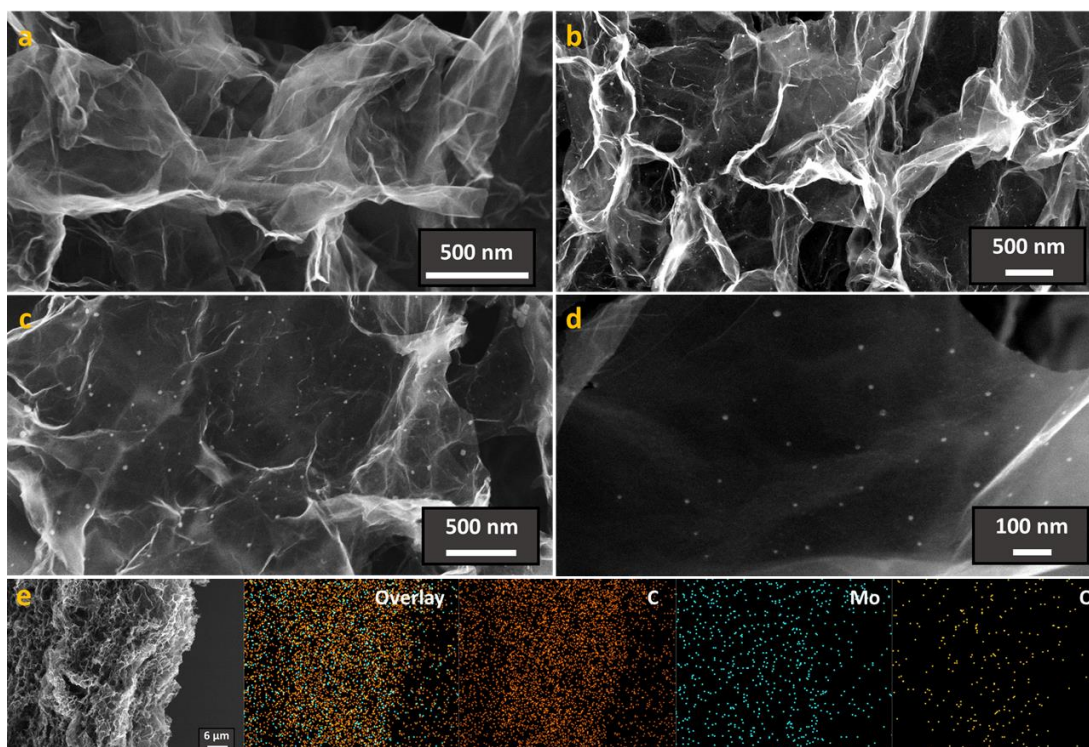


**Figure 6.24** (a) SEM image of GO[30sec] aerogel. (b-d) Different resolution SEM images of MoO<sub>2</sub>/GO[30sec] aerogel using 1 second flash Joule heating. (e) SEM image of MoO<sub>2</sub>/GO[30sec] aerogel and the corresponding EDX mappings.

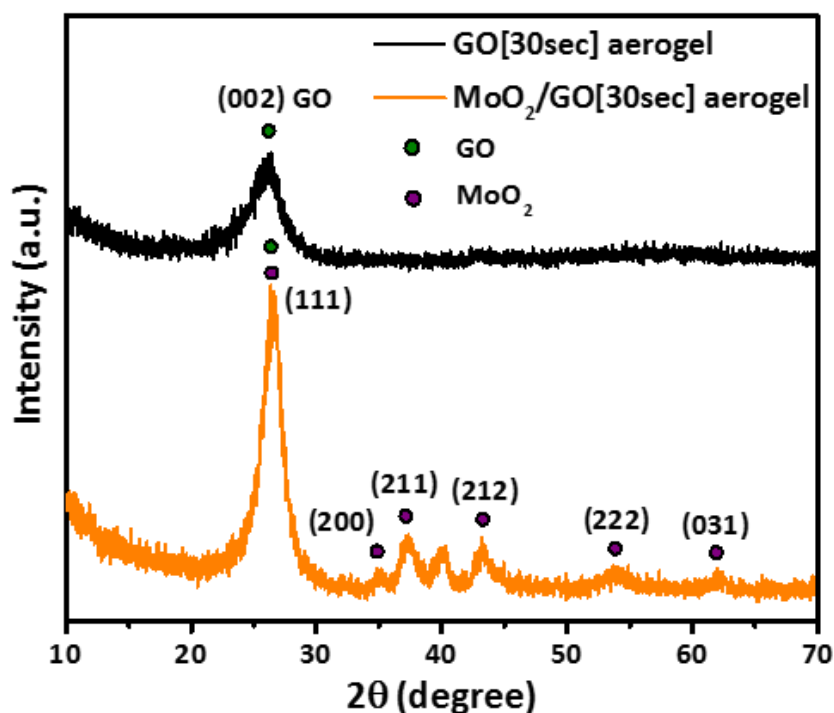


**Figure 6.25** XRD patterns of GO[30sec] aerogel and MoO<sub>2</sub>/GO[30sec] aerogel.

XRD pattern reveals that the Joule-heating-assisted GO[30sec] aerogel exhibits a characteristic peak at 25.6 °C (Figure 6.25), originating from the characteristic (002) plane of crystalline graphitic materials. The narrowing of the (002) peak width in the MoO<sub>2</sub>/GO[30sec] sample indicates that there is some re-stacking of rGO occurring

(even at the short heating time of 1 second). The XRD pattern of the MoO<sub>2</sub>/GO[30sec] aerogel shows several additional peaks, which can be attributed to the (111), (200), (211), (212), (222) and (031) planes of MoO<sub>2</sub> nanoparticles.<sup>334</sup> The relatively pronounced broadness of these peaks indicates the formation of relatively small MoO<sub>2</sub> particles with dimensions on the nanoscale, in line with the SEM images.

In order to assess the functional utility of these new materials, the MoO<sub>2</sub>/GO[30sec] aerogel was tested as catalyst for oxidative desulfurisation of hydrocarbon solutions in the presence of an oxidising agent. To this end, the MoO<sub>2</sub>/GO[30sec] aerogel was tested for the degradation of DBT in hexane (C<sub>DBT</sub> = 500 ppm·S) in the presence of tert-butyl hydroperoxide. Catalytic degradation of the DBT molecules by MoO<sub>2</sub> nanoparticle catalysts in the presence of peroxide species occurs in four key stages (Figure 6.26): (i) Nucleophilic reaction between the peroxide and molybdenum oxide forms hydroperoxymolybdate intermediates; (ii) The loss of alcoholic group to generate the catalytic monoperoxo intermediates; (iii) Electrophilic reaction leads to the formation of peroxy-molybdenum-oxide, the catalytically-active species in this reaction; (iv) Nucleophilic reaction between the sulfur atom in DBT molecules and peroxy-molybdenum-oxide results in oxidised sulfur compounds.<sup>334</sup> Fuel purification is based in the catalytic conversion of an organosulfur compound into its oxidised form through the reaction mechanism described above. As the oxidised organosulfur species are not soluble in hydrocarbons, they precipitate out and can be easily removed from the model fuels through filtration or simple sedimentation-decantation.

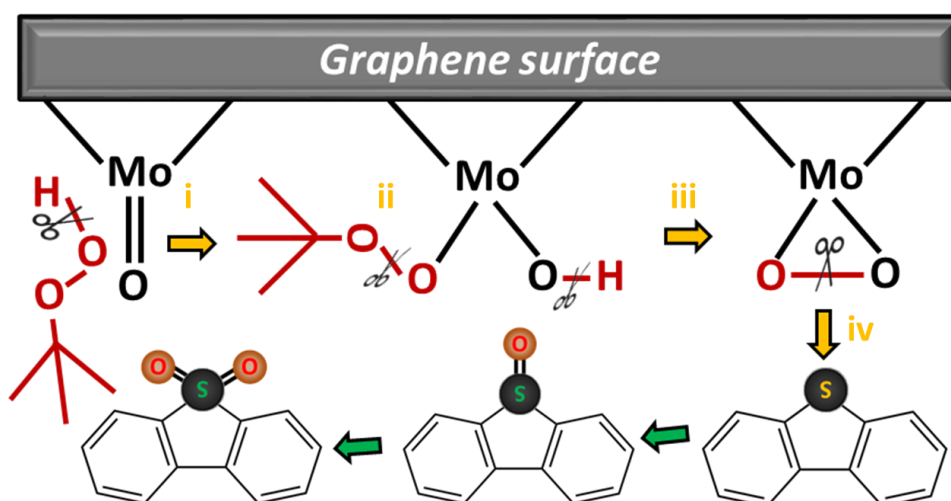


**Figure 6.26** Schematics to illustrate MoO<sub>2</sub> catalysts oxidative desulfurisation of DBT.

Catalytic performance of the MoO<sub>2</sub>/GO[30sec] aerogel for the conversion reaction of DBT into DBTO<sub>2</sub> reaches up to 99.9 % (Figure 6.27) after 12 hour reaction time, almost completely converting all DBT under the conditions chosen, showcasing the effectiveness of producing MoO<sub>2</sub> nano-catalysts through flash Joule heating.

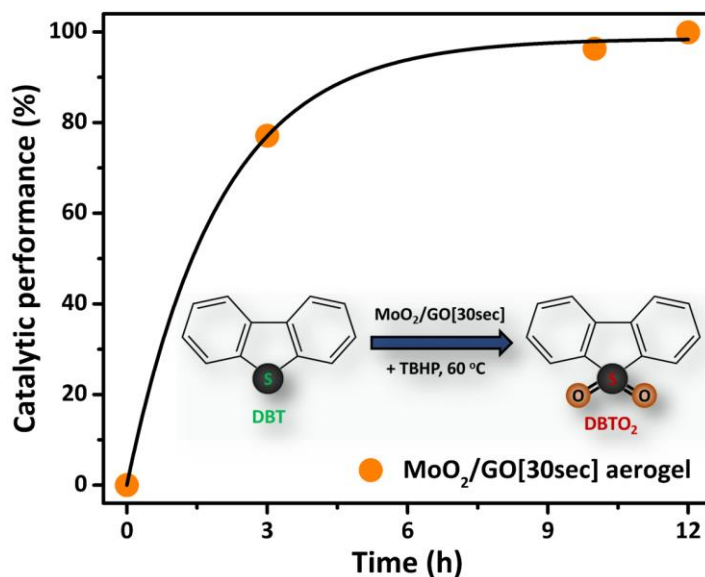


**Figure 6.27** Catalytic oxidative desulfurisation performance of MoO<sub>2</sub>/GO[30sec] aerogel.

In order to confirm that the catalytic activity originates only from the MoO<sub>2</sub> nanoparticles, various catalysts and experimental conditions were tested, as outlined in Table 6.2. As expected, no DBT conversion is observed in the absence of oxidation agents or catalysts. There is some DBT conversion imparted by the TBHP oxidation catalyst on its own but only ~30 % DBT conversion after 12 hours. When testing the pure as-synthesis and Joule-heating annealed rGO aerogels (i.e. aerogels without MoO<sub>2</sub> nanoparticles), no significant additional conversion is observed, confirming that the pure aerogels show no catalytic activity themselves. In contrast, the MoO<sub>2</sub>-containing aerogels (MoO<sub>2</sub>/GO[30sec] aerogel) shows excellent, near complete DBT conversion of 96.3 % and 99.9 % at 10 hrs and 12 hrs, respectively.

**Table 6.2** DBT oxidative catalytic performance of using different catalysts and experimental conditions.

Entry	Catalysts	Reaction time (h)	Sulfur conversion (%)
1	None <sup>a</sup>	12	0
2	None <sup>b</sup>	3	27.0
3	None <sup>b</sup>	12	27.2
4	GO[HT] aerogel <sup>c</sup>	12	33.1
5	GO[1sec] aerogel <sup>d</sup>	12	33.7
6	GO[30sec] aerogel <sup>e</sup>	12	28.7
7	MoO <sub>2</sub> /GO[30sec] aerogel <sup>f</sup>	10	96.3
8	MoO <sub>2</sub> /GO[30sec] aerogel <sup>f</sup>	12	99.9

a: No catalyst and TBHP were added. b: No catalyst but TBHP added. c: Hydrothermal GO aerogel without Joule heating treatment. d: Hydrothermal GO aerogel with 1 second Joule heating. e: Hydrothermal GO aerogel with 30 seconds Joule heating. f: Hydrothermal GO aerogel with 30 seconds Joule heating, followed by 1 second flash Joule heating to produce MoO<sub>2</sub> nanoparticle catalysts.

### 6.3 Conclusions

Specifically, high-temperature Joule-heating of GO-based aerogels to temperatures significantly above 1200 °C were systemically investigated to reveal some first structure-property relationships and demonstrate a range of potential applications. It was shown that GO-based aerogels can be readily heated to ultrahigh core temperatures >2500 °C via Joule heating at very high-power inputs of up to 120 W. The Joule-heated aerogels possess remarkably improved electrical conductivities, which are accredited to pronounced graphitic annealing and the formation of near defect-free graphene sheets under the high temperature conditions applied. High temperature Joule-heating was shown to exhibit extremely fast heating/cooling kinetics as well as excellent high-temperature stability and repeatability. Ultrahigh-temperature Joule-heating can be therefore used to directly anneal hydrothermally produced aerogels at much lower energy costs and process duration than achievable through conventional furnace treatments. The resulting Joule-heating annealed GO[30sec] aerogels exhibit high specific surface areas (due to complete removal of organic impurities), pronounced hydrophobicity (due to thermal reduction and graphitisation of GO) and outstanding thermal stabilities (due to the restoration of stable  $sp^2$ -colvent bonds).

Exploitation of high-temperature aerogel Joule-heating was demonstrated for a wide range of applications, including energy-efficient thermal regeneration of exhausted rGO aerogel sorbents as well as for Joule-heating induced synthesis of small metallic nanoparticle and  $MoO_2$  nano-catalysts. All applications explored in this Chapter have proven that flash Joule-heating is a powerful and facile approach, to carry out a range of thermal processes as substantially shorter durations and much lower energy costs, unavailable through traditional external heating processes.

Moreover, flash Joule-heating of rGO aerogels can also be exploited to control inorganic particle synthesis. In this context, heating duration has been shown a very facile tool to control particle size (reaching very small sizes of only 1.5 nm in the case of Pt nanoparticles) and to ensure high uniformity of the resulting inorganic/rGO hybrid materials. The utility of the nanoparticle decorated rGO aerogels, produced via flash Joule-heating, was demonstrated for catalytic desulfurisation of a model fuel. For example Joule-heating-produced  $MoO_2$ /GO[30sec] aerogels showed excellent catalytic activity for the oxidation of DBT (99.9 % conversion efficiency after 12 hrs).

This work therefore lays a solid foundation for the future exploration of nanocarbon aerogel Joule-heating to extremely high temperatures, for example in the context of synthesis of high-entropy-alloy nanoparticles, for the functionalisation of

nanocarbons with highly functional single atomic-sites, or the fabrication 3D thermoelectric materials.

## 6.4 Experimental

### 6.4.1 Materials synthesis

**Hydrothermal approaches to synthesizing GO-based aerogels.** L-ascorbic acid and GO in a weight ratio 4:1 was applied. In detail, 0.64 g L-ascorbic acid and 0.16 g GO flakes were mixed into 40 mL HPLC water, followed by ultrasonication to produce stable GO dispersions. Subsequently, 7.5 mL dispersion was sealed in a sample vial, followed by hydrothermal reduction at 50 °C for 24 hours to form GO hydrogel. The formed GO hydrogel was then soaked into HPLC water to wash out impurities. Then, the obtained hydrogel was frozen on top of a copper disk in liquid nitrogen, followed by freeze-drying to obtain the GO[HT] aerogel (Figure 6.28). The GO[HT] aerogel was thermally reduced at 1000 °C, for 2 h, under N<sub>2</sub>/H<sub>2</sub> atmosphere (5% H<sub>2</sub>), using a tube furnace (Carbolite Gero Limited) to obtain the rGO[HT] aerogel.

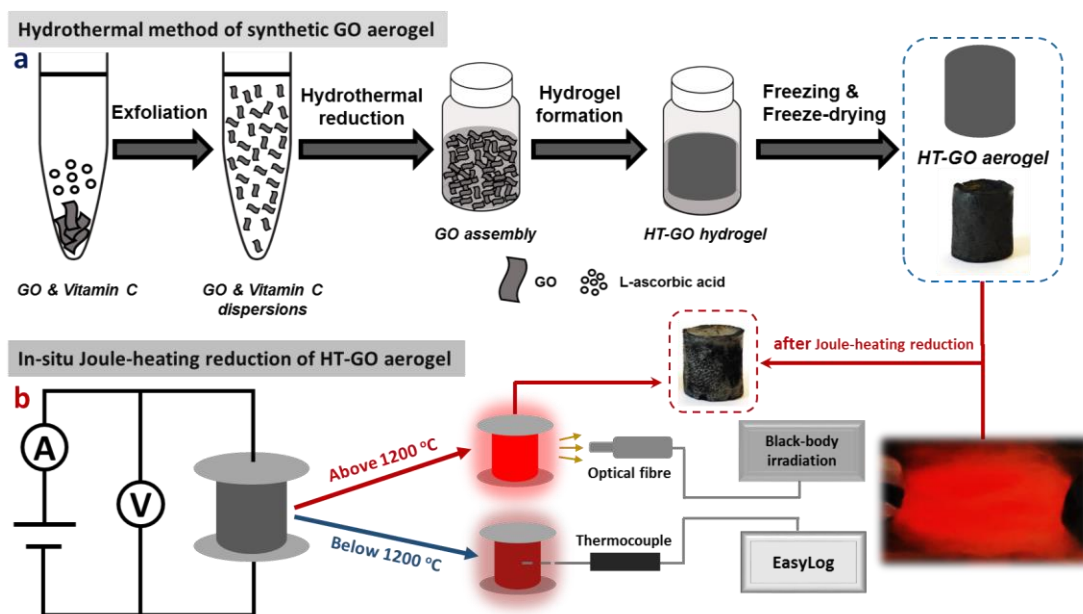


**Figure 6.28** (a) Schematic overview of hydrothermal approach to produce GO[HT] aerogels and (b) schematic overview of Joule-heating setup to produce Joule-heating annealed samples, such as the GO[30sec] aerogel discussed in the text.

In detail, the well-dispersed GO/ascorbic-acid mixtures were put into a seal-tightly vial in an oven to form hydrogel through random assembly (e.g. Van-der-Waals force,  $\pi$ - $\pi$  interactions, and covalent bonding).<sup>129</sup> After freezing and freeze-drying, the reference GO[HT] aerogel is obtained, as shown in the digital photo (Figure 6.28a). As the reducing abilities of ascorbic acid, the highly defective GO sheets will be partially reduced to rGO sheets exhibiting inferior electric-conductivity capacities.

Essentially, owing to GO[HT] aerogel is an inferior conductor, it can be connected with Joule heating set-up to execute energy-efficient Joule-heating to further thermally reduce itself. As the sudden supply of large amount of energies infusing into a GO[HT] aerogel will generate sudden high temperature that will quickly remove impurities (i.e. ascorbic acid), which are the main components leading to the aerogel electrically and thermally unstable. On account of the ultrafast removal of impurities, the GO[HT] aerogel becomes a structurally-electrically-thermally stable monolith to continue completing the rest Joule heating procedures. A digital photo of a GO[HT] aerogel covered by glass fibres under Joule heating with strong illumination is pictured in Figure 6.28b. After flash Joule heating, a digital photo in Figure 6.28b reveals that the monolithic GO[30sec] aerogel is still structurally intact. However, judging the outside morphology from the two digital photos, evidently, they are different, suggesting that flash Joule heating changed internal nanocarbon compositions (e.g. graphene quality, structural interconnections and bandgaps).

#### 6.4.2 Materials characterisation

**Raman mapping** was performed on a Renishaw InVia Raman equipment with an excitation laser wavelength of 697 nm between 1300 - 3000  $\text{cm}^{-1}$  continuously scanning on a focused area of 50  $\mu\text{m}$  x 50  $\mu\text{m}$ . The accumulated Raman spectra were then analysed by Dr Yifei Xu using software Image J. Raman mapping data were measured Dr Yifei Xu at University of Leeds, UK.

**Ultraviolet visible spectroscopy (UV-vis)** was measured on a VARIAN 50 Probe UV-visible Spectrometer to obtain the standard curves and dye concentrations after aerogel adsorption, for determining the aerogel dye sorption capacities.

**Thermogravimetric analysis-Fourier transform infrared spectroscopy (TGA-FTIR)** was measured using a combining equipment of the thermo gravimetry analyser (TA instruments, model: Q20) and the thermo Scientific iS10 Fourier Transform Infrared Spectrometer (thermo scientific, model: Nicolet S10), with a 10  $^{\circ}\text{C}\cdot\text{min}^{-1}$  ramping rate from 20  $^{\circ}\text{C}$  to 800  $^{\circ}\text{C}$  in air atmosphere. The TGA-FTIR was trained and helped by Dr Karine Alves Thorne at University of Leeds, UK.

#### 6.4.3 Ultrahigh temperature Joule-heating

The Joule heating measurements of aerogels are carried out in an air-tight custom-made set-up in  $\text{N}_2$  atmosphere, described in Chapter 2. In detail, the monolithic aerogel was directly connected with Joule heating set-up, followed by inserting a thermocouple into the centre of the aerogel to record core temperature. Another

thermocouple was attached at the surface of aerogel to measure the surface temperature. Then, stepwise Joule heating was carried out to record corresponding Joule heating parameters, such as temperature, current and voltage (more detailed measurements see Appendix 4). The furnace-reduced rGO[HT] aerogels were further thermally reduced via flash Joule heating with electrical current at  $I = 10.12$  A for 60 sec to produce the rrGO[HT] aerogels. The un-reduced GO[HT] aerogels was treated in the same setup for 30 sec or 300 sec at  $I = 10.12$  A to produce the GO[30sec] aerogel and the GO[300sec] aerogel. Other measurements were carried out, following the general procedures described in Chapter 2.

#### **6.4.4 Dye adsorption/desorption measurements**

In general, the methylene blue and Rhodamine b solutions in water with a concentration of  $12.5 \text{ mg}\cdot\text{L}^{-1}$  were used as model systems for dye adsorption, respectively. Specifically, an intact rGO[HT] aerogel was immersed in 10 mL of as-prepared model dye solution at room temperature, using an orbital shaker (100 rpm) to ensure constant agitation. Subsequently, 0.5 mL of solution aliquots were sampled at defined time intervals to be measured via UV-vis spectroscopy in order to determine adsorption kinetics. After dye sorption was completed, the intact aerogel was recovered simply via a pair of tweezers and was dried in an oven at a mild temperature. After that, the recovered rGO[HT] aerogel was contacted in Joule heating set-up to maintain Joule heating at  $I = 10.12$  A for 30 seconds for thermal desorption. At last, recycling of rGO[HT] aerogel for dye sorption was carried out via repeating dye adsorption and Joule-heating measurements with the regenerated samples at the same parameters described above.

#### **6.4.5 Pt NPs/rGO aerogel and MoO<sub>2</sub> NPs/GO[30sec] aerogel syntheses**

The Pt(acac)<sub>2</sub> was dissolved into chloroform to produce a 0.0005 M solutions. Then the rGO[HT] aerogel was soaked in 10 mL of as-prepared precursor solutions for 24 hours, using an orbital shaker for agitation. After soaking, the wet rGO[HT] aerogel was put into a fume-hood for 24 hrs so that the solvent could completely evaporate. Then, the dried rGO[HT] aerogel was measured within the Joule heating set-up, carrying out flash heating experiments for 1 sec or 10 sec at an electrical current of  $I = 10.12$  A to yield the respective Pt/rGO[1sec] and Pt/rGO[10sec] aerogels. Similarly, the MoO<sub>2</sub>/GO[30sec] aerogel was produced adopted the same method as used for the Pt/rGO aerogel, using a 0.001 M MoO<sub>2</sub>(acac)<sub>2</sub> precursor solutions.

#### 6.4.6 Oxidative catalytic desulfurisation measurements

The model fuel containing of 500 ppm S was prepared by dissolving 1.16 g DBT into 400 mL hexane solution. Specifically, 5 mg of MoO<sub>2</sub>/GO[30sec] aerogel catalyst were added to 5 mL as-prepared model fuel, followed by 3 minutes bath sonication to disperse the catalyst. Then, 0.15 mL of 70 wt% tert-butyl hydroperoxide (TBHP) aqueous solution was added to the catalyst-containing mixtures, followed by heating to 60 °C for 12 hrs on a hot plate, using a magnetic stirrer (600 rpm) for agitation during the reaction. After finishing the oxidative desulfurisation, the solution was filtered. The separated liquid phase was added to 1 mL CH<sub>3</sub>CN and agitated for 1000 rpm for 20 minutes at room temperature. DBT concentrations were determined by GC. GC sample was prepared using 1 mL of the supernatant phase, and 50 µL dodecane were added as an internal standard. The DBT conversion was calculated from the DBT peak area variations in the GC spectrum, compared against a standard curve.

## Chapter - 7

### Conclusions and Outlook

#### 7.1 Conclusions

Electrically-conducting and electrically-heatable 3D nanocarbon aerogels as supporting frameworks were systemically investigated and discussed in this PhD project. The Joule-heating temperature levels of the introduced nanocarbon aerogels were ranging from room temperature to above 2500 °C, which provide a broad range of heating temperatures in term of nanocarbon materials, hence offering a wide range of derived Joule-heating applications. Especially, the Joule-heating temperature of introduced nanocarbon aerogels is exploited following the rule (i.e. from intermediate Joule heating temperatures to high Joule heating temperatures) that is simply to gain a better understanding of potential electrical and thermal behaviours of Joule-heated aerogels, which are essential to instruct temperature-dependant applications.

#### Tuning the Heating Properties of Pure Nanocarbon Aerogels through Structural Control

Nanocarbons constructed 3D aerogel materials (e.g. CNT-based aerogels and GO-based aerogels) within various internal microstructures were fabricated to reveal the concealed correlations between electrical and thermal properties via Joule heating measurements. Conclusions indicated that the thermal properties of nanocarbon aerogels are highly tuneable via structural control solely. Essentially, the lower thermal conductivities the higher the Joule heating efficiency, owing to low thermal conductivity is capable of trapping more heats and avoiding largely convection-induced heat dissipations. This principle was also transferable to the solar-steam evaporation system, as expected the aerogel has lower thermal conductivity exhibiting better water evaporation capacity (Figure 7.1).

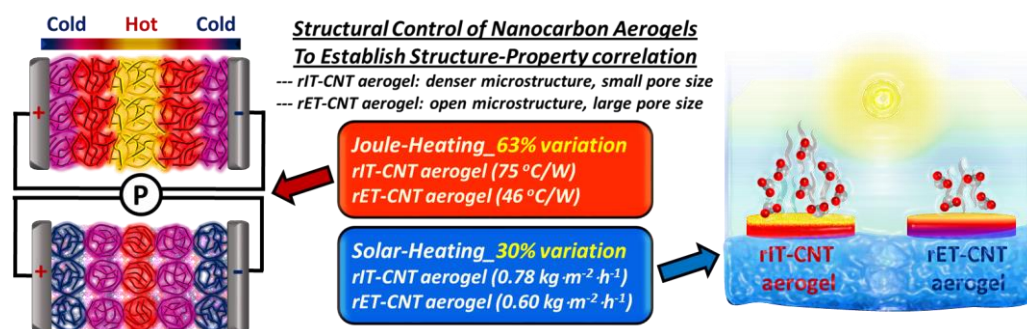


**Figure 7.1** Table of Contents of Chapter 3.

### Electrically-Heatable Graphene Aerogels as Nanoparticle Supports in Adsorptive Desulfurisation and High-Pressure CO<sub>2</sub> Capture

The GO-based aerogels were applied to decorate with functional hydrotalcites (e.g. MgAl-LDH, CuAl-LDH and NiAl-LDH), followed by thermal reduction to obtain multifunctional MMO/rGO aerogels or MNP/rGO aerogels for adsorptive desulfurisation from model fuels and pre-combustion high-pressure CO<sub>2</sub> capture. In detail: i) demonstration/quantification of substantial, graphene-aerogel-induced enhancements in functional nanoparticle performance (capacity, kinetics, selectivity, recyclability) for two industrially-important sorption applications as mentioned; ii) utilisation of direct electrical aerogel heating for extremely fast temperature-swing recycling of nanoparticles at practically-important low energy consumption; iii) record-high CO<sub>2</sub> sorption capacity of optimised hybrid aerogel sorbents under pre-combustion carbon capture conditions (high pressure, mid-range temperature); iv) facile fabrication method for nanoparticle/rGO hybrid aerogels at unusually high nanoparticle loadings (maximising the per-weight benefits of the graphene aerogel supports, Figure 7.2).

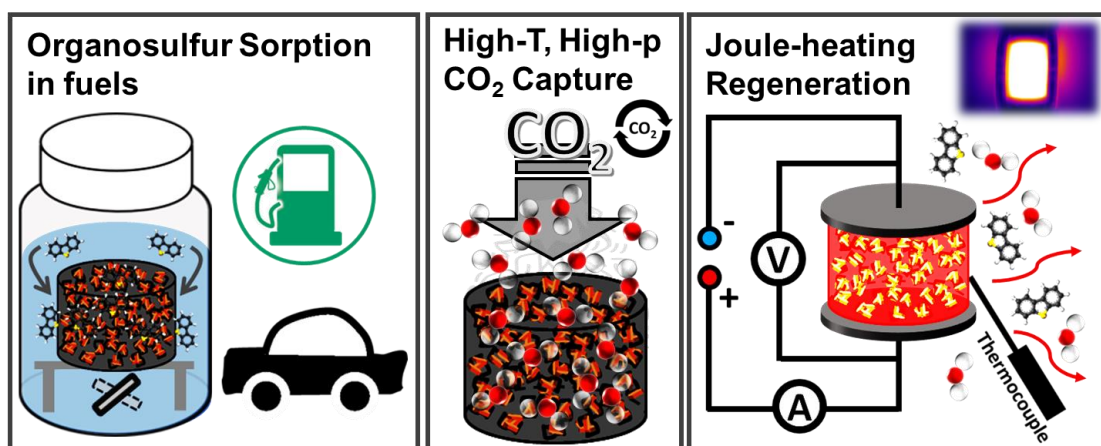


Figure 7.2 Table of Contents of Chapter 4.

### Boron-Nitride/Carbon-Nanotube Hybrid Aerogels as Multifunctional Desulfurisation Agents

BN adsorbents, which share similar structure with graphene, were combined with rCNT aerogels for high-performance adsorptive desulfurisation tests across a serial of sulfur-containing compounds. The mechanically robust BN/rCNT hybridised aerogels exhibited highly-porous internal microstructures and electrically-responsive characteristics, rendering them remarkable affinity to sulfur-containing compounds (owing to well-dispersed BN particles exposing more active sites) and novel capability for energy-efficient in-situ regeneration (owing to interconnected rCNT networks as heating mediums for electric-insulating BN sorbents). Essentially, BN-

sulfur interactions were carefully analysed to unearth adsorption mechanisms, where Lewis acid-base reactions were comprehensively elucidated (Figure 7.3).

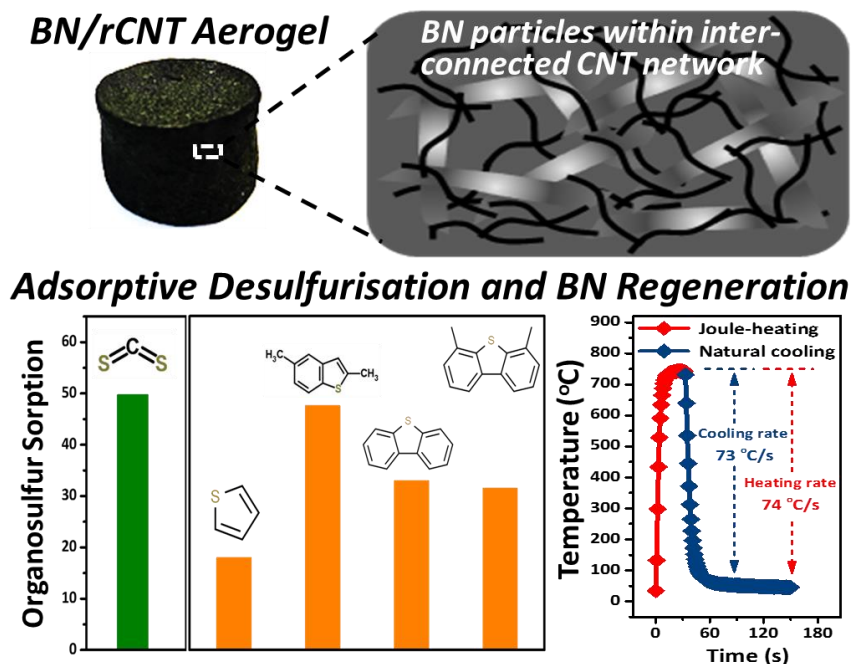


Figure 7.3 Table of Contents of Chapter 5.

#### High-Temperature Joule-Heating of Graphene Oxide Aerogels

Ultrahigh temperature Joule-heating (>2500 °C) of GO-based aerogels were characterised and analysed for targeting specific applications via conducting simple and convenient Joule-heating measurements in a house-made air-tight container, including ultrafast high-temperature graphitisation of defect-enriched GO nanosheets, graphene wedding, exceptional low energy-consumptions of thermal dye desorption (~0.001 kW·h per cycle), ultrasmall metallic nanoparticle (Pt, ~1.4 nm) fabrication in 1 second and functional catalytic metal-oxide-nanoparticle (MoO<sub>2</sub>, ~10 nm) synthesis. After ultrahigh temperature Joule-heating thermal treatments (> 2500 °C), the rGO-based aerogels enabled to easily Joule-heated above 1000 °C and maintained exceptional working durability. Additionally, the as-synthesised MoO<sub>2</sub>/GO[30sec] aerogel catalysts were utilized to catalyse sulfur-containing model fuels, resulting in a catalytic desulfurisation efficiency of 99.9 %, confirming the of high effectiveness of flash Joule-heating. All these remarkable results are stemmed from the pronounced electrical-thermal-mechanical properties of 3D nanocarbon aerogel materials, based on which, they enable to work as multifunctional supporting and conducting frameworks in other important fields, including high entropy alloy synthesis, single atom catalyst fabrication, ultrahigh strength nanocarbon material production and etc (Figure 7.4).

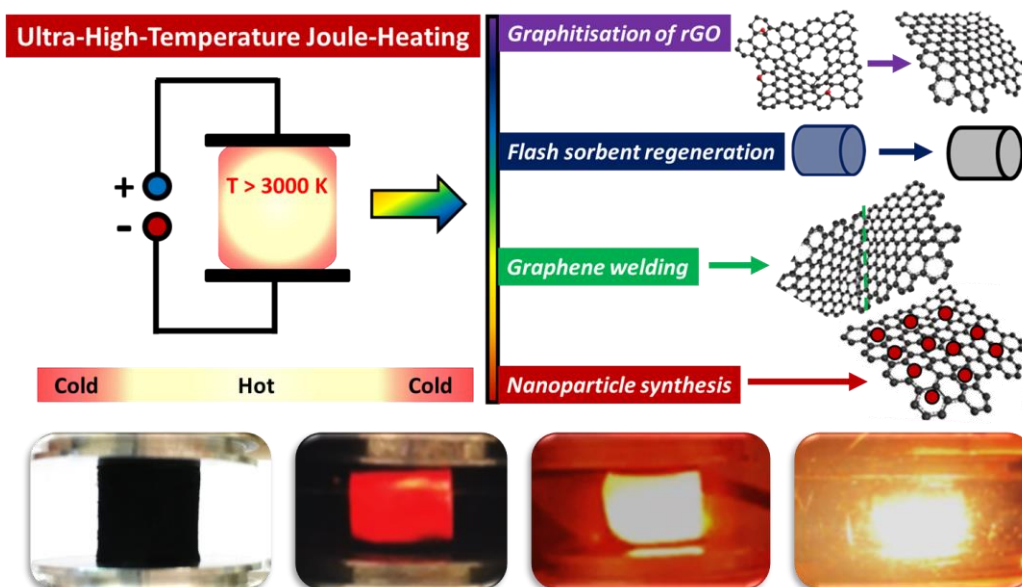


Figure 7.4 Table of Contents of Chapter 6.

## 7.2 Outlook

In light of the findings and conclusions in this PhD project, there are a broad range of interesting and meaningful applications can be extended in future.

For pure nanocarbon aerogels: i) the thermal conductivity and contact angle can be further reduced via adding polymers for improving solar-steam evaporation performance; ii) the phonon behaviours in 3D interconnected nanocarbons can be studied to understand how phonon scattering with advanced techniques and more theoretical mathematical models, consisting of defect density, boundary grain sizes, and nanocarbon sizes; iii) the electrical-thermal properties of nanocarbon aerogels from room temperature to close absolute zero temperature have not been reported, which is important to be exploited.

For functional nanoparticles decorated hybrid nanocarbon aerogels: i) ruling out sorption-related applications in this PhD project, implementations such as catalysis, sensors, supercapacitors, batteries, etc. are all available to be probed; ii) mechanically compressive hybrid aerogels can be continued investigating as flexible electronics, triboelectric nanogenerators, and catalysts in flow chemistry; iii) the pure BN shares similar properties with graphene, which can be assembled into 3D aerogel materials exclusively itself that are also available to work as high-surface-area support frameworks.

For ultrahigh temperature Joule-heating of nanocarbon aerogels: i) temperature-dependant applications ( $>2500\text{ }^{\circ}\text{C}$ ) is also needed for utilizing in other types of nanocarbon aerogels (such as graphene nanofibers, CNF, CNT); ii) the high-temperature Joule-heating can be further quantified by testing in vacuum with

advanced characterization techniques; iii) the measurements of Hall effects in 3D nanocarbon aerogels will be of significance to exploit; iv) high-entropy alloys synthesis is an essential researching field by flash Joule-heating; v) energy-efficient adsorption/desorption applications can be considered using Joule-heating (real-life and large-scale pre-combustion CO<sub>2</sub> capture).

### 7.3 Concluding Remarks

Fabrications and characterizations of 3D nanocarbon aerogels were specifically analysed and discussed in this PhD work, which offers a broad variety of fundamental studies for diverse applications, including different levels of Joule-heating, solar water evaporation, adsorptive desulfurisation, high-pressure CO<sub>2</sub> capture, oxidative catalytic desulfurisation and ultrafast nanoparticle synthesis. The facile nanocarbon aerogel fabrication methods recommended in this work can be readily transferable to other nanocarbon aerogel systems, which offer great significances for those who are interested in nanocarbon materials. The flash Joule heating of nanocarbon aerogels paves a solid as well as energy-efficient way for researchers who are interested in producing ultra-small nanoparticles and in regenerating exhausted sorbents in seconds. Additionally, this work also proposes ultrahigh temperature Joule-heating of electrically-conducting 3D bulk materials, which is especially vital to those who are working on the fundamental electrothermal studies of 3D aerogel materials. In short, the methodologies recommended in this work regarding nanocarbon aerogels, will be of importance and beneficial for other fundamental studies in electrocatalysis, mechanical engineering and physics, helping to build a totally understanding of nanocarbon-based materials and inspiring value-added real-life applications.

### References

1. M. J. Allen, V. C. Tung and R. B. Kaner, *Chem. Rev.*, **2010**, *110*, 132.
2. V. Chabot, D. Higgins, A. Yu, X. Xiao, Z. Chen and J. Zhang, *Energ. Environ. Sci.*, **2014**, *7*, 1564.
3. V.K.K. Upadhyayula, S. Deng, M.C. Mitchell and G.B. Smith, *Sci. Total Environ.*, **2009**, *408*, 1.
4. H. Fang, Y. Zhao, Y. Zhang, Y. Ren and S.L. Bai, *ACS Appl. Mater. Inter.*, **2017**, *9*, 26447.
5. S.R. Kwon, J. Harris, T. Zhou, D. Loufakis, J. G. Boyd and J. L. Lutkenhaus, *ACS Nano*, **2017**, *11*, 6682.
6. S. Sharma, A.K. Pathak, V.N. Singh, S. Teotia, S.R. Dhakate and B.P. Singh, *Carbon*, **2018**, *137*, 104.

7. X. Zhang, J. Xu, H. Yuan, S. Zhang, Q. Ouyang, C. Zhu, X. Zhang and Y. Chen, *ACS Appl. Mater. Inter.*, **2019**, *11*, 39100.
8. L. Yu, L. Wang, W. Xu, L. Chen, M. Fu, J. Wu and D. Ye, *J. Environ. Sci.*, **2018**, *67*, 171.
9. G. Ersan, O.G. Apul, F. Perreault and T. Karanfil, *Water Res.*, **2017**, *126*, 385.
10. K.A. Imran, J. Lou and K.N. Shivakumar, *J. Appl. Polym. Sci.*, **2018**, *135*, 40021.
11. J.E. Barrios-Vargas, B. Mortazavi, A.W. Cummings, R. Martinez-Gordillo, M. Pruneda, L. Colombo, T. Rabczuk and S. Roche, *Nano Lett.*, **2017**, *17*, 1660.
12. A. Oluwalowo, N. Nguyen, S. Zhang, J. G. Park and R. Liang, *Carbon*, **2019**, *146*, 224.
13. L. Chen, Y. Li, L. Chen, N. Li, C. Dong, Q. Chen, B. Liu, Q. Ai, P. Si and J. Feng, *Chem. Eng. J.*, **2018**, *345*, 536.
14. S.J. Kim, D.W. Kim, K.M. Cho, K.M. Kang, J. Choi, D. Kim and H.T. Jung, *Sci. Rep.*, **2018**, *8*, 1.
15. X. Li, B. Zhu and J. Zhu, *Carbon*, **2019**, *146*, 320.
16. H. Im, T. Kim, H. Song, J. Choi, J.S. Park, R. Ovalle-Robles, H.D. Yang, K.D. Kihm, R.H. Baughman and H. H. Lee, *Nat. Commun.*, **2016**, *7*, 1.
17. W. Wan, R. Zhang, W. Li, H. Liu, Y. Lin, L. Li and Y. Zhou, *Environ. Sci. Nano*, **2016**, *3*, 107.
18. J. Zou, J. Liu, A. S. Karakoti, A. Kumar, D. Joung, Q. Li, S. I. Khondaker, S. Seal and L. Zhai, *ACS Nano*, **2010**, *4*, 7293.
19. M. Yang, N. Zhao, Y. Cui, W. Gao, Q. Zhao, C. Gao, H. Bai and T. Xie, *ACS Nano*, **2017**, *11*, 6817.
20. G. Fu, X. Yan, Y. Chen, L. Xu, D. Sun, J. M. Lee and Y. Tang, *Adv. Mater.*, **2018**, *30*, 1704609.
21. Z. Wang, R. Wei, J. Gu, H. Liu, C. Liu, C. Luo, J. Kong, Q. Shao, N. Wang and Z. Guo, *Carbon*, **2018**, *139*, 1126.
22. Q. Zhang, F. Zhang, S. P. Medarametla, H. Li, C. Zhou and D. Lin, *Small*, **2016**, *12*, 1702.
23. X. Song, L. Lin, M. Rong, Y. Wang, Z. Xie and X. Chen, *Carbon*, **2014**, *80*, 174.
24. C. Chen, F. Li, Y. Zhang, B. Wang, Y. Fan, X. Wang and R. Sun, *Chem. Eng. J.*, **2018**, *350*, 173.
25. X. Zhang, J. Liu, B. Xu, Y. Su and Y. Luo, *Carbon*, **2011**, *49*, 1884.
26. Q. Zheng, Z. Cai, Z. Ma and S. Gong, *ACS Appl. Mater. Inter.*, **2015**, *7*, 3263.
27. Z. Chen, S. Yao and L. Liu, *J. Mater. Chem. A*, **2017**, *5*, 24651.
28. W. Zhan, S. Yu, L. Gao, F. Wang, X. Fu, G. Sui and X. Yang, *ACS Appl. Mater. Inter.*, **2018**, *10*, 1093.
29. Y. Qian, I. M. Ismail and A. Stein, *Carbon*, **2014**, *68*, 221.
30. P. Xu, Q. Gao, L. Ma, Z. Li, H. Zhang, H. Xiao, X. Liang, T. Zhang, X. Tian and C. Liu, *Carbon*, **2019**, *149*, 452.
31. R. Menzel, S. Barg, M. Miranda, D. B. Anthony, S. M. Bawaked, M. Mokhtar, S. A. Al-Thabaiti, S. N. Basahel, E. Saiz and M. S. P. Shaffer, *Adv. Funct. Mater.*, **2015**, *25*, 28.
32. Q. Zhang, X. Xu, H. Li, G. Xiong, H. Hu and T. S. Fisher, *Carbon*, **2015**, *93*, 659.

33. A.V. Dudchenko, C. Chen, A. Cardenas, J. Rolf and D. Jassby, *Nat. Nanotechnol.*, **2017**, *12*, 557.
34. S.A. Romanov, A.A. Alekseeva, E.M. Khabushev, D.V. Krasnikov and A.G. Nasibulin, *Carbon*, **2020**, *168*, 193.
35. C. Wang, S. Yang, Q. Ma, X. Jia and P.C. Ma, *Carbon*, **2017**, *118*, 765.
36. K.C. Lai, L.Y. Lee, B.Y.Z. Hiew, S. Thangalazhy-Gopakumar and S.Gan, *J. Environ. Sci.*, **2019**, *79*, 174.
37. M.F. Li, Y.G. Liu, G.M. Zeng, N. Liu and S.B. Liu, *Chemosphere*, **2019**, *226*, 360.
38. K.Q. Lu, X. Xin, N. Zhang, Z.R. Tang and Y.J. Xu, *J. Mater. Chem. A*, **2018**, *6*, 4590.
39. G. An, W. Ma, Z. Sun, Z. Liu, B. Han, S. Miao, Z. Miao and K. Ding, *Carbon*, **2007**, *45*, 1795.
40. X. Sun, S. Ji, M. Wang, J. Dou, Z. Yang, H. Qiu, S. Kou, Y. Ji and H. Wang, *J. Alloy. Compd*, **2020**, *819*, 153033.
41. J. Luo, J. Lai, N. Zhang, Y. Liu, R. Liu and X. Liu, *ACS Sustain. Chem. Eng.*, **2016**, *4*, 1404.
42. A. Filina, N. Yousefi, M. Okshevsky and N. Tufenkji, *ACS Appl. Bio Mater.*, **2019**, *2*, 1578.
43. V.K. Sharma, T.J. McDonald, H. Kim and V.K. Garg, *Adv. Colloid and Interface Sci.*, **2015**, *225*, 229.
44. S. Zhao, G. Zhang, Y. Gao, L. Deng, J. Li, R. Sun and C.P. Wong, *ACS Appl. Mater. Interf.*, **2014**, *6*, 22823.
45. Z.X. Cai, X.H. Song, Y.Y. Chen, Y.R. Wang and X. Chen, *Sensor. Actuat. B Chem.*, **2016**, *222*, 567.
46. W. Xia, C. Qu, Z. Liang, B. Zhao, S. Dai, B. Qiu, Y. Jiao, Q. Zhang, X. Huang and W. Guo, *Nano Lett.*, **2017**, *17*, 2788.
47. S. Han, D. Wu, S. Li, F. Zhang and X. Feng, *Adv. Mater.*, **2014**, *26*, 849.
48. G. Li, G. Hong, D. Dong, W. Song and X. Zhang, *Adv. Mater.*, **2018**, *30*, 1801754.
49. J. Cui, S. Yao, J.Q. Huang, L. Qin, W. G. Chong, Z. Sadighi, J. Huang, Z. Wang and J.K. Kim, *Energy Storage Mater.*, **2017**, *9*, 85.
50. M. Yan, Q. Jiang, T. Zhang, J. Wang, L. Yang, Z. Lu, H. He, Y. Fu, X. Wang and H. Huang, *J. Mater. Chem. A*, **2018**, *6*, 18165.
51. R. Du, N. Zhang, J. Zhu, Y. Wang, C. Xu, Y. Hu, N. Mao, H. Xu, W. Duan and L. Zhuang, *Small*, **2015**, *11*, 3903.
52. Z. Chen, Y. Zhang, L. Zhou, H. Zhu, F. Wan, Y. Wang and D. Zhang, *J. Hazard. Mater.*, **2017**, *332*, 70.
53. K. He, G. Chen, G. Zeng, A. Chen, Z. Huang, J. Shi, T. Huang, M. Peng and L. Hu, *Appl. Cata. B Environ.*, **2018**, *228*, 19.
54. A.B. Cundy, L. Hopkinson and R.L.D. Whitby, *Sci. Total Environ.*, **2008**, *400*, 42.
55. M.M. Khin, A.S. Nair, V.J. Babu, R. Murugan and S. Ramakrishna, *Energ. Environ. Sci.*, **2012**, *5*, 8075.
56. H. Han, M. K. Rafiq, T. Zhou, R. Xu, O. Mašek and X. Li, *J. Hazard. Mater.*, **2019**, *369*, 780.
57. R. Menzel, D. Iruretagoyena, Y. Wang, S.M. Bawaked, M. Mokhtar, S. A. Al-Thabaiti, S.N. Basahel and M.S.P. Shaffer, *Fuel*, **2016**, *181*, 531.

58. A. Garcia-Gallastegui, D. Iruretagoyena, V. Gouvea, M. Mokhtar, A.M. Asiri, S.N. Basahel, S.A. Al-Thabaiti, A.O. Alyoubi, D. Chadwick and M.S.P. Shaffer, *Chem. Mater.*, **2012**, *24*, 4531.
59. I. Andjelkovic, D.N.H. Tran, S. Kabiri, S. Azari, M. Markovic and D. Losic, *ACS Appl. Mater. Inter.*, **2015**, *7*, 9758.
60. J. Wang, L. Huang, Q. Zheng, Y. Qiao and Q. Wang, *J. Ind. Eng. Chem.*, **2016**, *36*, 255.
61. Q. Fang and B. Chen, *J. Mater. Chem. A*, **2014**, *2*, 8941.
62. G. Gorgolis and C. Galiotis, *2D Mater.*, **2017**, *4*, 032001.
63. Y. Jiang, S. Chowdhury and R. Balasubramanian, *Environ. Pollut.*, **2019**, *251*, 344.
64. J. Mao, Y. Tang, Y. Wang, J. Huang, X. Dong, Z. Chen and Y. Lai, *iScience*, **2019**, *16*, 133.
65. X.J. Yu, J. Qu, Z. Yuan, P. Min, S.M. Hao, Z.S. Zhu, X. Li, D. Yang and Z.Z. Yu, *ACS Appl. Mater. Inter.*, **2019**, *11*, 34222.
66. M. Hong, L. Yu, Y. Wang, J. Zhang, Z. Chen, L. Dong, Q. Zan and R. Li, *Chem. Eng. J.*, **2019**, *359*, 363.
67. O.T. Qazvini, R. Babarao and S.G. Telfer, *Chem. Mater.*, **2019**, *31*, 4919.
68. L. Su, H. Wang, M. Niu, S. Dai, Z. Cai, B. Yang, H. Huyan and X. Pan, *Sci. Adv.*, **2020**, *6*, 2375.
69. Q. Zhang, B. Zhang, Y. Yu, K. Zhao, P. He and B. Huang, *J. Mater. Sci.*, **2018**, *53*, 528.
70. D.G. Papageorgiou, I.A. Kinloch and R.J. Young, *Prog. Mater. Sci.*, **2017**, *90*, 75.
71. K. S. Novoselov and A. K. Geim, *Nat. Mater.*, **2007**, *6*, 183.
72. R. Zan, Q.M. Ramasse, R. Jalil, T. Georgiou, U. Bangert and K.S. Novoselov, *J. Phys. Conf. Ser.*, **2014**, *522*, 012077.
73. R. Zan, C. Muryn, U. Bangert, P. Mattocks, P. Wincott, D. Vaughan, X. Li, L. Colombo, R.S. Ruoff and B. Hamilton, *Nanoscale*, **2012**, *4*, 3065.
74. I.W. Frank, D.M. Tanenbaum, A.M. van der Zande and P.L. McEuen, *Journal of Vacuum Science & Technology B*, **2007**, *25*, 2558.
75. Y. Zhu, S. Murali, W. Cai, X. Li, J.W. Suk, J.R. Potts and R.S. Ruoff, *Adv. Mater.*, **2010**, *22*, 3906.
76. A.A. Balandin, S. Ghosh, W. Bao, I. Calizo, D. Teweldebrhan, F. Miao and C.N. Lau, *Nano Lett.*, **2008**, *8*, 902.
77. M.A. Worsley, P.J. Pauzauskie, T.Y. Olson, J. Biener, J.H. Satcher Jr and T.F. Baumann, *J. Am. Chem. Soc.*, **2010**, *132*, 14067.
78. X. Li, J. Yu, S. Wageh, A.A. Al-Ghamdi and J. Xie, *Small*, **2016**, *12*, 6640.
79. K.S. Novoselov, A.K. Geim, S.V. Morozov, D. Jiang, M.I. Katsnelson, I. Grigorieva, S. Dubonos and A.A. Firsov, *Nature*, **2005**, *438*, 197.
80. K.I. Bolotin, K.J. Sikes, Z. Jiang, M. Klima, G. Fudenberg, J. Hone, P. Kim and H.L. Stormer, *Solid State Commun.*, **2008**, *146*, 351.
81. S.W. Cranford and M.J. Buehler, *Phys. Rev. B Condens. Matter.*, **2011**, *84*, 205451.
82. X. Cai, L. Lai, Z. Shen and J. Lin, *J. Mater. Chem. A*, **2017**, *5*, 15423.
83. X. Yu, H. Cheng, M. Zhang, Y. Zhao, L. Qu and G. Shi, *Nat. Rev. Mater.*, **2017**, *2*, 1.

84. Z.H. Deng, L. Li, W. Ding, K. Xiong and Z.D. Wei, *Chem. Commun.*, **2015**, 51, 1893.
85. X. Li and L. Zhi, *Chem. Soc. Rev.*, **2018**, 47, 3189.
86. D. Mudusu, K.R. Nandanapalli, S. Lee and Y.B. Hahn, *Adv. Colloid Interface Sci.*, **2020**, 283, 102225.
87. N. Baig, M. Sajid and T.A. Saleh, *J. Environ. Manage.*, **2019**, 244, 370.
88. X. Liu, R. Ma, X. Wang, Y. Ma, Y. Yang, L. Zhuang, S. Zhang, R. Jehan, J. Chen and X. Wang, *Environ. Pollut.*, **2019**, 252, 62.
89. I.A. Kinloch, J. Suhr, J. Lou, R.J. Young and P.M. Ajayan, *Science*, **2018**, 362, 547.
90. U. Patil, S.C. Lee, S. Kulkarni, J.S. Sohn, M.S. Nam, S. Han and S.C. Jun, *Nanoscale*, **2015**, 7, 6999.
91. M. Yi and Z. Shen, *J. Mater. Chem. A*, **2015**, 3, 11700.
92. H.C. Lee, W.W. Liu, S.P. Chai, A.R. Mohamed, A. Aziz, C.S. Khe, N.M. Hidayah and U. Hashim, *RSC Adv.*, **2017**, 7, 15644.
93. F. Bonaccorso, A. Lombardo, T. Hasan, Z. Sun, L. Colombo and A.C. Ferrari, *Mater. Today*, **2012**, 15, 564.
94. X. Li, W. Cai, J. An, S. Kim, J. Nah, D. Yang, R. Piner, A. Velamakanni, I. Jung and E. Tutuc, *Science*, **2009**, 324, 1312.
95. F. Perreault, A.F. De Faria and M. Elimelech, *Chem. Soc. Rev.*, **2015**, 44, 5861.
96. A.J. Clancy, M.K. Bayazit, S.A. Hodge, N.T. Skipper, C.A. Howard and M.S.P. Shaffer, *Chem. Rev.*, **2018**, 118, 7363.
97. H.C. Schniepp, J.L. Li, M.J. McAllister, H. Sai, M. Herrera-Alonso, D.H. Adamson, R.K. Prud'homme, R. Car, D.A. Saville and I.A. Aksay, *J. Phys. Chem. B*, **2006**, 110, 8535.
98. J.W. Suk, R.D. Piner, J. An and R.S. Ruoff, *ACS Nano*, **2010**, 4, 6557.
99. D.R. Dreyer, A.D. Todd and C.W. Bielawski, *Chem. Soc. Rev.*, **2014**, 43, 5288.
100. M. Khan, M.N. Tahir, S.F. Adil, H.U. Khan, M.R.H. Siddiqui, A.A. Al-warthan and W. Tremel, *J. Mater. Chem. A*, **2015**, 3, 18753.
101. L.G. Guex, B. Sacchi, K.F. Peuvot, R.L. Andersson, A.M. Pourrahimi, V. Ström, S. Farris and R.T. Olsson, *Nanoscale*, **2017**, 9, 9562.
102. S. Nardecchia, D. Carriazo, M.L. Ferrer, M.C. Gutiérrez and F. del Monte, *Chem. Soc. Rev.*, **2013**, 42, 794.
103. N. Al-Jammal and T. Juzsakova, *Seq*, **2017**, 25, 36.
104. I. Rafique, A. Kausar, Z. Anwar and B. Muhammad, *Polym. Plast. Technol. Eng.*, **2016**, 55, 312.
105. J. Li, P.C. Ma, W.S. Chow, C. . To, B.Z. Tang and J.K. Kim, *Adv. Funct. Mater.*, **2007**, 17, 3207.
106. M.F.L. De Volder, S.H. Tawfick, R.H. Baughman and A.J. Hart, *Science*, **2013**, 339, 535.
107. Q. Cao, S. H. Hur, Z.T. Zhu, Y.G. Sun, C.J. Wang, M.A. Meitl, M. Shim and J.A. Rogers, *Adv. Mater.*, **2006**, 18, 304.
108. J. Huang, Y. Zhu, W. Jiang, J. Yin, Q. Tang and X. Yang, *ACS Appl. Mater. Inter.*, **2014**, 6, 1754.

109. D.J. Li, U. N. Maiti, J. Lim, D.S. Choi, W.J. Lee, Y. Oh, G.Y. Lee and S.O. Kim, *Nano Lett.*, **2014**, *14*, 1228.
110. B. Yu, F. Qi, B. Zheng, W. Hou, W. Zhang, Y. Li and Y. Chen, *J. Mater. Chem. A*, **2018**, *6*, 1655.
111. Y. Zhang and L. Zheng, *Nanoscale*, **2010**, *2*, 1919.
112. Y. Liao, H. Jiang, N. Wei, P. Laiho, Q. Zhang, S.A. Khan and E.I. Kauppinen, *J. Am. Chem. Soc.*, **2018**, *140*, 9797.
113. S. Zhang, L. Kang, X. Wang, L. Tong, L. Yang, Z. Wang, K. Qi, S. Deng, Q. Li and X. Bai, *Nature*, **2017**, *543*, 234.
114. B. Oktay, S. TÜRker, S. Karataş and N. Apohan, *J. Turkish Chem. Soc.*, **2017**, *5*, 283.
115. H. Maleki, *Chem. Eng. J.*, **2016**, *300*, 98.
116. W. Wan, R. Zhang, M. Ma and Y. Zhou, *J. Mater. Chem. A*, **2018**, *6*, 754.
117. H. Liu, B. Geng, Y. Chen and H. Wang, *ACS Sustain. Chem. Eng.*, **2017**, *5*, 49.
118. A. Lamy-Mendes, R.F. Silva and L. Durães, *J. Mater. Chem. A*, **2018**, *6*, 1340.
119. E. Cuce, P.M. Cuce, C.J. Wood and S.B. Riffat, *Renew. Sust. Energ. Rev.*, **2014**, *34*, 273.
120. Z. Li, Z. Liu, H. Sun and C. Gao, *Chem. Rev.*, **2015**, *115*, 7046.
121. H.P. Cong, J.F. Chen and S.H. Yu, *Chem. Soc. Rev.*, **2014**, *43*, 7295.
122. S.M. Jung, H.Y. Jung, M.S. Dresselhaus, Y.J. Jung and J. Kong, *Sci. Rep.*, **2012**, *2*, 849.
123. Y. Xie, Z. Meng, T. Cai and W.Q. Han, *ACS Appl. Mater. Inter.*, **2015**, *7*, 25202.
124. L. Sui, Y. Wang, W. Ji, H. Kang, L. Dong and L. Yu, *Int. J. Hydrog. Energy*, **2017**, *42*, 29820.
125. J. Yang, L.S. Tang, R.Y. Bao, L. Bai, Z.Y. Liu, W. Yang, B.H. Xie and M.B. Yang, *J. Mater. Chem. A*, **2016**, *4*, 18841.
126. X.H. Li, P. Liu, X. Li, F. An, P. Min, K.N. Liao and Z.Z. Yu, *Carbon*, **2018**, *140*, 624.
127. S. Barg, F.M. Perez, N. Ni, P. do Vale Pereira, R.C. Maher, E. Garcia-Tunon, S. Eslava, S. Agnoli, C. Mattevi and E. Saiz, *Nat. Commun.*, **2014**, *5*, 4328.
128. Z. Zeng, T. Wu, D. Han, Q. Ren, G. Siqueira and G. Nyström, *ACS Nano*, **2020**, *14*, 2927.
129. T. Liu, M. Huang, X. Li, C. Wang, C.X. Gui and Z.Z. Yu, *Carbon*, **2016**, *100*, 456.
130. P. Lv, X.W. Tan, K.H. Yu, R.L. Zheng, J.J. Zheng and W. Wei, *Carbon*, **2016**, *99*, 222.
131. A. Allahbakhsh and A. R. Bahramian, *Nanoscale*, **2015**, *7*, 14139.
132. S. Ye, Y. Liu and J. Feng, *ACS Appl. Mater. Inter.*, **2017**, *9*, 22456.
133. Y. Chen, L. Yang, S. Xu, S. Han, S. Chu, Z. Wang and C. Jiang, *RSC Adv.*, **2019**, *9*, 22950.
134. H. Ha, K. Shanmuganathan and C.J. Ellison, *ACS Appl. Mater. Inter.*, **2015**, *7*, 6220.
135. H. Huang, P. Chen, X. Zhang, Y. Lu and W. Zhan, *Small*, **2013**, *9*, 1397.
136. Y. Zhang, W. Fan, Y. Huang, C. Zhang and T. Liu, *RSC Adv.*, **2015**, *5*, 1301.
137. H. Yang, Z. Li, G. Sun, X. Jin, B. Lu, P. Zhang, T. Lin and L. Qu, *Adv. Funct. Mater.*, **2019**, *29*, 1901917.
138. N. Cherkasov, *J. Mol. Liq.*, **2020**, *301*, 112378.

139. Y.S. Al-Degs, A.H. El-Sheikh, R.Z. Al Bakain, A.P. Newman and M.A. Al-Ghouti, *Energy Technol.*, **2016**, *4*, 679.
140. Y. Shen, Q. Fang and B. Chen, *Environ. Sci. Technol.*, **2015**, *49*, 67.
141. S. Bolisetty, M. Peydayesh and R. Mezzenga, *Chem. Soc. Rev.*, **2019**, *48*, 463.
142. F. Wang, D. Wei, Y. Li, T. Chen, P. Mu, H. Sun, Z. Zhu, W. Liang and A. Li, *J. Mater. Chem. A*, **2019**, *7*, 18311.
143. R. Molinari, C. Lavorato and P. Argurio, *Catal. Today*, **2017**, *281*, 144.
144. K. K. Gangu, S. Maddila and S. B. Jonnalagadda, *Sci. Total Environ.*, **2019**, *646*, 1398.
145. H. Chang, H. Liang, F. Qu, B. Liu, H. Yu, X. Du, G. Li and S.A. Snyder, *J. Membr. Sci.*, **2017**, *540*, 362.
146. L.N. Nthunya, L. Gutierrez, S. Derese, E.N. Nxumalo, A.R. Verliefdde, B.B. Mamba and S. D. Mhlanga, *J. Chem. Technol. Biotechnol.*, **2019**, *94*, 2757.
147. D. Xia, F. Tan, C. Zhang, X. Jiang, Z. Chen, H. Li, Y. Zheng, Q. Li and Y. Wang, *Appl. Surf. Sci.*, **2016**, *377*, 361.
148. S. Cao, Q. Jiang, X. Wu, D. Ghim, H. G. Derami, P.I. Chou, Y.S. Jun and S. Singamaneni, *J. Mater. Chem. A*, **2019**, *7*, 24092.
149. A.M. Awad, S.M.R. Shaikh, R. Jalab, M.H. Gulied, M.S. Nasser, A. Benamor and S. Adham, *Sep. Purif. Technol.*, **2019**, *228*, 115719.
150. A. Kausar, M. Iqbal, A. Javed, K. Aftab, H. N. Bhatti and S. Nouren, *J. Mol. Liq.*, **2018**, *256*, 395.
151. B. Szczeńniak, J. Choma and M. Jaroniec, *Adv. Colloid Interface Sci.*, **2017**, *243*, 46.
152. S. Gadipelli and Z. X. Guo, *Prog. Mater. Sci.*, **2015**, *69*, 1.
153. S. An, B.N. Joshi, J.G. Lee, M. W. Lee, Y. I. Kim, M.W. Kim, H.S. Jo and S.S. Yoon, *Catal. Today*, **2017**, *295*, 14.
154. Y. Zheng, S. Zheng, H. Xue and H. Pang, *Adv. Funct. Mater.*, **2018**, *28*, 1804950.
155. L. Wang, C. Shi, L. Pan, X. Zhang and J.J. Zou, *Nanoscale*, **2020**, *12*, 4790.
156. G. Di, Z. Zhu, H. Zhang, J. Zhu, H. Lu, W. Zhang, Y. Qiu, L. Zhu and S. Küppers, *Chem. Eng. J.*, **2017**, *328*, 141.
157. N. B. Singh, G. Nagpal and S. Agrawal, *Environ. Technol. Innov.*, **2018**, *11*, 187.
158. X. Qu, P. J.J. Alvarez and Q. Li, *Water Res.*, **2013**, *47*, 3931.
159. M. Nagpal and R. Kakkar, *Sep. Purif. Technol.*, **2019**, *211*, 522.
160. A.M. Awad, R. Jalab, A. Benamor, M.S. Nasser, M.M. Ba-Abbad, M. El-Naas and A.W. Mohammad, *J. Mol. Liq.*, **2020**, *301*, 112335.
161. J. Luo, Y. Chao, Z. Tang, M. Hua, X. Li, Y. Wei, H. Ji, J. Xiong, W. Zhu and H. Li, *Ind. Eng. Chem. Res.*, **2019**, *58*, 13303.
162. N. A. Khan and S. H. Jhung, *Angew. Chem. Int. Ed.*, **2012**, *51*, 1198.
163. E. Yang, C. Yao, Y. Liu, C. Zhang, L. Jia, D. Li, Z. Fu, D. Sun, S.R. Kirk and D. Yin, *Fuel*, **2018**, *211*, 121.
164. K.X. Lee, H. Wang, S. Karakalos, G. Tsilomelekis and J.A. Valla, *Ind. Eng. Chem. Res.*, **2019**, *58*, 18301.

165. A. Rajendran, T.Y. Cui, H.X. Fan, Z.F. Yang, J. Feng and W.Y. Li, *J. Mater. Chem. A*, **2020**, *8*, 2246.
166. J. Xiong, J. Luo, J. Di, X. Li, Y. Chao, M. Zhang, W. Zhu and H. Li, *Fuel*, **2020**, *261*, 116448.
167. J. Xiong, L. Yang, Y. Chao, J. Pang, M. Zhang, W. Zhu and H. Li, *ACS Sustain. Chem. Eng.*, **2016**, *4*, 4457.
168. J. Xiong, J. Luo, L. Yang, J. Pang, W. Zhu and H. Li, *J. Ind. Eng. Chem.*, **2018**, *64*, 383.
169. K. X. Lee and J. A. Valla, *React. Chem. Eng.*, **2019**, *4*, 1357.
170. Q. Zhao, Z. Chang, X. Lei and X. Sun, *Ind. Eng. Chem. Res.*, **2011**, *50*, 10253.
171. A. Rajendran, H.X. Fan, J. Feng and W.Y. Li, *Chem. Asian J.*, **2020**, *15*, 1861.
172. J. Xiao, S. Sitamraju, Y. Chen, S. Watanabe, M. Fujii, M. Janik and C. Song, *AIChE J.*, **2015**, *61*, 631.
173. N.A. Khan, C.M. Kim and S.H. Jhung, *Chem. Eng. J.*, **2017**, *311*, 20.
174. A.E. Creamer and B. Gao, *Environ. Sci. Technol.*, **2016**, *50*, 7276.
175. A.A. Azmi and M.A.A. Aziz, *J. Environ. Chem. Eng.*, **2019**, *7*, 103022.
176. S. Chowdhury and R. Balasubramanian, *Sci. Rep.*, **2016**, *6*, 21537.
177. L. Keller, B. Ohs, L. Abduly and M. Wessling, *Chem. Eng. J.*, **2019**, *359*, 476.
178. S. Chowdhury, G. K. Parshetti and R. Balasubramanian, *Chem. Eng. J.*, **2015**, *263*, 374.
179. C.H. Yu, C.H. Huang and C.S. Tan, *Aerosol Air Qual. Res.*, **2012**, *12*, 745.
180. C.A. Scholes, K.H. Smith, S.E. Kentish and G.W. Stevens, *Int. J. Greenh. Gas Control.*, **2010**, *4*, 739.
181. J. Peng, D. Iruretagoyena and D. Chadwick, *J. CO<sub>2</sub> Util.*, **2018**, *24*, 73.
182. S.T. Wismann, J.S. Engbæk, S.B. Vendelbo, F.B. Bendixen, W.L. Eriksen, K. Aasberg-Petersen, C. Frandsen, I. Chorkendorff and P.M. Mortensen, *Science*, **2019**, *364*, 756.
183. S. Yao, X. Zhang, W. Zhou, R. Gao, W. Xu, Y. Ye, L. Lin, X. Wen, P. Liu and B. Chen, *Science*, **2017**, *357*, 389.
184. C. H. Lee and K. B. Lee, *Appl. Energy*, **2017**, *205*, 316.
185. Y. Hu, H. Cui, Z. Cheng and Z. Zhou, *Chem. Eng. J.*, **2019**, *377*, 119823.
186. X. Cui, H.Y. Su, R. Chen, L. Yu, J. Dong, C. Ma, S. Wang, J. Li, F. Yang and J. Xiao, *Nat. Commun.*, **2019**, *10*, 1.
187. L. Mohapatra and K. Parida, *J. Mater. Chem. A*, **2016**, *4*, 10744.
188. K.H. Goh, T.T. Lim and Z. Dong, *Water Res.*, **2008**, *42*, 1343.
189. X. Xiang, L. Bai and F. Li, *AIChE J.*, **2010**, *56*, 2934.
190. Y. Gao, Z. Zhang, J. Wu, X. Yi, A. Zheng, A. Umar, D. O'Hare and Q. Wang, *J. Mater. Chem. A*, **2013**, *1*, 12782.
191. G.J. Slotman and A. Fasolino, *J. Phys. Condens. Matter*, **2012**, *25*, 045009.
192. Y. Gong, G. Shi, Z. Zhang, W. Zhou, J. Jung, W. Gao, L. Ma, Y. Yang, S. Yang and G. You, *Nat. Commun.*, **2014**, *5*, 1.
193. Q. Weng, X. Wang, X. Wang, Y. Bando and D. Golberg, *Chem. Soc. Rev.*, **2016**, *45*, 3989.

194. D. Choi, N. Poudel, S. Park, D. Akinwande, S.B. Cronin, K. Watanabe, T. Taniguchi, Z. Yao and L. Shi, *ACS Appl. Mater. Inter.*, **2018**, *10*, 11101.
195. J. Xiong, L. Yang, Y. Chao, J. Pang, P. Wu, M. Zhang, W. Zhu and H. Li, *Green Chem.*, **2016**, *18*, 3040.
196. J. Xiong, W. Zhu, H. Li, W. Ding, Y. Chao, P. Wu, S. Xun, M. Zhang and H. Li, *Green Chem.*, **2015**, *17*, 1647.
197. Y. Cao, G. Li and X. Li, *Chem. Eng. J.*, **2016**, *292*, 207.
198. M. De Marco, R. Menzel, S.M. Bawaked, M. Mokhtar, A.Y. Obaid, S.N. Basahel and M.S.P. Shaffer, *Carbon*, **2017**, *123*, 616.
199. N.L.V. Carreño, M.T. Escote, A. Valentini, L. McCafferty, V. Stolojan, M. Beliatis, C.A. Mills, R. Rhodes, C.T.G. Smith and S.R.P. Silva, *Nanoscale*, **2015**, *7*, 17441.
200. A. Zhang, C. Wang, Q. Xu, H. Liu, Y. Wang and Y. Xia, *RSC Adv.*, **2015**, *5*, 26017.
201. H. Wan, J. Liu, Y. Ruan, L. Lv, L. Peng, X. Ji, L. Miao and J. Jiang, *ACS Appl. Mater. Inter.*, **2015**, *7*, 15840.
202. S. Goswami, I. Hod, J. D. Duan, C.W. Kung, M. Rimoldi, C.D. Malliakas, R.H. Palmer, O.K. Farha and J.T. Hupp, *J. Am. Chem. Soc.*, **2019**, *141*, 17696.
203. M. Lakhane, K. Bogle, R. Khairnar, S. Dahiwal, R. Sharma, V. Mokale and M. Mahabole, *Nano-Struct. Nano-Objects*, **2019**, *17*, 248.
204. T. Linhares, M.T.P. de Amorim and L. Durães, *J. Mater. Chem. A*, **2019**, *7*, 22768.
205. K. Jin, S. Zhang, S. Zhou, J. Qiao, Y. Song, J. Di, D. Zhang and Q. Li, *Nanoscale*, **2018**, *10*, 8180.
206. A.R. O. Raji, T. Varadhachary, K. Nan, T. Wang, J. Lin, Y. Ji, B. Genorio, Y. Zhu, C. Kittrell and J. M. Tour, *ACS Appl. Mater. Inter.*, **2016**, *8*, 3551.
207. X. Li, C. Shao, B. Zhuo, S. Yang, Z. Zhu, C. Su and Q. Yuan, *Int. J. Biol. Macromol.*, **2019**, *139*, 1103.
208. C. Boo and M. Elimelech, *Nat. Nanotechnol.*, **2017**, *12*, 501.
209. J. Ge, L.A. Shi, Y.C. Wang, H.Y. Zhao, H.B. Yao, Y.B. Zhu, Y. Zhang, H.W. Zhu, H.A. Wu and S.H. Yu, *Nat. Nanotechnol.*, **2017**, *12*, 434.
210. D. Fragouli and A. Athanassiou, *Nat. Nanotechnol.*, **2017**, *12*, 406.
211. J. Abrahamson, *Carbon*, **1974**, *12*, 111.
212. W. Bao, A.D. Pickel, Q. Zhang, Y. Chen, Y. Yao, J. Wan, K. Fu, Y. Wang, J. Dai and H. Zhu, *Adv. Mater.*, **2016**, *28*, 4684.
213. T. Li, A.D. Pickel, Y. Yao, Y. Chen, Y. Zeng, S.D. Lacey, Y. Li, Y. Wang, J. Dai and Y. Wang, *Nat. Energy*, **2018**, *3*, 148.
214. Y. Yao, K.K. Fu, S. Zhu, J. Dai, Y. Wang, G. Pastel, Y. Chen, T. Li, C. Wang and T. Li, *Nano Lett.*, **2016**, *16*, 7282.
215. Y. Yao, Z. Huang, P. Xie, L. Wu, L. Ma, T. Li, Z. Pang, M. Jiao, Z. Liang and J. Gao, *Nat. Nanotechnol.*, **2019**, *14*, 851.
216. Y. Yao, Z. Huang, P. Xie, S.D. Lacey, R. J. Jacob, H. Xie, F. Chen, A. Nie, T. Pu and M. Rehwoldt, *Science*, **2018**, *359*, 1489.

217. X. Hu, W. Xu, L. Zhou, Y. Tan, Y. Wang, S. Zhu and J. Zhu, *Adv. Mater.*, **2017**, *29*, 1604031.
218. F. Yavari, Z. Chen, A. V. Thomas, W. Ren, H.-M. Cheng and N. Koratkar, *Sci. Rep.*, **2011**, *1*, 1.
219. K. Wang, Y. Zeng, W. Lin, X. Yang, Y. Cao, H. Wang, F. Peng and H. Yu, *Carbon*, **2020**, *167*, 709.
220. Y. Fu, G. Wang, T. Mei, J. Li, J. Wang and X. Wang, *ACS Sustain. Chem. Eng.*, **2017**, *5*, 4665.
221. Y. Fu, G. Wang, X. Ming, X. Liu, B. Hou, T. Mei, J. Li, J. Wang and X. Wang, *Carbon*, **2018**, *130*, 250.
222. B. Huo, D. Jiang, X. Cao, H. Liang, Z. Liu, C. Li and J. Liu, *Carbon*, **2019**, *142*, 13.
223. Z. Deng, J. Zhou, L. Miao, C. Liu, Y. Peng, L. Sun and S. Tanemura, *J. Mater. Chem. A*, **2017**, *5*, 7691.
224. C. Li, Z. Y. Wu, H. W. Liang, J. F. Chen and S. H. Yu, *Small*, **2017**, *13*, 1700453.
225. N. Nguyen, S. Zhang, A. Oluwalowo, J.G. Park, K. Yao and R. Liang, *ACS Appl. Mater. Inter.*, **2018**, *10*, 27171.
226. R. Beams, L. G. Cançado and L. Novotny, *J. Phys. Condens. Matter*, **2015**, *27*, 083002.
227. T. Gao, Y. Li, C. Chen, Z. Yang, Y. Kuang, C. Jia, J. Song, E. M. Hitz, B. Liu and H. Huang, *Small Methods*, **2019**, *3*, 1800176.
228. V. Kashyap, A. Al-Bayati, S. M. Sajadi, P. Irajizad, S.H. Wang and H. Ghasemi, *J. Mater. Chem. A*, **2017**, *5*, 15227.
229. F. Tao, Y. Zhang, B. Wang, F. Zhang, X. Chang, R. Fan, L. Dong and Y. Yin, *Sol. Energy Mater. Sol. Cells*, **2018**, *180*, 34.
230. J. Yang, Y. Pang, W. Huang, S.K. Shaw, J. Schiffbauer, M.A. Pillers, X. Mu, S. Luo, T. Zhang and Y. Huang, *ACS Nano*, **2017**, *11*, 5510.
231. B. Bai, X. Yang, R. Tian, W. Ren, R. Suo and H. Wang, *Appl. Therm. Eng.*, **2019**, *163*, 114379.
232. X. Luo, C. Huang, S. Liu and J. Zhong, *Int. J. Energy Res.*, **2018**, *42*, 4830.
233. H. Su, J. Zhou, L. Miao, J. Shi, Y. Gu, P. Wang, Y. Tian, X. Mu, A. Wei and L. Huang, *SM&T*, **2019**, *20*, 02214.
234. G. Cheng, X. Wang, X. Liu, Y. He and B. V. Balakin, *Sol. Energy*, **2019**, *194*, 415.
235. X. Feng, J. Zhao, D. Sun, L. Shanmugam, J.K. Kim and J. Yang, *J. Mater. Chem. A*, **2019**, *7*, 4400.
236. X. Deng, Q. Nie, Y. Wu, H. Fang, P. Zhang and Y. Xie, *ACS Appl. Mater. Inter.*, **2020**, *23*, 26200.
237. L. Huang, J. Pei, H. Jiang and X. Hu, *Desalination*, **2018**, *442*, 1.
238. X. Ming, A. Guo, Q. Zhang, Z. Guo, F. Yu, B. Hou, Y. Wang, K. P. Homewood and X. Wang, *Carbon*, **2020**, *167*, 285.
239. G. Wang, Y. Fu, A. Guo, T. Mei, J. Wang, J. Li and X. Wang, *Chem. Mater.*, **2017**, *29*, 5629.
240. W. Chen, C. Zou, X. Li and H. Liang, *Desalination*, **2019**, *451*, 92.

241. Z.C. Xiong, Y.J. Zhu, D.D. Qin, F.F. Chen and R.L. Yang, *Small*, **2018**, *14*, 1803387.
242. Q. Gan, T. Zhang, R. Chen, X. Wang and M. Ye, *ACS Sustain. Chem. Eng.*, **2019**, *7*, 3925.
243. X. Wang, Y. He, X. Liu and J. Zhu, *Powder Technol.*, **2017**, *321*, 276.
244. L. Shi, Y. Wang, L. Zhang and P. Wang, *J. Mater. Chem. A*, **2017**, *5*, 16212.
245. S. Liu, C. Huang, X. Luo and Z. Rao, *Appl. Therm. Eng.*, **2018**, *142*, 566.
246. Y. Wang, C. Wang, X. Song, S. K. Megarajan and H. Jiang, *J. Mater. Chem. A*, **2018**, *6*, 963.
247. R. Hu, J. Zhang, Y. Kuang, K. Wang, X. Cai, Z. Fang, W. Huang, G. Chen and Z. Wang, *J. Mater. Chem. A*, **2019**, *7*, 15333.
248. Z. Yin, H. Wang, M. Jian, Y. Li, K. Xia, M. Zhang, C. Wang, Q. Wang, M. Ma and Q.-s. Zheng, *ACS Appl. Mater. Inter.*, **2017**, *9*, 28596.
249. B. Xia, Y. Yan, X. Wang and X. W. D. Lou, *Mater. Horiz.*, **2014**, *1*, 379.
250. C. Tang, H. S. Wang, H. F. Wang, Q. Zhang, G. L. Tian, J. Q. Nie and F. Wei, *Adv. Mater.*, **2015**, *27*, 4516.
251. X. Xu, Y. Sun, W. Qiao, X. Zhang, X. Chen, X. Song, L. Wu, W. Zhong and Y. Du, *Appl. Surf. Sci.*, **2017**, *396*, 1520.
252. C. Teng, J. Qiao, J. Wang, L. Jiang and Y. Zhu, *ACS Nano*, **2016**, *10*, 413.
253. L. Xiao, D. Wu, S. Han, Y. Huang, S. Li, M. He, F. Zhang and X. Feng, *ACS Appl. Mater. Inter.*, **2013**, *5*, 3764.
254. J. Xiao, Y. Tan, Y. Song and Q. Zheng, *J. Mater. Chem. A*, **2018**, *6*, 9074.
255. M. Wang, X. Duan, Y. Xu and X. Duan, *ACS Nano*, **2016**, *10*, 7231.
256. R. Liu, Y. Xu and B. Chen, *Environ. Sci. Technol.*, **2018**, *52*, 7043.
257. C. Cheng, S. Li, A. Thomas, N. A. Kotov and R. Haag, *Chem. Rev.*, **2017**, *117*, 1826.
258. L. Xu, G. Xiao, C. Chen, R. Li, Y. Mai, G. Sun and D. Yan, *J. Mater. Chem. A*, **2015**, *3*, 7498.
259. Z. Juanjuan, L. Ruiyi, L. Zaijun, L. Junkang, G. Zhiguo and W. Guangli, *Nanoscale*, **2014**, *6*, 5458.
260. B. Xie, Y. Zhang and R. Zhang, *J. Mater. Chem. A*, **2017**, *5*, 17544.
261. X. Xu, H. Li, Q. Zhang, H. Hu, Z. Zhao, J. Li, J. Li, Y. Qiao and Y. Gogotsi, *ACS Nano*, **2015**, *9*, 3969.
262. Y. Ma, Y. Yue, H. Zhang, F. Cheng, W. Zhao, J. Rao, S. Luo, J. Wang, X. Jiang and Z. Liu, *ACS Nano*, **2018**, *12*, 3209.
263. H. Huang, S. Yang, R. Vajtai, X. Wang and P. M. Ajayan, *Adv. Mater.*, **2014**, *26*, 5160.
264. Y. Hou, Z. Wen, S. Cui, X. Feng and J. Chen, *Nano Lett.*, **2016**, *16*, 2268.
265. Y. Song, H. Li, L. Yang, D. Bai, F. Zhang and S. Xu, *ACS Appl. Mater. Inter.*, **2017**, *9*, 42742.
266. S.A. Ganiyu, K. Alhooshani, K.O. Sulaiman, M. Qamaruddin, I.A. Bakare, A. Tanimu and T.A. Saleh, *Chem. Eng. J.*, **2016**, *303*, 489.
267. Y. Han, M.A. Sinnwell, S.J. Teat, M.L. Sushko, M.E. Bowden, Q.R.S. Miller, H.T. Schaef, L. Liu, Z. Nie and J. Liu, *Adv. Sci.*, **2019**, *6*, 1802056.

268. T.A. Saleh, *Nanotechnology in Oil and Gas Industries: Principles and Applications*, Springer, 2017.
269. S. Choi, J.H. Drese and C.W. Jones, *ChemSusChem*, **2009**, *2*, 796.
270. S. Radha and A. Navrotsky, *J. Phys. Chem. C*, **2014**, *118*, 29836.
271. S.I. Garcés-Polo, J. Villarroel-Rocha, K. Sapag, S.A. Korili and A. Gil, *Chem. Eng. J.*, **2018**, *332*, 24.
272. Z. Yong, V. Mata and A. E. Rodrigues, *Ind. Eng. Chem. Res.*, **2001**, *40*, 204.
273. M.J. Ramírez-Moreno, I.C. Romero-Ibarra, M.A. Hernández-Pérez and H. Pfeiffer, *Ind. Eng. Chem. Res.*, **2014**, *53*, 8087.
274. J. Boon, P.D. Cobden, H.A.J. Van Dijk, C. Hoogland, E.R.V. van Selow and M. van Sint Annaland, *Chem. Eng. J.*, **2014**, *248*, 406.
275. Y. Zou, X. Wang, Y. Ai, Y. Liu, J. Li, Y. Ji and X. Wang, *Environ. Sci. Technol.*, **2016**, *50*, 3658.
276. H. Zhu, X. Yang, E. D. Cranston and S. Zhu, *Adv. Mater.*, **2016**, *28*, 7652.
277. J. Kuljiraseth, A. Wangriya, J.M.C. Malones, W. Klysubun and S. Jitkarnka, *Appl. Catal. B Environ.*, **2019**, *243*, 415.
278. Y. Cheng, J. Lin, T. Wu, H. Wang, S. Xie, Y. Pei, S. Yan, M. Qiao and B. Zong, *Appl. Catal. B Environ.*, **2017**, *204*, 475.
279. W. Liu, J. Cai, Z. Ding and Z. Li, *Appl. Catal. B Environ.*, **2015**, *174*, 421.
280. J.S. Li, Y. Wang, C.H. Liu, S.L. Li, Y.G. Wang, L.Z. Dong, Z.H. Dai, Y.F. Li and Y.Q. Lan, *Nat. Commun.*, **2016**, *7*, 1.
281. J. Mu, C. Hou, G. Wang, X. Wang, Q. Zhang, Y. Li, H. Wang and M. Zhu, *Adv. Mater.*, **2016**, *28*, 9491.
282. S. Guo, Y. Jiang, L. Li, X. Huang, Z. Zhuang and Y. Yu, *J. Mater. Chem. A*, **2018**, *6*, 4167.
283. J.J. Bae, S.C. Lim, G.H. Han, Y.W. Jo, D.L. Doung, E.S. Kim, S.J. Chae, T.Q. Huy, N. Van Luan and Y.H. Lee, *Adv. Funct. Mater.*, 2012, **22**, 4819.
284. S. Pei, Q. Wei, K. Huang, H.M. Cheng and W. Ren, *Nat. Commun.*, **2018**, *9*, 1.
285. A. Garcia-Gallastegui, D. Iruretagoyena, M. Mokhtar, A.M. Asiri, S.N. Basahel, S.A. Al-Thabaiti, A.O. Alyoubi, D. Chadwick and M.S.P. Shaffer, *J. Mater. Chem.*, **2012**, *22*, 13932.
286. N.N.A. H. Meis, J.H. Bitter and K.P. de Jong, *Ind. Eng. Chem. Res.*, **2010**, *49*, 1229.
287. D. Iruretagoyena, M.S.P. Shaffer and D. Chadwick, *Adsorption*, **2014**, *20*, 321.
288. S. Li, Y. Shi, Y. Yang and N. Cai, *Energy Procedia*, **2013**, *37*, 2224.
289. Y. Song, D. Mandelli, O. Hod, M. Urbakh, M. Ma and Q. Zheng, *Nat. Mater.*, **2018**, *17*, 894.
290. X. Xu, Q. Zhang, M. Hao, Y. Hu, Z. Lin, L. Peng, T. Wang, X. Ren, C. Wang and Z. Zhao, *Science*, **2019**, *363*, 723.
291. G. Li, M. Zhu, W. Gong, R. Du, A. Eychmüller, T. Li, W. Lv and X. Zhang, *Adv. Funct. Mater.*, **2019**, *29*, 1900188.
292. L. Lu, J. He, P. Wu, Y. Wu, Y. Chao, H. Li, D. Tao, L. Fan, H. Li and W. Zhu, *Green Chem.*, **2018**, *20*, 4453.

293. J. Yin, J. Li, Y. Hang, J. Yu, G. Tai, X. Li, Z. Zhang and W. Guo, *Small*, **2016**, *12*, 2942.
294. K.N. Yun, Y. Sun, J.S. Han, Y.H. Song and C. J. Lee, *ACS Appl. Mater. Inter.*, **2017**, *9*, 1562.
295. R. Frisenda, E. Navarro-Moratalla, P. Gant, D.P. De Lara, P. Jarillo-Herrero, R.V. Gorbachev and A. Castellanos-Gomez, *Chem. Soc. Rev.*, **2018**, *47*, 53.
296. Y. Xue, P. Dai, X. Jiang, X. Wang, C. Zhang, D. Tang, Q. Weng, X. Wang, A. Pakdel and C. Tang, *J. Mater. Chem. A*, **2016**, *4*, 1469.
297. P. Wu, W. Zhu, Y. Chao, J. Zhang, P. Zhang, H. Zhu, C. Li, Z. Chen, H. Li and S. Dai, *Chem. Commun.*, **2016**, *52*, 144.
298. S. Byun, J.H. Kim, S.H. Song, M. Lee, J.J. Park, G. Lee, S.H. Hong and D. Lee, *Chem. Mater.*, **2016**, *28*, 7750.
299. D. R. Deng, F. Xue, C.D. Bai, J. Lei, R. Yuan, M. S. Zheng and Q. F. Dong, *ACS Nano*, **2018**, *12*, 11120.
300. F. An, X. Li, P. Min, H. Li, Z. Dai and Z.Z. Yu, *Carbon*, **2018**, *126*, 119.
301. Y.J. Jeong and M.F. Islam, *Nanoscale*, **2015**, *7*, 12888.
302. J. Xiong, W. Zhu, H. Li, L. Yang, Y. Chao, P. Wu, S. Xun, W. Jiang, M. Zhang and H. Li, *J. Mater. Chem. A*, **2015**, *3*, 12738.
303. R. Dehghan and M. Anbia, *Fuel Process. Technol.*, **2017**, *167*, 99.
304. J. Kou, C. Lu, W. Sun, L. Zhang and Z. Xu, *ACS Sustain. Chem. Eng.*, **2015**, *3*, 3053.
305. B. Liu, Y. Zhu, S. Liu and J. Mao, *J. Chem. Eng. Data*, **2012**, *57*, 1326.
306. S. Aslam, F. Subhan, Z. Yan, U.J. Etim and J. Zeng, *Chem. Eng. J.*, **2017**, *315*, 469.
307. P. Tan, D. M. Xue, J. Zhu, Y. Jiang, Q. X. He, Z. Hou, X. Q. Liu and L. B. Sun, *AIChE J.*, **2018**, *64*, 3786.
308. Q.X. He, Y. Jiang, P. Tan, X.Q. Liu, J.X. Qin and L.B. Sun, *ACS Appl. Mater Inter.*, **2017**, *9*, 29445.
309. P. Tan, Y. Jiang, L.B. Sun, X.Q. Liu, K. AlBahily, U. Ravon and A. Vinu, *J. Mater. Chem. A*, **2018**, *6*, 23978.
310. R. Neubauer, N. Kienzl, B. Bitschnau, H. Schroettner and C. Hochenauer, *Energy Fuels*, **2017**, *31*, 12942.
311. F. Sharif, L.R. Gagnon, S. Mulmi and E. P. L. Roberts, *Water Res.*, **2017**, *114*, 237.
312. M. Pan, C. Shan, X. Zhang, Y. Zhang, C. Zhu, G. Gao and B. Pan, *Environ. Sci. Technol.*, **2018**, *52*, 739.
313. J. Liu, X. Ge, X. Ye, G. Wang, H. Zhang, H. Zhou, Y. Zhang and H. Zhao, *J. Mater. Chem. A*, **2016**, *4*, 1970.
314. S. Marchesini, C.M. McGilvery, J. Bailey and C. Petit, *ACS Nano*, **2017**, *11*, 10003.
315. T. Liu, X. Mai, H. Chen, J. Ren, Z. Liu, Y. Li, L. Gao, N. Wang, J. Zhang and H. He, *Nanoscale*, **2018**, *10*, 4194.
316. M. Florent and T. J. Bandosz, *J. Mater. Chem. A*, **2018**, *6*, 3510.
317. C. Yang, J. Wang, Y. Chen, D. Liu, S. Huang and W. Lei, *Nanoscale*, **2018**, *10*, 10979.
318. I. Esteve-Adell, J. He, F. Ramiro, P. Atienzar, A. Primo and H. García, *Nanoscale*, **2018**, *10*, 4391.

319. T. Fukumaru, T. Fujigaya and N. Nakashima, *Sci. Rep.*, **2015**, *5*, 7951.
320. T. Kim, J. Hur and S. Jeon, *Semicond. Sci. Technol.*, **2016**, *31*, 055014.
321. S.A. Ganiyu, O.O. Ajumobi, S.A. Lateef, K.O. Sulaiman, I.A. Bakare, M. Qamaruddin and K. Alhooshani, *Chem. Eng. J.*, **2017**, *321*, 651.
322. P. Tan, J.X. Qin, X.Q. Liu, X.Q. Yin and L.B. Sun, *J. Mater. Chem. A*, **2014**, *2*, 4698.
323. Y.N. Prajapati and N. Verma, *Fuel*, **2017**, *189*, 186.
324. A. Samokhvalov, E.C. Duin, S. Nair and B.J. Tatarchuk, *Appl. Surf. Sci.*, **2011**, *257*, 3226.
325. H. Li, W. Zhu, S. Zhu, J. Xia, Y. Chang, W. Jiang, M. Zhang, Y. Zhou and H. Li, *AIChE J.*, **2016**, *62*, 2087.
326. Z. Li, P. Xiao, B.G. Zhang, Y. Li and Y.H. Lu, *Ceram. Int.*, **2015**, *41*, 11733.
327. G. Lee, E. A. Olevsky, C. Manière, A. Maximenko, O. Izhvanov, C. Back and J. McKittrick, *Acta Mater.*, **2018**, *144*, 524.
328. H. Xie, K. Fu, C. Yang, Y. Yao, J. Rao, Y. Zhou, B. Liu, D. Kirsch and L. Hu, *Small Methods*, **2018**, *2*, 1700371.
329. Y. Yao, F. Jiang, C. Yang, K. K. Fu, J. Hayden, C.F. Lin, H. Xie, M. Jiao, C. Yang and Y. Wang, *ACS Nano*, **2018**, *12*, 5266.
330. Y. Tang, X. Ma, Z. Wang, Z. Wu and Q. Yu, *Thermochim. Acta*, **2017**, *657*, 12.
331. M. Cao, D.B. Xiong, L. Yang, S. Li, Y. Xie, Q. Guo, Z. Li, H. Adams, J. Gu and T. Fan, *Adv. Funct. Mater.*, **2019**, *29*, 1806792.
332. N. Yousefi, X. Lu, M. Elimelech and N. Tufenkji, *Nat. Nanotechnol.*, **2019**, *14*, 107.
333. Y. Zhou, B. Natarajan, Y. Fan, H. Xie, C. Yang, S. Xu, Y. Yao, F. Jiang, Q. Zhang and J.W. Gilman, *Angew. Chem. Int. Ed.*, **2018**, *130*, 2655.
334. M.A. Astle, G.A. Rance, H.J. Loughlin, T.D. Peters and A.N. Khlobystov, *Adv. Funct. Mater.*, **2019**, *29*, 1808092.

## Appendix 1

### Tuning the Heating Properties of Pure Nanocarbon Aerogels through Structural Control

Appendix 1 provides extra data information for Chapter 3. The supporting information include thermal images, Raman, electrothermal data and Joule-heating performance of rHT-GO aerogels derived from hydrothermal methods.

#### A1.1 Thermal Images of rIT-CNT and rET-CNT aerogels

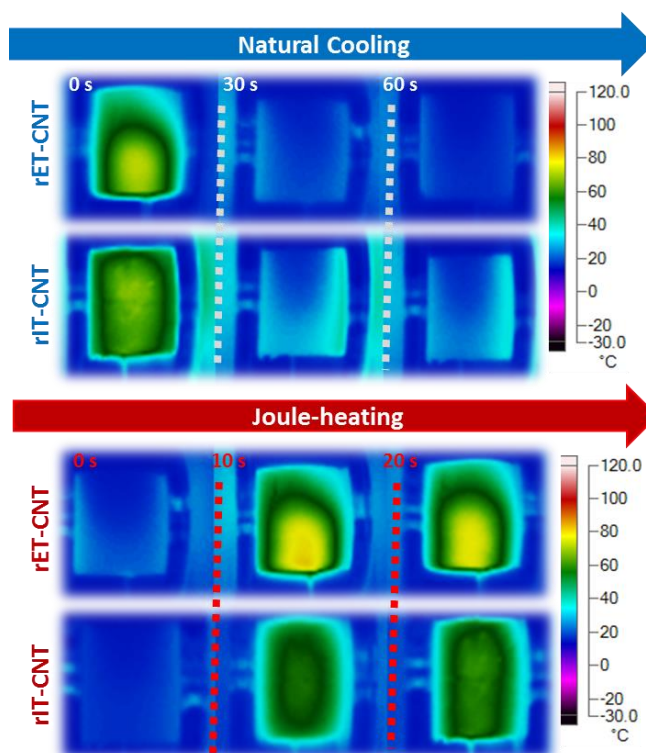


**Figure A1.1** (a) Thermal images of Joule-heating rET-CNT and rIT-CNT aerogels cooling at core temperature 150 °C, and (b) switching on the power heating aerogels to core temperature 150 °C.

In the interest of vision-directly understanding the heating efficiency strictly corresponds with thermal conductivity of nanocarbon aerogels, thermal images were taken for comparison. When the power is off and let the aerogel cool down, counting time internal to take instant cooling pictures from core temperature at 150 °C (Figure A1.1a). Judging from the thermal images, rET-CNT aerogel showed the fastest cooling speed due to its high thermal conductivity. On the contrary way, after cooling down to room temperature then switch on the power supply to take instant thermal images again (kept at same power to reach 150 °C, Figure A1.1b). Predictably, the rET-CNT aerogel exhibited more quicker thermal transmission effect

only took around 10 s, this phenomenon explains why the heating efficiency of the rET-CNT aerogel was undesired, which also directly correlates with its high thermal conductivity.

## A1.2 Thermal Reduction Level of rIT-GO Aerogels

The starting GO materials are the oxidised forms containing large fraction of defects (i.e. organic functional groups), therefore the rGO aerogels' graphitic degree is highly depended on how much these groups being removed. As a consequence, the synthesised rIT-GO aerogels were thermally reduced at 1000 °C, 800 °C and 500 °C, respectively, and were named correspondingly rIT-GO<sub>1000</sub>, rIT-GO<sub>800</sub> and rIT-GO<sub>500</sub> for following discussion.

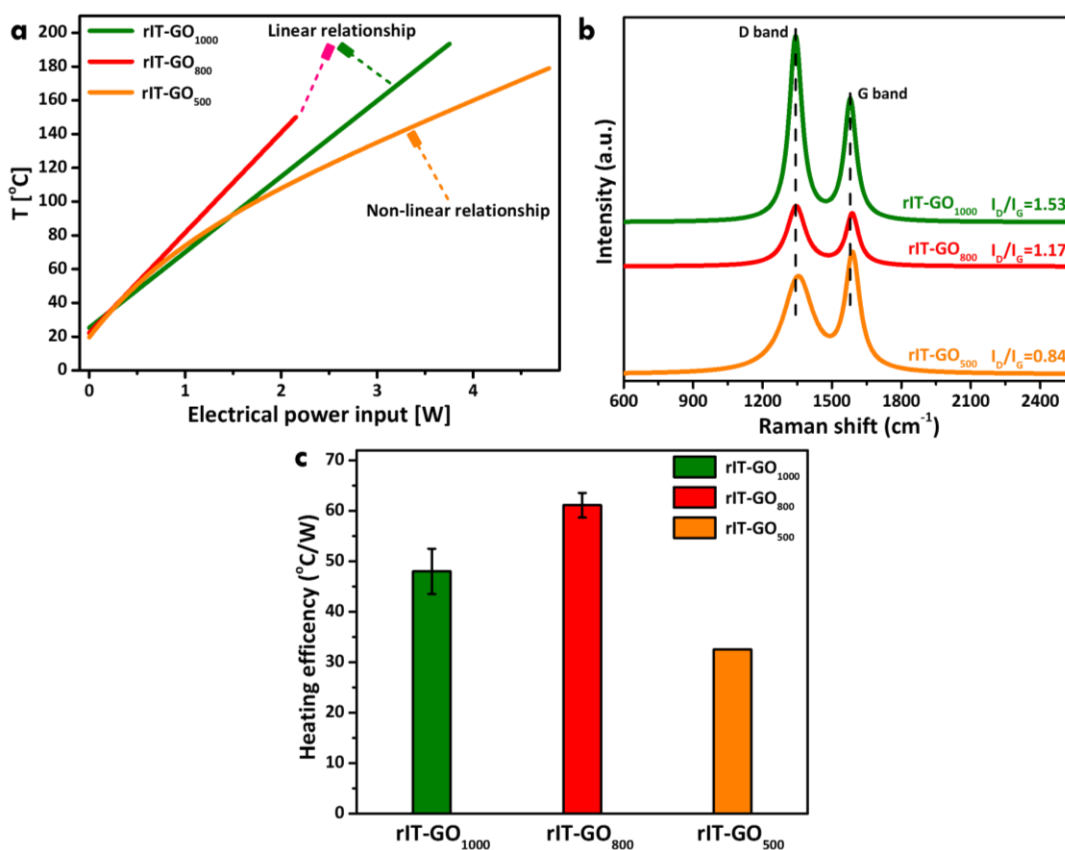


**Figure A1.2** (a) The relationship between electrical power input and the Joule-heating temperature of rIT-GO aerogels. (b) Raman spectra analysis of different temperature treated rIT-GO aerogels. (c) The Joule-heating efficiency of different rIT-GO aerogels at electrical power 2W.

The density of the three prepared rIT-GO aerogels presented a decreasing trend with the thermally reducing temperature arising, this was attributed to the higher temperature the more impurities will be removed. However, the obvious difference was that the electrical conductivity of the rIT-GO<sub>500</sub> aerogel ( $0.74 \text{ S}\cdot\text{m}^{-1}$ ) was an order of magnitude lower than the aerogels dealt with higher temperatures (around  $9 \text{ S}\cdot\text{m}^{-1}$ ).

<sup>1</sup>). This was due to the organic functional group contained GO sheets in the rIT-GO<sub>500</sub> aerogel inhibiting electrical current movements. Even the rIT-GO<sub>500</sub> aerogel can be Joule-heating to high temperature, however it's exceedingly unstable and the heating performance exhibited non-linear relationship during the Joule-heating procedure (Figure A1.2a), therefore limiting its practical application. While increasing the thermal temperature up to 800 °C and 1000 °C, the Joule-heating performance was improved significantly and presented well linear relationship between the electrical power and the Joule-heating temperature (Figure A1.2a), due to the adequately restored graphitic structure of rGO sheets.

Raman spectroscopy is one easy approach to determining the nanocarbon structure's graphitic degree and the results are shown in Figure A1.2b. All three rIT-GO aerogels exhibited two strong characteristic bands (G band and D band), which originate from the presence of the sp<sup>2</sup> and sp<sup>3</sup> hybridized carbons, respectively. The I<sub>D</sub>/I<sub>G</sub> value can judge the graphitic restoration of nanocarbon structures, the large the value the high the graphitic degrees of rGO sheets. Obviously, the I<sub>D</sub>/I<sub>G</sub> value increased from 0.84 to 1.53 with the temperature rising, meaning that more defected GO sheets in the aerogel structure were reduced to less defected rGO sheets, as a consequence, the electrical conductivity will improve, resulting in stable Joule-heating performance. One of an interesting phenomena was that the rIT-GO<sub>1000</sub> aerogel had a moderate heating ability compared to that of rIT-GO<sub>800</sub> aerogel (Figure A1.2c), this was because the high reduction temperature helped the GO sheets remove more impurities leading to higher thermal conductivity.

Specifically, the core temperature of rIT-GO<sub>800</sub> aerogel was slightly higher than the rIT-GO<sub>1000</sub> aerogel at electrical power 2W, which were caused by its lower thermal conductivity leading to less heating loss (Figure A1.2c). Based on above results, the clear point is that rIT-GO aerogel will acquire both excellent electrical and thermal conductivities at a high reductive temperature. The heating efficiency showed a clear difference between these three rIT-GO aerogels (Figure A1.6c), among them, the rIT-GO<sub>800</sub> and rIT-GO<sub>1000</sub> aerogels showed outstanding heating efficiency due to high electrical conductivities.

### **A1.3 Solar Thermal Heating**

As shown in Figure A1.3a, the Joule-heating temperature distributions from the aerogel center to edge is in line with the vertical temperature profiles, namely the rIT-CNT aerogel will trap more heat under identical conditions, owing to its low thermal conductivity. Time-dependent thermal images of the rIT-CNT membrane placing on or not on water and the pure water (as blank experiments) indicated that

blank water had small temperature variations over the lighting time (Figure A1.3c), while the surface temperature of membrane aerogel surged up significantly even directly floating on water. For example, the maximum surface temperature of rIT-CNT membrane on water reached up to 68.7 °C only within 1s solar lighting exposure, verifying that membrane aerogels are fast to generate heat. An important discovery was that the rIT-CNT membrane experienced 3.3 °C fluctuation at stable light expose, indicating efficient heat conducting from aerogel to water for steam evaporation (Figure A1.3b).

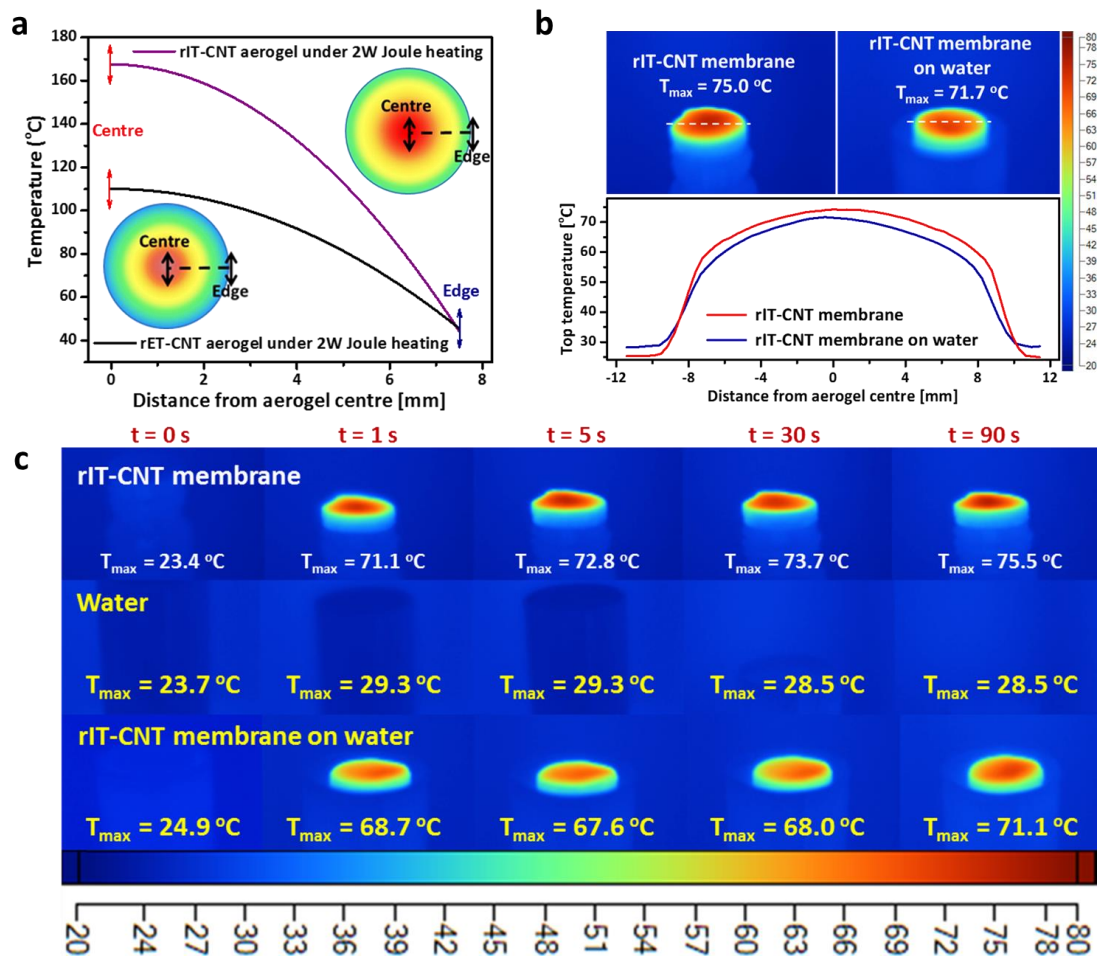


**Figure A1.3** (a) Joule-heating temperature distributions of rIT-CNT aerogel and rET-CNT aerogel from centre to edge at power 2W. (b) Thermal images of rIT-CNT membrane on or not on water at lighting time 300s, and the corresponding axis temperature distributions. (c) Thermal images of pure water, rIT-CNT membrane, and rIT-CNT membrane on the top of water at different time interval under one sun.

### A1.4 Joule-heating of Hydrothermal Aerogels

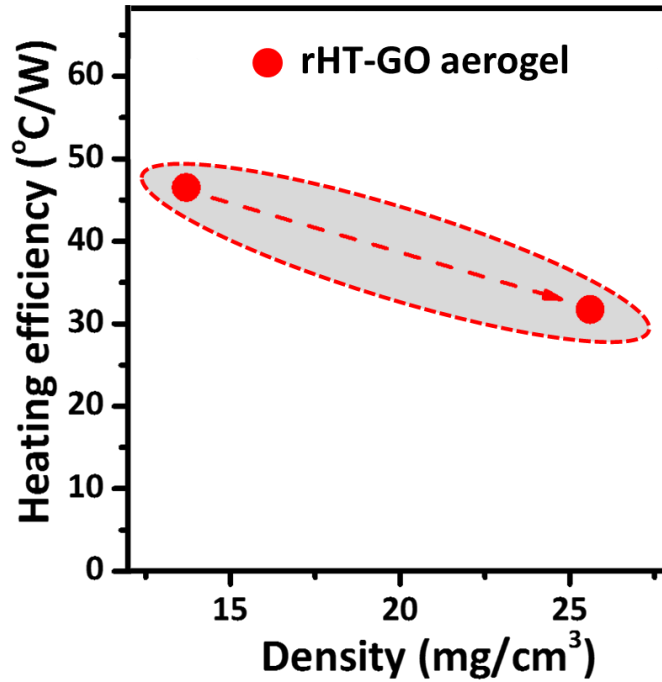


**Figure A1.4** Joule-heating performance of hydrothermal rGO aerogels (rHT-GO aerogels) with different densities.

**Table A1.1** The physical parameters of density-different rHT-GO aerogels.

Aerogel	$\rho$ <sup>b)</sup> [mg·cm <sup>-3</sup> ]	$\sigma$ <sup>c)</sup> [S·m <sup>-1</sup> ]	$\kappa$ <sup>d)</sup> [W·m <sup>-1</sup> ·K <sup>-1</sup> ]	$T_{\text{core}}$ <sup>e)</sup> [°C]
rHT-GO Aerogel <sup>a)</sup>	13.7	9.2	0.253	117
rHT-GO Aerogel <sup>a)</sup>	25.6	18.1	0.282	86

<sup>a)</sup> HT stands for hydrothermal approach; <sup>b)</sup>  $\rho$  represents aerogel density; <sup>c)</sup>  $\sigma$  represents electrical conductivity; <sup>d)</sup>  $\kappa$  represents thermal conductivity collected at a heating power 2W; <sup>e)</sup>  $T_{\text{core}}$  obtained from aerogel center at a heating power 2W.

## Appendix 2

### Electrically-Heatable Graphene Aerogels as Nanoparticle Supports in Adsorptive Desulfurisation and High-Pressure CO<sub>2</sub> Capture

Appendix 2 describes extra data information for Chapter 5, where XRD, TGA, BET, SEM, XPS, Raman, aerogel compressibility, liquid sorption fitting models and CO<sub>2</sub> sorption capacity data compared with reported literature are presented.

#### A2.1 Structural and Chemical Materials Characterization

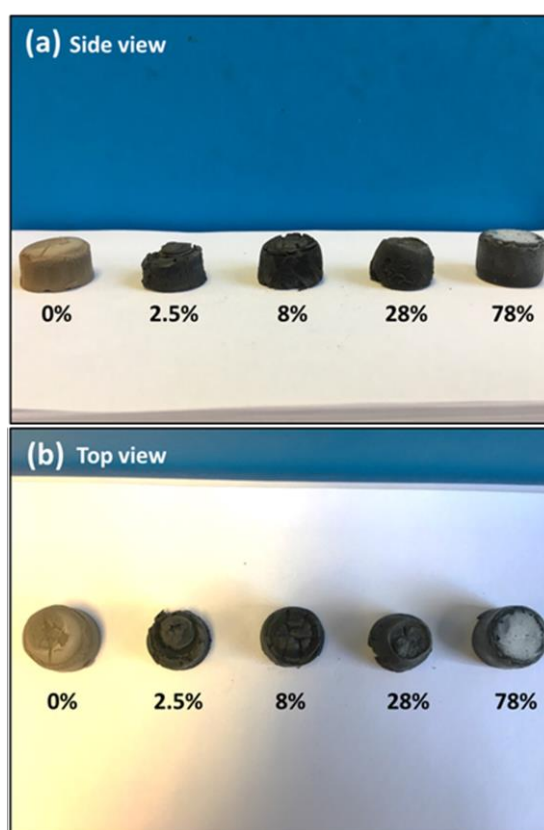


**Figure A2. 1** Digital images of MgAl-LDH/GO hybrid aerogels with different MgAl-LDH loadings. (a) Side view and (b) top view.

**Table A2.1** Average crystallite size ( $D_p$ ) and lattice spacing ( $d_{\text{spacing}}$ ) of MgAl-LDH powder and MgAl-LDH/GO aerogel from Figure 4.7a.

Adsorbents	$D_p$ <sup>a)</sup> (nm)	$d_{\text{spacing}}$ <sup>b)</sup> (nm)
MgAl-LDH powder	29.4	0.77
MgAl-LDH/GO aerogel	20.4	0.77

<sup>a)</sup> Average crystal size and <sup>b)</sup> lattice spacing as determined from the (003) LDH XRD peak.

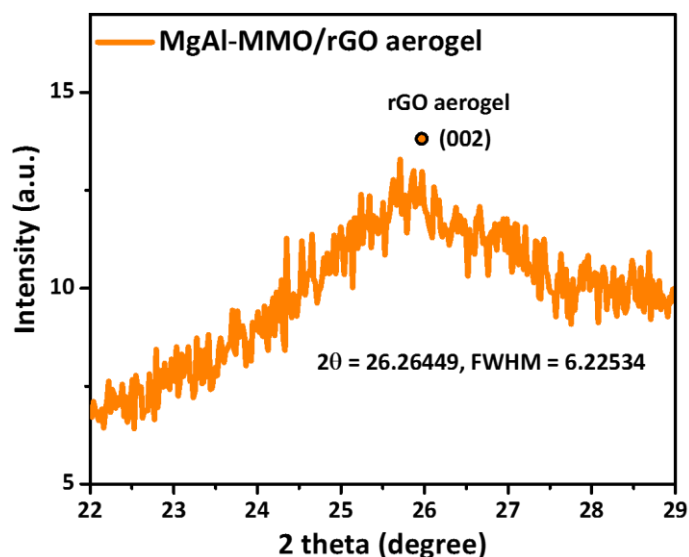


**Figure A2.2** Magnified view of the rGO (002) peak in the XRD pattern of the MgAl-MMO/rGO aerogel (see also main text, Figure 4.7b).

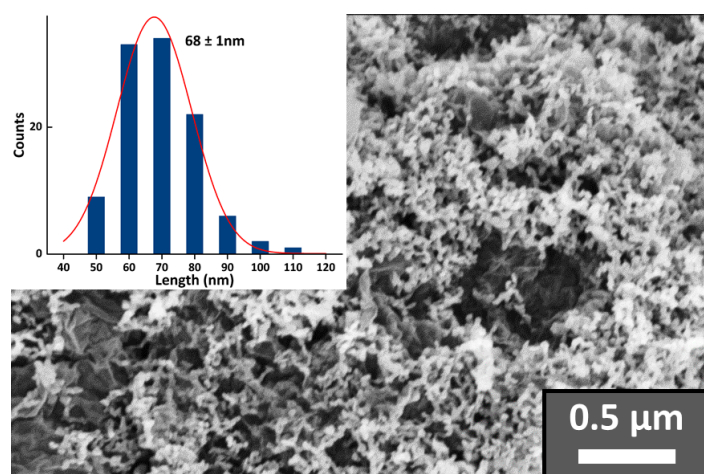


**Figure A2.3** SEM image of the MgAl-MMO/rGO aerogel (78 wt% MMO loading), and particle size distribution (as measured from the longest particle dimension via the Image J software).

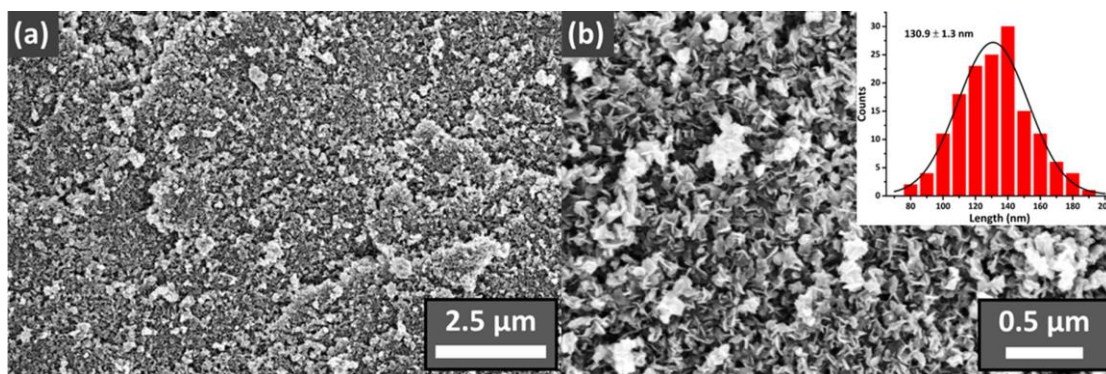


**Figure A2.4** SEM images of the unsupported MgAl-MMO powders. (Insert small picture is the nanoparticle size distribution obtained via Image J analysis)

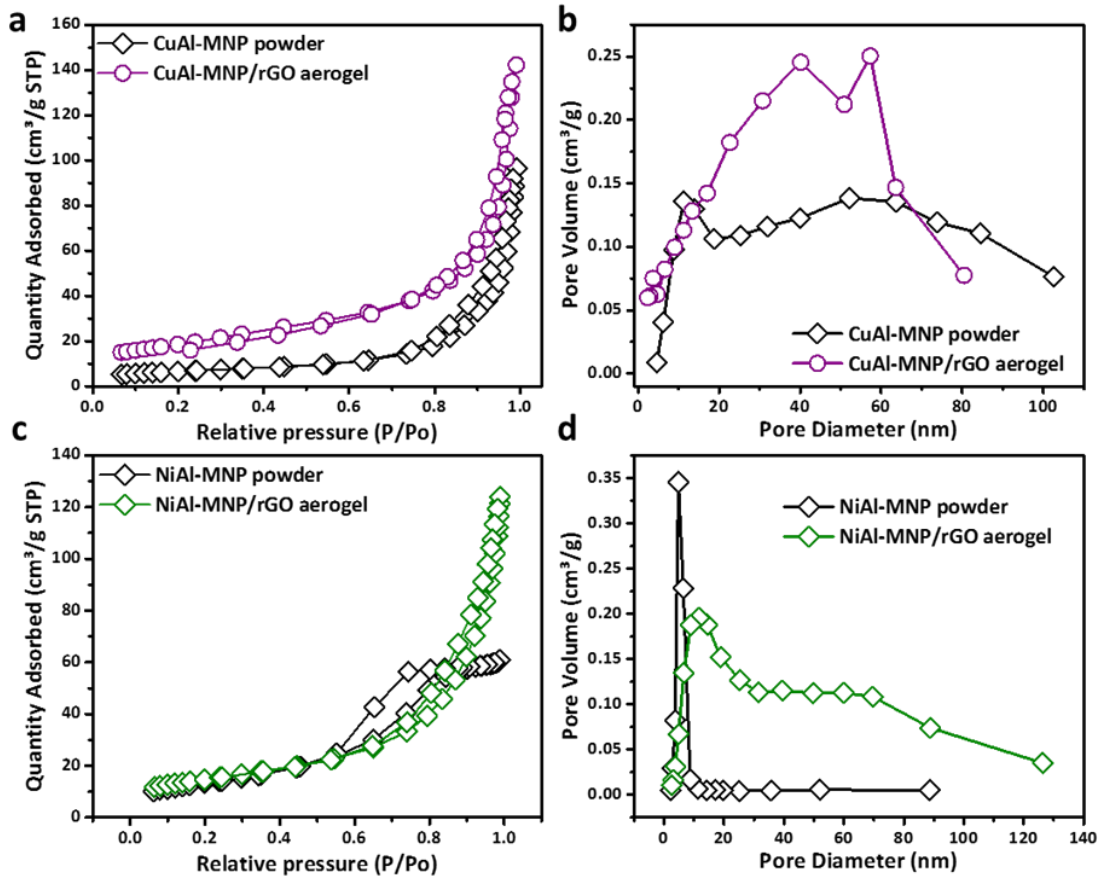


**Figure A2.5** (a) N<sub>2</sub> adsorption-desorption isotherms and, (b) BJH pore-size distributions of CuAl-MNP powder and CuAl-MNP/rGO aerogel. (c) N<sub>2</sub> adsorption isotherms and, (d) BJH pore-size distributions of NiAl-MNP powder and NiAl-MNP/rGO aerogel.

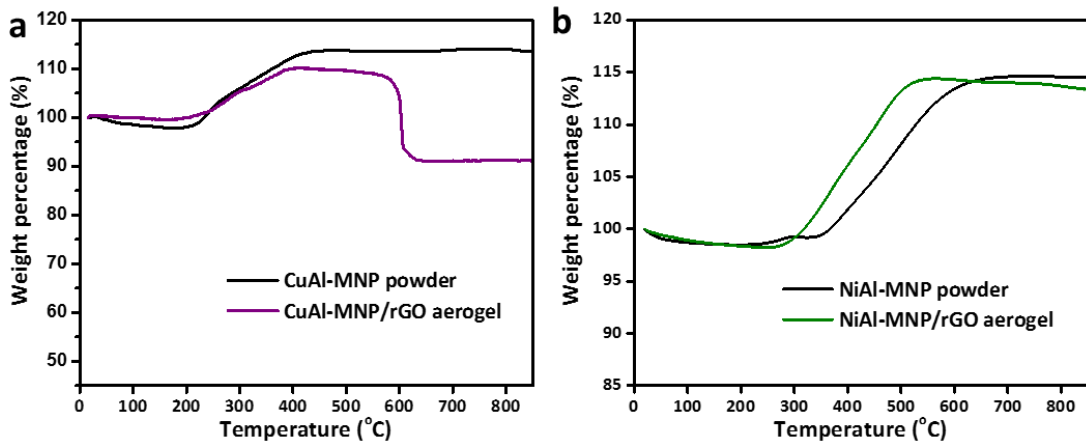


**Figure A2.6** (a) TGA profile of the CuAl-MNP powder and the CuAl-MNP/rGO aerogel. (b) TGA profile of the NiAl-MNP powder and the NiAl-MNP/rGO aerogel. All TGA profiles collected in oxidative air atmosphere. The increase in weight upon temperature ramping is due to metal oxidation and further confirms the metallic nature of the LDH-derived CuAl and NiAl nanoparticles.

## A2.2 Organosulfur Sorption Experiments

### Sorption mechanism

Sorption of aromatic organosulfur compounds (such as DBT, DMDBT) onto MgAl-MMO sorbents is mainly based on Lewis acid-base and cation- $\pi$  interactions (electronic interaction between mixed metal cations and  $\pi$ -electron clouds of DBT molecules).<sup>1</sup>

The Ni-based and Cu-based metal particle systems (NiAl-MNP and CuAl-MNP) show overall lower organosulfur uptakes compared to MgAl-MMO due to the absence of cation- $\pi$  interactions.<sup>2</sup> However, both the CuAl-MNP and NiAl-MNP systems show substantially increased DBT equilibrium capacities when supported within rGO aerogels (Table 4.3).

### DBT sorption isotherms

The DBT sorption isotherms of the MgAl-MMO powder and the MgAl-MMO/rGO aerogel were analysed using Freundlich model and Langmuir model:

$$q_e = K_F C_e^{1-n} \quad (\text{Freundlich model})$$

$$q_e = \frac{q_m C_e K_L}{1 + C_e K_L} \quad (\text{Langmuir model})$$

Where  $q_e$  is the adsorbed DBT at equilibrium ( $\text{mg}\cdot\text{g}^{-1}$ ),  $C_e$  is the DBT concentration at equilibrium ( $\text{mg}\cdot\text{g}^{-1}$ ),  $K_F$  is the Freundlich constant ( $\text{mg}^{1-n}\cdot\text{L}^n\cdot\text{g}^{-1}$ ) related to the sorption capacity, and  $n$  is the factor representing adsorption intensity,  $q_m$  is the maximum organosulfur uptake capacity ( $\text{mg}\cdot\text{g}^{-1}$ ), and  $K_L$  is related to the energy of adsorption ( $\text{L}\cdot\text{mg}^{-1}$ ). The resulting fitting parameters are displayed below, indicating that the Langmuir model provides the best fit.

**Table A2.2** Isotherms fitting parameters for DBT sorption onto MgAl-MMO powder and MgAl-MMO/rGO aerogel

Sample	Freundlich model			Langmuir model		
	$K_F$ ( $\text{mg}^{1-n}\cdot\text{L}^n/\text{g}$ )	$n$ ( $\text{L}\cdot\text{mg}^{-1}$ )	$R^2$	$q_m$ ( $\text{mg}\cdot\text{g}^{-1}$ )	$K_L$ ( $\text{L}\cdot\text{mg}^{-1}$ )	$R^2$
MgAl-MMO powder	0.129	0.72	0.986	0.72	0.019	0.999
MgAl-MMO/rGO aerogel	0.242	0.68	0.940	1.66	0.022	0.987

## Post-sorption XPS

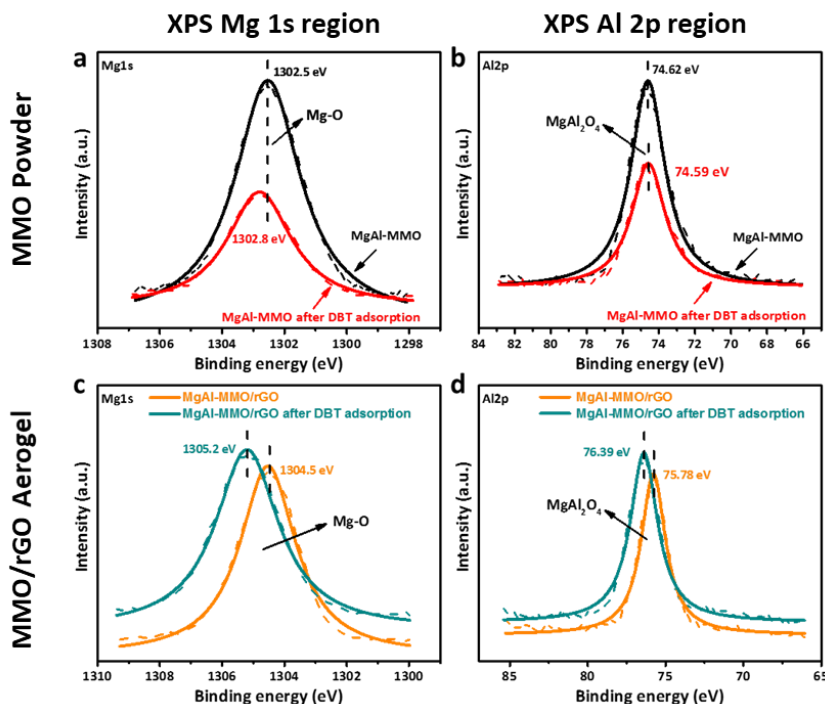


**Figure A2.7** XPS analysis of Mg1s and Al2p of MgAl-MMO powder and MgAl-MMO/rGO aerogel adsorbents before and after DBT adsorption. (a) Mg1s and (b) Al2p spectra of MgAl-MMO powder before DBT sorption (black trace) and after DBT sorption (red trace). (c) Mg1s and (d) Al2p spectra of the MgAl-MMO/rGO aerogel before DBT sorption (yellow trace) and after DBT sorption (blue trace).

## A2.3 Joule-Heating Experiments

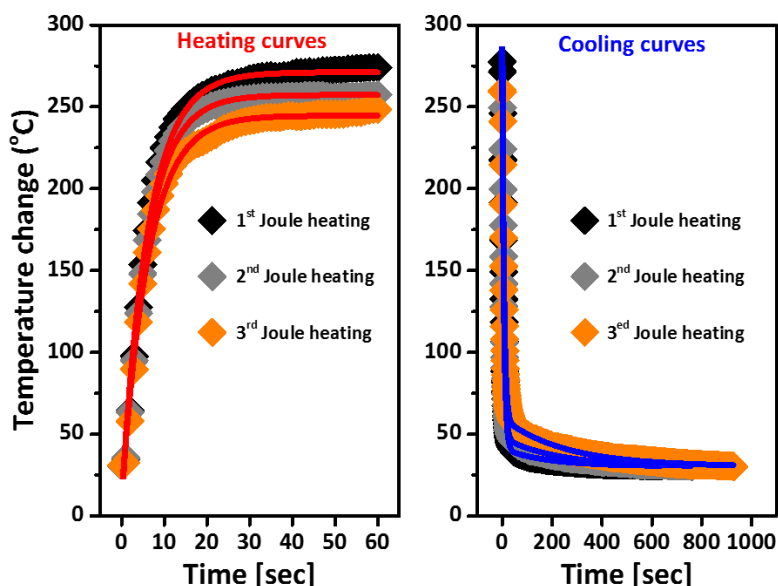


**Figure A2.8** Evolution of aerogel surface temperature upon Joule heating at constant power input (Heating curves) and upon natural cooling once input of the electrical power is stopped (Cooling curves). Data were collected for three cycles of Joule-heating and subsequent natural heating of MgAl-MMO/rGO aerogel, with each data set fitted with an exponential function.

**Table A2.3** Lifetime parameters for the Joule heating and natural cooling of MgAl-MMO/rGO aerogel, as obtained by exponential fitting of the temperature evolution data in Figure A2.11.

Joule heating cycles	Heating kinetics	Cooling kinetics	Cooling kinetics
	$\tau_1$ (s)	$\tau_1$ (s)	$\tau_2$ (s)
1 <sup>st</sup>	6.2	6.9	179
2 <sup>nd</sup>	5.9	6.9	229
3 <sup>rd</sup>	6.2	7.1	250
AVERAGE	6.1	7.0	220

The evolution of the surface temperature of the MgAl-MMO/rGO aerogel during Joule heating (Joule heating curves in Figure A2.8) and during subsequent natural cooling (cooling curves in Figure A2.8) were fitted by exponential functions of the following form:

$$T = A_1 e^{\frac{t}{\tau_1}} + A_2 e^{\frac{t}{\tau_2}} + T_0$$

Where  $T$  is the temperature at time  $t$ ,  $T_0$  is the starting temperature,  $\tau$  is the lifetime parameter, and  $A$  the pre-exponential factor. While the Joule heating curves can be fitted with a mono-exponential expression, the cooling curves require a bi-exponential fit, suggesting two different components to the cooling behavior. The very fast initial cooling component is likely due to rapid rGO framework cooling, reflecting the excellent thermal conductivity of the graphitic rGO framework. The second component (around two orders of magnitude slower than the first component) could be either related to the slower cooling kinetics of the MMO nanoparticles embedded in the aerogels, or, more like, reflect other heat transfer mechanism such as convection-related cooling (e.g. based on diffusion of heated gas out of the interior of the aerogel monolith which can be expected to be significantly slower than radiative heat dissipation of the rGO framework).

**Table A2.4** Estimated energy consumptions of furnace-based and Joule-heating-based thermal regenerations.

Regeneration method	Furnace <sup>a</sup>	Joule-heating <sup>b</sup>
Heating range	From 20 °C to 250 °C	From 20 °C to 250 °C
Duration at 250 °C	5 min	5 min
Heating rate	5 °C·min <sup>-1</sup>	720 °C·min <sup>-1</sup>
Input power	P ~ 410 W	P ~ 9.7 W

Energy consumption (W·h)

~ 350

~ 0.9

<sup>a</sup> Furnace model: LE 6/11/P300 (NO. 209226,  $T_{\max}$ = 1100 °C, 1.8 kW, Germany)<sup>b</sup> A custom-made Joule-heating set-up. The electrical current and voltage are recorded during Joule-heating regeneration for energy-consumption calculation.

In both furnace-based and Joule-heating-based regeneration methods the exhausted MgAl-MMO/rGO aerogel sorbents, were heated from 20 °C to 250 °C and then kept at 250 °C for 5 min. Details on regeneration conditions used to calculate energy consumption and furnace details are listed above, in Table A2.4.

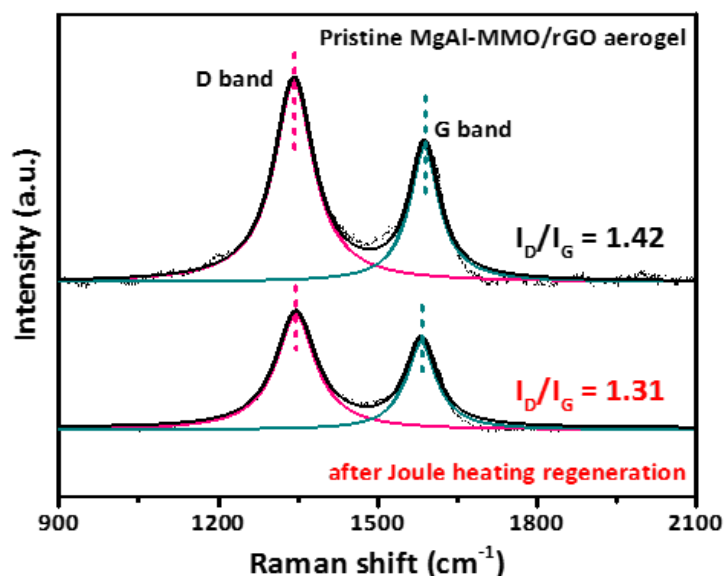


**Figure A2.9** Raman analysis of pristine MgAl-MMO/rGO aerogel and the exhausted aerogel after Joule heating regeneration.

**Table A2.5** Composition analysis of XPS C1s from the pristine MgAl-MMO/rGO aerogel and after Joule heating regeneration

Aerogel	C=C (sp <sup>2</sup> )	C-OH	C=O
Pristine MgAl-MMO/rGO	53 %	16 %	18 %
MgAl-MMO/rGO after Joule heating regeneration	53 %	9 %	13 %

## A2.4 Comparative CO<sub>2</sub> Sorption Data

Sorption of CO<sub>2</sub> onto MgAl-MMO adsorbents is attributed to Lewis acid-base interactions between the acidic CO<sub>2</sub> molecules and the basic Mg-O sites on the MMO surface. Comparison between different carbon-supported MMO systems is challenging due different measurement conditions applied in the literature. For example, some CO<sub>2</sub> uptake measurements are conducted in the presence of water vapour which is known to significantly increase the intrinsic CO<sub>2</sub> uptake capacity for

MMOs. Many studies also promote intrinsic CO<sub>2</sub> capacity by MMO modification with 1-10 % alkali-ions, also known to significantly boost CO<sub>2</sub> uptake onto MMO systems. Therefore, the data of references [8] and [9] in Table A2.7 are not directly comparable to the MMO powder and aerogel systems studies in this work (in this work CO<sub>2</sub> adsorption measurements are carried out in dry CO<sub>2</sub> atmosphere and the MgAl-MMO is used in its un-promoted form). However, even in comparison with the water- and alkali-promoted systems, our MgAl-MMO/rGO aerogel sorbents perform extremely well in elevated-temperature CO<sub>2</sub> capture across a very broad pressure range, including high CO<sub>2</sub> pressures (Table 4.6), low CO<sub>2</sub> pressures (Table A2.6) and intermediate CO<sub>2</sub> pressures (Table A2.7). In fact, it can be expected that the CO<sub>2</sub> sorption performance of the aerogel-supported MMO systems studied here can be even further boosted in the future, e.g. through water- or alkali-promotion.

**Table A2.6** Low-pressure CO<sub>2</sub> sorption capacities (0.05-0.2 bar) at elevated temperature (300 °C) of carbon-supported MgAl-MMO sorbents, reported in the literature, compared against MgAl-MMO/rGO aerogel sorbent prepared in this work.

CO <sub>2</sub> adsorbents	CO <sub>2</sub> uptake capacity (mmol CO <sub>2</sub> ·g <sup>-1</sup> ads)	Intrinsic CO <sub>2</sub> uptake capacity (mmol CO <sub>2</sub> ·g <sup>-1</sup> MMO)	T (°C)	P (bar)	MMO weight loading	Ref.
MgAl-MMO on CNF	0.13	1.30	250	0.05	10	5
MgAl-MMO on CNF, Na-promoted	0.22	2.20	250	0.05	10	5
MgAl-MMO on MWCNT	0.26	0.42	300	0.2	68	6
MgAl-MMO on rGO	0.24	0.30	300	0.2	80	7
MgAl-MMO on coal-derived graphitic support	0.49	0.52	300	0.1	95	8
MgAl-MMO on coal-derived graphitic support, K-promoted	0.84	0.88	300	0.1	95	8
MgAl-MMO on mixed MWCNT/GO support, K-promoted	0.46	0.54	300	0.2	85	9
MgAl-MMO on rGO aerogel [this work]	0.55	0.71	300	0.2	78	This Work

**Table A2.7** CO<sub>2</sub> sorption capacities at 1 bar pressure (p<sub>CO<sub>2</sub></sub> = 1 bar) and high temperature (T = 300 °C) of different solid-state sorbent systems, reported in the literature, compared against MgAl-MMO powders and MgAl-MMO/rGO aerogel sorbent prepared in this work.

CO <sub>2</sub> adsorbents	Total CO <sub>2</sub> uptake	T	P	Ref.
----------------------------	------------------------------	---	---	------

	capacity (mmol CO <sub>2</sub> ·g <sup>-1</sup> ads)	(°C)	(bar)	
Hydrotalcite (HTC)	0.22	300	1	3
Ni-MO-5 [5% Ni oxides decorated HTC]	0.57	300	1	3
Co-MO-5 [5% Co oxides decorated HTC]	0.17	300	1	3
Fe-MO-5 [5% Fe oxides decorated HTC]	0.12	300	1	3
13X [a commercial zeolite]	0.18	300	1	3
A100 [a commercial MOF, Basolite MIL-53-Al]	0.07	300	1	3
AC [activated carbon]	0.00	300	1	3
MgAl-LDH powder	0.28	300	1	6
MgAl-LDH/GO powder [7 wt% GO]	0.45	300	1	6
MgAl-LDH/GO powder [12 wt% GO]	0.38	300	1	6
MgAl-LDH/GO powder [33 wt% GO]	0.30	300	1	6
MgAl-LDH/GO powder [83 wt% GO]	0.10	300	1	6
MgAl-MMO [a commercial hydrotalcite after calcination]	0.50	300	1	4
MgAl-MMO powder [this work]	0.43	300	1	This Work
MgAl-MMO/rGO aerogel [this work]	0.82	300	1	This Work

## References

- 1 R. Neubauer, M. Husmann, C. Weinlaender, N. Kienzl, E. Leitner, C. Hochenauer, *Chem. Eng. J.* **2017**, *309*, 840.
- 2 J. Kou, C. Lu, W. Sun, L. Zhang, Z. Xu, *ACS Sustain. Chem. Eng.* **2015**, *3*, 3053.
- 3 S.I. Garcés-Polo, J. Villarroel-Rocha, K. Sapag, S.A. Korili, A. Gil, *Chem. Eng. J.* **2018**, *332*, 24.
- 4 Z. Yong, V. Mata, A.E. Rodrigues, *Ind. Eng. Chem. Res.*, **2001**, *1*, 204.
- 5 J. Boon, P.D. Cobden, H.A.J. Van Dijk, C. Hoogland, E.V. van Selow, M. van Sint Annaland, *Chem. Eng. J.*, **2014**, *248*, 406.
- 5 A. Garcia-Gallastegui, D. Iruretagoyena, M. Mokhtar, A.N. Asiri, S.N. Basahel, S.A. Al-Thabaiti, A.O. Alyoubi, D. Chadwick, M.S. Shaffer, *J. Mater. Chem.*, **2012**, *28*, 13932.
- 7 D. Iruretagoyena, M.S. Shaffer, D. Chadwick, *Adsorption*, **2014**, *20*, 321.
- 8 L.K. Bhatta, S. Subramanyam, M.D. Chengala, MU.M. Bhatta, K. Venkatesh, *Ind. Eng. Chem. Res.*, **2015**, *43*, 10876.
- 9 M. De Marco, R. Menzel, S.M. Bawaked, M. Mokhtar, A.Y. Obaid, S.N. Basahel, M.S. Shaffer, *Carbon*, **2017**, *123*, 616.

## Appendix 3

### Boron-Nitride/Carbon-Nanotube Hybrid Aerogels as Multifunctional Desulfurisation Agents

Appendix 3 contains extra data including EDX mapping, XPS, adsorptive desulfurisation performance, and Joule-heating related measurements.

#### A3.1 EDX mapping of BN/rCNT Hybrid Aerogels

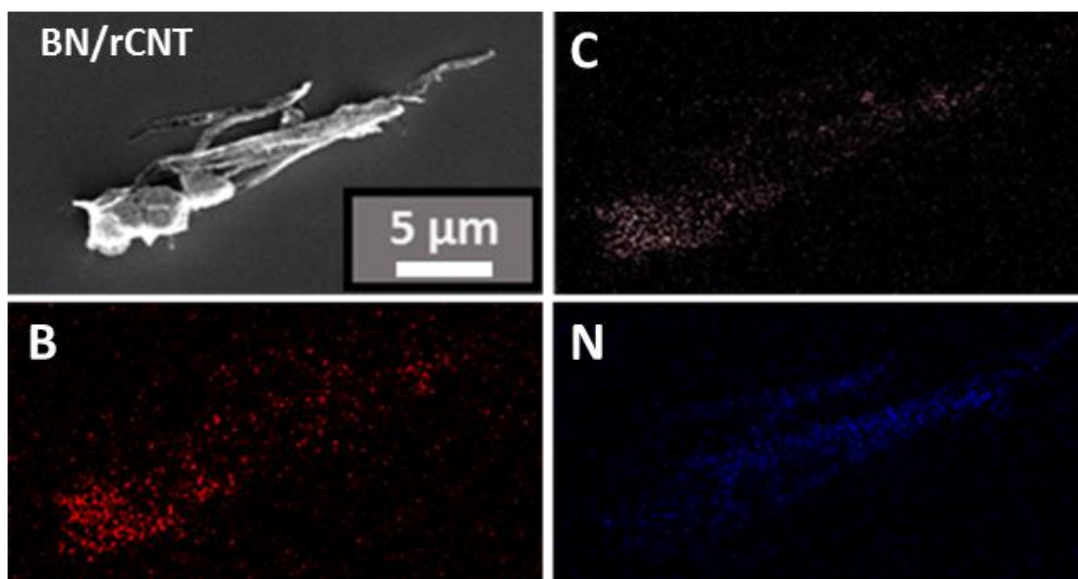


Figure A3.1 SEM image and EDX mappings of BN/rCNT aerogel.

#### A3.2 Sorption at Different Temperatures

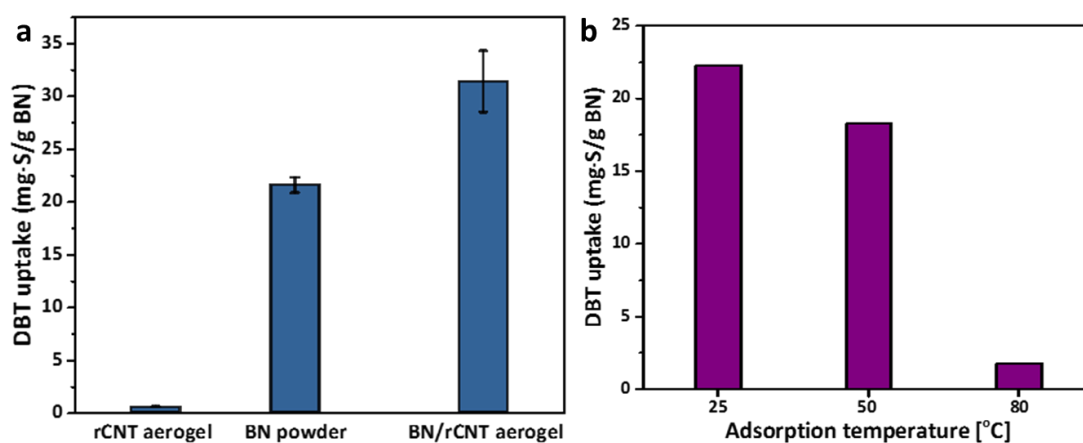
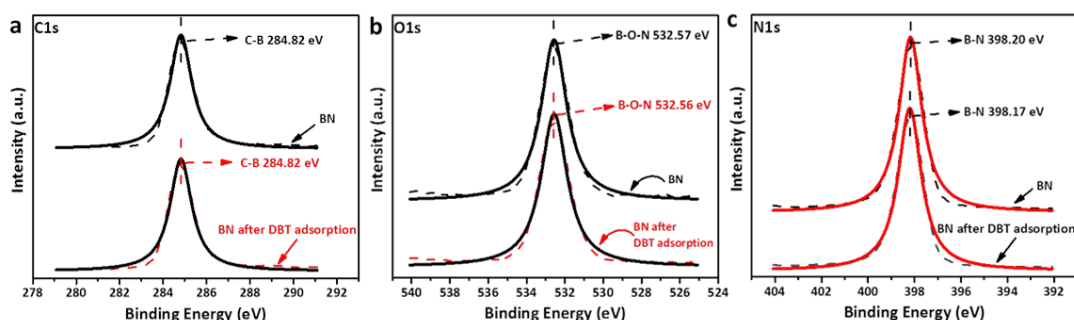


Figure A3.2 (a) DBT uptake capacities for rCNT aerogel, BN powder and BN/rCNT aerogel (DBT in n-octane, initial DBT concentration 500 ppm S). (b) DBT adsorption onto BN powder at different temperatures (DBT in n-octane, initial DBT concentration 500 ppm S).

### A3.3 XPS analysis



**Figure A3.3** XPS spectra of BN powder before and after DBT adsorption. (a) C1s, (b) O1s and (c) N1s spectra of BN powder before and after DBT adsorption.

### A3.4 Joule Heating Energy Calculation

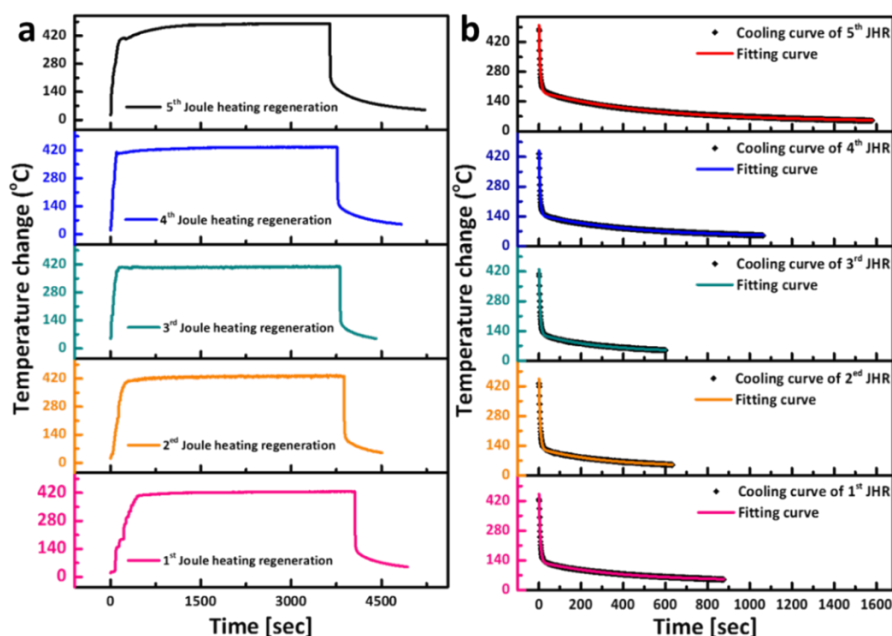


**Figure A3.4** (a) Heating curves and (b) cooling curves of post-adsorption BN/rCNT aerogel over 5 Joule-heating cycles

**Table A3.1** Parameters of the Joule heated post-adsorption BN/rCNT aerogel, including temperature (T), electrical current (I), voltage (U), resistance (R), input electrical power (P), energy consumption (Q).

Aerogel	Physical parameters					
	T (°C)	I (A)	U (V)	R (Ω)	P (W)	Q (kW·h)
rBN/CNT [1 <sup>st</sup> ]	427	1.45	11.60	8.0	16.82	0.017
rBN/CNT [2 <sup>ed</sup> ]	434	1.55	12.53	8.1	19.43	0.019
rBN/CNT [3 <sup>rd</sup> ]	410	1.30	13.52	10.4	17.58	0.018
rBN/CNT [4 <sup>th</sup> ]	435	1.47	10.96	7.5	16.11	0.016
rBN/CNT [5 <sup>th</sup> ]	481	1.80	11.23	6.2	20.21	0.020
Average	438	1.52	11.97	8.1	18.03	0.018

### A3.4 Joule Heating Measurements

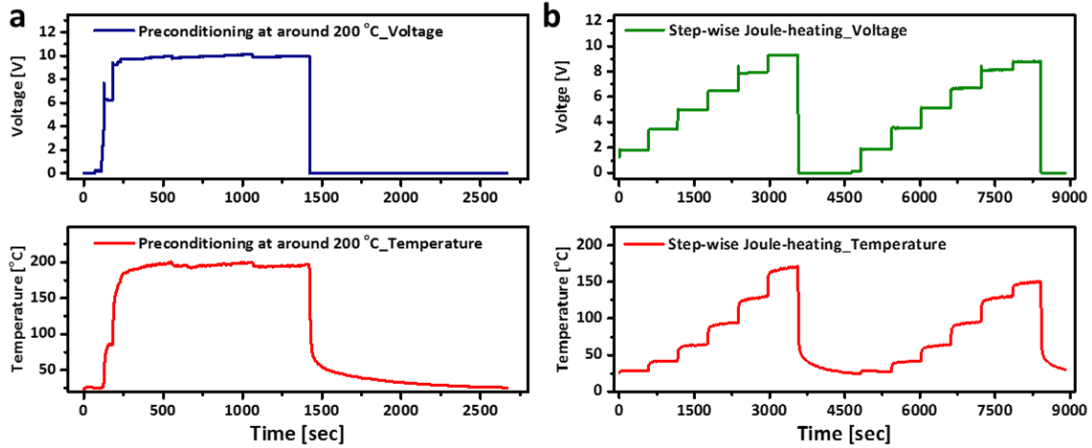


**Figure A3.5** Voltage and temperature control of BN/rCNT aerogel under Joule-heating. (a) Preconditioning of BN/rCNT aerogel at around 200 °C for 20 minutes to remove impurities (e.g. water and gases). (b) Stepwise Joule-heating.

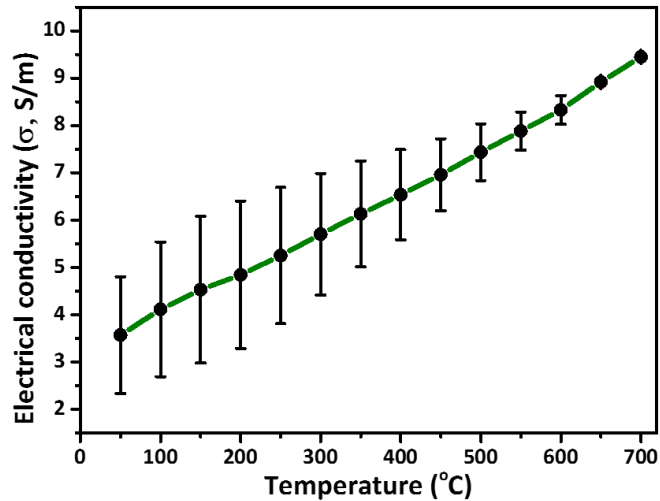


**Figure A3.6** Joule-heating temperature versus electrical conductivity of the produced BN/rCNT aerogel adsorbent.

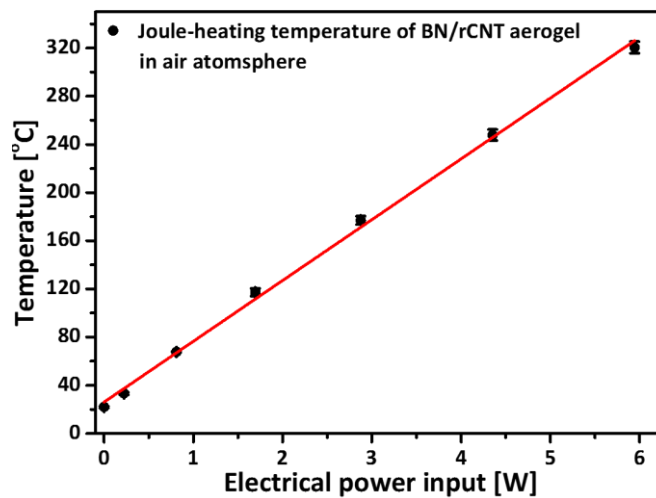


**Figure A3.7** Joule-heating of BN/rCNT aerogel in air atmosphere.

## Appendix 4

### High-Temperature Joule-Heating of Graphene Oxide Aerogels

Appendix 4 contains extra data including SEM images, XPS spectra, theoretical models, Joule heating temperature measurements of GO-based aerogels, XRD patterns, Raman spectra and Raman mapping.

#### A4.1 Joule Heating of GO[HT] aerogels

In order to intuitively visualize that the GO[HT] aerogel cannot carry out stepwise Joule heating measurements when temperature is above 400 °C as above-mentioned, the corresponding experiments were performed as shown in Figure A4.1. For instance, the electrical current is stably kept at  $I = 0.75$  A, but the voltage is not stable and suddenly surging up to above 20 V, where leads to the aerogel burning as observed in the inserted digital pictures. After burning, the aerogel will be automatically disconnected with the electrodes resulting in short circuit. As a consequence, carrying out stepwise Joule heating of a highly GO-defective GO[HT] aerogel to high temperature is inapplicable.

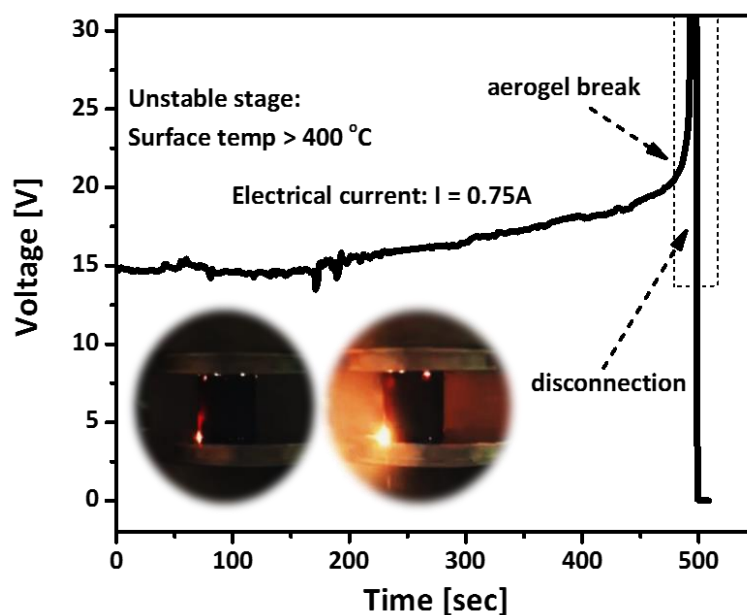


**Figure A4.1** Direct stepwise Joule heating of GO[HT] aerogels above 400 °C is not working, owing to high fractions of impurities and highly defective GO sheets. Digital images show that the GO[HT] aerogel will be burning due to sudden pulse of voltage surging.

As shown in Figure A4.2, the GO[30sec] aerogel also can work stable at 800 °C and 900 °C for long time that is comparable to the rrGO[HT] aerogel, this is important for

temperature-dependant applications, such as reaction preconditioning, gas adsorption/desorption and high temperature sensors.

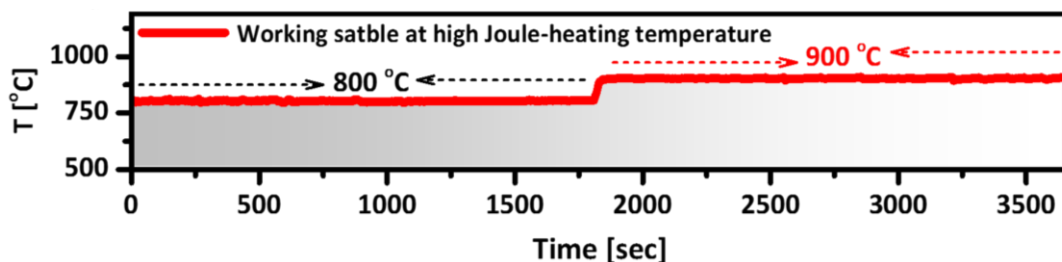


**Figure A4.2** Long time Joule heating working temperature at 800 °C and 900 °C of GO[30sec] aerogels.

#### A4.2 XPS Spectra of rGO[HT] Aerogel and rrGO[HT] Aerogel

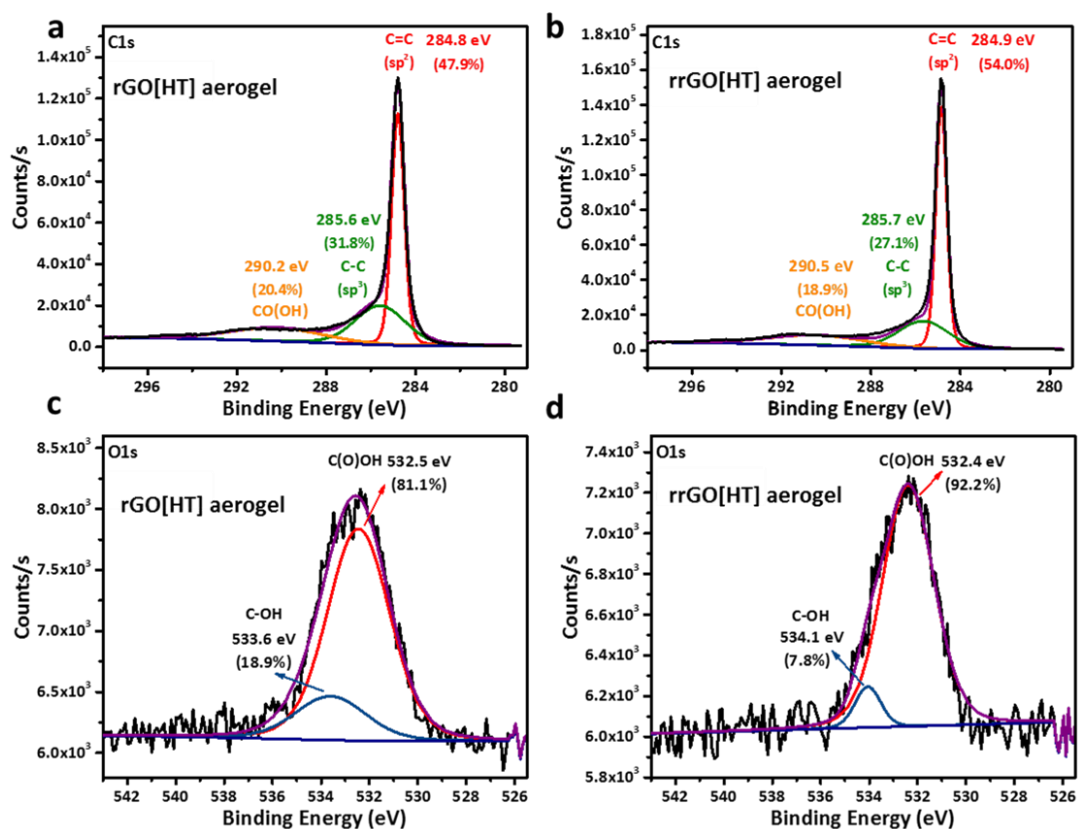


**Figure A4.3** XPS C1s peak analyses of rGO[HT] aerogel (a) and rrGO[HT] aerogel (b), respectively. XPS O1s peak analyses of rGO[HT] aerogel (c) and rrGO[HT] aerogel (d), respectively.

Ultrahigh temperature Joule-heating can further graphitize rGO sheets that can be confirmed via the XPS characterization technique. High resolution C1s XPS spectroscopy indicates that the sp<sup>2</sup> components increased from 47.9 % in rGO[HT] aerogel to 54.0 % in rrGO[HT] aerogel (Figure A4.3a and Figure A4.3b), while the sp<sup>3</sup> components dropped from 31.8 % to 21.7%, correspondingly. The decrease of sp<sup>3</sup> components in the rrGO[HT] aerogel can be confirmed by the values of full width at

half maximum of C1s peak, which declined from around 0.66 eV in rGO[HT] aerogel to around 0.55 eV in rrGO[HT] aerogel.

### A4.3 Charge Transport Mechanisms

In order to understand the charge transport behaviours in GO[HT] aerogel, GO[HT] aerogel after preconditioning and GO[30sec] aerogel, the Mott variable range hopping (VRH) model is introduced, as shown in Equation 1:

$$\sigma(T) = \sigma_0 T^{-\frac{1}{2}} \exp\left(-\left(\frac{T_0}{T}\right)^{-\frac{1}{d+1}}\right) \quad \text{Equation 1}$$

Where  $\sigma$  is the temperature-dependent thermal conductivity ( $\text{S}\cdot\text{m}^{-1}$ ) of the samples;  $\sigma_0$  is the prefactor;  $T_0$  is the temperature coefficient;  $d$  is the hopping space dimensionality. The fitted results according to the VRD model are shown in Figure A4.4.

In terms of GO[HT] aerogel, which is highly defective and impurities-contained, therefore its charge transport behaviour was specifically studied including using 1D VRH model, 2D VRH model and 3D VRH model. As shown in Figure A4.4a-A4.4c, the linear coefficient of the GO[HT] aerogel using 1D ( $R^2 > 0.921$ ), 2D ( $R^2 > 0.929$ ) and 3D VRH model ( $R^2 > 0.933$ ) is gradually increased, suggesting that the electrical conductivity of GO[HT] aerogel follows well with 3D carriers hopping between the interconnected highly defective GO sheets, across the whole aerogel monolith. This also indicates that the electrical current can reach everywhere of the aerogel structure to execute uniform Joule-heating, which is an essential theoretical background for GO-based aerogels executing uniform Joule-heating.

Importantly, the GO[HT] aerogel after thermal preconditioning via Joule heating where some impurities (e.g. adsorbed gases, chemical agents, and oxygen components in GO sheets) will be partially removed, leading to form more transport paths for carriers hopping in the entire aerogel monolith. As expected, the 3D VRD model fitting result shows excellent linear coefficient ( $R^2 > 0.986$ ), which confirms above assumptions (Figure A4.4c). As to the GO[30sec] aerogel that endured 30 s ultrahigh temperature Joule-heating treatment ( $> 2500$  °C), its linear coefficient matches outstandingly consistent with the 3D VRH model ( $R^2 > 0.998$ , Figure A4.4c), confirming that the impurities have been removed and the defective GO sheets have been well reduced to highly graphitized rGO sheets that provides large amounts of  $\text{sp}^2$ -bonded structures for carriers hopping. In summary, the GO-based aerogels are describing well with the 3D VRH model, no matter how defective the GO sheets are, offering the prerequisite that the electrons will reach up to the entire aerogel

monolith to carry out uniform Joule heating. However, to gain a better understanding why the electrical conductivity of GO[30sec] aerogel is substantially higher than the GO[HT] aerogel, bandgap concept is introduced below.

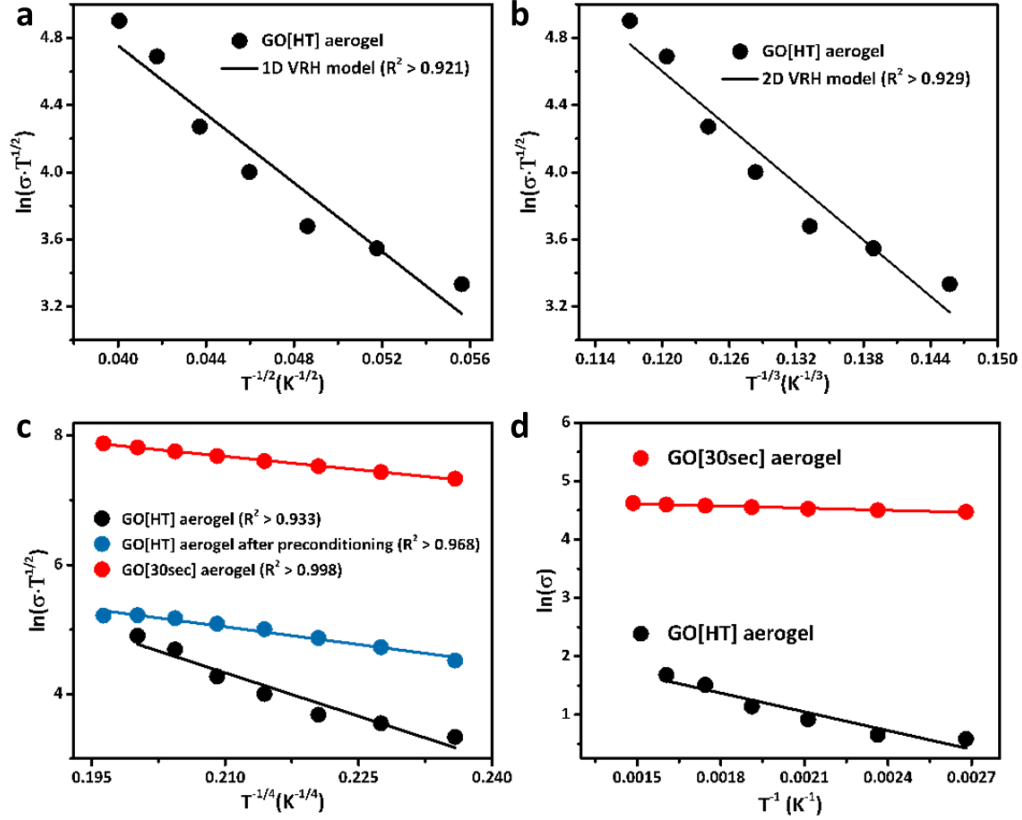


**Figure A4.4** (a) 1D VRH model fitting and (b) 2D VRH model fitting of GO[HT] aerogel. (c) 3D VRH model of GO[HT] aerogel, GO[HT] aerogel after preconditioning and GO[30sec] aerogel. (d) Arrhenius model fitting of GO[HT] aerogel and GO[30sec] aerogel (bandgap for GO[HT] aerogel is 0.09 eV and for GO[30sec] aerogel is 0.01 eV).

Studying the bandgaps in different reduction levels of GO aerogels is a short-cut to understand why the electrical conductivity of GO[30sec] aerogel improved significantly in contrast to GO[HT] aerogel. Therefore, the Arrhenius thermal activation model is used, as shown in Equation 2.

$$\sigma(T) = \sigma_a \exp\left(-\frac{E_a}{k_B T}\right) \quad \text{Equation 2}$$

Where  $\sigma_a$  is a pre-exponential factor;  $E_a$  is the activation energy; and  $k_B$  is the Boltzmann's constant. The detailed fitting results of Arrhenius thermal activation model is shown in Figure A4.4d. As  $E_a$  represents bandgap (namely energy barrier) in the Arrhenius thermal activation model, herein, the bandgaps of GO[HT] aerogel and GO[30sec] aerogel can be obtained after linear data fitting via  $E_a = k_B s$  ( $s$  is the linear fitting slope). According to obtained results, the bandgaps of GO[HT] aerogel and GO[30sec] aerogel are corresponding 0.09 eV and 0.01 eV, clearly manifesting the

pronounced improvement of electrical conductivity in GO[30sec] aerogel originates from considerable bandgap decrease.

#### **A4.4 Joule Heating Duration of Hydrothermal GO aerogels**

SEM images of as-prepared GO[HT] aerogel, GO[30sec] aerogel and GO[300sec] aerogel are presented in Figure A4.5a-f. In terms of GO[HT] aerogel, it profiles typical random morphology with clear hierarchies and macropores (Figure A4.5a), which is in concert with most reported hydrothermal GO aerogels. As to the GO[30sec] aerogel (Figure A4.5c), it maintains original morphology but showing much more interconnected and dense structures. Notably, the morphology of GO[300sec] aerogel is distinctly of difference in contrast to the GO[HT] aerogel and GO[30sec] aerogel, showing apparent signs of rGO restacking and reformation (Figure A4.5e). High magnification SEM images further clearly certify the microstructural variations, from less crystallization to high crystallization (Figure A4.5b, A4.5d, A4.5f). This crystallinity is also testified by XRD pattern (as shown in Figure A4.5g), namely the prominent characteristic peak (002) in XRD pattern gradually becomes sharper and more symmetric. Correspondingly, the Raman spectroscopy demonstrates that the super crystallinity in GO[300sec] aerogel is not derived from rGO sheets aggregations during high temperature Joule heating. As expected, the  $I_D/I_G$  ratio increased from 0.95 in GO[HT] aerogel to 1.83 in GO[30sec] aerogel, suggesting the excellent graphitization ability of flash Joule heating (Figure A4.5h). However, the  $I_D/I_G$  ratio substantially decreased to only 0.14 in the GO[300sec] aerogel, but with a pronounced sharp 2D band (the sharp 2D linewidth is around  $180\text{ cm}^{-1}$ ), indicating the formation of highly crystalline graphene (Figure A4.5h). In order to clarify that these nanosheets are near-perfect monolayer graphene with random stacking instead of aggregation, the Raman data are fitted with Lorentz fitting and the 2D band only exhibits a single Lorentzian peak, completely proving above assumptions. This result also explains the distinct morphology in SEM images of GO[300sec] aerogel compared to other two aerogels.

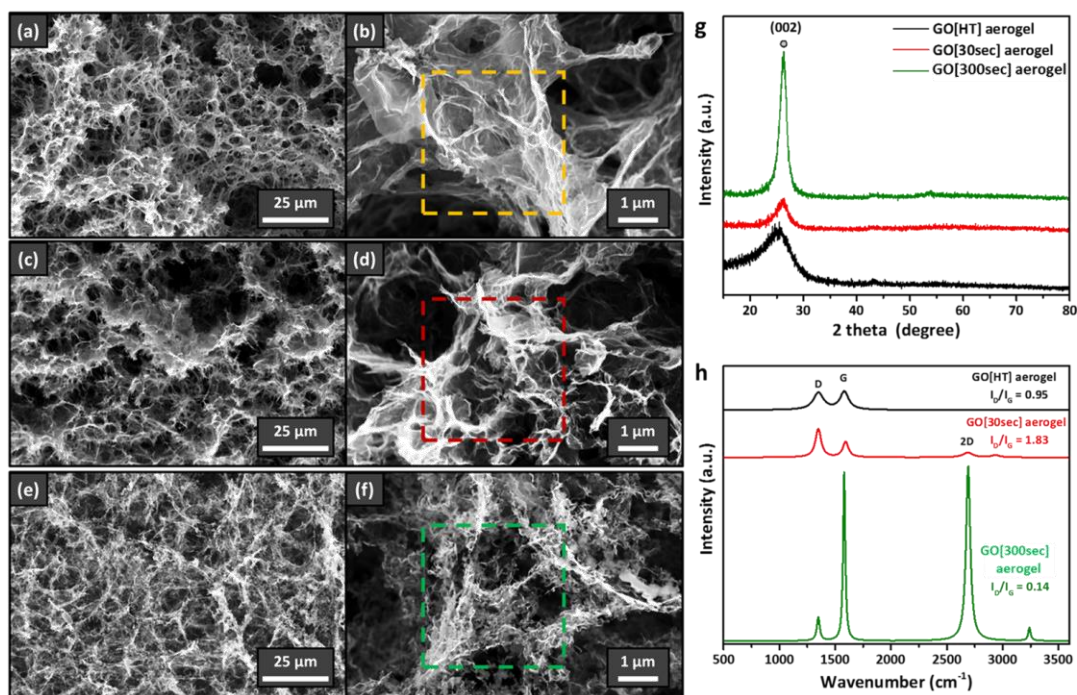


**Figure A4.5** SEM images of GO[HT] aerogel (a-b), GO[30sec] aerogel (c-d) and GO[300sec] aerogel (e-f) at different magnification. (g) XRD patterns and (h) Raman spectra of GO[HT] aerogel, GO[30sec] aerogel and GO[300sec] aerogel.

The surface homogeneity and morphology of as-prepared aerogels can be also detected via Raman mapping, as observed in Figure A4.6a-c. The obtained  $I_D/I_G$  ratios in Raman mapping follow well with the Raman spectroscopy, and the surface homogeneity gradually improved accompanying with different levels of thermal reduction. In detail, the surface of GO[HT] aerogel presents a dense and ununiform defective density as well as random morphology (Figure A4.6a), while the GO[HT] aerogel profiles more uniform  $I_D/I_G$  ratio distributions (Figure A4.6b), confirming a more homogeneous surface generated after flash Joule heating. In contrast, the surface homogeneity improved significantly in the GO[300sec] aerogel, in which the defective density plummets and the surface morphology presents outstanding uniformity (Figure A4.6c). In terms of TEM images (Figure A4.6d-f), all as-discussed aerogels exhibit very thin nanosheets indicating large-spaced nanosheet reassembly at hydrothermal stages rather than nanosheet aggregation (also demonstrating the well exfoliation of GO starting materials), but with the GO[300sec] aerogel exhibiting obvious and random nanosheet restacking (i.e. clear ridges formed, see Figure A4.6f), suggesting the successful reformation of microstructure or probably graphene welding appeared, after long time ultrahigh temperature Joule heating.

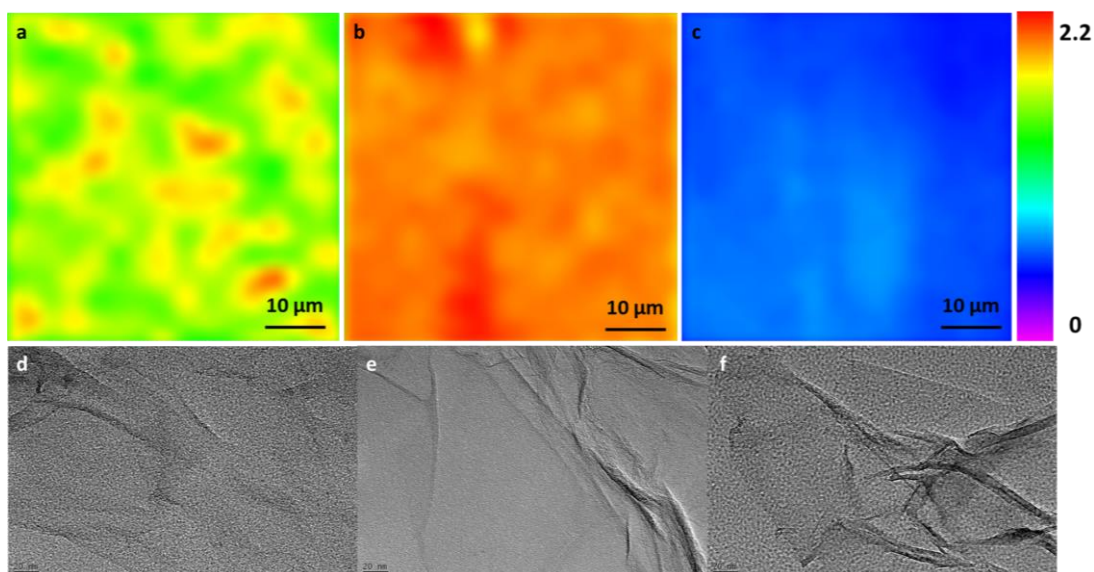


**Figure A4.6** (a-c) Raman mappings of the intensity ratio of the D peak to the G peak ( $I_D/I_G$ ) for the GO[HT] aerogel, GO[30sec] aerogel and GO[300sec] aerogel. TEM images of GO[HT] aerogel (d) and GO[30sec] aerogel (e) and GO[300sec] aerogel (f).

Additionally, XPS spectroscopy was also applied to analyse the elemental compositions and bonding states of as-discussed aerogels. For the GO[HT] aerogel, the XPS full spectra show that only carbon, oxygen and nitrogen elements are existed, but with carbon and oxygen dominations. However, after flash Joule heating, there is no nitrogen element anymore, and even the oxygen element is nearly nondetectable in GO[300sec] aerogel (Figure A4.7a), demonstrating the well graphitisation through flash Joule heating. The carbon compositions increased from 77.2 wt% in GO[HT] aerogel to 99.4wt% in GO[300sec] aerogel, accompanying with oxygen decrease. For the high-resolution C1s peak after deconvolution analysis in Figure A4.7b, there are clear three asymmetric shoulders existed belonging to oxygen-contained functional groups in GO[HT] aerogel. Corresponding, same analysing results of O1s peak in Figure A4.7e. However, the asymmetric shoulders apparently decreased and the C1s peak became more symmetric and sharper after thermal reduction, meaning the removal of large amounts of functional groups and forming a large number of  $sp^2$ -bonded structures. The deconvolution results of C1s in terms of  $sp^2$ -bonded structures marked a pronounced improvement, up to 57.5% in the GO[300sec] aerogel. In addition, the O1s peak in the GO[30sec] aerogel and GO[300sec] aerogel become very symmetric, suggesting only one type of oxygen-contained functional group left indicating the difficulty to fully recover structure-perfect graphene nanosheets. In summary, the XPS results demonstrate that ultrahigh temperature Joule heating ( $>2500$  °C) of a highly defective GO aerogel for only 30 seconds is completely enough to enhance its structural-electrical-thermal stability for various applications, but time-saving and energy-efficient.

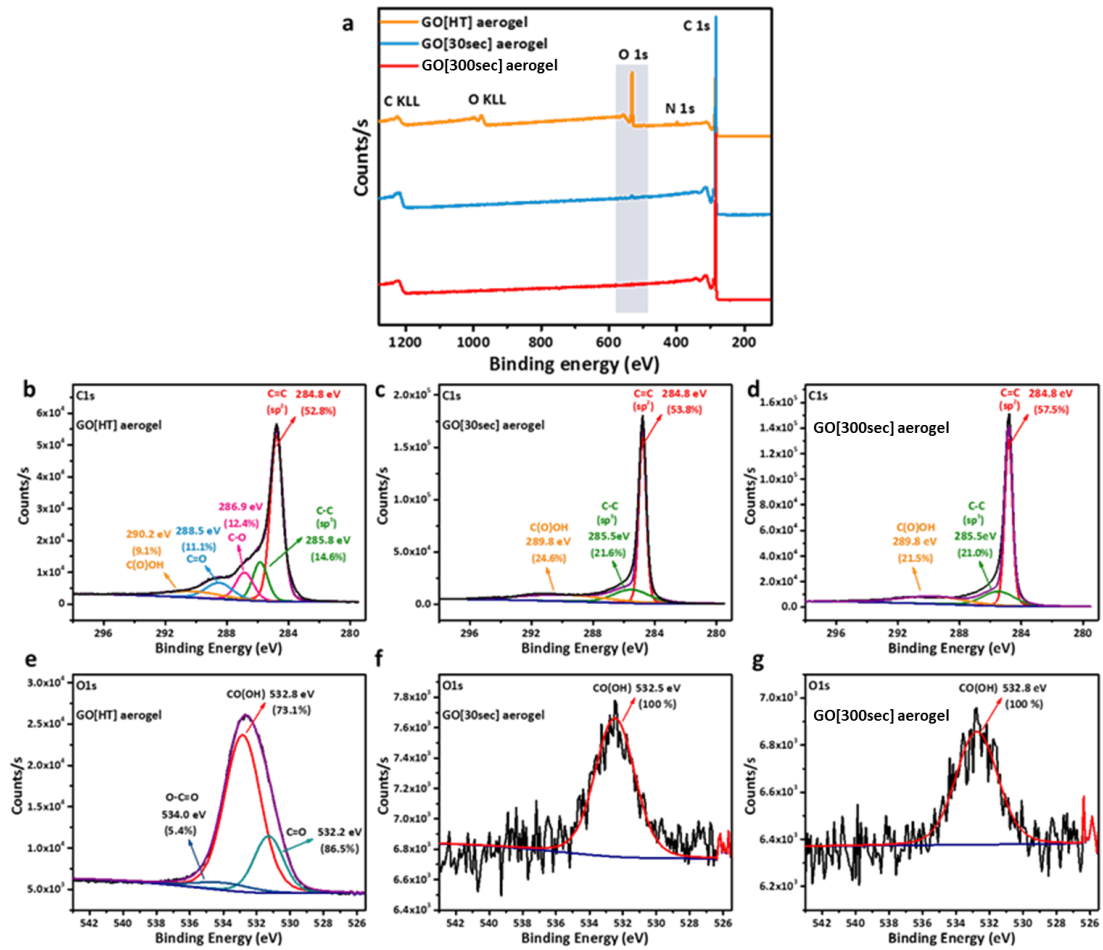


**Figure A4.7** (a) XPS full spectra of GO[HT] aerogel, GO[30sec] aerogel and GO[300sec] aerogel. XPS C1s spectra of GO[HT] aerogel (b), GO[30sec] aerogel (c) and GO[300sec] aerogel (d). XPS O1s spectra of GO[HT] aerogel (e), GO[30sec] aerogel (f) and GO[300sec] aerogel (g).

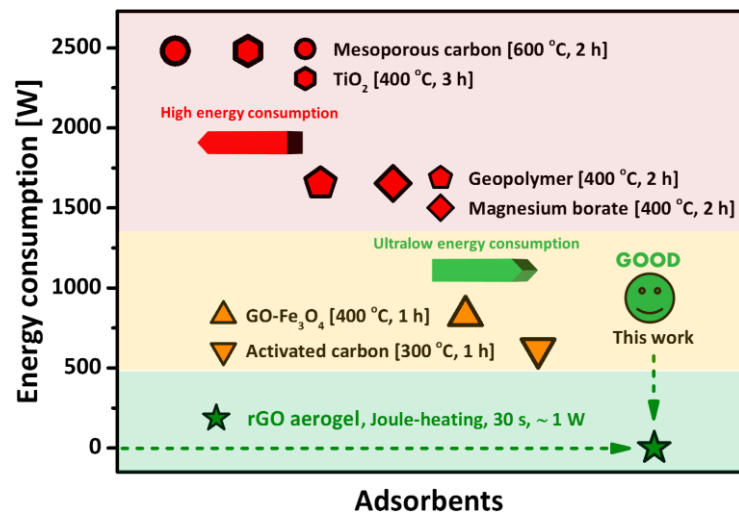


**Figure A4.8** Energy consumption comparison of dye-saturated adsorbent via traditional thermal methods from reported studies and flash Joule-heating in this work. Clearly, the sudden generated >2500 °C will decompose the dyes immediately, therefore the Joule heating time can also be shortened to save more energies, for example only 1 second Joule heating in future.

## A4.5 Flash Joule Heating of Producing Functional Nanoparticles

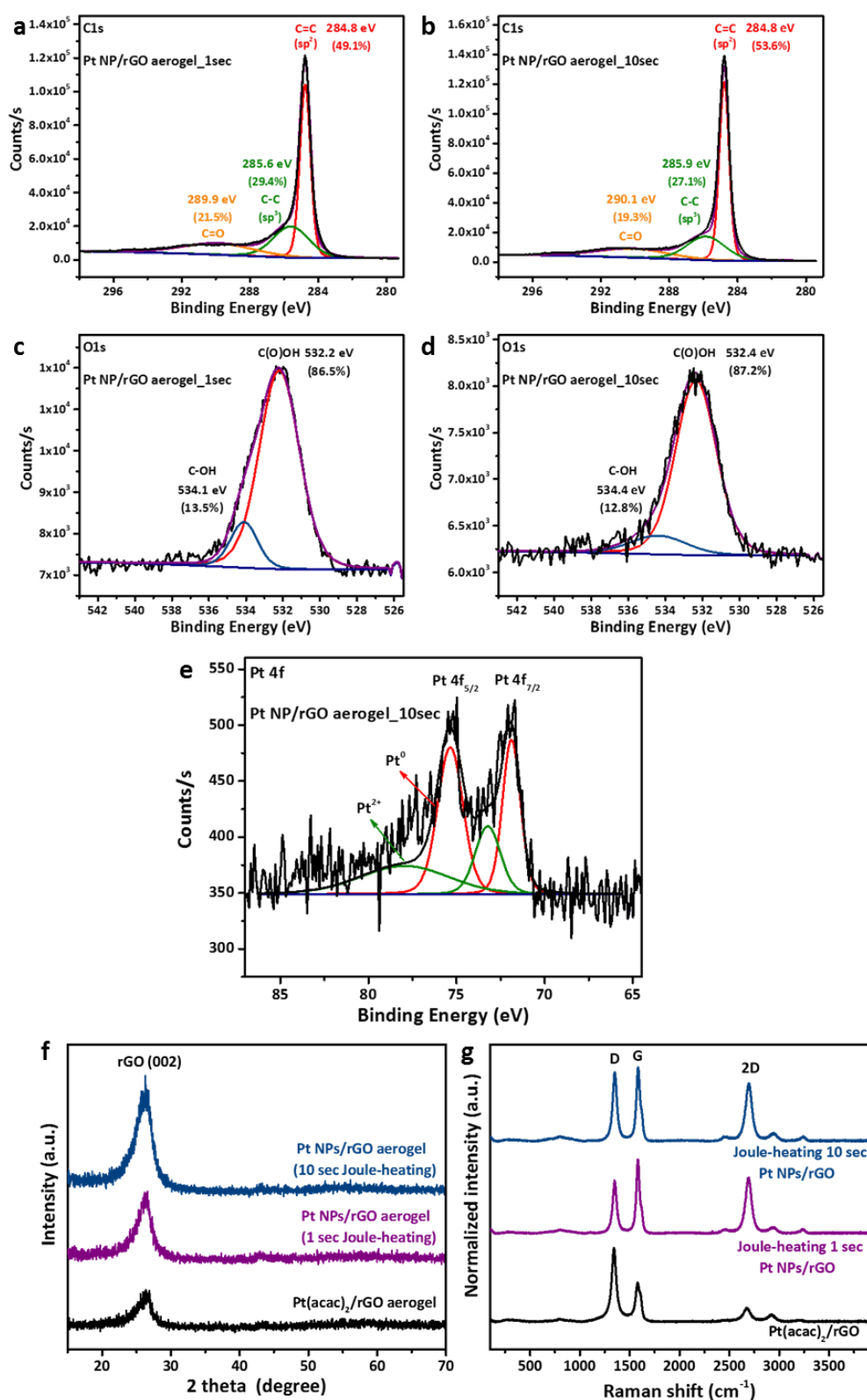


**Figure A4.9** XPS C1s peak of Pt NP/rGO aerogel\_1sec (a) and Pt NP/rGO aerogel\_10sec (b). XPS O1s peak of Pt NP/rGO aerogel\_1sec (c) and Pt NP/rGO aerogel\_10sec (d). XPS Pt 4f peak of Pt NP/rGO aerogel\_10sec (e). XRD patterns of pure rGO, Pt NP/rGO aerogel\_1sec and Pt NP/rGO aerogel\_10sec (f). Raman spectra of pure rGO, Pt NP/rGO aerogel\_1sec and Pt NP/rGO aerogel\_10sec (g).

In the light of better understanding that the flash Joule heating of metal precursors decorated rGO aerogels, hence XPS, XRD and Raman techniques were used to analyse structural variations. As the flash Joule heating temperature is ultrahigh, even the rGO aerogel which has been thermally treated at 1000 °C for 2 hrs also exhibiting obviously structural difference, with the  $sp^2$ -bonded components increased from 49.1 % in rGO aerogel with 1 second flash Joule heating (Figure A4.9a) to 53.6 % in rGO aerogel with 10 second flash Joule heating (Figure A4.9b), highlighting that even very short time Joule heating will cause clear component variations. These component variations can also be confirmed by the deconvolution of high-resolution XPS O1s peak (Figure A4.9c and A4.9d). The deconvolution analysis of high-resolution XPS Pt4f peak shows that the Pt NPs are dominated in the formation of metallic states which are in consistency with reported studies (Figure A4.9e), confirming the high metallic forming efficiency by flash Joule heating. XRD patterns also highlight that the longer Joule heating, the more crystalline the graphene nanosheets, namely the main diffraction peak of (002) plane are more pronounced and narrower (Figure A4.9f). Similarly, the peaks of G band and 2D band in the Raman spectra also have been way improved than that of corresponding starting  $Pt(acac)_2/rGO$  aerogels (Figure A4.9g), which are in concert with the XPS results.